Gaseous Detonation Initiation and Stabilization by Hypervelocity Projectiles

Thesis by

Michael Jiro Kaneshige

In Partial Fulfillment of the Requirements

for the Degree of

Doctor of Philosophy

California Institute of Technology

Pasadena, California

1999

(Submitted January 26, 1999)

Abstract

An experimental investigation of gaseous detonations initiated and stabilized by high-speed spherical projectiles has been carried out. Detonation initiation by projectiles is closely related to propulsion concepts such as the ram accelerator and the oblique detonation wave engine, in which, theoretically, rapid combustion occurs in detonation waves stabilized on solid objects. The criteria for initiation and stabilization by projectiles are also related to other initiation and propagation criteria such as blast initiation and failure of diffracting detonations. Experimental data of this type are useful for identifying relevant assumptions and important processes, and for providing validation for computational and analytical models.

Experiments were performed in the Caltech T5 shock tunnel laboratory. T5 was used in a shock-compression light gas gun mode, with 25.4-mm diameter nylon spheres and velocities around 2300 m/s. Gaseous mixtures studied included $2H_2+O_2+\beta N_2$ ($1\leq \beta \leq 3.76$), $C_2H_4+3O_2+5N_2$, and $C_2H_2+2.5O_2+9.4N_2$ at initial pressures of 0.08 – 2.56 bar. Flow visualization results obtained by differential interferometry, shadowgraphy, and intensified CCD imaging were augmented by wall pressure records.

A wide variety of results were observed, including non-detonative shock-induced combustion, unstably initiated detonations, stabilized prompt initiations, and stabilized delayed initiations. These results can be roughly correlated in terms of the ratio of projectile velocity to mixture Chapman-Jouguet detonation speed, and the ratio of projectile diameter to detonation cell size or reaction zone thickness, although the effects of confinement and unsteadiness complicate this categorization.

Two basic approaches to modeling the results have been attempted. In the first, a global model for initiation is based on an existing blast-initiation model using the hypersonic blast-wave analogy. This model is simple, and roughly predicts the experimental results, but suffers from a number of assumptions and approximations that restrict its usefulness and accuracy. The second approach, based on the local shock curvature, is not directly capable of predicting global initiation and failure, but illustrates the mechanism responsible for decoupling of the reaction zone from the shock front in cases of detonation failure. Coupled with a separate model for the shock shape, shock-curvature theory can be used for quantitative global predictions.

Acknowledgements

A number of people have influenced the work presented in this thesis. My advisor, Joseph Shepherd, has alternately led and prodded me through a challenging and immensely rewarding graduate school experience. He has given me the freedom to pursue my own course, and guidance when I needed it. I will always be indebted to him. Professor Hans Hornung was intimately involved in my research from the beginning, and I am grateful to him for his ongoing interest, and thoughtful contributions, and generous access to T5. I also thank Professors David Goodwin and Dan Meiron for taking the time to read my thesis and for serving on my examination committee.

Various members of the research groups in the Explosion Dynamics Laboratories and T5 have contributed to my research and education. Any specific list would be incomplete, but certain individuals deserve mention. Jacques Bélanger was instrumental in getting the experimental work started by designing and building the gas gun modifications to T5, and providing a crash course in operating T5. Raza Akbar patiently answered endless questions about detonations, and became a close friend through our work together in the Detonation Physics Laboratory.

Many individuals and groups throughout the Caltech community supported my efforts professionally. The staff of the Aero machine shop, the GALCIT secretaries, and the Caltech librarians each went beyond the call of duty at times.

My parents taught me the tenacity required to survive graduate school, and always encouraged me in whatever challenges I chose to pursue. Their support has been invaluable and essential. Last but certainly not least, Stacy Cooper has been a dear companion and confidant, without whom my last four years would not have been nearly as fulfilling.

This work was supported in part by the National Science Foundation through a Graduate Research Fellowship, and by Caltech.

Contents

List of Figures

List of Tables

Nomenclature

Roman characters

c	product-species concentration, moles per volume
C_D	drag coefficient
c_p	specific heat at constant pressure
D	detonation velocity
d	projectile diameter
E_0	cylindrical blast energy, dimensions of energy per length
$\hat{E}_a$	non-dimensional activation energy (Eq. 3.52)
E_a	Arrhenius reaction rate activation energy (Eq. 3.51)
$E_{c,x}$	critical energy for cylindrical detonation initiation, energy per length
$E_{p,x}$	energy deposited by projectile per length of travel (Eq. 3.1)
F	sonic parameter-like function (Eqs. 3.26 and 3.39)
F_d	projectile drag force
G	curvature coefficient (Eqs. 3.35 and 3.41)
G_1	in-plane curvature coefficient (Eqs. 3.63 and 3.65)
G_1	transverse curvature coefficient (Eqs. 3.64 and 3.66)
H	scale factor for orthogonal curvilinear coordinates, 1-$\kappa_1 y$
h	specific enthalpy, energy per mass
h_m	enthalpy of reaction, energy per mole
I	similarity blast solution integral (Eq. 3.3 and Table 3.1)
k_f	Arrhenius reaction rate frequency factor (Eq. 3.51)
M	Mach number
m	Arrhenius reaction rate reaction order
M_2	post-shock Mach number

M_n	post-shock shock-normal Mach number
P	pressure
$\hat{q}$	non-dimensional reaction-rate parameter (Eq. 3.52)
$\tilde{q}$	non-dimensional heat release, Q/RT_1
Q	energy released per mass of mixture
$\tilde{R}$	universal gas constant, 8.314 J/mol-K
R	gas constant, $\hat{R}/W$
r	radial coordinate, distance from the flow axis
R_c	radius of curvature of the shock at the nose
R_p	projectile radius, $d/2$
r_s	blast wave radius
s	streamwise distance
T	temperature
t	time
t_{ind}	induction time
T_s	post-shock temperature
U	projectile velocity
u	x-velocity
U_s	blast wave velocity
v	specific volume, $1/\rho$
V	total fluid velocity
v	y-velocity
W	molecular weight
X	axial shock coordinate normalized by shock-nose radius of curvature, z/R_c
x	shock-aligned coordinate (Fig. 3.1)

Y	radial shock coordinate normalized by shock-nose radius of curvature, r/R_c
y	shock-normal coordinate (Fig. 3.1)
z	axial coordiante, distance along the projectile path

Greek characters

α	dilution ratio
β	shock or detonation wave angle, relative to the flow axis
Δ	reaction zone thickness; shock stand-off distance, Eq. (6.2)
δ	flow deflection angle
γ	ratio of specific heats, c_p/c_v
κ_1	in-plane (x-y) shock curvature
κ_2	transverse (y-ζ) shock curvature
μ	Mach angle, $\sin^{-1}(1/M_\infty)$
ϕ	non-dimensional temperature change (Eq. 3.68)
ρ	density
λ	detonation cell width (Fig. 1.2(a))

Acronyms

CJ	Chapman-Jouguet
DDT	Deflagration-to-Detonation Transition
GDT	GALCIT Detonation Tube
ICCD	Intensified CCD (Charge-Coupled Device)
NASP	National AeroSpace Plane
NDWE	Normal Detonation Wave Engine
ODWE	Oblique Detonation Wave Engine
PLIF	Planar Laser-Induced Fluorescence
ZND	Zeldovich-von Neumann-Döring

Subscripts

∞	free stream condition
1	initial state
CJ	pertaining to the Chapman-Jouguet condition

Chapter 1 Introduction

1.1 Overview

Flow over a blunt body is a classic benchmark for fluid dynamic analyses, either purely theoretical or computational, under a wide range of conditions. This model and its variants are used to demonstrate understanding of the relevant physics at high and low ranges of Reynolds number and Mach number, in non-reactive and reactive media, and in different numbers of dimensions. Although significant work has been done (see Chapter 2), one of the least studied regimes is that of hypersonic, reactive flow. This type of flow has current relevance to both applied and fundamental studies (see Section 1.2).

The present work is concerned with initiation and stabilization of detonation waves on high-speed projectiles in combustible gas mixtures. When a projectile is shot into a combustible mixture at supersonic speed, the result is determined by the properties of the mixture, the speed, size, and shape of the projectile, and by the dimensions and nature of the mixture containment. The projectile may serve as an ignition source for combustion. If ignition occurs, it will generally take the form of deflagration or detonation. The deflagration process is much slower than the supersonic projectile speed, and always occurs behind the bow shock of the projectile. Detonations, however, may propagate faster than the projectile, and may be coupled or decoupled from it.

Substantial analytical and numerical efforts have been aimed at all regimes of combusting flows over supersonic blunt bodies, and a number of experimental programs have demonstrated shock-induced combustion and initiated but decoupled detonation, but very little experimentation has been done on detonations stabilized on projectiles. Naturally, the theoretical and numerical models applied to practical and fundamental detonation stabilization phenomena must be validated by comparison with experiments. The aim of this work is to fill this gap with an experimental investigation of the critical conditions governing the transition between shock-induced combustion and detonation initiation and stabilization.

1.2 Motivation

The essential reason gaseous detonations are of interest is that they liberate chemical energy rapidly and violently into thermal and mechanical energy. From a practical perspective, this property makes detonations relevant principally to safety, where they are to be avoided, and to certain propulsion

concepts, where they are to be desired and controlled. On a fundamental scientific level, detonations are of interest because they represent a nexus between gas dynamics and chemistry.

The application of the present work to safety analyses is relatively weak, although any scientific understanding gained through one avenue of investigation can benefit others. Most of the traditional dynamic detonation parameters are of direct interest to real detonation hazards, and correlations between the different parameters have been useful for physical interpretation of the underlying mechanisms, and for making quantitative estimates of one parameter from existing data concerning another. Considering the critical conditions for projectile initiation as dynamic parameters naturally extends this process.

Several propulsion applications of detonations that require stabilizing a wave on an object are more clearly related to projectile initiation. The super-detonative ram accelerator and the external-propulsion accelerator superficially resemble detonation initiation and stabilization on a projectile, although the present experiments should not be considered developmental of those devices. However, certain aspects of the flow, such as the necessary conditions for initiation and stabilization on an object, and the behavior of reflecting shock and detonation waves, are of direct importance. In particular, oblique detonation waves are a common component of stabilized detonation propulsion schemes, and are notoriously tricky to study experimentally. Finally, as with other engineering applications of detonation or other high-speed combustion processes, computational modeling is necessary as a design tool, and requires validation against experimental data. The range of conditions and phenomena observed in the present projectile-initiation experiments are similar to what a simulation must be able to reproduce for realistic analysis of propulsion designs.

Use of projectile-initiation data for production of finite-rate chemical kinetic data has been proposed [54]. Since there is no clear way of measuring an individual reaction rate from projectile-initiation data, and since optimization of a global mechanism can be done far more easily with other types of data, it seems unlikely that reaction-rate information will be derived in this way. However, modeling of the flow around a projectile using a detailed reaction mechanism may certainly serve as a challenging test of the integration of the mechanism with a flow solver. Likewise, hypersonic flow over a blunt body has been extensively studied, including consideration of the effects of finite-rate dissociation [58, 59]; and the possibility of exothermal reactions is a natural extension of these studies.

1.2.1 Propulsion

Most propulsion concepts incorporating detonation waves utilize oblique detonations stabilized on an object, relative to a moving gas mixture. The notable exceptions are the normal detonation wave engine, which is considered inferior to the oblique detonation wave engine because of practical and theoretical performance limitations, and the pulsed detonation engine, which uses the completely

unsteady process of detonations propagating through a stationary mixture.

Oblique Detonation Wave Engine

The only steady detonation-based concept under consideration for air-breathing aircraft propulsion is the oblique detonation wave engine (ODWE). Although more development work has been done on conventional supersonic combustion ramjet (scramjet) engines, the ODWE offers some potential advantages for propulsion of hypersonic aircraft.

Detonations are well suited for hypersonic propulsion because they inherently represent supersonic combustion. Supersonic combustion is necessary because the inlet diffuser process necessary to decelerate an incoming hypersonic flow to subsonic speeds normally generates excessive stagnation pressure losses that seriously degrade engine performance. Combustion in the form of detonation occurs very rapidly, permitting a very short combustor, relative to a deflagration-based combustor. Thus, an ODWE may be more compact than a conventional scramjet. However, ODWEs have some notable disadvantages; this perhaps explains the lack of development of the concept. Compared to a deflagration-based scramjet, stagnation pressure losses in the combustor of an ODWE are large. In common with the scramjet, the ODWE faces the difficulty of mixing fuel into a supersonic air stream in a short distance, and can not generate thrust at subsonic speeds. Furthermore, stabilized detonations have been studied much less than stabilized deflagrations.

The concept of the ODWE, and that of its predecessor, the normal detonation wave engine (NDWE), originated during the 1950s and 1960s, but were eclipsed by rocket engines for hypersonic propulsion. Interest was renewed by National Aerospace Plane (NASP) type efforts to develop a hypersonic air-breathing vehicle, although most attention was directed at scramjets. The demise of the NASP project predictably led to a decrease in work on both engine concepts. Pratt et al. [92] give a comprehensive review of the current state of ODWE development, and Shepherd [103] gives a general discussion of oblique detonation waves, and their application to propulsion.

Ram Accelerator

An application of oblique detonation waves for propulsion that is closer to deployment is the superdetonative ram accelerator. Rather than propelling a vehicle through the atmosphere, the ram accelerator is restricted to accelerating a projectile through a tube. The advantage is that the projectile does not carry its propellant, and indeed is normally considered to be completely passive. An obvious disadvantage is the limitation of thrust to the projectile travel within the tube. High speeds require high accelerations and/or a long tube, virtually eliminating the possibilities of launching manned vehicles or of steering the launcher. Therefore, the ram accelerator is best suited to applications involving a fixed launcher and simple projectiles, such as insertion of bulk raw materials into low earth orbit, hypersonic research, and impact dynamics studies.

Ram accelerators generate thrust by compressing the propellant mixture between the projectile and the tube wall, to the point of ignition, and then expanding the combustion products on the rear of the projectile. Combustion can take the form of deflagration or detonation, depending on the speed of the projectile, and is actually found to transition from deflagration to detonation as the projectile accelerates. The classic arrangement has a non-reactive bow shock attached to the front of the projectile and reflecting from the tube wall as a detonation wave, confining combustion to the sides of the projectile, since combustion ahead generates negative thrust.

Prototype ram accelerators have been built at the University of Washington [49], the Institute of Saint-Louis in France [101], and at the U.S. Army Research Laboratory in Aberdeen, Maryland [68, 69], among others. Performance has been encouraging, although the theoretical limitations have not been approached. Reviews of the history, state of the art, and prospects of the ram accelerator are given by Hertzberg et al. [48, 50], Bogdanoff [17], Rom [96], and Bruckner [18].

Other Concepts

More speculative concepts for the use of detonation waves in propulsion are the external propulsion accelerator (Rom [95, 96]) and the detonation-driven hollow projectile (Thibault et al. [112]). Both are like the ram accelerator in that they propose to accelerate projectiles within a combustible mixture, and thus have roughly the same operational limitations.

The projectile in the external propulsion accelerator travels in an "unconfined" mixture, and while the detonation-driven hollow projectile has been proposed for travel in an unconfined mixture, its advantages may be retained or even enhanced in a launch-tube geometry. Few studies and no demonstrations have been made of either device.

1.2.2 Dynamic Parameters

Propagating detonation waves not near failure are very well understood in some aspects such as mean wave speed, pressure, and related parameters (see Section 4.2). These "hydrodynamic" or "static" parameters can be evaluated with remarkably accurate results using a control volume approach, ignoring the microscopic spatial and temporal structure of the wave, and considering only equilibrium chemistry. Therefore, they are rarely the subject of active research, and are generally treated as engineering quantities.

Less understood are the "dynamic parameters" of detonation (Lee [73]), which are related to the microscopic structure of detonations and determine their behavior near initiation and failure. The key ingredient in the analysis of dynamic parameters that makes them challenging is the finite rate of the elementary chemical reactions which give rise to the spatial and temporal structure of detonations. Numerous theories and models exist that capture the *general* behavior of the dynamic parameters, but the broad generality and accuracy characteristic of prediction of the static

parameters are elusive. Thus, dynamic parameters are common subjects of detonation research.

Dynamic parameters quantify the dynamic aspects of detonation initiation and failure. Examples are the critical energy of initiation, the critical tube diameter from which a propagating detonation can diffract and not fail, and the minimum tube diameter in which a detonation can propagate. The detonation cell size is also generally considered a dynamic parameter because it characterizes the microscopic initiation, propagation, and failure processes that continuously occur within a detonation front (see Section 4.3).

The critical conditions necessary for detonation initiation by a projectile may also be considered dynamic parameters. In particular, for a given mixture and thermodynamic state (and possibly for a specific set of boundary and initial conditions), the critical projectile size and velocity are dynamic parameters. Of course, having two parameters for a single criteria is not aesthetically pleasing. Possibly the product of the two quantities is a more appropriate parameter.

Like the established dynamic parameters, the critical product of projectile speed and size describes an initiation process that involves competition between chemical heat release and the quenching effects of expansion. To fully define the quantity of interest, the dimensionality (two or three dimensions), geometry (e.g., conical, spherical, flat), and boundary and initial conditions (containment size and shape, entrance process, and distance from entrance) must be specified. The description is further complicated by the issue of stability. Nominally, an initiated detonation will be stabilized on the initiating projectile (at least in the limits of infinitely large containment and long travel distance) if the projectile velocity is greater than the detonation speed. The processes of initiation by sub-CJ and super-CJ projectiles may be significantly different, however, since the sub-CJ initiation is globally unsteady, whereas the super-CJ initiation must eventually be steady (or perhaps periodic).

Dynamic parameters are important generally because they define how and when detonations will occur, which is important whether they are desired (as in propulsion devices) or not (as in hazard evaluations). Progress in understanding one dynamic parameter often leads to better understanding of others. Many models relate the physics involved in one process with those in another. Likewise, all of the considerations that contribute to deciding failure or initiation of detonation around a projectile (e.g., expansion around the projectile, unsteadiness at entry, shock reflection off containment walls) are also relevant when considering other dynamic parameters. Therefore, studying and understanding projectile initiation should lead to better understanding of other dynamic parameters of detonation.

1.2.3 CFD Validation

For all the applications of detonations mentioned above, computational modeling is an important design tool. In some ways, accurate modeling of detonations (and related phenomena during initiation

and failure) is very difficult. In terms of numerical magnitude, the detonation front requires high spatial and temporal resolution, while realistic chemistry modeling requires tracking a large number of species and reactions. Simplified models are plentiful, but are generally only qualitatively useful, or are accurate in a limited range of conditions. Of key importance to any model, and especially for simplified versions, is validation against experimental data. For this, flow over a blunt projectile is a standard, yet challenging case.

Ballistic experiments can be tricky to model or simulate because frequently, among other difficulties, the boundary and initial conditions defining the experiment are either not well known or else seriously complicate the model. Typically, extrapolation boundary conditions at the outside and rear boundaries of the solution domain are used to simulate an unconfined geometry (e.g., Lefebvre and Fujiwara [76]). Unsteady numerical solutions are allowed to run until a pseudo-steady flow is established. Thus, the simulations are designed to be independent of extraneous effects such as wave reflections from walls and the starting process. This is natural for studies focused on the flow around the projectile.

Likewise, a common goal of experiments is to eliminate the effects of the boundaries and the entry process from the results (e.g., Higgins [51]). Certainly, close attention must be paid to the boundary effects in order to draw conclusions and also to provide useful data for comparison with models and simulations. Confinement tends to have a positive effect on detonation initiation, although the influence of the containment may not be apparent. It can also be difficult to tell from instantaneous images if the phenomena observed are steady or transient. In the present experiments, some effort was made to reduce the effect of the entry process, but generally the containment could not be ignored. Instead, care was taken to specify the actual boundary conditions clearly. In fact, it is felt that simulations should be able to demonstrate accurate modeling of these effects, especially where the purpose is to eventually serve practical engine or launcher design efforts.

1.3 Background Concepts

Comprehensive discussion of elementary detonation theory and the general state of the science will not be given here. Excellent sources on the subject are available elsewhere. General discussion of detonation theory and phenomena is given by by Strehlow [109] and Fickett and Davis [37]. Oblique detonation waves are discussed by Pratt et al. [92] and Shepherd [103]. A brief explanation of basic principles, with some emphasis on particular details relevant to the present study, will be provided.

1.3.1 Hydrodynamic Theory

The simplest possible detonation model is the hydrodynamic theory, which considers the wave as having no spatial or temporal structure. Analysis proceeds by applying the integral forms of the

basic conservation equations (mass, momentum, and energy), and an equation of state, typically for the ideal, perfect gas. The energy equation includes a term to account for heat release from combustion. The fluid properties can be considered constant on both sides of the wave, or different properties can be used on either side. The solution of the governing equations is often considered

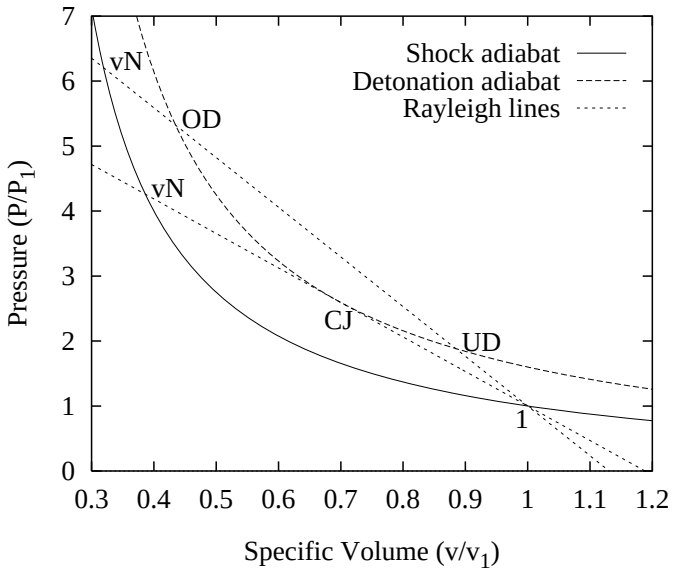

Figure 1.1: Rankine-Hugoniot plot with $\tilde{q} = 1.5$, $\gamma = 1.4$.

graphically in the pressure-specific volume plane, as in Fig. 1.1. Eliminating velocity gives the Hugoniot (adiabat) curves, corresponding to no combustion (shock adiabat) and with combustion (detonation adiabat). The amount of chemical energy release is specified by the non-dimensional quantity $\tilde{q} = \frac{Q}{RT_1}$, where Q is the energy released per mass of mixture. Combining the mass and momentum equations gives the Rayleigh line, the slope of which depends on the detonation Mach number. For arbitrary Mach number larger than a certain minimum, the Rayleigh line intersects the detonation adiabat at two points, corresponding to the overdriven (OD) and underdriven (UD) solutions. The underdriven solution normally can not be obtained in a steady process, but overdriven waves are observed. Figure 1.1 was generated with constant fluid properties in the reactants and products.

1.3.2 Chapman-Jouguet Condition

At a certain minimum Mach number, the Rayleigh line in Fig. 1.1 is tangent to the detonation adiabat. This is the Chapman-Jouguet (CJ) condition. One unique characteristic of the CJ point is that the Mach number of the products, relative to the wave, is unity. Another unique characteristic is that the entropy of the products is a minimum. However, the most notable characteristic is that propagating detonations tend to travel very near the CJ speed. The most physically intuitive explanation for this fact is that detonations are usually initiated by a sudden release of energy or

impulse, but are subsequently unsupported. Initially, the detonation is overdriven and the flow of products is subsonic, such that expansion waves reach the detonation from behind and cause it to decelerate. As the wave decays to the CJ state, the flow behind approaches the sonic condition, and expansion waves become unable to penetrate the detonation, so its velocity stabilizes.

1.3.3 ZND Model

The hydrodynamic model is elegantly simple, and is very successful at predicting mean properties of propagating detonations (see Section 4.2), even while ignoring the thickness and structure. The simplest model that includes any consideration of structure is the Zeldovich-von Neumann-Döring (ZND) model. In the ZND model, a non-reactive, adiabatic shock wave is followed by a reaction zone of finite thickness [37]. Usually the reaction zone can be broken down into an induction zone, where the thermodynamic state is roughly constant, and a recombination zone, where most of the chemical reaction and heat release occur. In the simplest version, the flow approaches the CJ state at the end of the reaction zone.

Structure in the ZND model is restricted to the direction normal to the wave front. It can include time variation, but usually only steady solutions are considered. Thus, the governing equations become ordinary differential equations. Initial conditions are taken to be the post-shock state, where the shock strength is determined from the hydrodynamic model and the Chapman-Jouguet condition. The effects of chemistry are included in the fluid properties and in the energy equation. Progress of each elementary reaction is determined from rate equations, which normally take the Arrhenius form. The main result of computing the ZND structure is a value for the thickness of the reaction zone. The reaction-zone thickness is not particularly meaningful by itself, since real detonations do not exhibit a unique thickness. However, the calculated ZND thickness can be interpreted as an average and can be correlated to other scales.

1.3.4 Observed Detonation Structure

Fully three-dimensional and unsteady detonations always exhibit instability that manifests itself as irregularities that travel across the propagating wave front. These irregularities form Mach stems where the reflected waves appear as transverse waves behind the main front, see Fig. 1.2(a). The spacing of adjacent transverse waves is a characteristic of the mixture composition and thermodynamic state, and the speed of the wave. Since most detonations propagate at the CJ speed, wave speed is normally not specified, and CJ speed is assumed. As the transverse waves travel back and forth across the main wave, they trace a cellular pattern on a plane surface. This cellular pattern can be recorded, and the widths of the cells indicate the spacing of the transverse waves (see Section 4.1.1). Fig. 1.2(b) shows a typical record made by the soot foil technique. The detonation wave

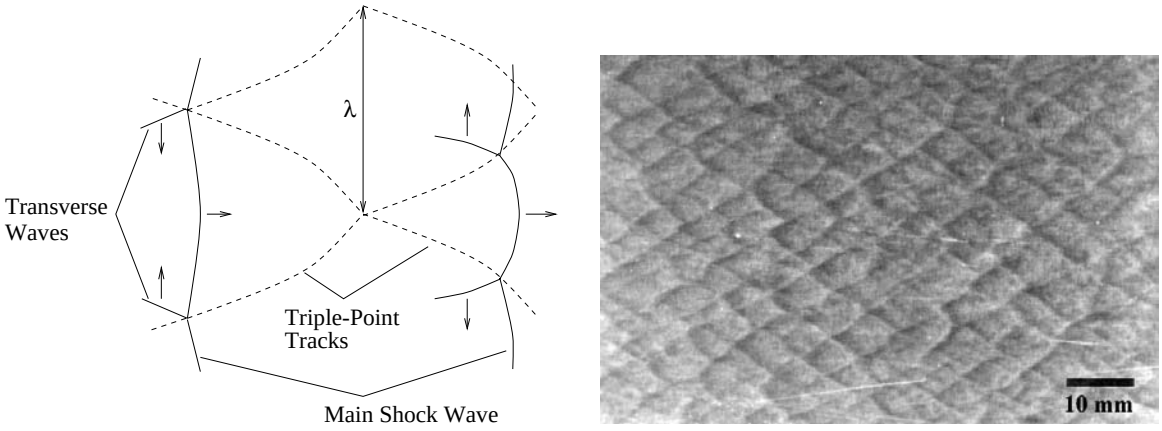

(a) Detonation cellular structure.

(b) Soot foil record from GDT shot 533: $2H_2+O_2+2N_2$ at 50 kPa initial pressure.

Figure 1.2: Cellular structure of a gaseous detonation wave and an example soot foil record.

travelled from left to right in the image.

1.3.5 Predicting Cell Size

Numerous models and numerical simulations of the cellular structure of detonation waves exist and succeed at capturing the essence of the flow [93, 107]. General dependence of cell size on flow conditions (activation energy, pressure, wave speed, etc.) are reproduced, and computational results are remarkably realistic in appearance. However, virtually all models and simulations use highly simplified chemistry or gasdynamics models. High-resolution three-dimensional calculations rapidly become more expensive as more reactions are considered, so most models consider only a single, irreversible, Arrhenius rate reaction.

The approach taken in the present work, as described in Section 4.3, is to compute reaction-zone thicknesses for CJ detonations using detailed chemistry and the steady ZND model, and to correlate experimentally measured cell sizes to the computed reaction-zone thicknesses. The empirical correlation masks much of the simplification and uncertainty in the mathematical model and reaction mechanism, while being cheap to implement and reasonably accurate within certain restrictions. In particular, a given correlation is useful for a specific fuel-oxidizer-dilution combination and equivalence ratio, over a range of dilution and initial pressure.

1.3.6 Methods of Producing Stationary Detonations

Initiation by projectiles is a relatively novel method of studying stabilized detonation waves. Several other techniques have been attempted, each with some advantages and disadvantages. As noted by

Shepherd [103], the central problem faced by any method that relies on a supersonic gas stream is providing the gas with a sufficient stagnation enthalpy for detonation to occur, without igniting it prematurely. If a premixed gas is accelerated from rest, such that its static conditions are the stagnation conditions, it will usually burn immediately. This can be avoided by accelerating the fuel and oxidizer separately, and mixing under lower static conditions, but this introduces the problem of thoroughly mixing the fuel and oxidizer at high speeds.

Stationary Wedge

Many efforts at stabilizing an oblique detonation on a stationary wedge have only succeeded in stabilizing a shock wave with slow combustion behind it. Recently, evidence was provided by Morris et al. [89] of oblique detonation waves generated by an expansion tube flow over a wedge.

Underexpanded Supersonic Jet

Theoretically, normal detonation waves can be stabilized as a Mach disk in an underexpanded jet. No successful demonstrations with this technique are known, despite some efforts [45].

Gasdynamic Wedge

Although not truly stabilized, as in a projectile flow, one method that directly avoids some of the difficulties inherent in the others is the gasdynamic wedge. In this configuration, two layers of explosive with different detonation velocities are separated by a membrane. A detonation is initiated in the higher detonation-speed explosive, and the combustion products drive a wedge into the lower-speed explosive which propagates forward at the higher detonation speed. From a reference fixed in the wedge, the less sensitive mixture is flowing at super-CJ speed over the wedge, so under appropriate conditions, a stabilized oblique detonation is expected. Oblique detonations have been observed with this technique by Viguier et al. [119] and Tonello et al. [114].

1.3.7 Phenomenology of Projectile Initiation

For a given mixture and initial conditions, the result of shooting a projectile at high speed is primarily determined by the projectile size and velocity. Other influences, such as projectile shape, containment geometry, and entry process, are considered secondary. The global question of detonation initiation or failure can be considered in terms of large and small values of the projectile size and shape, yielding four distinct limit regimes, as illustrated in Fig. 1.3.

In all cases, the projectile velocity is assumed to be supersonic, and large enough to induce combustion. That is, the stagnation temperature is at least as large as the autoignition temperature. If this requirement is relaxed, a completely non-reactive shock can occur for both small and large

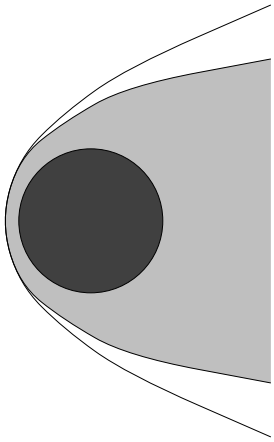

(a) Steady shock-induced combustion

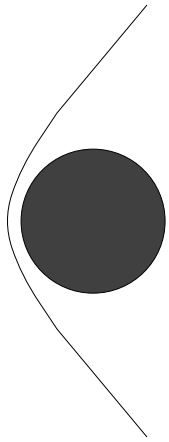

(b) Stabilized detonation

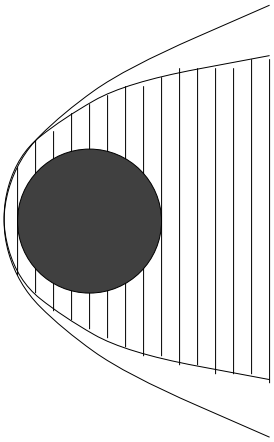

(c) Unsteady shock-induced combustion

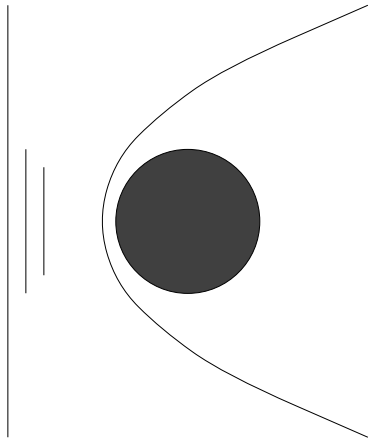

(d) Unstable detonation initiation

Figure 1.3: Regimes based on projectile size and velocity.

projectiles, at low supersonic speeds. In Fig. 1.3(a), the velocity is above the CJ speed, so the part of the bow wave on the stagnation streamline has the strength of an overdriven detonation, and fluid passing through this region ignites quickly. However, expansion of the flow around the projectile is strong enough to quench the combustion, and the flow separates into reacted and unreacted regions where the expansion just manages to quench the thermal explosion. If the projectile is large enough that the expansion is too weak to quench the combustion before the wave has decayed to the CJ state, the bow wave is expected to become a straight, self-supporting CJ detonation in the far field, as shown in Fig. 1.3(b). The case shown in Fig. 1.3(c) is similar to that shown in Fig. 1.3(a) in that expansion around the projectile quenches combustion, but at lower speed, ignition does not occur promptly behind any part of the bow wave. When ignition does occur, it is observed to form

nonsteady oscillations. As the velocity decreases to the point that the stagnation temperature equals the autoignition temperature, the frequency of these oscillations approaches zero. Finally, at low velocity but large projectile size (Fig. 1.3(d)), the stagnation region behind the initial bow shock is large enough to support a thermal explosion that develops into a detonation. The detonation wave outruns the projectile, leaving it with a non-reactive bow shock in a free stream of combustion products.

Of course, the scheme illustrated in Fig. 1.3 is highly simplified. No effects of boundary or initial conditions are considered, except to conceptually set up the globally unstable case of Fig. 1.3(d). Some hypothetical mechanisms leading to the different phenomena have been described, although detailed models are necessary for quantitative analysis. In particular, how and when transitions between the different regimes occur are not considered. In fact, in some cases it may not be meaningful to consider limits of size and velocity simultaneously. For instance, the configuration shown in Fig. 1.3(a) is appropriate if the projectile speed is fixed at some super-CJ value and the projectile size is decreased sufficiently. At any small size, if the velocity is increased sufficiently, a stabilized detonation may result.

Another factor to consider is the possibility that the flow solution for a given size and speed may not be unique. For example, stabilized detonation and shock-induced combustion may both be solutions at a particular condition, and in reality the actual event may be determined by the initial and boundary conditions.

The focus of the present study is on stabilized detonation initiation and failure, but consideration of other possible outcomes is relevant and sometimes necessary.

1.3.8 Hypersonic Blast-Wave Analogy

An important concept used in the Lee-Vasiljev model of critical projectile initiation is the hypersonic blast-wave analogy (see Chapter 3). A thorough discussion of the analogy is given by Anderson [5]. A brief review will be given here.

Briefly, the hypersonic blast-wave analogy relates the drag force on a body in steady, inviscid hypersonic flow to the instantaneous release of energy along a line. The analysis begins by noting that the equations of motion governing steady flow over a slender body in the hypersonic limit are similar to the equations for unsteady flow in one less spatial dimension, assuming a hypersonic blast wave. For steady axisymmetric flow, the analogous unsteady flow has cylindrical symmetry. The axial coordinate z in the steady axisymmetric flow relates to the time coordinate t in the unsteady cylindrical flow through the relation $z = V_\infty t$, where V_∞ is the axial flow velocity.

Strictly speaking, the steady flow equations are formulated for a slender body, assuming the perturbation velocities are small compared to the free-stream velocity. This is not valid for a blunt body, since the perturbation velocity in the stagnation region is on the order of the free-stream

velocity, but the approximation is good far from the stagnation region.

Neglecting heat transfer to the body and heat release from chemical reactions, the only energy addition to the gas is the mechanical work done by the body, which per length, is equal to the drag force. The amount of energy deposited by the body drag in a distance δx is equivalent to the release of the same amount of energy in the unsteady cylindrical case in a time $\delta x/V_\infty$. For a blunt body, the energy due to drag is concentrated at the front of the body, which is equivalent to an instantaneous release of the same amount of energy in the unsteady cylindrical flow. Therefore,

$$F_d = E_0 \tag{1.1}$$

where F_d is the drag force on the body, and E_0 is the cylindrical blast energy.

The usefulness of the blast-wave analogy stems from the existence of exact solutions to the strong blast. The solution for the spherical blast wave is given by Taylor [111], and solutions are also given for the cylindrical case by Sedov [100].

1.4 Scope

Primarily through experiment, the work presented here aims to expand understanding of the behavior of combustion processes initiated in gases by high-speed projectiles. In particular, the conditions necessary for initiation of detonation at projectile speeds above the Chapman-Jouguet detonation speed have been explored.

Of ultimate interest is a predictive model that is independent of a particular chemical mixture and condition. In this direction, experiments were performed with a variety of mixtures and pressures. Stoichiometric mixtures with several fuels were used, with various amounts of nitrogen dilution, and at a range of initial pressures. Initial temperature was not varied. Although the lateral dimensions of the containment were not varied, effects of distance from the entrance were investigated.

A number of topics explored or measured by other investigators were not considered, and these are worth mentioning. Although equipment was built to allow use of a different launch tube bore, variation of projectile size and shape was not performed. Only one type of projectile was used: 25.4-mm diameter spheres. Some variation in projectile velocity occurred as a result of changing the launcher conditions and through random variations in its performance, but no systematic effort was made to control velocity, and the actual variation was small. Because emphasis was placed on super-CJ velocities, shock-induced combustion was observed, but oscillating combustion was not, and consequently this behavior was not studied. Finally, while projectile velocity was measured, usually between several sets of detectors, variation of the velocity during the projectile flight was not measured, and in fact the velocity was assumed constant. Therefore, no conclusions about drag

or thrust were made.

In the following chapters, the experimental program, some theoretical considerations, and supporting work will be discussed. Previous work on projectile-initiated detonation and related topics are described in Chapter 2. Chapter 3 outlines current theory that predicts critical conditions for detonation initiation. Characterizing detonable mixtures is not as simple as specifying chemical composition and thermodynamic state. Chapter 4 describes the process and presents results of the supporting mixture-characterization work. Chapters 5 and 6 cover the main experimental program and its results, respectively.

Chapter 2 Literature Review

This chapter reviews the work and results of previous researchers in three areas: experimental, theoretical, and computational. Of course, these divisions are somewhat arbitrary. Many workers have made contributions in more than one category, and the distinctions are vague in some cases.

Much work has been done on combustion induced by projectiles, but most of it has not dealt with detonation initiation. Of the work that has, far more has been theoretical than experimental. This chapter attempts to make mention of all of the relevant studies. Those focused entirely on non-detonative combustion are of less interest and are consequently not covered in depth. In contrast, attention is drawn to previous work on detonation initiation that has not been recognized by contemporary workers.

2.1 Experimental

A number of groups have studied phenomena related or similar to projectile-initiated detonation, but most of the phenomena have not involved bona fide detonations. Even fewer groups have observed stabilized detonations. For convenience of discussion, all experimental efforts in this field are categorized by institution, as in Table 2.1, which is organized roughly chronologically. Prior to the present work, several groups in the U.S. performed projectile-initiated combustion experiments: the National Bureau of Standards [98], Lincoln Laboratory at the Massachusetts Institute of Technology [86], and Sandia National Laboratories in Albuquerque [12]. More recently, experiments were performed at the University of Washington in conjunction with the ram accelerator program [54]. In Russia and the former Soviet Union, experiments at Moscow State University produced a range of phenomena, including stabilized detonations [24], while recent work performed at the Russian Academy of Sciences in Novosibirsk focused on sub-CJ projectile speeds [118]. Two sets of experiments were performed at the French-German Research Institute in Saint-Louis, France (ISL) [10, 78]. Most recently, a group at Nagoya University in Japan performed a series of experiments resulting in observation of stabilized detonation initiation [36, 66].

One obstacle to comparing the various sets of experimental data available in the literature and including it in an analysis is determining the effect of the particular experimental conditions in each case. Various groups have used a wide variety of projectile sizes and shapes, containment vessels, and diagnostics. Section 2.1.1 summarizes the experimental conditions of various researchers. Discussion of their results follows in Section 2.1.2.

2.1.1 Experimental Conditions

Table 2.1 lists details of the experimental apparatus used by a number of researchers including, for comparison, that of the present work. The latter are discussed in greater detail in Chapter 5. The entries are grouped by source institute and numbered for reference. As can be seen, most projectiles used have been spherically blunt, with a few being conical or flat faced. The present work concerns primarily spherical projectiles.

The diagnostics used can affect the interpretation of experimental results. Even different diffractive flow visualization techniques (schlieren, shadow, etc.) may lead to different conclusions, as reaction fronts may appear differently in schlieren and shadowgraph images.

Most researchers have used schlieren or shadowgraph imaging. However, several variations have been used, including double-pass schlieren (McVey and Toong [86], Struth [110]), dual-schlieren for obtaining images at two different stations (McVey and Toong [86]), and streak photography (Vasiljev [118]). Framing schlieren images were taken by Vasiljev [118] and by the Nagoya group [36, 56, 65, 66]. The present study has employed, in addition to shadowgraphy and differential interferometry, intensified CCD imaging of natural fluorescence. Although most studies have employed flow visualization, Higgins and Bruckner [54] extracted a great deal of information from pressure measurements alone. In fact, aside from the limited multiple-frame flow visualization results, transient pressure measurements are the only means that have been used to reveal the evolution of the wave structure around a projectile along its path. As such, they are very useful for distinguishing steady from non-steady flows.

The cross-sectional dimensions of the containment vessel, relative to the projectile size, determine the "boundedness" of the flow. Generally, smaller confinement cross-section (relative to projectile size and/or detonation cell size) is more conducive to detonation initiation (see Higgins [52]). In fact, with small enough confinement, the projectile may act as a leaky piston, generating overdriven unsteady detonations at sub-CJ projectile velocities.

The method used to isolate the test gas from the launch process has a strong effect on the steadiness of the flow around the projectile. Most studies have used plastic diaphragms to separate the test gas from an upstream blast chamber before the experiment. A notable exception is Horii et al. [56], who did not separate the launch tube exit from the test chamber. Zeldovich and Leipunsky [124] (not listed in Table 2.1) used spring-actuated gate valves at the entrance and exit of the test chamber to avoid diaphragm effects. Higgins and Bruckner [54] used different diaphragm thicknesses and buffer techniques in a study of the influence of the entrance process on detonation initiation.

Many sources do not give sufficient information to fully reproduce the conditions of their experiments. In particular, the travel distance of the projectile from the entrance to the main diagnostic (imaging) station is often not given. The numbers listed for Benedick [12] and Higgins [51] represent the overall length of the containment, since in these cases observations were made along the

Table 2.1: Summary of experimental apparatus used by various researchers.

Case	Projectile	Diagnostic	X-Section (mm)	Entrance	Travel (mm)	Source
1	19.94-mm sphere	schlieren	153 dia.	blast chamber +	2171	Ruegg and Dorsey [98]
2	〃	〃	〃	0.013-mm diaphragm	〃	Ruegg and Dorsey [99]
3	9-mm sphere	schlieren,	200 sq.	blast chamber +	∼150/400	Struth [110]
4	〃	shadowgraph	〃	0.012-mm mylar diaphragm	〃	Behrens et al. [10]
5	15-mm sphere/cylinder	shadowgraph	〃	〃	〃	Lehr [77, 78]
6	15-mm 75° cone/cylinder	〃	〃	〃	〃	〃
7	12.7-mm sphere	schlieren		blast chamber +	305/635	McVey and Toong [86]
8	〃	〃		mylar diaphragm	〃	Alpert and Toong [4]
9	12.7-mm flat cylinder	〃		〃	〃	〃
10	12.7-mm sphere/cylinder	schlieren	350 dia.	ambient air +	2540	Chernyavskii et al. [20]
11	34-mm sphere/cylinder	shadowgraph	〃	0.1-mm polyethylene	〃	Chernyi et al. [24]
12	100 – 200-mm dia. plate	photography	1200 sq.	ambient air + 0.1-mm polyethylene	7300	Benedick [12]
13	7.62-mm sphere/cylinder	streak,				Vasiljev [118]
〃	7.62-mm flat cylinder	(framing) schlieren				〃
14	50 – 220-mm dia. plate					Vasil'ev et al. [117]
15	6.35-mm sphere	pressure	180 dia.	sabot stripper	900	Higgins and Bruckner [54]
16	9.35-mm sphere	〃	〃	(CO_2 at 0.17 atm) +	〃	
17	12.7-mm sphere	〃	〃	0.013 – 0.4-mm mylar	〃	
18	15.9-mm sphere	〃	〃	〃	〃	
19	19.2-mm sphere	〃	〃	〃	〃	
20	10, 12-mm sphere/cylinder	framing schlieren	145.2 dia.	launch tube	490	Kasahara et al. [65]
21	10-mm cone/cylinder	visible and UV	〃	connected directly	〃	Kasahara et al. [66],
	θ_n = 30 to 180°	framing schlieren	〃	to test chamber	〃	Endo et al. [36]
	25.4-mm sphere	diff. interferometry	152 sq.	blast chamber +	595	Bélanger et al. [11]
	〃	shadowgraph	〃	0.025-mm mylar diaphragm	〃	Kaneshige and Shepherd [64]
	〃	+ICCD	+ 152 dia.	〃	1595	Present Work

entire length. In some cases, information was extracted from heavily cross-referenced and vague descriptions. For instance, Chernyi et al. [24] refer to the earlier work of Chernyavskii et al. [20] for description of their setup, but some differences are apparent, such as the projectile diameter. Thus it is unclear if the travel distance was changed. Lehr [78] refers to Behrens et al. [10], who refer to Struth [110], for discussion of their apparatus. Apparently, the same apparatus was used in all three studies. Behrens et al. [9] fill some gaps in the description, particularly concerning the change from 9-mm diameter projectiles to 15 mm. Two numbers are listed in Table 2.1 for Struth [110] for travel distance because the entrance diaphragm could be placed at two different locations, farther from the photographic station for lower pressures, and closer for higher pressures, to counter the increased effect of drag. However, none of the publications provided specific dimensions, and of course, which diaphragm station was used in each experiment is generally not clear. In fact, one case in which the travel distance was stated (150 mm, Lehr [78]) was not consistent with the practice stated by Struth [110] of using a longer distance at low pressure (186 torr in this case).

2.1.2 Results and Conclusions

Tabulated experimental conditions (supplemented by Table 2.1) and results obtained from literature sources are given in this section. The results presented do not represent all of the data described in the original sources. In many cases, the bulk of the results were given in a processed form that prevents secondary analysis. The goal here is to present raw conditions and results that can be compared with the like from other sources.

In the tables in this section, the experimental conditions are cross referenced with Table 2.1 by the numbers in the columns labeled "Case." The descriptions of results deserve some explanation. "Shock-induced combustion" generally implies smooth decoupling of the reaction zone from the bow shock, although some unsteady disturbances, particularly of very small amplitude, may be apparent in the original publications. "Regular" and "irregular" are used to differentiate different types of oscillations that occur in shock-induced combustion, and correspond to the "regular" and "large-disturbance" regimes of Toong [115]. "DDT" refers to deflagration-to-detonation transition; that is, shock-induced combustion transitioning to a detonation, which could become stabilized on the projectile or outrun it. This differs significantly from the conventional definition of DDT, in which a propagating flame accelerates and generates shock waves which develop into a detonation. However, DDT is the most appropriate term for the observed phenomena. When a detonation wave was observed to outrun the projectile, it is described as an unstable detonation. Therefore, a DDT can also be an unstable detonation. The descriptions given reflect the data available.

Moscow State University

The first unequivocal published evidence of a detonation wave stabilized on a projectile was obtained at Moscow State University. Chernyi and Chernyavskii [23] and Chernyavskii et al. [20] presented

Table 2.2: Results from Moscow State University.

Mixture	Pressure (atm)	Speed (m/s)	Case	Result
$2H_2+O_2$	0.132	2570	10	regular shock-induced combustion
″	0.245	2580	″	shock-induced combustion, DDT
″	0.245	2890	″	shock-induced combustion, DDT, stable detonation?
″	0.245	2860	″	shock-induced combustion, DDT
″	0.245	3060	″	DDT
″	0.329	2800	″	stable detonation
″	0.500	3300	″	stable detonation
$2H_2+O_2+3.76N_2$	0.118	1890	11	shock
″	1.283	2000	″	stable detonation

a photograph of a spherically blunt 12.7-mm diameter projectile traveling at 3300 m/s through a mixture of $2H_2+O_2$ at 0.5 atm, in which the bow wave decayed to a straight, stable CJ wave away from the projectile nose. The authors reported the far-field normal propagation velocity of the wave to be equal to the CJ speed, based on the projectile velocity and measured wave angle. Direct measurement of the wave angle from the published image yields a value 2.6° smaller than the CJ wave angle, corresponding to a wave speed about 3% below the CJ speed. While this discrepancy seems minor, it is significant compared to the uncertainty in the CJ speed as well as that of the angle measurement. The apparent source of the discrepancy is the wave angle measurement, resulting from poor quality of the published image, distortion of the wave by the tilted projectile, and uncertainty of the axis of flight.

In another case, with a projectile velocity of 2890 m/s in $2H_2+O_2$ at 0.245 atm, a bow shock with oscillating combustion was seen to transition to a conical detonation behind the projectile. This is unusual because the bow wave would be weaker, and presumably less likely to transition to detonation, farther away from the stagnation region. No theoretical or numerical analysis has predicted the occurrence of this configuration, except possibly during an unsteady transition. However, the relative size of the containment (27.6 projectile diameters) and the projectile travel distance (200 diameters) suggest that the flow was stabilized. Other cases of stabilized or nearly stabilized detonations are shown, but the structures were not as clear.

If the flow was stabilized, the straight portion of the bow wave was not propagating at the CJ speed. Based on the wave angle, the normal velocity was 2598 m/s (the authors gave 2700 m/s), whereas the CJ speed was 2763 m/s. This discrepancy, though apparently small (6% versus the authors' 2.3%), is large compared to the uncertainty in the CJ speed calculations (0.6%, see Sec-

tion 4.2). This velocity deficit suggests that the combustion was competing with a strong expansion process. Alternatively, the flow could have been unsteady. In this case, the detonation was presumably initiated by reflection of the bow shock from the chamber wall, and was in the process of propagating forward along the bow shock. This is an example of a condition for which either a stabilized detonation or shock-induced combustion could occur, depending on the boundary conditions. In this experiment, the projectile entered the test chamber through a diaphragm, moving from ambient conditions to the sub-atmospheric test conditions. The bow shock would initially be weakened by the transition, possibly explaining why a detonation was not initiated during the entry process. Most experiments involve an entrance diaphragm with lower pressure or vacuum upstream of the test gas, resulting in a transient unsteady shock that tends to encourage initiation [51]. The phenomenon of stabilized delayed initiation is discussed further in Section 6.4.

Later work with 34-mm diameter blunt cylinders in stoichiometric H_2-air mixtures was presented by Chernyi et al. [24]. Stabilized detonation was obtained at a projectile velocity of 2000 m/s, with a wave angle consistent with a detonation speed 2% below the CJ speed.

Experiments with non-detonative combustion were also performed. In addition to a few examples in the previously mentioned publications, Chernyi [22] (which appears to be a direct translation of [21]) presented several photographs of smooth and pulsating shock-induced combustion, although the experimental conditions were not described in detail.

Institute of Saint-Louis

Two distinct sets of experiments were performed at the ISL. The first, in which 9-mm spheres were used, was reported by Struth [110] and Behrens et al. [10]. The second, involving 15-mm spherically-blunt and conical-tipped cylinders, was reported by Lehr [77, 78]. Experiments with 9-mm and 15-mm conical projectiles, bridging the two studies, were reported by Behrens et al. [9].

In the first series, only shock-induced combustion was observed. Behrens et al. [10] noted that with $2H_2+O_2+3.76N_2$ at 0.55 atm, velocities higher than the CJ speed produced smooth shock-induced combustion, whereas lower velocities produced unsteady instabilities. $4H_2+O_2+3.76N_2$ at 0.72 atm produced instabilities up to 110% of the CJ speed. Similarly, near-stoichiometric H_2-O_2 mixtures at 0.24 atm exhibited oscillating shock-induced combustion at velocities up to about 115% of the CJ speed. In the mixtures with air, the period of oscillation was found to be approximately equal to the induction time for the state behind the normal portion of the bow shock. The oscillation period in the mixtures without N_2, however, did not show clear dependence on the induction time.

Attention in the first ISL series was also directed at the state behind the projectile. By observing shock waves propagating in the gas column bounded by the reaction zone, they determined that the reactants were only partially consumed, as may be expected since the combustion was generally intermittent. Occurrence of detonation waves in the wake region also indicated the presence of

Table 2.3: Results from ISL.

Mixture	Pressure (atm)	Speed (m/s)	Case	Result
$2H_2+O_2+3.76N_2$	0.234	2660	3	shock-induced combustion
″	″	2265	″	regular shock-induced combustion
″	″	2130	″	regular shock-induced combustion
$2H_2+O_2+3.76N_2$	0.55	1900	4	regular shock-induced combustion
″	″	1925	″	regular shock-induced combustion
″	″	1700	″	regular shock-induced combustion
$2H_2+O_2+3.76N_2$	0.421	1685	5	regular shock-induced combustion
″	″	1804	″	regular shock-induced combustion
″	″	1931	″	regular shock-induced combustion
″	″	2029	″	regular shock-induced combustion
″	″	2058	″	shock-induced combustion
″	″	2119	″	shock-induced combustion
″	″	2257	″	shock-induced combustion
″	″	2369	″	shock-induced combustion
″	″	2490	″	shock-induced combustion
″	″	2605	″	shock-induced combustion
$2H_2+O_2$	0.245	1862	″	shock-induced combustion w/expanding wake
″	″	1892	″	shock-induced combustion w/expansion on sides
″	″	1924	″	shock-induced combustion w/expansion on sides
″	″	1992	″	conical shock-induced combustion
″	″	2160	″	unstable detonation
″	″	2177	″	unstable detonation
″	″	2362	″	unstable detonation
″	″	2365	″	unstable detonation
″	″	2424	″	unstable detonation — looks stabilized
″	″	2705	″	unstable detonation — looks stabilized
$2H_2+O_2+3.76N_2$	0.555	2379	6	shock-induced combustion
″	″	2417	″	shock-induced combustion

unreacted gases.

In addition to further shock-induced combustion observations on spherical and conical projectiles, true detonation phenomena were observed by Lehr [77, 78]. With undiluted stoichiometric H_2-O_2 at 186 torr (24.8 kPa), projectile speeds from 1892 m/s to 2705 m/s resulted in phenomena ranging from steady shock-induced combustion to unstable detonation initiation.

Some of these detonations appeared to be stabilized. In these cases the waves were straight in the far-field, suggesting that they had decayed to a self-sustaining CJ state. The CJ speed value presented by Lehr was lower than the projectile velocities in some of these cases, supporting the notion that the waves were stabilized. Also, the observed wave angles agreed well with the expected CJ wave angles, using Lehr's CJ speed values. However, the stated CJ speed of 2550 m/s was lower than the value of 2773 m/s measured in the GALCIT detonation tube, and corroborated by equilibrium calculations (see Sec. 4.2). Similarly low detonation speeds for stoichiometric H_2-O_2 at low pressure were reported by other sources, for example Lewis and von Elbe [80]. These values

were measured in small-diameter tubes, where at low pressure, large cells would interact with the tube and result in a significant velocity deficit.

Lehr discriminated between stabilized and non-stabilized initiation cases by comparing the projectile speed to the assumed CJ speed. In fact, some of the waves that appeared exactly like stabilized detonations occurred at projectile velocities even below his assumed detonation speed. Therefore, the detonations were clearly not stabilized, their appearance notwithstanding. The close proximity of the unsteady detonation waves to the projectile was most likely due to the short travel distance used in the ISL experiments (150 mm, or 10 diameters).

Chernyi and Chernyavskii [23] also recognized this misinterpretation by Lehr, and presented experimental and calculated values of the detonation speed (about 2750 m/s) from Wagner [121] that agree with our value and refute that of Lehr. In fact, Lehr also cited Wagner [121] as a source of CJ speed data. It is unclear why the lower value was used.

University of Washington

Projectile initiation experiments at the University of Washington ram accelerator laboratory [51–54] focused on sub-CJ projectile speeds using pressure measurements along the side of the containment vessel. This diagnostic technique was unique in that most previous researchers have not reported pressure measurements, preferring instead more graphic flow-visualization methods. In some ways, pressure signals are more conclusive than imaging for distinguishing detonation initiation from shock-induced combustion and steady from non-steady flows, although the lack of flow visualization prevents direct observation of the flow around the projectile and therefore the mechanisms responsible for detonation initiation or failure.

Figures 2.1 and 2.2 show the bulk of the experimental results given by Higgins [51]. Entrance effects were found to be important at higher pressures, and additional experiments were performed to evaluate these effects by providing a buffer section between the sabot separation tank and the test chamber. Figure 2.1 shows only data without a buffer section, although data from experiments with different diaphragm thicknesses are plotted together. The data did not seem to be affected by diaphragm thickness. Also, the data were originally sorted according to prompt vs delayed initiation. In Fig. 2.1, no distinction has been made between the two cases.

The data shown in Fig. 2.2 were originally categorized by entrance diaphragm technique (thickness and buffer) as well as delayed vs prompt initiation. The diaphragm technique showed little effect on the results, so no distinction has been made here; delayed and prompt initiation have not been distinguished either.

As mentioned above, Higgins [51] noted the occurrence of unsteady "delayed initiation," in which a detonation was initiated by the projectile after it had traveled some distance through the test section. Ample evidence was provided to show that the initiation was not caused by bow-

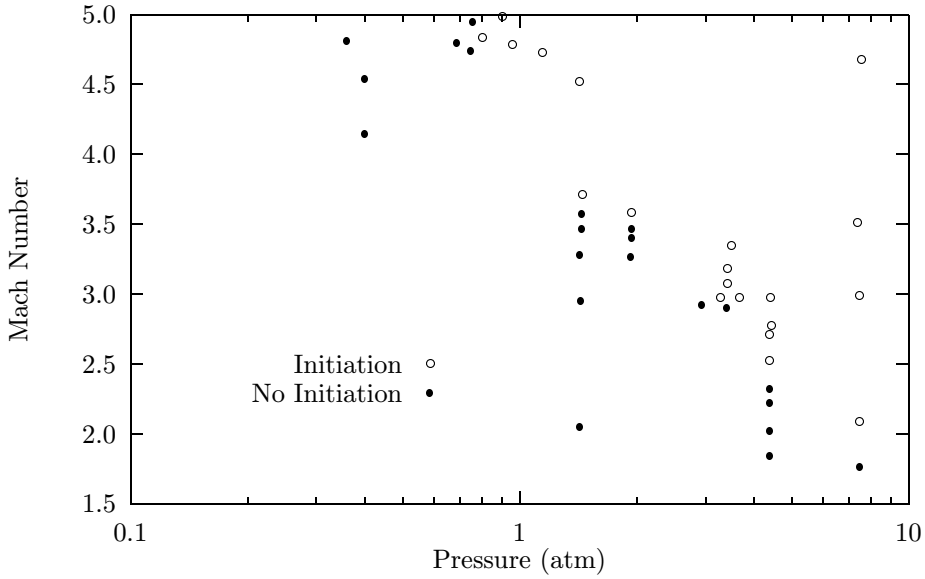

Figure 2.1: Results from the University of Washington with 12.7-mm spheres in $2H_2+O_2+7Ar$ (from Fig. 5.8 of Higgins [51]).

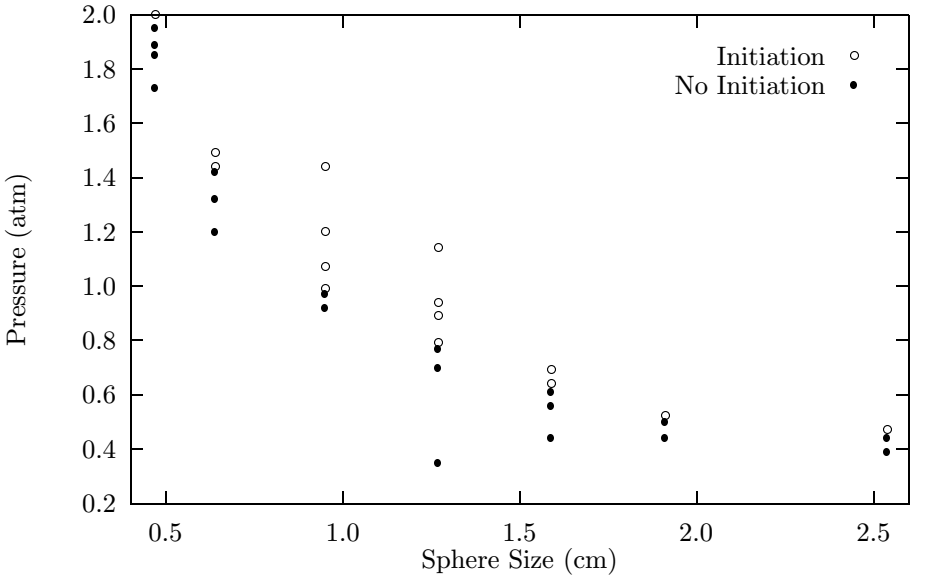

Figure 2.2: Results from the University of Washington in $2H_2+O_2+7Ar$, with projectile speed equal to CJ speed (from Fig. 5.11 of Higgins [51]).

wave reflection off the tube wall, but was clearly occurring close to the projectile. However, no mechanism was suggested for this phenomenon. Since it was observed only (and always) near the critical conditions for initiation, and at projectile speeds equal to the CJ speed, this "marginal" behavior seems natural. Any random fluctuation in mixture composition or temperature might be sufficient for transition to occur. However, for a couple of reasons, initiation should become less likely after some travel through the test mixture. First, drag should cause the projectile velocity to drop, reducing its rate of energy deposition. Second, entrance effects normally promote initiation, so that if it does not occur near the entrance diaphragm (or upon reflection of the bow shock from the wall), it is less likely to occur later.

Thus, upon closer examination, unsteady delayed initiation seems unnatural, and some specific mechanism must be responsible for its occurrence. Several possibilities can be suggested. First, perhaps the projectile experiences thrust and acceleration. This seems unlikely because although previous studies (Ruegg and Dorsey [98]) have found a reduction in drag caused by combustion, thrust on spherical projectiles has not been reported. Second, steps were taken to eliminate the entrance diaphragm as a cause of initiation by placing a pressure-matched buffer upstream of it. The intention was that since the projectile would enter the test section with a bow shock already developed, it would not generate an overdriven wave as it penetrated the diaphragm. This effort may have been too effective, resulting in the bow shock diffracting upon penetration, inhibiting initiation at the entrance. Finally, while drag would reduce the projectile speed, exposure to shock-heated and compressed gases would increase its surface temperature. Shock-induced combustion oscillations are known to originate near the stagnation point, and normally the gas temperature there drops through the thermal boundary layer. The second effect serves to counter the first by quenching reactions in the stagnation region near the body. The increase in the surface temperature could reduce the quenching effect and cause the gas in the region to explode. Inevitably, at this point all of these hypothetical effects are speculative.

Russian Academy of Sciences, Novosibirsk

Vasiljev [118] at the Russian Academy of Sciences reported on results of experiments with 7.62-mm diameter flat and spherically blunt cylinders in stoichiometric C_2H_2 mixtures using streak, schlieren, and framing schlieren photography. Vasil'ev et al. [117] describe further work with flying plates (over a range of diameters) in gasoline-air mixtures. All projectile velocities were below the CJ speed. Unfortunately, neither the experimental apparatus nor the results were described in sufficient detail for secondary analysis.

Sandia National Laboratories, Albuquerque

As part of a larger investigation of fuel-air explosions at Sandia National Laboratories, Benedick [12] reported a series of experiments with high-velocity flying plates in mixtures of 8% by weight MAPP gas in air. The plates were accelerated by unconfined high explosive, much as described by Vasil'ev et al. [117], and observed by an unspecified high-speed photographic technique. The gas mixture was contained in a rectangular plastic sheet enclosure, which provided rigid containment on one side (the ground) and essentially no containment on the other sides. The results of these experiments are unique because of the large projectiles (100 – 200-mm diameter) and large containment (1200 mm square) dimensions. The usefulness of these results to the current study are limited by the fact that the projectiles were flat plates, which differ significantly from spherical blunt bodies, and also by the use of MAPP gas. The chemical analysis of the MAPP gas was provided in detail, but nonetheless characterization data (e.g., cell width) are scarce.

Table 2.4: Results with flying plates in MAPP-air mixture from Sandia (from Table 1 of [12]).

Diameter (mm)	Velocity (m/s)	Initiation Mode
200	2380	shock reflection
200	2310	continuous
200	2100	shock reflection
150	2500	shock reflection
100	2440	shock reflection
100	2180	no detonation

Massachusetts Institute of Technology

Experiments at the Lincoln Laboratory at the Massachusetts Institute of Technology concentrated on pulsating shock-induced combustion. Table 2.5 summarizes conditions and results for which raw data could be obtained from McVey and Toong [86] and Alpert and Toong [4]. Significantly more data were presented in these publications, but in processed graphical form. The analysis focused on the instability regimes and oscillation frequencies observed around spheres, and to a lesser extent flat cylinders. Schlieren photographs were taken at two stations, and two separate photographs could be taken at the second station. This permitted direct measurement of oscillation frequencies and transition between different regimes.

Most of the effort was directed at understanding the pulsating combustion phenomena. Oscillations were found to occur in two regimes, referred to as "regular" and "large-disturbance." Regular oscillations were characterized as being relatively small amplitude and spatially and temporally regular. Large-disturbance oscillations were characterized as being relatively large amplitude and less regular. Under some conditions, only the regular regime was observed. Under other conditions, with

Table 2.5: Results from MIT.

Mixture	Pressure (atm)	Speed (m/s)	Case	Result
$2H_2+O_2+3.76N_2$	0.395	1969	7	regular shock-induced combustion
$C_2H_2+15O_2$	0.197	1640	″	regular shock-induced combustion
H_2+2O_2	0.263	2024	8	regular/irregular shock-induced combustion
″	″	2016	″	irregular shock-induced combustion
H_2+2O_2+2Ar	″	1613	9	irregular shock-induced combustion

no apparent changes in mixture, pressure, speed, or observation position, either or both types of oscillations were observed. In both cases, the frequency of oscillation was found to be a function of the flow conditions, but aside from some necessary conditions, occurrence of the two regimes appeared random. By measuring oscillation frequencies of the regular regime in flows around spheres, McVey and Toong [86] confirmed their wave-interaction model, which related the oscillation period to the induction period of the gas behind the normal portion of the bow shock. Alpert and Toong [4] extended this work to the large-disturbance regime with a more complex wave-interaction model. However, little quantitative verification of this model was given. They did determine some factors controlling the occurrence of the large disturbance regime, such as the enthalpy of combustion. Also, transition from the large disturbance regime to the regular or smooth regimes was observed along the path of the projectile, but never the opposite.

Toong [115] and Toong [116] reviewed the work with spheres and also discussed experiments with conical projectiles and projectiles traveling through a transition between different mixtures. Conical projectiles were found to exhibit instabilities similar to blunt bodies (both regular and large-disturbance regimes), as well as a unique conical instability. The instability pattern on a projectile traveling from one mixture to another was observed to change predictably but with some interesting transition phenomena. No specific conclusions were reached from these experiments.

National Bureau of Standards

The National Bureau of Standards published the first known example of flow visualization of projectile-initiated combustion [91]. Smooth and pulsating shock-induced combustion were both reported, although quantitative results were scant.

Ruegg and Dorsey [98] presented a more complete summary of experiments with stoichiometric mixtures of H_2 and air. The shock stand-off distances and shapes were measured and compared with those for non-reactive flows. Stand-off distance was found to increase because of the combustion. Distances measured between the bow shock and the reaction zone (end of the induction zone) were converted to time values and these compared well with induction time data. Velocity measurements between three detection stations allowed drag coefficients to be measured. Drag was

Table 2.6: Results from the National Bureau of Standards.

Mixture	Pressure (atm)	Speed (m/s)	Case	Result
$2H_2+O_2+3.76N_2$	0.5	1757	1	shock-induced combustion
″	″	1961	″	irregular shock-induced combustion
″	″	2247	″	irregular shock-induced combustion
″	″	2574	″	shock-induced combustion
″	0.10	2043	″	shock
″	0.25	1839	″	shock-induced combustion
″	″	2002	″	regular shock-induced combustion
″	″	2084	″	shock-induced combustion
″	″	2411	″	shock-induced combustion
″	″	2656	″	shock-induced combustion
$CH_4+2(O_2+3.76N_2)$	0.50	2138	2	irregular shock-induced combustion
$C_5H_{12}+8(O_2+3.76N_2)$	0.25	2159	″	irregular shock-induced combustion
″	1.00	1873	″	irregular shock-induced combustion

reduced significantly (about 50%) by combustion.

Results of a few additional experiments, some using different fuels, were given by Ruegg and Dorsey [99]. These and previous data are presented in Table 2.6.

Nagoya University

Experiments at Nagoya University have studied shock-induced combustion [56, 65] and detonation initiation [36, 66]. Table 2.7 presents data from Kasahara et al. [65], which were the only experiments using spherically-blunt projectiles and gas mixtures like those in the present study. The other studies were restricted to flat or cone-nosed projectiles, or relatively exotic mixtures with CO as the primary fuel. The detonation initiation results with conical projectiles from Endo et al. [36] and Kasahara et al. [66] are interesting, but of limited value for quantitative comparison with the present study. A summary of the results reported by Kasahara et al. [66] is given in Table 2.8.

Table 2.7: Results from Nagoya University with $2H_2+O_2+3.76N_2$ (case 20 of Table 2.1).

Diameter (mm)	Pressure (atm)	Speed (m/s)	Result
10	0.75	1980	Irregular shock-induced combustion
″	″	1780	Irregular shock-induced combustion & envelope oscillation
″	″	1920	Regular shock-induced combustion
″	″	1760	Regular shock-induced combustion & envelope oscillation
″	″	1750	Steady shock-induced combustion
″	″	2030	Regular shock-induced combustion
12	″	1930	Regular shock-induced combustion
10	0.50	2000	Steady shock-induced combustion
″	0.60	1990	Regular shock-induced combustion
″	0.75	2030	Regular shock-induced combustion

Smooth shock-induced combustion and different regimes of oscillating shock-induced combustion were observed with various mixtures, pressures, and projectile sizes, shapes, and velocities. Most of the observations made in these experiments were also made by previous researchers. However, in addition to the smooth, regular oscillation, and irregular oscillation regimes, long period oscillations were observed superimposed on the combustion oscillations. Kasahara et al. [65] referred to these as "envelope oscillations."

Table 2.8: Results from Nagoya University with 10-mm diameter conical projectiles in $2H_2+O_2$ (case 21 of Table 2.1).

Shot Number	Nose angle (degrees)	Pressure kPa	Speed m/s	Result
119	120	33.3	2920	stabilized delayed initiation
128	120	33.0	2860	stabilized delayed initiation
130	120	50.5	2730	stabilized prompt initiation
134	120	21.3	2830	stabilized delayed initiation
137	120	40.5	2910	stabilized prompt initiation
138	120	9.5	2830	shock-induced combustion
140	60	33.6	2960	shock-induced combustion
141	180	33.6	2890	stabilized prompt initiation
142	90	33.3	2810	stabilized delayed initiation
143	150	33.4	2820	stabilized prompt initiation
146	60	50.3	2980	shock-induced combustion
147	90	51.2	2800	stabilized prompt initiation
148	180	10.0	2840	shock-induced combustion
149	180	51.3	2750	stabilized prompt initiation
151	120	34.2	2810	stabilized prompt initiation
153	90	21.1	2930	stabilized delayed initiation
173	120	32.9	2840	stabilized prompt initiation

Detonations (and shock-induced combustion) initiated by conical projectiles were reported by Endo et al. [36] and Kasahara et al. [66]. Experiments were performed with stoichiometric H_2-O_2 at various initial pressures, projectile velocities and nose angles. At higher pressure, the critical nose angle for initiation was found to be lower, as expected.

Also observed was a type of delayed initiation in which a normal detonation followed the projectile steadily and anchored an oblique wave. This phenomenon was also observed by Chernyavskii et al. [20] and the present study, and is discussed further in Section 6.4

Miscellaneous Related Work

A number of different experimental techniques have direct or indirect relevance to projectile initiated detonation. These techniques deserve mention, although data generated with them will not be included for further discussion.

Stanford Experiments using an expansion tube to accelerate combustible gas mixtures over models were described by Kamel et al. [62] and Morris et al. [89]. The key limitation to using expansion tubes to study reacting flows is the tendency of the mixture to react in the tube before it reaches the test section, due to shock heating, particularly during opening of a diaphragm. Kamel et al. [62] described experiments with mixtures of CH_4 and C_2H_4 with O_2 and N_2. Planar Laser-Induced Fluorescence (PLIF) imaging was the primary diagnostic, and the model was spherically blunt. The PLIF results showed combustion taking place along the sides of the model.

Flow over a 40° wedge of stoichiometric H_2-O_2 mixtures diluted with N_2 were examined with schlieren and PLIF imaging by Morris et al. [89]. By varying the free stream pressure and N_2 dilution, phenomena ranging from shock-induced combustion to a steady oblique detonation were observed.

Institute of Saint-Louis The problem of accelerating a combustible mixture in an expansion tube without preignition was approached at the Institute of Saint-Louis by accelerating hydrogen fuel and air separately in an expansion tube and Ludwieg tube, respectively (Srulijes et al. [105]). With this setup, they claimed to be able to accelerate H_2-air mixtures to super-CJ speeds at up to 200 kPa and 350 K static conditions. Flow visualization clearly showed combustion effects in flow over a sphere. However, complete mixing of the fuel and air was not clearly demonstrated.

McGill University Higgins et al. [55] simulated projectile initiation with the propagationg energy release along a detonating cord. This technique is interesting because it directly addresses the similarity of initation by projectiles to cylindrical blast initiation, which is central to the blast model of Lee and Vasiljev (see Section 3.1). It is intermediate between the two cases, since a blast wave is the initiation mechanism, but the blast propagates axially as well as radially. Because the detonation speed in the detonating cord was substantially faster than the CJ speed in the gas mixtures, a regime not easily studied with ballistic facilities could be explored. As a method of generating cylindrical critical energy data, the detonating cord eliminates many uncertainties concerning efficiency and release rate that are associated with other techniques such as exploding wire and spark discharge. The only complicationg with interpreting the data as cylindrical critical energy is the axial propagation speed of the blast wave, which is ideally infinite.

2.2 Theoretical

Theoretical analysis of the critical conditions for, and phenomena associated with projectile-initiated detonations has been performed by virtually every investigator of the topic, but the key contributors have been at Moscow State University, Massachusetts Institute of Technology, and McGill University. Except for the latter, these groups have had experimental efforts in conjunction with the theoretical

developments. The work of each group has followed distinct avenues and sought different results. The Moscow State University work covered many aspects of detonation initiation and propagation beyond the scope of this discussion, but the studies presently relevant concentrated on the decay of detonation waves from the bow of a projectile to either a steady, straight Chapman-Jouguet wave in the far field or a decoupled shock and reaction zone. The means of analysis ranged from pure reasoning and mathematical analysis to numerical solutions of ordinary differential equation approximations to the governing partial differential equations. Work at MIT was concerned more with unsteady oscillations observed in shock-induced combustion, and therefore relates indirectly to detonation initiation by projectiles. This analysis was performed mostly on the basis of one-dimensional models of the stagnation region of a projectile. Finally, the initiation models of Lee at McGill University, Vasiliev at the Russian Academy of Sciences, and Endo et al. at Nagoya University do not consider the details of the flow around the projectile, but relate it to a similar flow and utilize existing results.

2.2.1 Moscow State University

Gilinskii et al. [44] computed the flow around a sphere and a spherically blunt cylinder with a stabilized detonation of zero thickness, and analyzed the possibility of reaction zone detachment where the flow behind the wave was supersonic. The calculations assumed combustion to be instantaneous behind the shock, leading automatically to a stabilized detonation. The flow behind the bow wave was solved differently in two angular regions, the first consisting mostly of subsonic and transonic flow and the second consisting entirely of supersonic flow. In the subsonic region, a system of ordinary differential equations was formed by approximating angular variations with polynomial functions. Flow in the supersonic region was solved by the method of characteristics.

Flow around a sphere and around a blunted cylinder were noted to be identical up to the characteristics propagating from the change in curvature where the hemispherical nose and cylindrical body meet. The effect of heat release on the bow wave was studied, and found to cause the wave stand-off distance to increase and the wave to become less curved. Also, the transition to the CJ state was examined, and found to occur at smaller distances from the axis with larger amounts of heat release.

While detachment of the reaction zone from the bow shock was not analyzed in the subsonic region because of the interdependence on the flow solution (i.e., the elliptic nature of the governing equations), splitting at a discrete point on the wave in the supersonic region was considered. In the supersonic region, only flow outside the detachment point would be affected by the splitting, so the solution for the un-detached flow could be used for the region closer to the body. Reaction zone detachment was considered by matching the pressure and flow angle downstream of the bow wave on either side of the detachment point (essentially a polar analysis). The values on the inside were

determined by the angle of the detonation wave at that point. To match these, the flow outside the detachment point consisted of an oblique shock and deflagration. The two regions were separated by an expansion propagating into the detonation products. Since this construction is generally valid regardless of the angle of the detonation wave, it does not determine the point at which detachment will occur, and therefore is not particularly useful for predicting flows.

Gilinskii and Zapryanov [43] followed closely the approach of Gilinskii et al. [44] for flow past two-dimensional profiles, and compared the results with flow past axisymmetric bodies. The primary conclusion was that the bow detonation wave in the absence of reaction zone detachment approaches the CJ state asymptotically in the case of flow over two-dimensional profiles, whereas it is reached at a finite distance for flow over axisymmetric bodies.

Gilinskii and Chernyi [42] considered flows with detached reaction zones. The flow model consisted of two regions of frozen flow behind the bow shock: an induction zone, and a combustion products zone. These two areas were separated by an infinitesimally thin flame front. No effects of chemical reactions were considered within the regions of reactants and products. The distance to the flame front along streamlines was computed by integrating a finite reaction rate equation which was a function of pressure and temperature. Solution of the flow in the two regions was achieved with a method identical to that used by Gilinskii et al. [44] and Gilinskii and Zapryanov [43], with the additional matching condition across the flame front.

Also, splitting of the reaction zone from the shock was considered as a perturbation of a thin detonation that attains the CJ state. Starting with a solution for the bow wave shape assuming a thin detonation front, i.e., solving the detonation jump conditions across the bow wave, the flow behind the shock, including a simple induction zone and the effects of curvature of the shock, was computed. Since the assumed wave shape decayed to a straight CJ wave, the computed induction zone thickness did not grow unbounded, and therefore could not directly indicate reaction zone decoupling. However, two possible criteria were suggested for identifying a point where decoupling would occur, if allowed. These were the presence of an inflection point in the flame front shape, and a non-monotonic variation of Mach number in the flow downstream of the flame. This model was approximate in a number of ways, including the assumption of a thin induction zone and infinitesimal flame, use of a simple Arrhenius rate equation for the induction zone thickness, and a somewhat arbitrary criteria for the onset of reaction zone decoupling. However, the use of a solution with an assumed thin reaction zone should not be considered a severe simplification for evaluation of critical conditions for splitting, since this represents a perturbation to the stabilized case. This method is closely related to the approach described in Section 3.2.

Reference to experimental results, presumably those presented by Chernyi [22], give the condi-

tions as M_1=5.5, T_1=300 K, and P_1=0.25 atm in stoichiometric H_2-air. Based on the calculation results presented, the predicted critical diameter for this condition appears to be 200-300 mm.

Levin [79] predicted conditions under which the overdriven detonation in front of a two-dimensional body in steady flow or one-dimensional body in unsteady flow could decay to a CJ wave. The model of the flow consisted of an adiabatic shock wave, followed by an induction zone with constant properties, and finally an instantaneous flame. A number of assumptions and simplifications were made, and the final conclusion was that steady CJ detonations could not be initiated and stabilized on bodies in normal chemical mixtures (i.e., with second-order kinetics). The authors extended this conclusion to explain why stable detonations had not been observed in experiments, although the model was not formulated for axisymmetric flows.

Gilinskii [40] again considered axisymmetric steady flow around a sphere, with an adiabatic induction zone followed by a zone of non-equilibrium chemical reaction. The combustion was modeled by a single first-order reaction in the second flow region. Thus, the beginning of the second flow region essentially represented a recombination zone. The same numerical scheme as used by Gilinskii et al. [44] and Gilinskii and Zapryanov [43] was used, and various results presented, but no conclusions were drawn concerning stabilization of a CJ detonation.

Gilinskii [41] used the same basic method as earlier studies (e.g., Gilinskii and Chernyi [42]), but with only a single flow region and with detailed chemical kinetics. Seven species and eight reactions of H_2-air combustion were considered, and the differential equations for density and species concentrations were solved implicitly along streamlines, instead of explicitly as were the other equations. Comparison with images from experiments with projectiles was made, but apparently only on the basis of shock shape and position, in which case recommendations were made for which set of reaction rate constants were most appropriate. No attempt was made to compare the observed reaction front shapes with calculation results, nor even to identify reaction front locations in the results.

Chernyi [22] (translation of Chernyi [21]), basically compiled and reviewed the work of the previous (and other) articles [42–44]. Experimental results were also presented for projectiles in H_2-O_2 and H_2-air mixtures, but no more information was given concerning the experimental conditions. From Gilinskii [41], conditions of one of the experiments with smooth shock-induced combustion are known as M_1=5.5, P_1=0.5 atm, T_1=300 K, H_2-air over a 15-mm diameter spherically blunt projectile.

Chernyi and Gilinski [25] and Chernyi and Gilinskii [26], likewise, summarized the work and results of [40, 42–44].

2.2.2 Massachusetts Institute of Technology

Although the theoretical (and experimental) work performed at MIT with oscillating shock-induced combustion did not directly pertain to detonation initiation, it is relevant indirectly, as the oscillations are likely caused by an unstable detonation-like structure at the projectile nose, and may be related to the phenomena leading to detonation cells.

McVey and Toong [86] developed a wave-interaction model for the flow behind the bow shock in the stagnation region, and used it to relate the oscillation period observed in projectile shock-induced combustion experiments with shock tube induction time measurements. A number of simplifications and assumptions were made. For instance, the induction time for a fluid particle after crossing the bow shock was taken as a function of the post-shock conditions, without modification for the variation of conditions along a streamline. Also, solutions for non-reactive flows were used to estimate a number of properties of the flow, including shock stand-off distance, velocity along the stagnation streamline, and velocity behind the projectile. The induction zone was assumed to be small compared to the shock stand-off distance. The accuracy and effect of these approximations vary, but the resulting model agreed well with experimental data from the regular regime of oscillations.

Alpert and Toong [4] extended the comparison of induction time data to projectile shock-induced combustion oscillation periods, to the large-disturbance regime by developing a more sophisticated wave-interaction model. Whereas the model of McVey and Toong [86] assumed that forward-running reaction shocks incident on the bow shock were acoustic, and did not consider the effect of enthalpy of combustion, Alpert and Toong [4] linked the enthalpy of combustion to the strength of the reaction shocks. In addition, the overall oscillation period was taken as a sequence of four reaction-shock interactions with the bow shock. Both wave-interaction models predicted that the oscillation periods should be approximately proportional to the induction time corresponding to the post-shock state on the stagnation streamline, and the proportionality constants for particular cases were derived. These proportionalities agreed well with data from the regular and large-disturbance regimes. However, the particular number of reaction-shock interactions per oscillation period assumed in the detailed mechanism, while crucially important to the predicted oscillation period, seems arbitrary and artificial. The physical arguments presented to support the chosen number are vague. However, the apparent conclusion that the regular regime is caused by acoustic waves and their effect on the induction zone while the large-disturbance regime results from strong shocks linked to the amount of heat release and a series of wave interactions per major oscillation, seems valid.

2.2.3 McGill University and Russian Academy of Sciences

Lee [74] and Vasiljev [118] developed a simple model for predicting projectile initiation of detonations, based on the hypersonic blast-wave analogy. The blast analogy was introduced in Section 1.3.8, and the application to projectile initiation modeling is discussed in Section 3.1.

2.2.4 Nagoya University

Endo et al. [36] presented a model similar to the Lee-Vasiliev model, using the critical velocity and curvature from $D_n(\kappa)$ theory (specifically from Yao and Stewart [122]) and a modification of the spherical blast solution. The use of the $D_n(\kappa)$ critical velocity and curvature seems more rational than the critical energy model suggested by Lee [74]. However, the $D_n(\kappa)$ model was developed for near-normal waves, not the oblique waves encountered around projectiles, and no specific validation of the model in this application has been given. Use of the spherical blast model for the wave shape is similar to using the cylindrical blast solution and hypersonic blast analogy, with similar assumptions and limitations.

This model was used to predict critical nose angles for initiation by conical nosed projectiles at varying initial pressures and velocities in H_2-air mixtures, and the results were compared with experimental results. In rough agreement with the experimental results, the model predicted lower critical nose angles at higher pressures, and higher critical angles at higher projectile velocities. The latter appears to be contrary to the predictions from other theories, including the blast model of Lee and Vasiljev.

2.3 Computational

As with experiments, most numerical analysis has dealt with shock-induced combustion, not detonation initiation.

Ahuja et al. [2] used a shock-fitting finite-difference code to simulate some of the experimental conditions of Lehr [78]. Supposedly, the complete axisymmetric Navier-Stokes equations were solved, although the inclusion of viscosity is unclear. The gas mixture was stoichiometric H_2-air at 320 torr, and projectile Mach numbers were 5.11 and 6.46. The projectile was a 15-mm diameter sphere. Shock fitting was used to reduce the number of grid points needed (since the bow shock does not need to be resolved, and the free stream is outside the computational domain) and to avoid shock smearing. Chemistry was treated with seven species and seven reactions. Only pseudo-steady flows were simulated. The computational domain extended from the bow shock to the body, and from the stagnation streamline to an angle about 90° from the stagnation streamline. Boundary conditions at the shock were the shock-jump conditions, and the outflow boundary was handled with second-order

extrapolation. The body surface boundary condition was no-slip, zero pressure gradient, adiabatic, and non-catalytic.

The Mach 5.11 simulation produced oscillations at very close to the same frequency as measured by Lehr [78] and predicted by the model of McVey and Toong [86]. Small-amplitude, high-frequency oscillations were detected in the Mach 6.46 case, even though none were observed in the experiment. This was attributed to greater sensitivity in the numerical shadowgraphs. In comparison with a control simulation using shock capturing, better resolution was obtained, although no mention was made of results obtained by other researchers using shock capturing.

Ju and Sasoh [61] performed simulations complementary to the experiments of Higgins [51]. The numerical scheme used detailed chemistry (9 species and 35 reactions) and an axisymmetric implicit LU-SGS TVD method. Except for the upstream boundary, extrapolation boundary conditions were used. Mixtures of $2H_2+O_2+7Ar$ at pressures of 0.2 to 10 bar were used with a 12.7-mm diameter spherical projectile and Mach number between 2 and 5. In all cases, the projectile speed was lower than the CJ speed of the mixture. Initial conditions consisted of a converged steady flow solution with frozen chemistry.

Critical values of pressure and Mach number for detonation initiation were determined and compared with experimental results and the Lee-Vasiliev model. At lower pressures, the simulations predicted lower critical velocity, and at higher pressures they predicted higher critical velocity than determined by experiments. No explanation was offered concerning the discrepancy at lower pressures. At higher pressures, diaphragm effects were suggested as a cause of the lower critical velocities in experiments. As pointed out, the stagnation temperature in the highest pressure experiments should not have been sufficient to ignite the mixture within the test time. Also, in a plot of critical projectile velocity vs initial pressure, the simulations showed a local minimum of critical velocity around 1 bar. Evidence was presented suggesting that this minimum was caused by chemical kinetic effects (see Fig. 6.5(a)), although it had not been observed in experiments.

Lefebvre and Fujiwara [76] used detailed chemistry (8 species and 19 reactions) and a total variation diminishing (TVD) upwind scheme with implicit finite-difference chemistry to simulate supersonic reacting flow over a conical (axisymmetric) body with finite nose radius. The mixture was $2H_2+O_2+3.76N_2$ at 0.1 atm, with Mach numbers ranging from 2.5 to 10. The cone half-angle was fixed at 30° while the nose radius was varied from 2.25 mm to 14.0 mm. The initial state consisted of a converged steady solution with frozen chemistry. Extrapolation boundary conditions were used for all boundaries except the upstream and body surfaces.

Within the conditions explored, the lowest speeds (2050 m/s, 2.25 mm nose radius) resulted in shock-induced combustion with the combustion occurring along the body surface, and the highest

speeds (4050 m/s, 14 mm nose radius) resulted in stabilization of a detonation wave on the body. At intermediate speeds, various transition phenomena were observed. At intermediate speeds and large nose radii (e.g., 2040 m/s, 14 mm nose radius), unsteady normal detonations were generated that propagated upstream from the downstream boundary. These unsteady detonations were observed at speeds above the CJ velocity. Therefore, they would be expected to stabilize on the body after propagating ahead and losing the support of the body. Unfortunately, the simulations were apparently not run long enough to see this. Alternatively, the detonation could fail after decelerating and re-initiate after being overtaken by the body again. In this case, the flow might become periodic. However, if the detonation would eventually become stabilized on the body, this would represent a case in which a stabilized detonation or shock-induced combustion could occur, depending on the boundary conditions. Presumably, suitable boundary conditions could have been applied in these simulations to prevent the unsteady detonation from being initiated at the downstream boundary, and since the upstream part of the bow wave was steady and stable, no detonation would have occurred.

Matsuo and Fujii [85] Numerical simulations of the experimental conditions of Lehr [78] were performed using an axisymmetric, non-MUSCL total variation diminishing (TVD) explicit scheme. Detailed chemistry (8 species and 19 reactions) was solved linearly implicitly. The computational domain apparently consisted of one quadrant, from the body surface to the furthest extent of the bow wave. Simulations of the conditions that led to pulsating shock-induced combustion in experiments accurately matched the flow features and oscillation frequencies. Examination of the flow on the stagnation streamline qualitatively confirmed the wave interaction model of Alpert and Toong [4]. No quantitative comparison was made.

Matsuo and Fujii [84] presented simulations using simplified, two-step chemistry, and otherwise similar methods as Matsuo and Fujii [85]. This was done to permit a parametric study of flow characteristics as a function of the chemical energy release. By varying the activation energy from low values to high, instability phenomena were observed ranging from nearly steady, to small-amplitude periodic oscillations corresponding to the regular regime, to large-amplitude irregular oscillations corresponding to the large-disturbance regime. Therefore, the unsteadiness regime was shown to be determined by the energy release. However, no conclusion was drawn concerning the observation of Alpert and Toong [4] that different regimes could occur under identical conditions, sometimes depending on the travel distance of the projectile.

Yungster et al. [123] performed steady axisymmetric calculations of flows corresponding to the experiments of Lehr [78]. Finite rate chemistry (seven species and eight reactions) were used with an implicit TVD scheme. The computational domain was apparently one quadrant. Boundary

conditions were not described.

Simulation results were compared with experimental data for 15-mm diameter spherical projectiles in stoichiometric mixtures of H_2-O_2 and H_2-air. Good agreement was shown for both sub-CJ and super-CJ speeds. However, the super-CJ case was misinterpreted by taking the detonation speed given by Lehr, which was inaccurate (see Section 2.1.2 and Chapter 4). In fact, the projectile speed was less than the CJ speed, and the bow wave, which did appear to be a detonation, could not have been steady. The presentation of a simulation of a stabilized detonation wave at this condition is intriguing, but clearly inaccurate.

Chapter 3 Theoretical Considerations

What makes purely theoretical treatment of detonation initiation by projectiles difficult, and numerical simulation attractive is the interaction between the projectile shock shape and the occurrence of combustion behind the shock. The shock shape determines if and where combustion occurs, while the combustion partially determines the shock shape. This suggests the possibility of a non-unique solution. Such a possibility was hinted by Gilinskii et al. [44] and Chernyi [22], and agrees with the observed sensitive dependence on boundary conditions.

Several analytical approaches are suggested given this situation. First, the shock shape can be assumed, based on some approximation. For instance, the blast models of Lee, Vasiliev, and Endo et al. essentially neglect the effect of combustion on the wave and use a non-reactive blast model to determine the wave shape. Prediction of detonation initiation is then based on conditions behind the shock. Second, flow solutions can be obtained assuming a simple coupled detonation wave, and given a criterion for the validity of the solution, limits of detonation initiation can be found. By following this procedure from both sides (assuming detonation initiation and stabilization, and conversely reaction-zone splitting) different limits might be found, indicating a region of non-uniqueness. In order to make global predictions, the entire flow, including the subsonic region in the stagnation area, must be solved. This normally requires discretized calculations. Predictions of global initiation and failure are difficult to make strictly from theoretical considerations, although progress can be made with predicting reaction-zone splitting as a function of wave shape. These two approaches, with and without assumption of a given wave shape, are described in greater detail below.

3.1 Blast Models

One approach to predicting initiation of detonations by projectiles is through a simplified global energetics analysis, as represented by the models of Lee [74], Vasiljev [118], and Endo et al. [36]. These models compare the energy deposited by the projectile into the gas mixture with a separate model for the minimum energy required to initiate a detonation. Their distinguishing feature is the assumption that the shock wave around the projectile is a simple, non-reactive blast wave. That is, they neglect the effect of combustion on the wave shape and the initiation and stabilization of detonation. The purpose of this section is to describe a framework in which variations of this concept can be considered.

The basic principle is that the rate of energy deposition by the projectile must be greater than

the minimum required to initiate a detonation:

$$E_{p,x} \geq E_{c,x} \tag{3.1}$$

Assuming that the projectile is adiabatic and inert, the rate of deposition by the projectile is equal to the fluid-dynamical drag:

$$E_{p,x} = F_d \tag{3.2}$$

As developed by Lee [74], the analysis begins with the similarity solution for a strong cylindrical blast wave in a perfect gas. In the form used by Lee [74], the blast wave velocity – radius relationship is:

$$U_s^2 = \left(\frac{E_0}{2\pi I \rho_\infty}\right)\frac{1}{r_s^2} \tag{3.3}$$

where U_s and r_s are respectively the blast wave velocity and radius, E_0 is the blast energy, I is an integral function of γ, and ρ_∞ is the initial density.

Equation 3.3 is utilized to obtain an expression for the critical energy for cylindrical detonation initiation by supposing that the critical condition occurs when the wave speed is half of the CJ speed when the radius of the wave has grown to $k\lambda$, where λ is the mixture CJ cell size and k is some constant factor. Lee [74] suggested the ad hoc value of 3.2 for k. Equation 3.3 then simplifies to

$$E_0 = \frac{\pi}{2}(3.2)^2 I \rho_\infty \lambda^2 D_{CJ}^2 \tag{3.4}$$

Equation 3.4 illustrates the factors involved in the critical energy model. The integral I is based on the similarity solution of the non-reactive cylindrical blast wave, and is a function of the ratio of specific heats, γ. Table 3.1 lists some values of I computed for different γ. The procedure for computing I will not be discussed here, but follows the method of Sedov [100]. Previous applications

Table 3.1: Values of integral I for different γ.

γ	I	γ	I
1.20	1.277	1.50	0.494
1.25	1.019	1.55	0.445
1.30	0.846	1.556	0.440
1.35	0.721	1.60	0.404
7/5	0.627	1.65	0.370
1.45	0.553	5/3	0.359

of this model used the value of I for $\gamma = 1.4$ regardless of the γ of the mixture in question. For example, the $2H_2$+O_2+7Ar mixture used by Higgins [51] has γ=1.556, resulting in I=0.440. It can be argued that the difference is negligible compared with other sources of uncertainty in the model, but it is included here for completeness. Certainly, the resulting relation for critical energy

is questionable. The form of Eq. 3.4 is analogous to the more developed and validated spherical critical energy case [73], but no known comparison between Eq. 3.4 and experimental data has been performed. The value taken for k can be viewed as a correlation factor for applying an equation of the form of Eq. 3.4 to experimentally measured values. The value of 3.2 suggested by Lee [74] was based on speculative and untested assumptions. Nonetheless, the form of Eq. 3.4 is generally accepted as exhibiting the proper scaling relationships.

The next step is to equate the critical energy relation to the drag force on a hypervelocity body (see Section 1.3.8). The drag force is typically modeled by

$$F_d = \frac{1}{2}\rho_\infty V_\infty^2 \left(\frac{\pi d^2}{4}\right) C_D \tag{3.5}$$

where C_D is typically taken as 0.92 for hypersonic flow. Combining Eqs. 3.4 and 3.5 and solving for V_∞/D_{CJ} gives

$$\frac{V_\infty}{D_{CJ}} = 2(3.2)\sqrt{\frac{I}{C_D}}\frac{\lambda}{d} \tag{3.6}$$

Eq. 3.6 gives the critical condition for detonation initiation in terms of the two ratios V_∞/D_{CJ} and λ/d.

The Lee-Vasiliev model is attractive in its simplicity and approximate prediction of experimental observations. However, this simplicity fails to reflect the complexity and dynamics of real phenomena, and is inherently valid only in limiting cases. For instance, as with all hypersonic theories, it is valid only at high Mach numbers, where in this case the minimum valid Mach number is unknown. Due to the additional assumptions of the blast wave analogy, it is only valid far from the initiating projectile, in the case of a blunt projectile, despite the fact that initiation and failure is generally determined by the flow near the projectile. Use of the similarity blast solution for unreactive gases is another strong approximation, in that the effect of energy release by combustion is neglected. Clearly, in the case of detonation initiation, the effect of chemical energy release on the blast wave is not negligible. Since the blast wave analogy was developed for steady flows, application to inherently unsteady flows such as unstable initiation (initiation at sub-CJ velocities) is questionable at best. Finally, the strongest limitation of the Lee-Vasiliev model is the reliance on an unproven ad hoc critical energy model.

3.2 Shock-Curvature Models

In contrast to the global approach to detonation initiation taken by the blast models, failure of a detonation wave as it decays from the projectile nose can also be considered as a local phenomenon. In a steady flow, detonation stabilization is likely to be determined locally, in the vicinity of the shock. Therefore, such an analysis should contain the most relevant physics. However, since the

local conditions are determined globally, the results are more difficult to apply to initiation and stabilization predictions, without additional modeling of the rest of the flow.

An introduction to the shock-curvature approach to reacting flows, and some preliminary results are given here. The approach follows closely those of Hornung [60] and Gilinskii and Chernyi [42].

Briefly, flow conditions (i.e., velocities and the thermodynamic state) behind a shock wave can be computed given the upstream conditions and the wave angle relative to the flow direction, using appropriate shock-jump conditions. Variation of these conditions along the shock can also be computed in terms of the local shock curvature. The gradients perpendicular to the shock can then be related to the gradients along the shock by the equations of motion. Thus, the total gradients of all the flow variables can be determined immediately behind the shock. This allows a higher-order estimate of the flow behavior behind the shock. For instance, for reacting flow, the rate of change of the thermodynamic state and velocity along a streamline can be added to the shock-jump conditions for a better estimate of the reaction zone thickness.

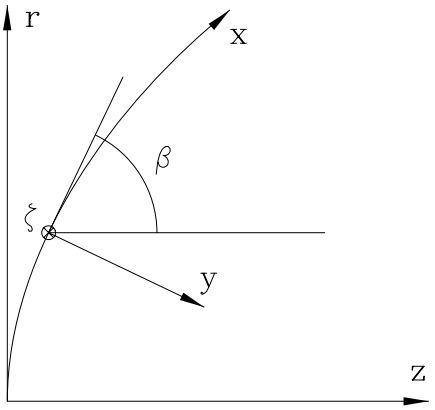

Figure 3.1: Cylindrical and shock-fitted curvilinear coordinates.

3.2.1 Basic Equations

The equations of motion for steady axisymmetric flow without swirl, written in cylindrical coordinates, are given by Eqs. (3.7 – 3.8) (respectively continuity, momentum, and energy). In addition to the pressure and density, enthalpy is taken to be a function of the product-species concentration, c.

$$\nabla \cdot (\rho \mathbf{u}) = 0 = \frac{1}{r}\frac{\partial}{\partial r}(r\rho u_r) + \frac{\partial}{\partial z}(\rho u_z) \tag{3.7}$$

$$\frac{d\mathbf{u}}{dt} + \frac{\nabla P}{\rho} = 0 = (u_r\frac{\partial u_r}{\partial r} + u_z\frac{\partial u_r}{\partial z} + \frac{1}{\rho}\frac{\partial P}{\partial r})\hat{r} + (u_r\frac{\partial u_z}{\partial r} + u_z\frac{\partial u_z}{\partial z} + \frac{1}{\rho}\frac{\partial P}{\partial z})\hat{z} \tag{3.8}$$

$$h(P,\rho,c) + \frac{u^2+v^2}{2} = \text{constant} \tag{3.9}$$

The equations of motion are converted to an orthogonal curvilinear coordinate system fixed in the shock, as illustrated in Fig. 3.1 and described by Hayes and Probstein [47, chap. 5]. In this coordinate system, the x-axis is locally aligned with the shock, so that the shock angle β varies with x. The y-axis is perpendicular to the shock, and the ζ-axis is tangent to the shock but perpendicular to x. As shown in Fig. 3.2, lines of constant x are straight and perpendicular to the shock. Lines of

constant y are likewise parallel to the shock and curved. Since the coordinate system is defined by the shock profile, the shock angle β is also the orientation of the coordinate system with respect to the global cartesian frame.

Equations (3.10 – 3.13) relate the velocities and derivatives in the familiar cylindrical coordinate system of Eqs. (3.7) and (3.8) to those in the curvilinear system. $H = 1 - \kappa_1 y$ is the x scale factor, which represents the relative length of the x coordinate at different distances from the shock, and κ_1 is the shock curvature in the $x - y$ plane, given by $\kappa_1 = -\frac{d\beta}{dx}$.

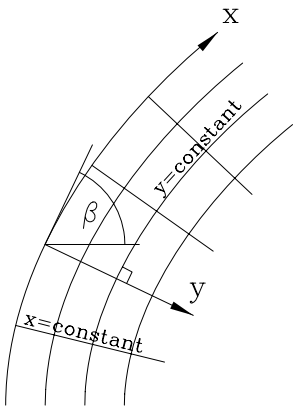

Figure 3.2: Geometry of the orthogonal curvilinear coordinate system.

$$u_r = u\sin\beta - v\cos\beta \tag{3.10}$$

$$u_z = u\cos\beta + v\sin\beta \tag{3.11}$$

$$\frac{\partial}{\partial r} = \frac{\sin\beta}{H}\frac{\partial}{\partial x} - \cos\beta\frac{\partial}{\partial y} \tag{3.12}$$

$$\frac{\partial}{\partial z} = \frac{\cos\beta}{H}\frac{\partial}{\partial x} + \sin\beta\frac{\partial}{\partial y} \tag{3.13}$$

Applying these relations to Eqs. (3.7) and (3.8) yields

$$\frac{\partial(r\rho u)}{\partial x} + \frac{\partial(r\rho v H)}{\partial y} = 0 \tag{3.14}$$

$$u\frac{\partial u}{\partial x} + Hv\frac{\partial u}{\partial y} - \kappa_1 uv + \frac{1}{\rho}\frac{\partial P}{\partial x} = 0 \tag{3.15}$$

$$u\frac{\partial v}{\partial x} + Hv\frac{\partial v}{\partial y} + \kappa_1 u^2 + \frac{H}{\rho}\frac{\partial P}{\partial y} \tag{3.16}$$

which are the same as Eqs. (5.1.6a – 5.1.6c) of Hayes and Probstein [47]. Restricting the analysis to $y = 0$ and denoting partial derivatives with x and y subscripts from now on, Eqs. (3.14 – 3.16) become

$$(\rho u)_x + (\rho v)_y - \rho v\kappa_1 + \frac{\rho u\sin\beta - \rho v\cos\beta}{r} = 0 \tag{3.17}$$

$$uu_x + vu_y - \kappa_1 uv + \frac{P_x}{\rho} = 0 \tag{3.18}$$

$$uv_x + vv_y + \kappa_1 u^2 + \frac{P_y}{\rho} = 0 \tag{3.19}$$

The continuity equation can be written more concisely by substituting $\kappa_2 = \cos\beta/r$ (see Appendix G), where κ_2 is the shock curvature in the $y - \zeta$ plane:

$$(\rho u)_x + (\rho v)_y - \rho v(\kappa_1 + \kappa_2) + \rho u\kappa_2\tan\beta = 0 \tag{3.20}$$

An additional equation is provided by differentiating the energy equation with respect to y:

$$uu_y + vv_y + h_\rho \rho_y + h_P P_y + h_c c_y = 0 \tag{3.21}$$

3.2.2 Gradients and Total Derivatives

Solving Eqs. (3.18 – 3.21) for the y-derivatives of the pressure, density, and velocity components in terms of the post-shock conditions and their x-derivatives yields:

$$\begin{aligned}
P_y F &= \rho h_c c_y + \left(\frac{\rho h_\rho}{v^2} - 1\right)\rho u v_x - \left(\frac{u^2 + \rho h_\rho}{v}\right)\rho u_x - \rho h_\rho \frac{u}{v}\rho_x - \frac{u}{v}P_x \\
&\quad + \rho^2 h_\rho(\kappa_1 + \kappa_2) + \frac{\rho^2 h_\rho}{v}\left(\frac{\kappa_1 u^2}{v} - u\kappa_2 \tan\beta\right) && (3.22) \\
u_y &= \kappa_1 u - \frac{u u_x}{v} - \frac{P_x}{\rho v} && (3.23) \\
v v_y F &= -h_c c_y + \rho u h_P v_x + \left(\frac{u^2 + \rho h_\rho}{v}\right)u_x + \frac{u h_\rho}{v}\rho_x + \frac{u}{\rho v}P_x + (\rho h_P - 1)\kappa_1 u^2 \\
&\quad - \rho h_\rho(\kappa_1 + \kappa_2) + \frac{\rho h_\rho}{v} u\kappa_2 \tan\beta && (3.24) \\
\rho_y F &= \frac{\rho}{v^2} h_c c_y - \frac{\rho^2 u h_P}{v^2} v_x + \frac{\rho}{v}\left(\rho h_P - 1 - \frac{u^2}{v^2}\right)u_x + \frac{u}{v}(\rho h_P - 1)\rho_x - \frac{u}{v^3}P_x \\
&\quad - \rho\kappa_1(\rho h_P - 1)\left(\frac{u^2}{v^2} + 1\right) + \rho\kappa_2(\rho h_P - 1)\left(\frac{u}{v}\tan\beta - 1\right) && (3.25)
\end{aligned}$$

where

$$F = 1 - \rho\left(h_P + \frac{h_\rho}{v^2}\right) \tag{3.26}$$

Equations (3.22 – 3.25) are equivalent to Eqs. (18 – 21) of Hornung [60] (see also Kaneshige and Hornung [63]), except for the addition of terms containing κ_2 to account for three-dimensionality. The chemical energy release term $h_c c_y$ is left unexpanded until a reaction rate model is chosen.

Total time derivatives can be formed from the x and y derivatives, according to Eq. (3.27)

$$\frac{d}{dt} = u\frac{\partial}{\partial x} + v\frac{\partial}{\partial y} \tag{3.27}$$

and derivatives with respect to streamwise distance can be obtained from Eq. (3.28)

$$\frac{d}{ds} = \frac{1}{V}\frac{d}{dt} \tag{3.28}$$

For example, using the x-differentiated energy equation to eliminate ρ_x,

$$uu_x + vv_x + h_P P_x + h_\rho \rho_x = 0 \tag{3.29}$$

the total derivatives of P, ρ, u, v, and the deflection angle δ are given by:

$$
\begin{aligned}
F\frac{dP}{dt} &= \rho h_c \frac{dc}{dt} + \kappa_1 G \frac{\rho^2 h_\rho}{v} && (3.30)\\
F\frac{d\rho}{dt} &= \frac{\rho h_c}{v^2}\frac{dc}{dt} - \kappa_1 G \frac{\rho}{v}(\rho h_P - 1) && (3.31)\\
\frac{du}{dt} &= \kappa_1 \left[uv - \frac{1}{\rho}\frac{P_x}{\kappa_1} \right] && (3.32)\\
F\frac{dv}{dt} &= -\frac{h_c}{v}\frac{dc}{dt} - \kappa_1 \left[G\frac{\rho h_\rho}{v^2} + F\left(u^2 - \frac{u}{\rho v}\frac{P_x}{\kappa_1} \right) \right] && (3.33)\\
F\frac{d\delta}{dt} &= \frac{u h_c}{v V^2}\frac{dc}{dt} + \kappa_1 \left[G\frac{\rho u h_\rho}{v^2 V^2} - \frac{F}{\rho v}\frac{P_x}{\kappa_1} \right] && (3.34)
\end{aligned}
$$

where

$$
G = u^2 + v^2 - v\frac{u_x}{\kappa_1} + u\frac{v_x}{\kappa_1} - \frac{u}{\rho v}\frac{P_x}{\kappa_1} + \frac{\kappa_2}{\kappa_1}(v^2 - uv\tan\beta) \qquad (3.35)
$$

Equations (3.30) and (3.31) are equivalent to Eqs. (31) and (32) of Hornung [60]. Examination of these equations reveals that in each case except $\frac{du}{dt}$, the right-hand side consists of three parts proportional to the reaction rate, κ_1, and κ_2, i.e., due to combustion, in-plane shock curvature, and transverse shock curvature. If the curvature terms are neglected, these equations become the standard ZND structure equations (Shepherd [103], Fickett and Davis [37]).

3.2.3 Perfect Gas

To explicitly evaluate the post-shock conditions and their x-derivatives, the perfect-gas equations of state are assumed:

$$
P = \rho R T \qquad\qquad \frac{\partial h}{\partial T} = c_p \qquad (3.36)
$$

The shock-jump conditions are:

$$
\begin{aligned}
\frac{P}{P_\infty} &= \frac{2\gamma M_\infty^2 \sin^2\beta - (\gamma-1)}{\gamma+1} & \frac{\rho}{\rho_\infty} &= \frac{(\gamma+1)M_\infty^2 \sin^2\beta}{(\gamma-1)M_\infty^2 \sin^2\beta + 2}\\
\frac{u}{V_\infty} &= \cos\beta & \frac{v}{V_\infty} &= \frac{(\gamma-1)M_\infty^2 \sin^2\beta + 2}{(\gamma+1)M_\infty^2 \sin\beta}
\end{aligned} \qquad (3.37)
$$

and the x-differentiated shock-jump conditions are:

$$
\begin{aligned}
\frac{P_x}{P_\infty} &= -\kappa_1 \frac{4\gamma M_\infty^2 \sin\beta\cos\beta}{\gamma+1} & \frac{\rho_x}{\rho_\infty} &= -\kappa_1 \frac{4(\gamma+1)M_\infty^2 \sin\beta\cos\beta}{\left[(\gamma-1)M_\infty^2 \sin^2\beta + 2\right]^2}\\
\frac{u_x}{V_\infty} &= \kappa_1 \sin\beta & \frac{v_x}{V_\infty} &= \kappa_1 \cos\beta \left[\frac{2-(\gamma-1)M_\infty^2 \sin^2\beta}{(\gamma+1)M_\infty^2 \sin^2\beta} \right]
\end{aligned} \qquad (3.38)
$$

The x-derivatives are all directly proportional to the κ_1 curvature. Using the perfect gas assumption, the parameters F and G expand to

$$F = \frac{1}{\gamma-1}\left[\frac{1-M_n^2}{M_n^2}\right] = \frac{\gamma+1}{\gamma-1}\left[\frac{M_\infty^2\sin^2\beta-1}{(\gamma-1)M_\infty^2\sin^2\beta+2}\right] \tag{3.39}$$

$$\frac{G}{V_\infty^2} = \frac{2\cos^2\beta}{\gamma+1}\left[\frac{3M_\infty^2\sin^2\beta+1}{M_\infty^2\sin^2\beta}\right] + \left[1+\frac{\kappa_2}{\kappa_1}\right]\frac{2[(\gamma-1)M_\infty^2\sin^2\beta+2][1-M_\infty^2\sin^2\beta]}{(\gamma+1)^2M_\infty^4\sin^2\beta} \tag{3.40}$$

$$= \frac{8}{\gamma+1}\cos^2\beta - \frac{\sin\delta\cos\delta\cos\beta}{\sin\beta\cos^2(\beta-\delta)} - \frac{\kappa_2}{\kappa_1}\frac{\sin(\beta-\delta)\cos\beta\sin\delta}{\cos^2(\beta-\delta)} \tag{3.41}$$

where Eq. (3.41) has been simplified by eliminating M_∞ using the oblique-shock deflection angle relation:

$$\cot\delta = \tan\beta\left[\frac{(\gamma+1)M_\infty^2}{2(M_\infty^2\sin^2\beta-1)}-1\right] \tag{3.42}$$

and M_n is the post-shock Mach number normal to the shock, given by:

$$M_n^2 = \frac{(\gamma-1)M_\infty^2\sin^2\beta+2}{2\gamma M_\infty^2\sin^2\beta-(\gamma-1)} \tag{3.43}$$

The streamline derivatives of P, ρ, and δ, written in terms of variables β, δ, and M_2 ($M_n = M_2\sin(\beta-\delta)$), are given by Eqs. (3.44 – 3.46):

$$\frac{1}{\rho_\infty V_\infty^2}\frac{dP}{ds} = 2\frac{(\gamma-1)}{(\gamma+1)}\frac{\sin\beta}{\cos\beta}\frac{\cos^2(\beta-\delta)}{\sin\delta}\frac{h_c}{V_\infty^3}\frac{dc}{dt} + \frac{1}{1-M_2^2\sin^2(\beta-\delta)}\times$$
$$\left\{\kappa_1\left[\frac{\sin\delta\cos\delta}{\cos(\beta-\delta)} - \frac{8\sin\beta\cos\beta\cos(\beta-\delta)}{\gamma+1}\right] + \kappa_2\sin\beta\sin\delta\frac{\sin(\beta-\delta)}{\cos(\beta-\delta)}\right\} \tag{3.44}$$

$$\frac{1}{\rho_\infty}\frac{d\rho}{ds} = 2\frac{(\gamma-1)}{(\gamma+1)}\frac{\sin\beta\cos^4(\beta-\delta)}{\cos^3\beta\sin\delta\sin^2(\beta-\delta)}\frac{h_c}{V_\infty^3}\frac{dc}{dt} + \frac{2\cos(\beta-\delta)}{\gamma+1}\times$$
$$\left\{\kappa_1\left[\frac{\cos\delta}{\sin(\beta-\delta)\cos\beta} - \frac{8}{\gamma+1}\frac{\sin\beta\cos^2(\beta-\delta)}{\sin\delta\sin(\beta-\delta)}\right] + \kappa_2\frac{\sin\beta}{\cos\beta}\right\} \tag{3.45}$$

$$\frac{d\delta}{ds} = 2\frac{(\gamma-1)}{(\gamma+1)}\frac{\cos^4(\beta-\delta)}{\cos^2\beta\sin\delta}\frac{h_c}{V_\infty^3}\frac{dc}{dt} + \frac{\cos(\beta-\delta)}{1-M_2^2\sin^2(\beta-\delta)}\times$$
$$\left\{\kappa_1\left[\frac{\sin 2\delta}{\sin 2\beta} - \frac{4}{\gamma+1}\left(1-(2-M_2^2)\sin^2(\beta-\delta)\right)\right] + \kappa_2\frac{\sin(\beta-\delta)\sin\delta}{\cos\beta}\right\} \tag{3.46}$$

Equations (3.44) and (3.46) agree with Eq. (4.3) of Gilinskii and Chernyi [42] except for notation differences and the addition of the energy release term.

3.2.4 Streamline Curvature

For the planar non-reactive case (i.e., if only the κ_1 term is retained), the ratio of streamline curvature to shock curvature can be computed independently of shock curvature. The streamline curvature, defined as positive for streamlines curved toward the projectile, is given by the negative of Eq. 3.46.

The result is plotted in Fig. 3.3(a), which is identical to Fig. 2 of [60].

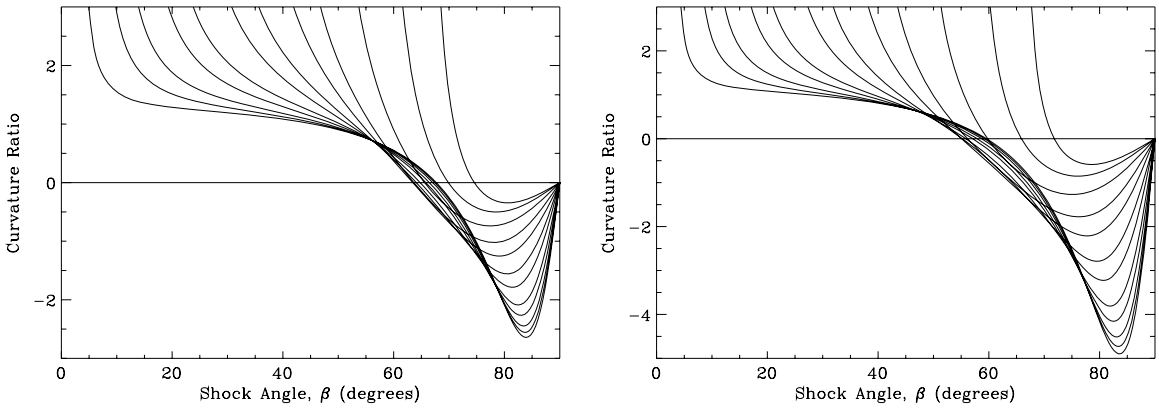

(a) Plane shock

(b) Axisymmetric shock

Figure 3.3: Ratio of streamline curvature to in-plane shock curvature versus shock angle for non-reactive planar and axisymmetric flow, with γ=1.4 and M_∞=1.1, 1.2, 1.4, 1.7, 2, 2.5, 3, 4, 5, 7, 10, 20, from top to bottom.

If the transverse curvature and heat release terms are included, the ratio becomes a function of the local shock curvatures. In order to compare these results with the planar case, a relationship between the shock angle and the curvatures must be assumed. Although arbitrary, a hyperbolic bow-shock shape correlation, as presented by Billig [16] and described in Section 6.1.2, is a natural choice, and provides the necessary constraint. Non-dimensionalizing by the radius of curvature of the shock at the nose, R_c, and taking the origin at the shock vertex, the shape becomes dependent only on the Mach angle, $\mu = \sin^{-1}(1/M_\infty)$ (see [60] and [63]):

$$Y = \tan\mu\sqrt{X(X + 2/\tan^2\mu)} \tag{3.47}$$

From Eq. (3.47), the slope and curvature of the shock can be obtained:

$$\frac{dY}{dX} = \tan\beta = \frac{X\tan^2\mu + 1}{\sqrt{X(X\tan^2\mu + 2)}} \tag{3.48}$$

$$\kappa_1 R_c = \frac{-\frac{d^2Y}{dX^2}}{\left[1 + \left(\frac{dY}{dX}\right)^2\right]^{3/2}} = \left[\frac{X^2\tan^2\mu}{\cos^2\mu} + \frac{2X}{\cos^2\mu} + 1\right]^{-3/2} \tag{3.49}$$

Solving Eq. (3.48) for X,

$$X = \cot^2\mu\left[\sqrt{\frac{\tan^2\beta}{\tan^2\beta - \tan^2\mu}} - 1\right] \tag{3.50}$$

$\kappa_1 R_c$ can then be obtained as a function of shock angle, β. The transverse curvature is given

simply by $\kappa_2 R_c = \cos\beta/Y$ (see Appendix G). The non-reactive axisymmetric results are plotted in Fig. 3.3(b) for the same conditions as used in Fig. 3.3(a). Qualitatively, no differences are apparent between the planar and axisymmetric cases. Quantitatively, they are close at small angles, but the ratio is more negative near the nose in the axisymmetric case.

The rate of chemical energy release is based on the Arrhenius rate equation:

$$\frac{dc}{dt} = \rho^m k_f \exp\left(\frac{-E_a}{\tilde{R}T}\right) \tag{3.51}$$

The dimensional parameters appearing in Eq. (3.51) are the activation energy, E_a, the frequency factor, k_f, and the reaction order, m. The partial derivative of enthalpy with respect to product-species concentration, h_c, is related to the enthalpy of reaction h_m by $h_c = -h_m/\rho$. Non-dimensionalizing the density and pressure by ρ_∞ and P_∞ respectively, and introducing the non-dimensional parameters $\hat{q}$ and $\hat{E}_a$:

$$\hat{q} = \frac{h_m k_f \rho_\infty^{m-1} R_p}{a_\infty^3} \qquad\qquad \hat{E_a} = \frac{\gamma E_a}{a_\infty^2 W} \tag{3.52}$$

the energy release rate appearing in Eqs. (3.44 – 3.46) becomes

$$-\frac{h_c}{V_\infty^3}\frac{dc}{dt} = \frac{\hat{\rho}^{m-1}\hat{q}}{R_p M_\infty^3} \exp\left(\frac{-\hat{E}_a\hat{\rho}}{\hat{P}}\right) \tag{3.53}$$

The non-dimensional parameters $\hat{q}$ and $\hat{E}_a$ depend only on the dimensional chemical rate parameters, upstream conditions, and the projectile radius, R_p. Applying these relations to the ratio of streamline curvature to in-plane shock curvature (Eq. 3.46) yields:

$$\begin{aligned} -\frac{1}{\kappa_1}\frac{d\delta}{ds} \;=\; & 2\frac{(\gamma-1)}{(\gamma+1)}\frac{\cos^4(\beta-\delta)}{\cos^2\beta\sin\delta}\frac{\hat{\rho}^{m-1}\hat{q}}{M_\infty^3\kappa_1 R_c}\frac{R_c}{R_p}\exp\left(\frac{-\hat{E}_a\hat{\rho}}{\hat{P}}\right) - \frac{\cos(\beta-\delta)}{1-M_2^2\sin^2(\beta-\delta)} \times \\ & \left\{\left[\frac{\sin 2\delta}{\sin 2\beta} - \frac{4}{\gamma+1}\left(1-(2-M_2^2)\sin^2(\beta-\delta)\right)\right] + \frac{\kappa_2}{\kappa_1}\frac{\sin(\beta-\delta)\sin\delta}{\cos\beta}\right\} \end{aligned} \tag{3.54}$$

The ratio of the projectile and shock-nose radii of curvature, R_c/R_p, is generally a function of M_∞ and γ for non-reacting shocks. The general function is unknown, but the special case for $\gamma = 1.4$ is given by Eq. (6.3). Since this function shows Mach number independence at high Mach number, and $\gamma \approx 1.4$ for the mixtures of interest, the hypersonic limit value of $R_c/R_p = 1.143$ is used here.

Real combustion reactions consist of a number of species participating in a number of simultaneous reversible elementary reactions, each of which can be characterized by separate values of E_a, k_f, and m. Treating the overall reaction with a single Arrhenius rate is an approximation, although the important explosive character is retained. The general case requires writing the enthalpy (3.9)

as a function of the concentrations of all the species:

$$h(P, \rho, c_i) = \text{constant}, \ i = 1, \ldots, n \tag{3.55}$$

Then the energy release term $h_c \frac{dc}{dt}$ becomes a sum over all the species $\sum h_{ci} \frac{dc_i}{dt}$. The time derivative of each concentration is a sum over all the reactions involving that species. Since the reaction rates are not functions of the shock curvature, this generalization could be made without seriously altering Eqs. (3.30 – 3.34).

Since one of the most important explosive characteristics for detonations is the induction delay (or reaction zone thickness), the global rate parameters are often matched to induction time data or calculations performed with a large number of species and elementary reactions. The overall reaction order, m, can be fitted to data, but is usually approximately 2.

The method of Frank-Kamenetskii [38, p.353] can be used to compute E_a and k_f from induction time data. The rate equation (3.51) can not be integrated in closed form, and so is linearized using the approximation

$$\frac{E_a}{\tilde{R}T} \simeq \frac{E_a}{\tilde{R}T_s} - \frac{E_a \Delta T}{\tilde{R}T_s^2} \tag{3.56}$$

Further relating the temperature and product-species concentration by $\rho c_v dT = h_m dc$ for a constant-volume process, Eq. (3.51) becomes

$$\frac{c_v}{h_m} \frac{dT}{dt} = \rho^{m-1} k_f \exp\left(\frac{-E_a}{\tilde{R}T_s}\right) \exp\left(\frac{E_a \Delta T}{\tilde{R}T_s^2}\right) \tag{3.57}$$

which can be integrated in closed-form. The problem can also be posed for a constant-pressure process, or for flow through a reaction zone (i.e., along the Rayleigh line). The approximation given by Eq. (3.56) breaks down quickly as ΔT becomes large, but since this occurs at the end of the induction zone, the upper limits of integration can be taken as $\Delta T \to \infty$ and $t \to t_{ind}$. Performing the integration yields

$$t_{ind} = \frac{\tilde{R}T_s}{E_a} \frac{c_v T_s}{\rho^{m-1} h_m k_f} \exp\left(\frac{E_a}{\tilde{R}T_s}\right) \tag{3.58}$$

Computing induction times for two conditions, with detailed chemistry, Eq. (3.58) can be used to determine the global activation energy:

$$\frac{E_a}{\tilde{R}} = \frac{\ln(t_{ind,1}/t_{ind,2}) - 2\ln(T_{s,1}/T_{s,2}) + (m-1)\ln(\rho_{s,1}/\rho_{s,2})}{1/T_{s,1} - 1/T_{s,2}} \tag{3.59}$$

The pre-exponential temperature and density dependence of the induction time are often neglected (the latter justified in the strong-shock limit), leading to the simpler relation:

$$\frac{E_a}{\tilde{R}} \approx \frac{\ln(t_{ind,1}) - \ln(t_{ind,2})}{1/T_{s,1} - 1/T_{s,2}} \tag{3.60}$$

Once the activation energy is known, Eq. (3.58) can be used again to solve for $h_m k_f$:

$$h_m k_f = \frac{\tilde{R}T_s}{E_a} \frac{c_v T_s}{\rho^{m-1} t_{ind}} \exp\left(\frac{E_a}{\tilde{R}T_s}\right) \tag{3.61}$$

Some values of $E_a/\tilde{R}$ and $h_m k_f$ for mixtures used experimentally, and computed using Eqs. (3.59) and (3.61) assuming second-order kinetics, are given in Table 3.2. The induction time values were computed using a constant-volume model similar to the reaction zone model described in Chapter 4, for conditions corresponding to CJ detonations at 1 bar and 300 K. The ratio of specific heats in each

Table 3.2: Global rate parameters and frozen shock γ for mixtures of interest, computed for conditions corresponding to CJ detonations at 1 bar initial pressure.

Mixture	$E_a/\tilde{R}$ (K)	$h_m k_f$ (J-m^3/kg^2-s)	γ
$2H_2$+O_2+N_2	1.4×10^4	2.2×10^{15}	1.32
$2H_2$+O_2+$2N_2$	1.4×10^4	1.5×10^{15}	1.32
$2H_2$+O_2+$3N_2$	1.4×10^4	1.3×10^{15}	1.32
$2H_2$+O_2+$3.76N_2$	1.5×10^4	1.4×10^{15}	1.32
C_2H_4+$3O_2$+$5N_2$	2.2×10^4	1.2×10^{16}	1.23
C_2H_2+$2.5O_2$+$9.4N_2$	1.4×10^4	5.3×10^{14}	1.27

case was taken as the frozen-shock value, computed by STANJAN [94]. For the sake of determining induction times from the computations, the point of maximum energy release was used to define the end of the induction zone. For cases with well-defined induction zones (generally equivalent to large activation energy), the exact definition used to identify the induction zone is not important. Otherwise, the resulting induction time values can be sensitive to the definition.

All of the values in Table 3.2 fall within about an order of magnitude of each other, so some representative results, in the form of the ratio of streamline curvature to in-plane shock curvature, have been computed using the hydrogen-air values, and are presented in Fig. 3.4. For the sake of computing $\hat{q}$, the projectile radius was taken as 12.7 mm. Curves are plotted for a number of values of $\hat{q}$, several of which are of particular interest. The lowest curves are for negative $\hat{q}$, corresponding to endothermic reactions. As the heat release becomes exothermic, the magnitude of the curvature ratio near the nose decreases. For endothermic and thermally

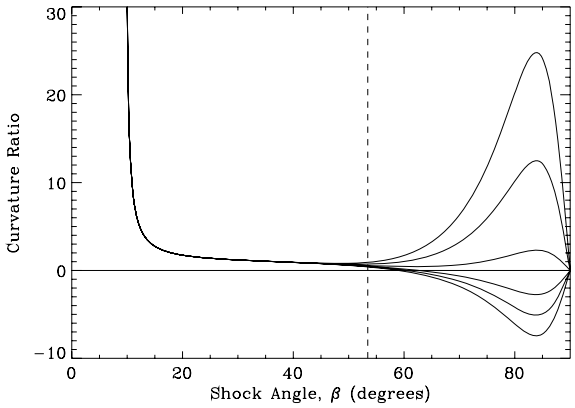

Figure 3.4: Ratio of streamline curvature to in-plane shock curvature versus shock angle, for $\hat{E}_a$=50.0, γ=1.32 and M_∞=6.0. $\hat{q}$=-30000, 0, 30000, 94800, 225000, 383000 from bottom to top. Dashed vertical line at $\beta = 53.4°$ represents the CJ angle in hydrogen-air at 1.0 bar.

neutral reactions, the curvature ratio is negative near the nose, crosses zero at the Crocco point (where the streamline curvature is zero), and becomes positive.

As $\hat{q}$ increases, the streamline curvature near the nose increases and eventually becomes positive everywhere. The top three curves ($\hat{q}$=94800, 225000, and 383000) correspond to initial pressures of 0.421, 1.0, and 1.7 bar. These pressures represent the experimental conditions of shots 1015, 1807, and 1812, respectively. Shots 1015 and 1807 resulted in shock-induced combustion, while shot 1812 resulted in a stabilized detonation (see Figs. B.43, B.47, and B.53). The latter two have a significant effect on the curvature ratio near the nose. Even so, all of the curves converge around β=40°, so that even at the higher pressures, beyond a certain point along the shock the effect of combustion is negligible. For this case, the CJ angle is β_{CJ}=53.5°. At that angle, the curvature ratios corresponding to 1.0 and 1.7 bar are two to three times larger than than that at 0.421 bar. Since the critical pressure for detonation initiation and stabilization was experimentally found to be around 1.5 bar, this suggests that the effect of curvature near the CJ angle may be useful for predicting failure. However, this analysis does not clearly identify a specific critical pressure.

3.2.5 Induction Time

By combining the total derivatives of the pressure and density (Eqs. 3.30 and 3.31) using the perfect gas equation of state, the total derivative of the temperature can be computed:

$$\frac{1}{T_\infty}\frac{dT}{dt} = \frac{\gamma M_n^2 - 1}{1 - M_n^2}\frac{h_c}{c_p T_\infty}\frac{dc}{dt} - \frac{v}{(1 - M_n^2)c_p T_\infty}(\kappa_1 G_1 + \kappa_2 G_2) \tag{3.62}$$

The temperature is interesting because its increase is a good indication of the progress of the reaction. A progress variable related to the product concentration would be equally useful. Equation (3.62) illustrates the effect of shock curvature on the reaction zone. Without the curvature terms, the rate of change of the temperature depends on the reaction rate, and with a temperature dependent reaction rate, the feedback mechanism responsible for the explosive nature of combustion is apparent. The curvature coefficients G_1 and G_2 are given by:

$$G_1 = u^2 + v^2 - v\frac{u_x}{\kappa_1} + u\frac{v_x}{\kappa_1} - \frac{u}{\rho v}\frac{P_x}{\kappa_1} \tag{3.63}$$

$$G_2 = v^2 - uv\tan\beta \tag{3.64}$$

which, written in terms of β and δ for the perfect gas case, become:

$$\frac{G_1}{V_\infty^2} = \frac{8}{\gamma + 1}\cos^2\beta - \frac{\sin\delta\cos\delta\cos\beta}{\sin\beta\cos^2(\beta - \delta)} \tag{3.65}$$

$$\frac{G_2}{V_\infty^2} = -\frac{\sin(\beta - \delta)\cos\beta\sin\delta}{\cos^2(\beta - \delta)} \tag{3.66}$$

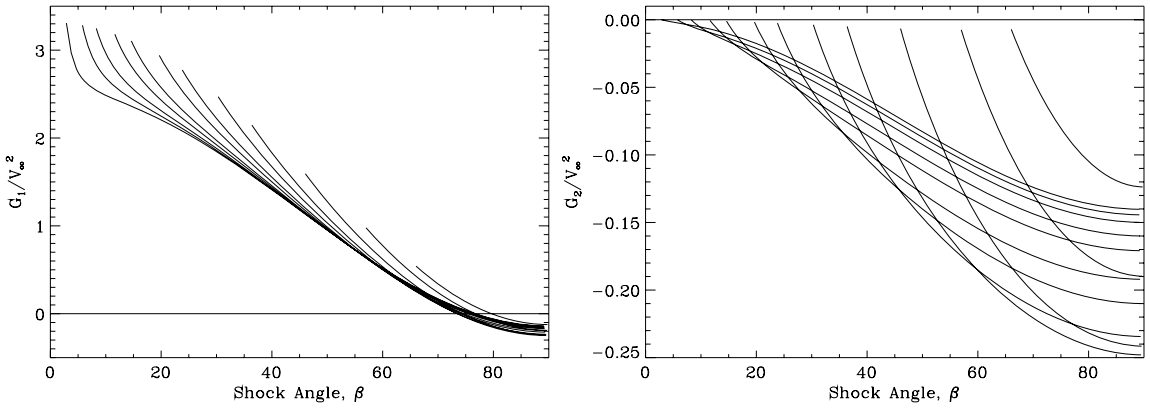

(a) In-plane curvature coefficient, G_1

(b) Transverse curvature coefficient, G_2

Figure 3.5: Normalized G_1 and G_2 for a perfect gas with γ=1.4 and M_∞=1.1, 1.2, 1.4, 1.7, 2, 2.5, 3, 4, 5, 7, 10, 20. Mach number increases from right to left along the top in both cases. Each curve terminates at the corresponding Mach angle.

G_1 and G_2 determine the signs and influence the magnitudes of the curvature effects. These parameters are plotted versus shock angle, for a set of Mach numbers, in Fig. 3.5. G_1 changes sign from negative near the nose to positive at smaller angles, while G_2 is always negative. Therefore, the in-plane curvature, κ_1, has a positive effect on the temperature rise near the nose and a negative effect at smaller angles, with the sign change occurring in the sonic region. In contrast, the transverse curvature, κ_2, always has a positive effect on the temperature rise. At the nose ($\beta = 90°$), the two coefficients are equal, as expected since the shock shape is identical in both planes at that point. At wave angles smaller than the point at which G_1 is zero, the magnitude of G_1 grows, while G_2 approaches zero. This suggests that the effect of transverse curvature tends to be small compared to the effect of in-plane curvature.

By omitting the curvature terms of Eq. (3.62) entirely, an equation for the basic ZND reaction zone structure is obtained (Shepherd [103], Fickett and Davis [37]). Omitting only the κ_2 curvature term and considering only the nose yields an equation consistent with the equations of Detonation Shock Dynamics theory (Bdzil et al. [7]).

From here on, the analysis presented is analogous to that of Eckett et al. [35]. Expanding the heat release term using the Arrhenius rate equation discussed earlier (3.53) and non-dimensionalizing, Eq. (3.62) becomes

$$\frac{R_p}{V_\infty T_\infty}\frac{dT}{dt} = \frac{1-\gamma M_n^2}{1-M_n^2}\frac{(\gamma-1)\hat{\rho}^{m-1}\hat{q}}{M_\infty}\exp\left(\frac{-E_a}{\tilde{R}T}\right) - \frac{vR_p}{(1-M_n^2)c_pT_\infty V_\infty}(\kappa_1 G_1 + \kappa_2 G_2) \qquad (3.67)$$

Using the Frank-Kamenetskii approximation (3.56) and substituting

$$\phi = \frac{E_a(T - T_s)}{\tilde{R}T_s^2} \tag{3.68}$$

Eq. (3.67) becomes

$$\frac{R_p}{V_\infty T_\infty}\frac{\tilde{R}T_s^2}{E_a}\frac{d\phi}{dt} = \frac{1-\gamma M_n^2}{1-M_n^2}\frac{(\gamma-1)\hat{\rho}^{m-1}\hat{q}}{M_\infty}\exp\left(\frac{-E_a}{\tilde{R}T_s}\right)\mathrm{e}^{\phi} - \frac{vR_p}{(1-M_n^2)c_pT_\infty V_\infty}(\kappa_1 G_1 + \kappa_2 G_2) \tag{3.69}$$

which has the form

$$a\frac{d\phi}{dt} = b\mathrm{e}^{\phi} - c \tag{3.70}$$

where

$$a = \frac{R_p}{V_\infty}\frac{\tilde{R}T_s}{E_a}\frac{T_s}{T_\infty} \tag{3.71}$$

$$b = \frac{(1-\gamma M_n^2)}{1-M_n^2}\frac{(\gamma-1)\hat{\rho}^{m-1}\hat{q}}{M_\infty}\exp\left(\frac{-E_a}{\tilde{R}T_s}\right) \tag{3.72}$$

$$c = \frac{vR_p}{(1-M_n^2)c_pT_\infty V_\infty}(\kappa_1 G_1 + \kappa_2 G_2) \tag{3.73}$$

At this point, assuming constant properties, i.e., that a, b, and c are constant, is helpful. This assumption is equivalent to the large activation energy approximation. Proceeding in this way, Eq. (3.70) can be further reduced to

$$\frac{d\phi}{d\tau} = \mathrm{e}^{\phi} - \alpha \tag{3.74}$$

by substituting

$$\tau = \frac{b}{a}t \qquad\qquad \alpha = \frac{c}{b} \tag{3.75}$$

Equation (3.74) has the solution

$$\phi = \ln\left[\frac{\alpha}{1 - \mathrm{e}^{\alpha\tau}(1-\alpha)}\right] \tag{3.76}$$

which has an explosive character. The end of the induction zone occurs at τ_{ind} when $\phi \to \infty$:

$$\tau_{ind} = \frac{1}{\alpha}\ln\left(\frac{1}{1-\alpha}\right) \tag{3.77}$$

Substituting back to obtain t_{ind},

$$t_{ind} = \frac{a}{c}\ln\left(\frac{b}{b-c}\right) \tag{3.78}$$

A special case of Eq. (3.78) is the induction time behind a straight shock, which is obtained in the

limit $c \to 0$:

$$t_{ind} = \frac{a}{b} \tag{3.79}$$

The difference between Eqs. (3.78) and (3.79) illustrates the effect of shock curvature on the reaction zone. Eq. (3.78) becomes singular as $c \to b$, that is, if the in-plane curvature effects are strong enough, whereas Eq. (3.79) shows no such singularity.

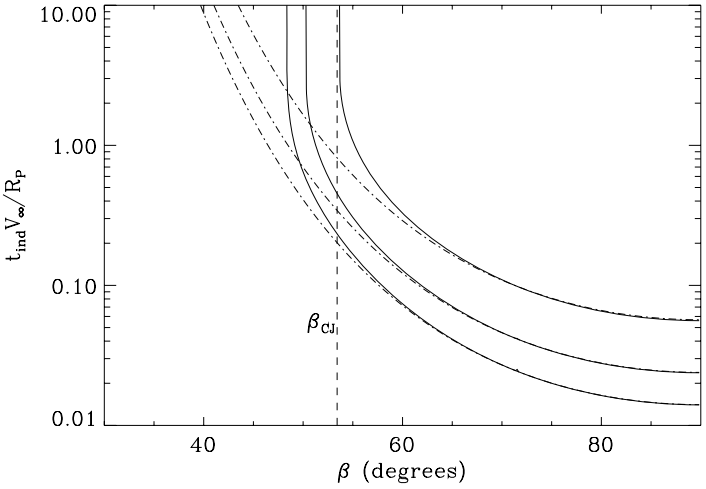

Figure 3.6: Induction time calculations with and without curvature effects in hydrogen-air at 0.421, 1.0, and 1.7 bar, from top to bottom. Hyperbolic shape used for curved shock.

Induction times from Eqs. (3.78) and (3.79), non-dimensionalized by R_p/V_∞, are plotted versus wave angle for stoichiometric hydrogen-air in Fig. 3.6. The solid curves were computed with curvature effects included (3.78), and the dashed curves were computed with curvature effects omitted (3.79). The rate parameters described in Section 3.2.4 were used (i.e., $\hat{E}_a$=50.0; $\hat{q}$=94800, 225000, 383000; γ=1.32). Whereas the straight-shock induction times continuously increase with decreasing wave angle, the curved shock induction times become singular at finite wave angles, illustrating the profound effect shock curvature has on the reaction zone. Barely visible at the nose (β=90°), the straight-shock induction times are larger than the curved-shock values, as previously noted (cf. Fig. 3.5). The three curves represent initial pressures of 0.421, 1.0, and 1.7 bar, which correspond to the conditions of shots 1015, 1807, and 1812 (Figs. B.43, B.47, and B.53). The first two resulted in shock-induced combustion, and the third resulted in a stabilized detonation. Figure 3.6 shows the curved-shock and straight-shock induction time solutions diverging near the CJ angle for all three pressures, with the divergence more pronounced at the lower pressures. The curved-shock curve for 0.421 bar even becomes singular above the CJ angle, suggesting that these calculations could be useful for predicting detonation failure.

Figure 3.7 shows induction time calculations for ethylene and acetylene mixtures, analogous to those for hydrogen-air shown in Fig. 3.6. Straight-shock and curved-shock calculations are represented by dashed and solid curves respectively, and each pair of curves corresponds to an initial pressure studied experimentally. The three pressures in each graph span experimentally observed cases of shock-induced combustion (at the lowest pressure) and stabilized detonation (highest pressure). The reaction-rate parameters were computed using the procedure described in Section 3.2.4,

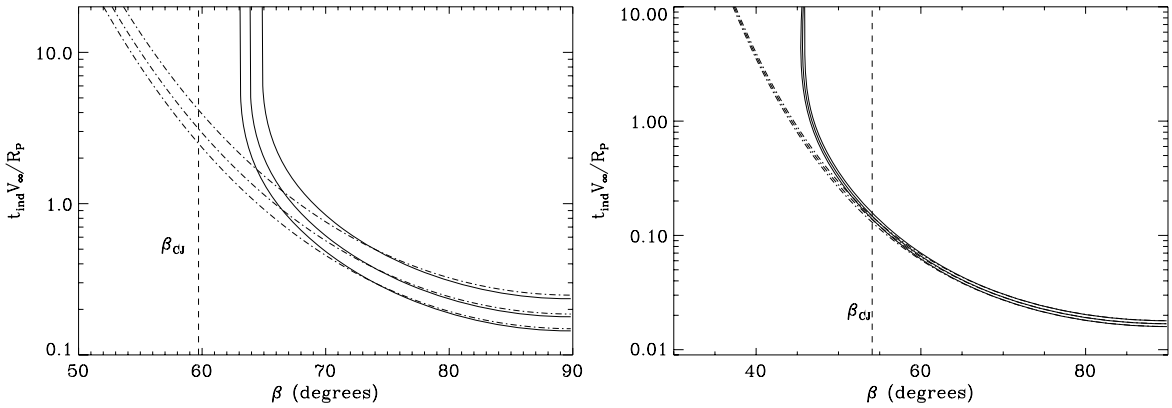

(a) C_2H_4+3O_2+5N_2 at 0.3, 0.4, and 0.5 bar ($\hat{E}_a$=72.6; $\hat{q}$=1170000, 1560000, 1950000; γ=1.23)

(b) C_2H_2+2.5O_2+9.4N_2 at 0.8, 0.85, and 0.9 bar ($\hat{E}_a$=44.4; $\hat{q}$=137000, 146000, 154000; γ=1.27)

Figure 3.7: Induction time calculations in C_2H_4 and C_2H_2 mixtures.

but for the relevant pressures.

Figures 3.7(a) and 3.7(b) do not show the same kind of agreement with experimental observations as Fig. 3.6. Figure 3.7(a) seems to predict detonation failure at all three pressures, even though stabilized initiation was observed at 0.5 bar in shot 1822 (Fig. B.81). Conversely, Fig. 3.7(b) suggests that all cases should result in stabilized detonation, even though shock-induced combustion was observed at 0.8 bar in shot 1837 (Fig. B.88).

Clearly, these preliminary results are not conclusive. A number of approximations and assumptions were made in developing the model which may account for the disagreement, and some of which could be relaxed in further work. The use of a hyperbolic shock shape developed for non-reactive flows is an obvious problem, since combustion can significantly affect the bow wave shape. It is definitely invalid for modeling the reaction zone behind a stabilized detonation. Extension of the hyperbolic shock shape correlation to reactive flows, or curve fits of actual shock shapes could be useful here. The single irreversible Arrhenius reaction rate (with no depletion) and constant properties is another serious simplification. This may be best generalized by performing numerical calculations with detailed chemical kinetics and realistic thermodynamic properties.

Chapter 4 Mixture Characterization

A detonable gas can be uniquely described by its chemical composition and thermodynamic state (pressure and temperature). In the present study, temperature was not controlled, but can be assumed to be fixed at the ambient condition, about 298 K. In order to compare results using different mixtures and pressures, it is necessary to characterize them with a set of standard parameters. Two canonical parameters that are very useful are the Chapman-Jouguet detonation speed and the cell size (both discussed in Section 1.3). Both can be experimentally measured. CJ detonation speed can be computed accurately, while the cell size, which is an imprecisely defined quantity anyway, can be modeled with varying accuracy. CJ speed calculations are so highly trusted that calculation results are normally used to characterize a mixture, rather than experimentally measured values. Only semi-empirical models exist to predict cell size, so experimental data are more valuable, with modeling serving to interpolate and extrapolate the experimental data.

4.1 Detonation Tube Experiments

The standard apparatus for detonation studies is the detonation tube. The GALCIT Detonation Tube was used to measure detonation wave speeds and cell sizes for mixtures and conditions not represented in the literature.

4.1.1 GALCIT Detonation Tube

Akbar [3] described the GALCIT Detonation Tube (GDT), illustrated in Fig. 4.1, in detail. The discussion to follow is a brief overview of the facility and the procedures used to generate data for the present study.

The GDT is composed of three stainless steel sections with 280-mm (11-inch) inside diameter, 25.4-mm (1-inch) wall thickness, and 7.3-m (24-ft) total length. Detonations are initiated by a staged ignition system consisting of an oxygen-acetylene driver and exploding wire. The acetylene and oxygen mixture is injected into the tube just prior to a shot (injection time typically 2 seconds) and is detonated by the exploding wire a short delay after the injection. For the present purposes, the opposite end of the tube was closed by a flange and contained a soot foil for recording detonation cell patterns.

The foil was an aluminum 3003 sheet, 0.508 mm (0.020 in) thick and 0.914 m x 0.610 m (2 ft x 3 ft), rolled to the shape of the detonation tube. The upstream edge of the foil was riveted to an aluminum

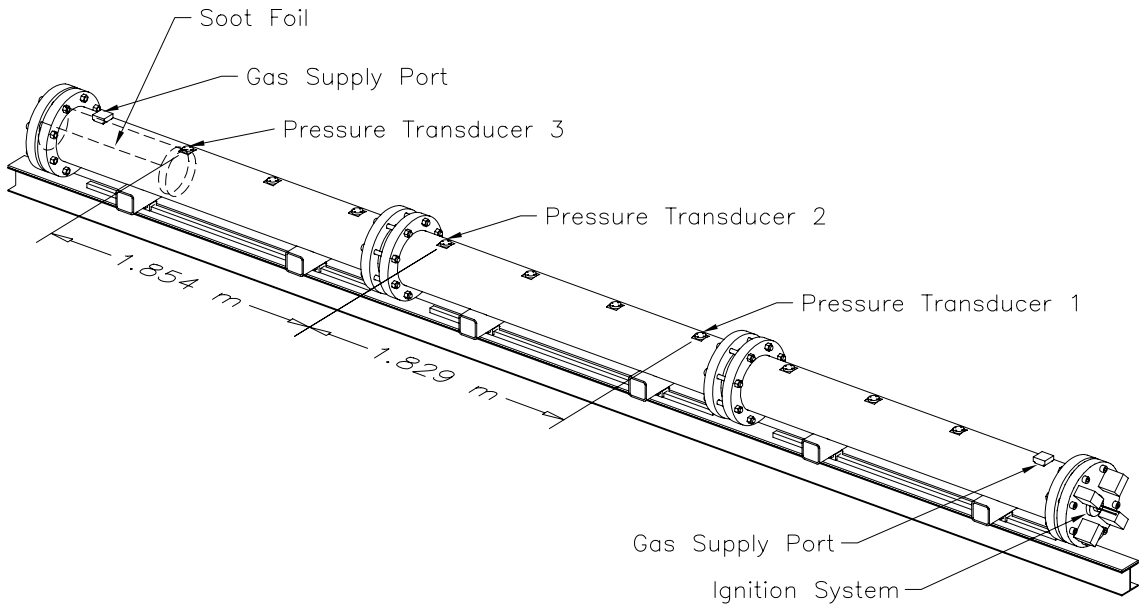

Figure 4.1: The GALCIT Detonation Tube.

ring 76 mm (3 in) wide, 4.8 mm (3/16 in) thick, and slightly smaller in diameter than the inside of the tube, to secure it against the incident detonation wave. The downstream edge was simply clamped at two points by a threaded spreader mechanism. Soot was applied to the foil by placing it inside a vertical closed aluminum tube and burning a kerosene-soaked cloth strip inside the tube. Air flow through the tube was restricted, and the sooty flame deposited a fairly uniform and consistent layer of soot, ideal for recording detonation cells, on the inside of the foil.

Piezoelectric pressure transducers (generally three) were mounted along the length of the tube to record detonation arrival times and pressures. Average wave speeds between transducer pairs were computed from the arrival time measurements.

Cell size measurements were made directly and manually from the soot foils. The dimension measured and described as cell size was the cell width, or the cell dimension transverse to the direction of wave propagation (see Fig. 1.2(a)). A number of cells were measured from each foil, to accumulate a statistically meaningful description of the foil, since cells would typically vary by 50% in size and in some cases well-defined cells were nonexistent. At least 10 cells were measured when possible, and average values were recorded along with the difference between smallest and largest.

4.1.2 Results

Table 4.1 summarizes the cell size measurements made using mixtures and pressures of interest to the projectile experiments. These mixtures and conditions were tested to fill gaps in the data available from the literature. Detonation velocity data are not presented here, but are discussed in conjunction with velocity calculations, in Section 4.2. The data are organized by mixture and are

sorted by initial pressure.

Table 4.1: Experimental cell size data

Mixture	GDT Shot	P_i kPa	λ mm	$\pm$ mm
$2H_2+O_2+N_2$	542	10.0	31.0	5.5
	532	11.5	26.3	10.3
	556	25.0	8.3	2.3
	531	26.5	8.5	2.5
	551	39.5	6.0	1.5
	530	41.0	5.5	1.0
	557	50.0	4.3	0.8
	523	51.5	5.0	1.0
	543	100.0	3.0	1.0
	522	101.5	3.3	0.8
$2H_2+O_2+2N_2$	539	26.5	11.8	2.8
	558	49.4	6.5	1.0
	533	50.9	5.8	1.8
	559	55.7	5.3	0.8
	534	57.2	6.5	1.5
	538	101.5	4.3	1.8
$2H_2+O_2+3N_2$	540	26.5	14.0	3.0
	541	26.5	14.0	3.0
	536	51.5	9.8	2.3
	544	83.1	6.3	1.3
	535	84.6	6.8	1.3
	537	101.5	5.8	0.8

Mixture : $C_2H_4+3O_2+\beta N_2$

β	GDT Shot	P_i kPa	λ mm	$\pm$ mm
0.0	891	15.0	2.0	1.0
	890	50.0	0.8	0.3
2.5	930	50.0	2.8	0.8
3.0	892	30.0	5.0	2.0
	893	70.0	3.5	1.5
4.0	713	45.0	4.3	0.8
4.5	711	45.0	5.8	1.3
5.0	929	30.0	9.3	1.8
	693	31.5	7.8	2.3
	698	35.0	6.5	1.0
	696	40.0	5.8	1.3
	697	45.0	5.3	1.3
	695	50.0	5.5	1.0
	928	55.0	7.5	1.5
	694	80.0	5.0	1.0
5.5	710	46.5	7.5	2.0
6.0	712	45.0	8.5	2.5
	894	60.0	9.5	2.5
	895	80.0	9.0	3.0
7.0	931	50.0	10.5	2.0
9.0	896	50.0	20.0	4.0
	897	90.0	13.0	4.0
11.28	898	50.0	37	11
	899	100.0	22.5	7.5

4.2 Detonation Velocity and Pressure Calculations

Chapman-Jouguet detonation velocities and pressures were computed with STANJAN, a computer program for solving chemical equilibrium problems [94]. With certain modifications, it can also compute equilibrium conditions behind a shock of arbitrary velocity, i.e., overdriven detonations. STANJAN uses the element potential method to find the solution (pressure, temperature, species mole numbers) with minimum Gibbs energy, given various constraints. For gas computations, it assumes ideal gas behavior and uses JANAF thermodynamic data (e.g., Chase et al. [19]) for a caloric state function. Equilibrium calculations are very reliable for computing CJ velocities and post-detonation conditions in gases.

Figures 4.2(a) and 4.2(b) show results of STANJAN CJ velocity calculations for relevant mixtures, along with values measured in the GDT (where available). Wave speeds measured in detonation tubes typically agree with CJ calculations as long as the tube is long enough for the wave to be

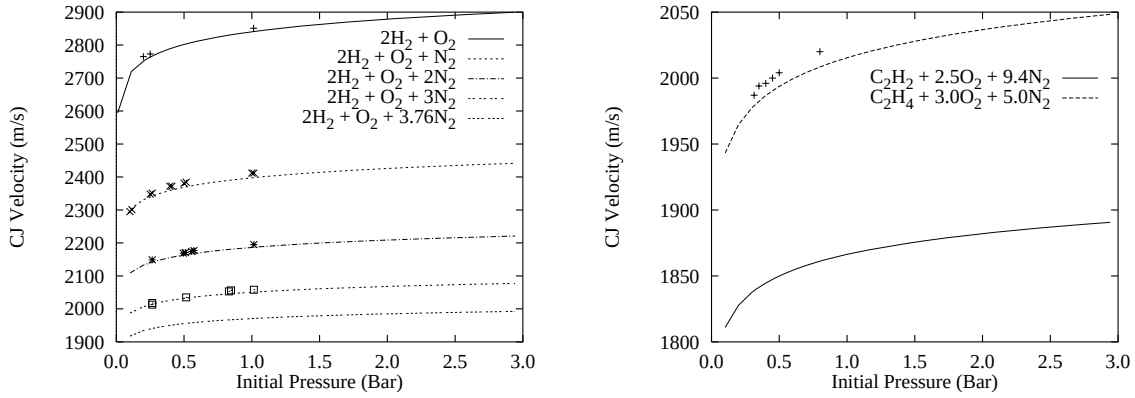

(a) H_2-O_2-N_2 (b) C_2H_2-air and C_2H_4+3O_2+5N_2

Figure 4.2: Chapman-Jouguet velocities at varying initial pressure, computed by STANJAN, and detonation speeds measured in the GALCIT Detonation Tube.

independent of the initiation process, and as long as confinement and loss effects are negligible. If the wave is not far enough from the initiation, it tends to be overdriven, or faster than a CJ wave. Confinement and loss effects cause the wave to propagate slower than the CJ speed, and generally become important if the tube diameter is less than about 10 cell widths.

The CJ velocity is seen to be a weak function of pressure but a strong function of fuel and dilution. The computed velocities are in excellent agreement with the experimental values. The discrepancy for the C_2H_4 data in Fig. 4.2(b) appears large because of the narrow range of velocities plotted. In fact the maximum discrepancy is about 0.6%.

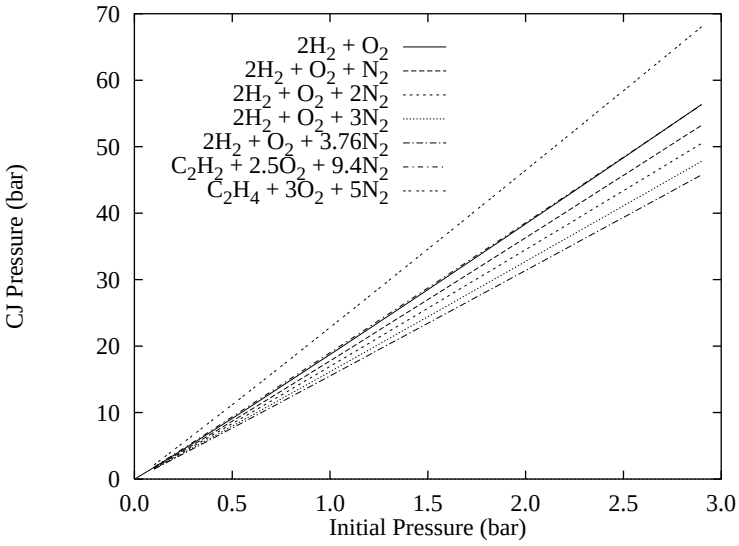

Figure 4.3: Chapman-Jouguet detonation pressures for various mixtures at varying initial pressure, computed by STANJAN.

In addition to CJ velocities, equilibrium calculations provide pressure and other conditions behind CJ detonations, and the same information for detonations of arbitrary velocity (i.e., overdriven detonations). For reference, CJ detonation pressure is plotted in Fig. 4.3 as a function of initial pressure for the relevant mixtures. As can be seen, the

various mixtures do not differ dramatically, and the detonation pressures increase approximately linearly with initial pressure. The constant of proportionality ranges from about 15 to 22. Measured detonation pressures also tend to agree with predictions, although not as precisely as velocities, because of the short time scales and multidimensional structure of the waves as they pass over the wall pressure transducers.

4.3 Detonation Cell Size Predictions

Predicting detonation cell size is significantly more difficult than predicting hydrodynamic parameters such as velocity and pressure. Hydrodynamic parameters are determined by zero-dimensional equilibrium constraints on the pre- and post-detonation states. In contrast, cell size is a roughly defined quantity that is determined by non-steady, three-dimensional fluid dynamics and non-equilibrium (finite-rate) chemistry, and no generally accepted analytical or computational technique exists for its prediction. Under limited conditions, semi-empirical models can be used to interpolate and extrapolate experimental data.

4.3.1 Correlation Theory

The first difficulty in predicting cell size is defining and characterizing a unique quantity that it represents. Referring to a soot foil record, the cell width, λ, (size is usually taken to mean width) is defined as the maximum dimension of the diamond-shaped cells, perpendicular to the direction of travel of the detonation wave, as shown in Fig. 1.2(a). The cellular pattern is etched into the soot by the detonation wave, apparently by the intersections of the main wave front and transverse waves. If the vessel in which the detonation propagates is large enough (relative to the cells), the cellular pattern is presumed to be characteristic of the mixture and its initial state, and not the geometry of the containment. Unfortunately, real cellular patterns show varying degrees of regularity, with only the most regular patterns resembling Fig. 1.2(a). Cells in irregular patterns are often distorted and vary in size by an order of magnitude. Furthermore, the most practical method of measuring cells from soot foils is by hand, and this introduces a significant element of subjectivity. Different individuals frequently produce very different cell size values from the same foil. The result is that cell size can not be measured precisely except in a statistical sense.

Cell Width Data

Figures 4.4-4.7 show cell width data for mixtures of interest. All mixtures are stoichiometric, with varying N_2 dilution and initial pressure. While trends are apparent in the log plots, the scatter is seen to be large, sometimes 70% of the average value at a particular condition.

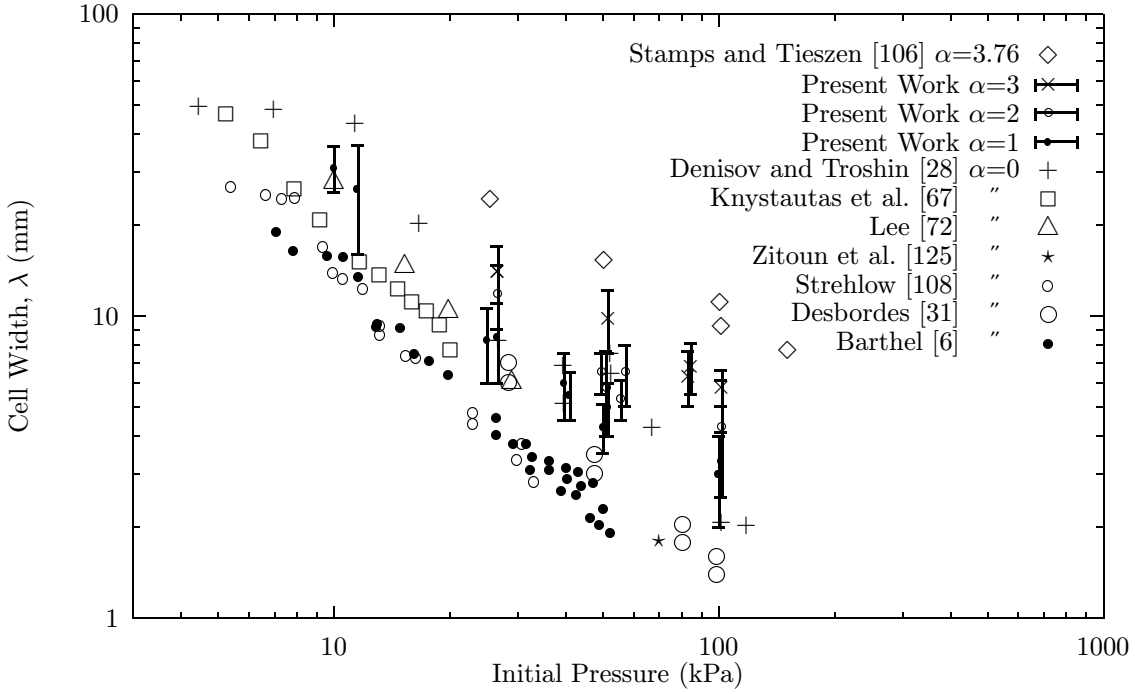

Figure 4.4: Cell width versus pressure for $2H_2+O_2+\alpha N_2$ mixtures.

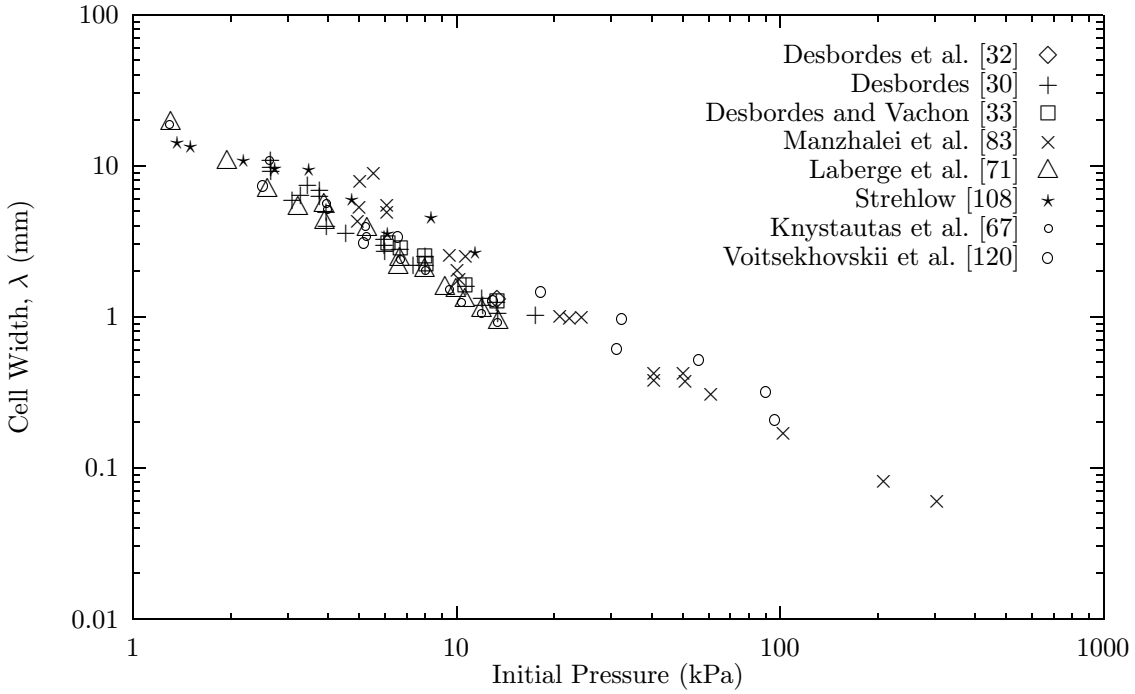

Figure 4.5: Cell width versus pressure for $C_2H_2+2.5O_2$.

Figure 4.4 shows a collection of cell width data for H_2-O_2-N_2 mixtures with several dilution ratios, as a function of initial pressure. H_2-O_2 and H_2-air data are available from a number of sources in the literature. To provide coverage of intermediate dilution ratios (where some T5 experiments were performed), data from GDT experiments are shown with error bars. The data are seen to fall in bands corresponding to varying dilution ratio.

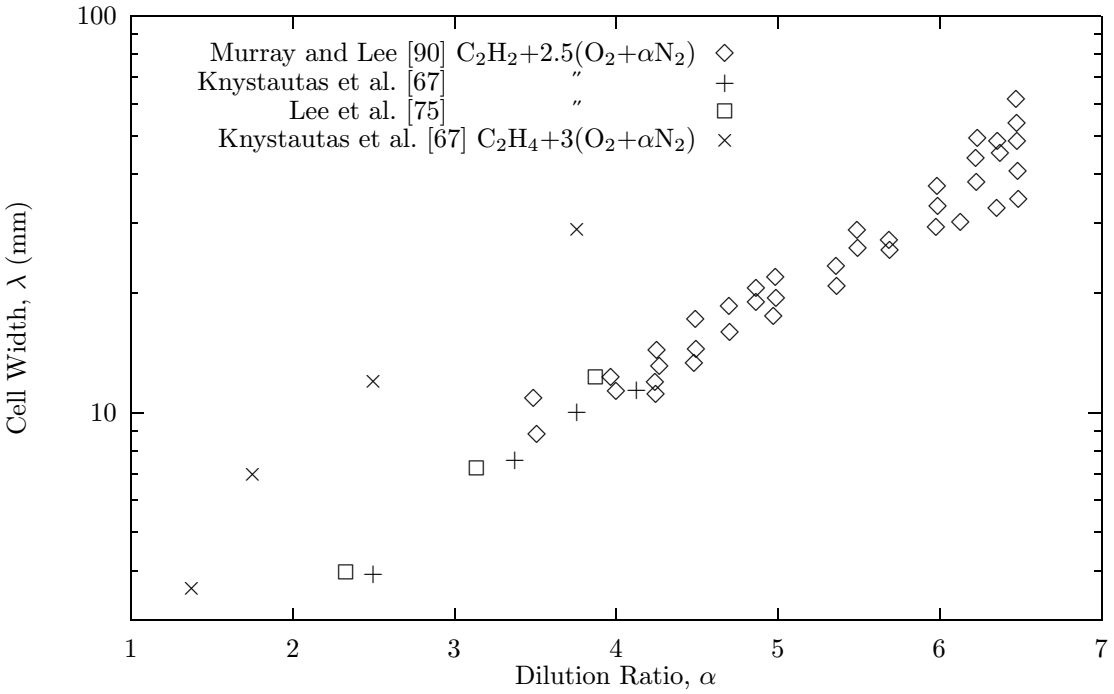

Figure 4.6: Cell width versus dilution ratio for C_2H_2+2.5(O_2+αN_2) and C_2H_4+3(O_2+αN_2) at 1 atm initial pressure.

Figure 4.5 shows cell width data for C_2H_2-O_2 mixtures as a function of initial pressure. Figure 4.6 shows cell width data for C_2H_2-O_2 and C_2H_4-O_2 mixtures diluted with N_2 as a function of dilution ratio. Figure 4.7 shows cell width data for C_2H_4-O_2 mixtures with no dilution and with a dilution ratio used in the T5 experiments, as a function of initial pressure. Figures 4.4-4.7 illustrate the inverse dependence of cell width on initial pressure, for a given mixture. Correlations of the form

$$\lambda \propto \frac{1}{P^{\alpha}} \tag{4.1}$$

are frequently used to condense cell width data. However, this requires data for each mixture of interest, at a number of initial pressures. Because of the statistical nature of cell width measurements, a meaningful correlation requires a large number of measurements. Similar correlations could be constructed for the effect of dilution at fixed initial pressure, but the extension to a correlation for the dependence on both dilution and initial pressure is difficult and clumsy.

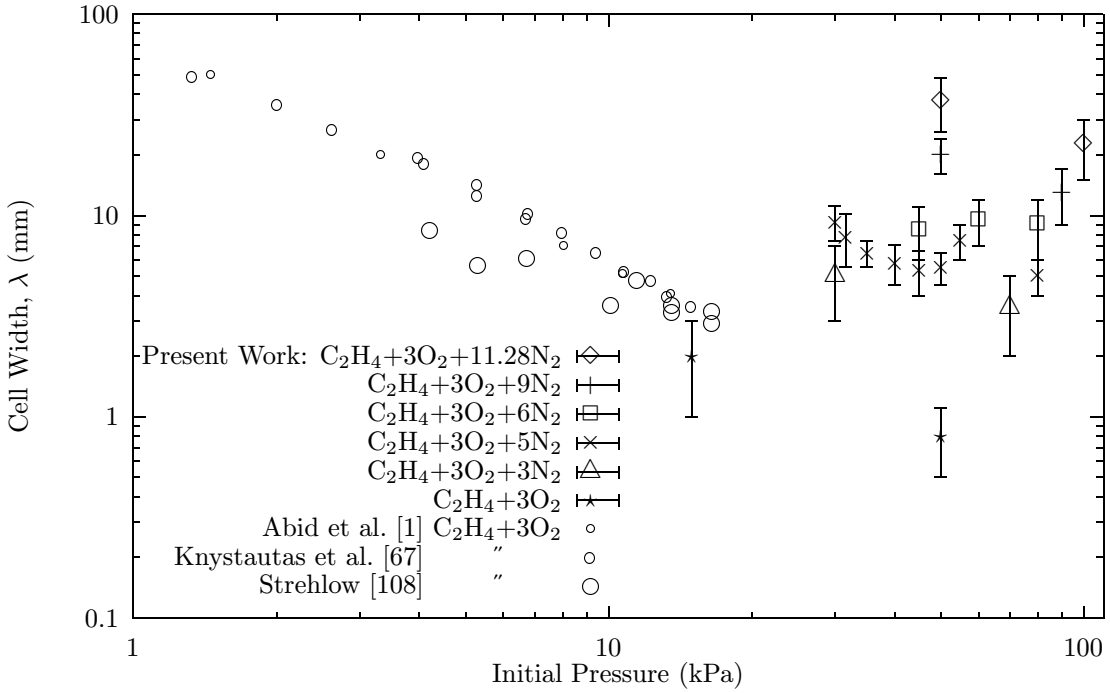

Figure 4.7: Cell width versus pressure for $C_2H_4+3O_2+\alpha N_2$ for several values of α.

Reaction Zone Thickness

Instead of correlating cell width to the basic parameters that define the mixture (equivalence ratio, dilution ratio, initial pressure, initial temperature), a more elegant approach is to relate cell width to another length scale which is a simpler function of the defining parameters. In other words, the cell width is the result of three-dimensional unsteady gasdynamics and chemistry acting on the mixture with a given initial thermodynamic state, but it may be proportional to a scale that can be computed for the mixture without making detailed multidimensional calculations. Since chemical reaction distinguishes detonations from shocks and introduces the length scale, the simplified calculations attempt to accurately model the relevant chemistry. Normally this involves integrating the governing reaction rate and conservation equations from the initial (post-shock) reactant state to the final product state. The initial state is taken as the condition behind a shock travelling at the CJ velocity, which is separately computed as described in Section 4.2. The flow is assumed to be steady and one-dimensional (or sometimes unsteady and zero-dimensional, i.e., constant volume). In this case, a length scale can be extracted from the calculation results, using an arbitrary definition of the reaction zone thickness. The most common definition is the distance from the leading shock to the point of maximum temperature gradient, or heat release.

In principle, each elementary reaction introduces its own length scale, so there is no single scale that determines the cell width. If only one reaction is involved, a unique scale can be defined in

terms of the reaction rate parameters. For systems with a large number of reactions, the effect of extracting an arbitrarily defined length from the computation results is to sacrifice some information about the process.

4.3.2 Finite-Rate Chemical Kinetics Calculations

As described above, reaction zone thicknesses are computed by integrating the reaction rate and relevant conservation equations after a shock wave moving at the CJ speed, and extracting the distance from the shock to the point of maximum temperature gradient. This model is typically referred to as the Zeldovich-von Neumann-Döring (ZND) model.

The Chemkin-II FORTRAN library was used to handle the reaction rate and fluid property computations.

4.3.3 Reaction Mechanisms

Even using the simple ZND model, the accuracy of the calculation is dependent on the accuracy of the reaction rate parameters. Unlike the equilibrium calculations used to predict bulk detonation properties like wave speed, the reaction rates are not generally known to high precision. Finite-rate kinetics calculations require a list of elementary reactions to follow, and rate parameters for each. The list of possible elementary reactions for a given set of reactants is, in principle, infinitely long, so some judgement must be applied to limit the list to the relevant reactions. Furthermore, determination of rate parameters is a subject of ongoing research for many reactions. The list of reactions and their rate parameters constitutes a "reaction mechanism". Ultimately, any reaction mechanism is useful under a only limited range of conditions, including mixture concentrations and thermodynamic state.

Offsetting the uncertainty in the reaction zone calculations caused by the reaction mechanism is the accommodating nature of the cell width correlations. As long as the calculations reproduce the correct dependence on dilution and initial pressure, the correlation will allow them to be useful for predicting cell size. The mechanism used for this work was reported by Lutz et al. [82]. It was also reported by Lutz [81], along with some validation for H_2-O_2 and CH_4-O_2 mixtures. As described by Lutz et al. [82], an earlier version of the mechanism was reported by Miller et al. [88] along with validation for C_2H_2 oxidation. No validation has been found for C_2H_4 mixtures.

4.3.4 Results

Figures 4.8-4.10 show the results of computing the reaction zone thickness Δ corresponding to each of the data points shown in Figs. 4.4-4.7 and plotting cell width as a function of reaction zone thickness. The major effect is to collapse all the data for a particular fuel onto a single curve. Since

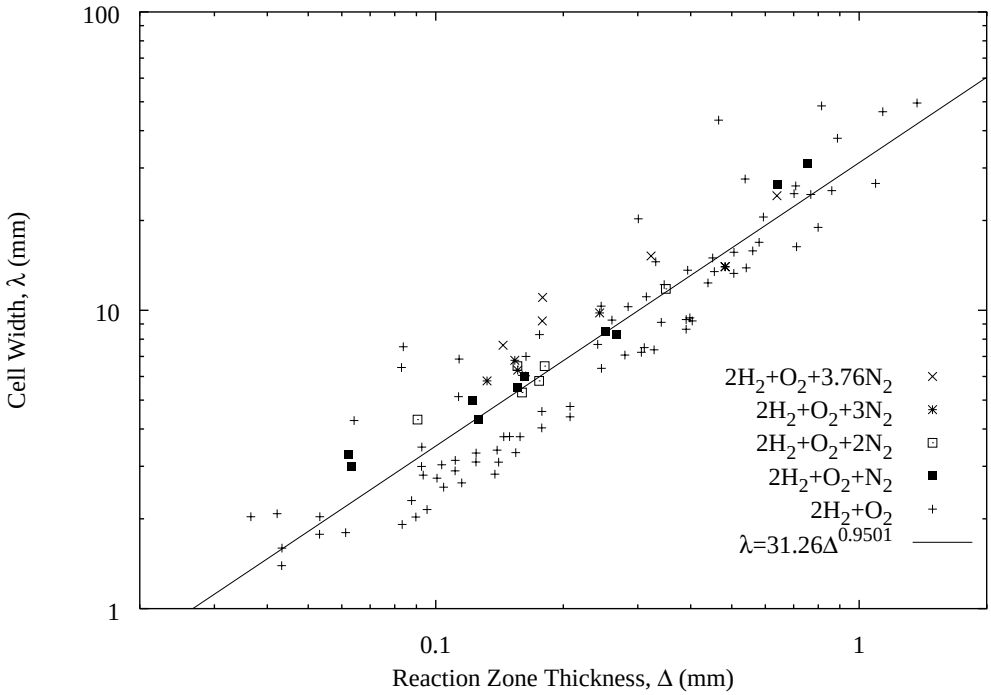

Figure 4.8: Cell width versus reaction zone thickness for H_2-O_2-N_2 mixtures.

the data fall onto straight lines in the log plots, power law functions have been fit to the data by the least-squares method, and the resulting correlations are displayed on the plots.

The correlation theory described in Section 4.3.1 suggests that the cell width should be proportional to the reaction zone thickness, and therefore the correlations should be linear. Power law correlations have been used to improve the agreement, particularly since the simple theory neglects the multiple length scales actually present. In fact the correlations are all reasonably close to being linear anyway, indicating that the deviation from the simple theory is not large.

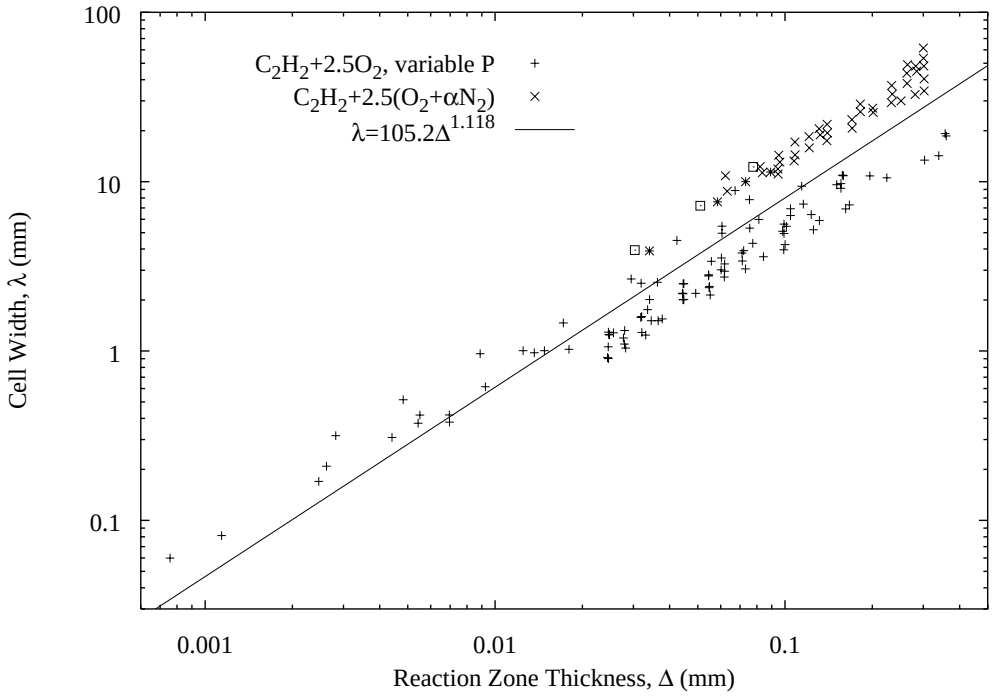

Figure 4.9: Cell width versus reaction zone thickness for C_2H_2-O_2-N_2 mixtures.

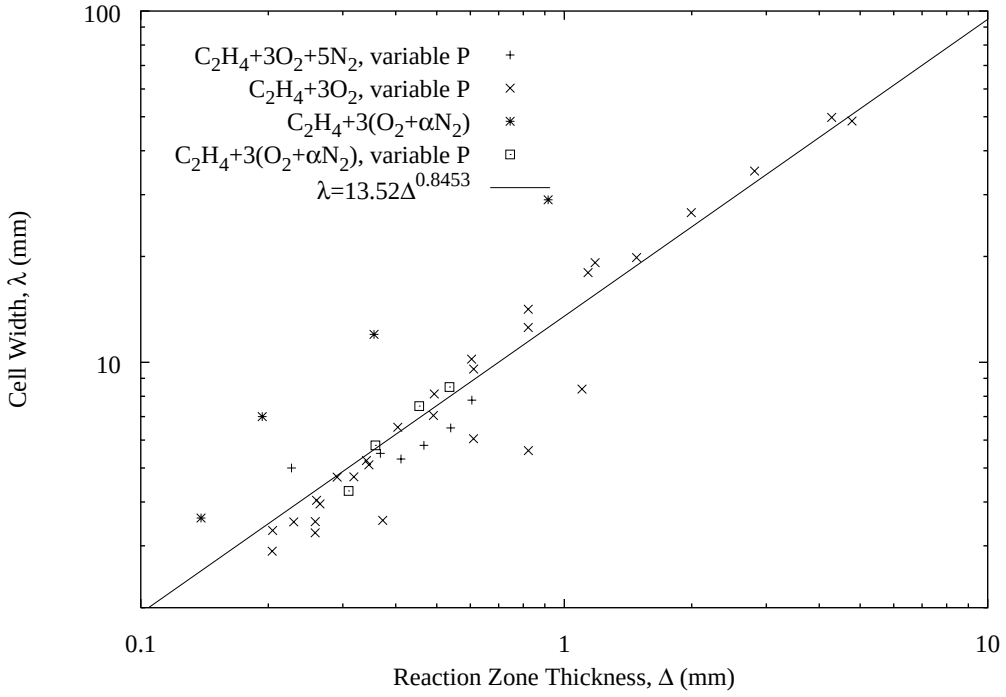

Figure 4.10: Cell width versus reaction zone thickness for C_2H_4-O_2-N_2 mixtures.

Chapter 5 Experimental Details

5.1 Goals

The abilities of the available facilities and the work done by other researchers shaped the goals set for these experiments. The general goal was the identification and quantification of critical conditions for detonation initiation by high-speed projectiles. Given that very few data exist for projectile velocities exceeding the Chapman-Jouguet speed, transition phenomena at super-CJ speeds were particularly interesting. In order to discuss global transition criteria, it was felt that a number of parameters should be controlled. The simplest parameters to control in our setup were mixture composition and pressure. Finally, the transition between detonation initiation and failure is not necessarily a distinct point, but may exhibit a range of phenomena between a clear failure and clear detonation. As well, the nature of the initiated detonation may not be the same in all cases. Therefore, photographic images were sought.

In preparation for performing projectile experiments, a safety assessment was performed, and the resulting document is included as Appendix E.

5.2 T5 Shock Tunnel

The T5 shock tunnel was used to provide propellant gas for the launching of projectiles, essentially. Detailed understanding of the design and operation of T5, particularly in its normal configuration, is not prerequisite for understanding the launch mechanism. A comprehensive discussion of T5 is given by Hornung [57]. As background for the launch mechanism, a brief explanation is given here.

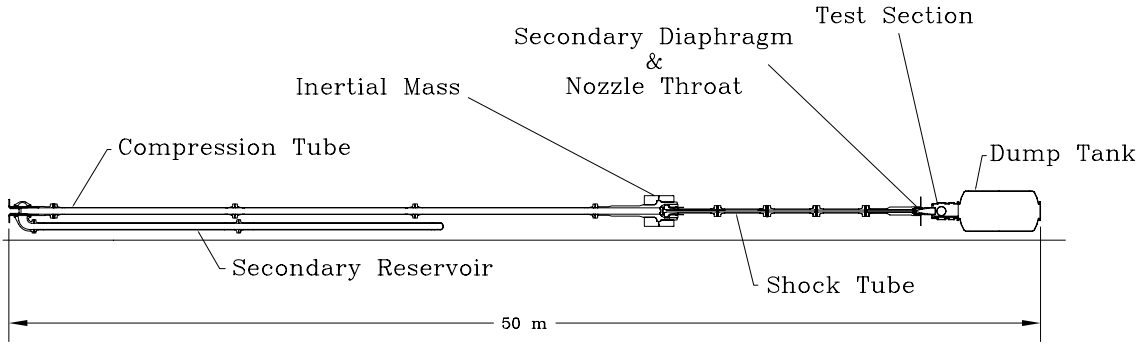

Figure 5.1: Elevation schematic of T5 Shock Tunnel.

Figure 5.1 shows an elevation schematic of T5 in its normal configuration. The major components

are the secondary reservoir, compression tube, inertial mass, shock tube, test section, and dump tank. Before a test, the piston is loaded in the end of the compression tube. Pressurized air in the secondary reservoir is used to accelerate the piston down the compression tube. Driver gas, typically a mixture of helium and argon, is compressed between the piston and the main diaphragm, inside the inertial mass. The main diaphragm, which is a scored stainless steel plate, bursts at a pressure determined by its thickness and the depth of the scoring. As the resulting shock wave propagates down the shock tube, the pressure in the driver gas remains roughly constant due to the advancing piston. Under tuned conditions, the piston decelerates to rest at the end of the compression tube.

At the end of the shock tube, the shock wave reflects off the end wall. The test gas, heated and compressed by the incident and reflected shock waves, accelerates through the throat and nozzle and into the test section and dump tank. During the shot, the movement of the piston and the secondary reservoir air cause the facility to recoil. The secondary reservoir can slide relative to the compression tube, which is fixed to the inertial mass and shock tube. The compression tube, inertial mass, and shock tube move also, while the test section and dump tank remain stationary.

Standard diagnostics consist of an accelerometer mounted on the compression tube, two piezoelectric pressure transducers at the end of the compression tube near the main diaphragm, two pressure transducers along the length of the shock tube, plus two pressure transducers at the end of the shock tube, just upstream of the end wall. Optical imaging is typically performed through windows on the test section, and signals from sensors inside the test section can be passed through a feed-through plate on the test section.

5.3 Modifications to T5

For the purposes of the present experiments, T5 was modified at two locations: at the nozzle/test section area to create a sort of light-gas gun, and at the downstream end of the dump tank, where experimental hardware and the projectile catcher were located. The experiments were carried out in three series, and the hardware configuration and instrumentation differed slightly in each series. Figure 5.2 shows the T5 dump tank area with gas gun and experimental modifications, for series I, II, and III. Table 5.1 summarizes the configurations used in each series.

5.3.1 Gas Gun Modifications

During gas gun experiments, T5 was operated as usual, except that the nozzle throat and transition were replaced by a specialized throat and launch tube support block. The launch tube was supported by this block and by a linear bearing in the T5 test section. The 25.4-mm diameter spherical projectile was placed in the throat, between a neck in the throat block and the mylar diaphragm separating the shock tube volume from the dump tank. T5 was operated with helium in

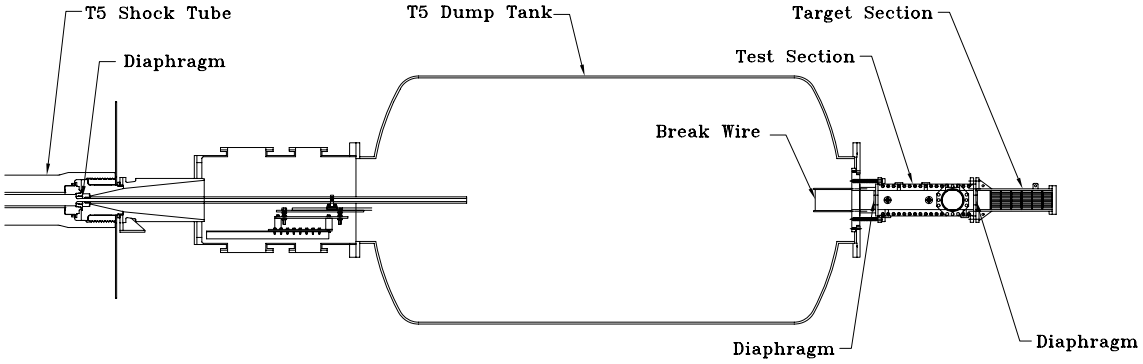

(a) Series I

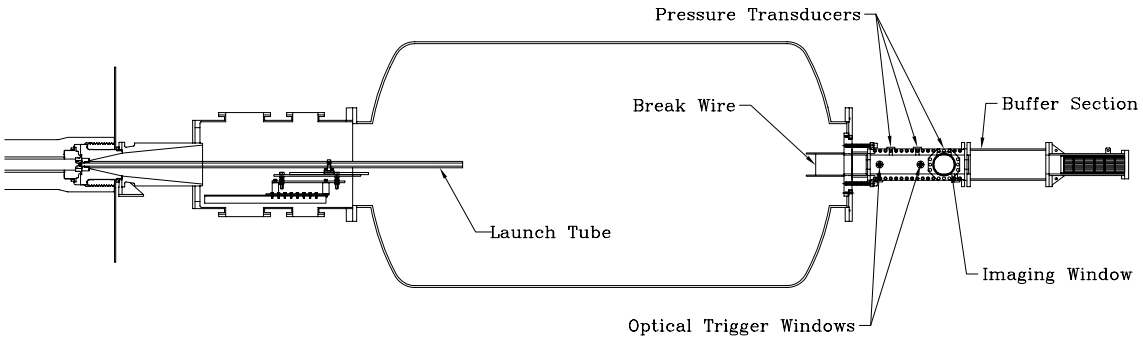

(b) Series II

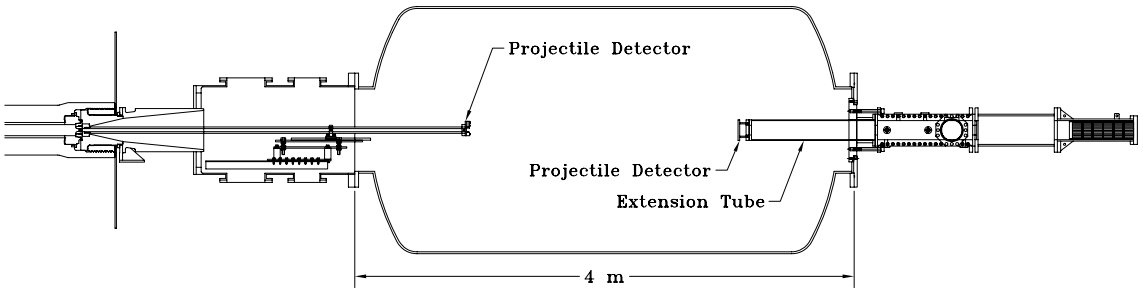

(c) Series III

Figure 5.2: T5 dump tank cross section showing gas gun modifications and detonation test apparatus used in different experiment series.

Table 5.1: Summary of experiment series.

	I	II	III
T5 Shot Numbers	857-865	1003-1032	1800-1840
Timing Strategy	passive	passive	active
Primary Trigger	break wire	break wire	pressure transducer, laser
Optical Diagnostics	differential interferometer	differential interferometer, shadowgraph	shadowgraph, ICCD
Catcher	target only	target and buffer	target and buffer
Extension Tube	No	No	Yes
Mixtures	$2H_2+O_2+N_2$	$2H_2+O_2+\beta N_2$	$2H_2+O_2+\beta N_2$ $C_2H_4+3O_2+5N_2$ $C_2H_2+2.5O_2+9.4N_2$
Velocities Achieved	2520 - 2620	2060 - 2580	2200 - 2440

the shock tube, rather than the more typical nitrogen or air. The T5 conditions used are tabulated in Appendix A.2. A discussion of the methods and results from gun modeling efforts are given in Appendix D.

The projectiles were commercially available 25.4-mm diameter nylon spheres. These were chosen following considerations described by DeRose and Intrieri [29]. Nylon gives high performance because it has one of the highest strength/weight ratios (75×10^3 m^2/s^2) of the conventional polymers, and is much lighter (1.1 g/cm^3) than the common metals. Experience has led to the conclusion that alternative materials may provide better performance (see Section 7.2.1). Since the maximum stress experienced by the projectile is equal to its base pressure (neglecting friction with the launch tube and frontal pressure), the maximum permissible propellant pressure is strictly limited to the ultimate strength of nylon, 83 MPa. In practice, the projectiles survived the launch process when the reflected shock pressure was below around 40 MPa. Typical projectile speeds were around 2300 m/s. In practice, timing issues and uncertainty related to changing T5 conditions motivated very little variation of gun conditions.

5.3.2 Test Station

The test chamber where combustible gases were contained, and the projectile catcher, were mounted on the downstream door of the T5 dump tank. They were bolted together and supported by a wheeled trolley resting on the same rails used for the T5 dump tank and shock tube translation. This assembly was bolted to an adapter plate in the door, which was modified for the purpose. Because the dump tank and shock tube were necessarily translated to the extreme downstream position after each shot to allow space for piston extraction, the test and target sections were unbolted and removed from the rails between shots. This was also necessary for replacement of mylar diaphragms and trip wires, inspection, and cleaning.

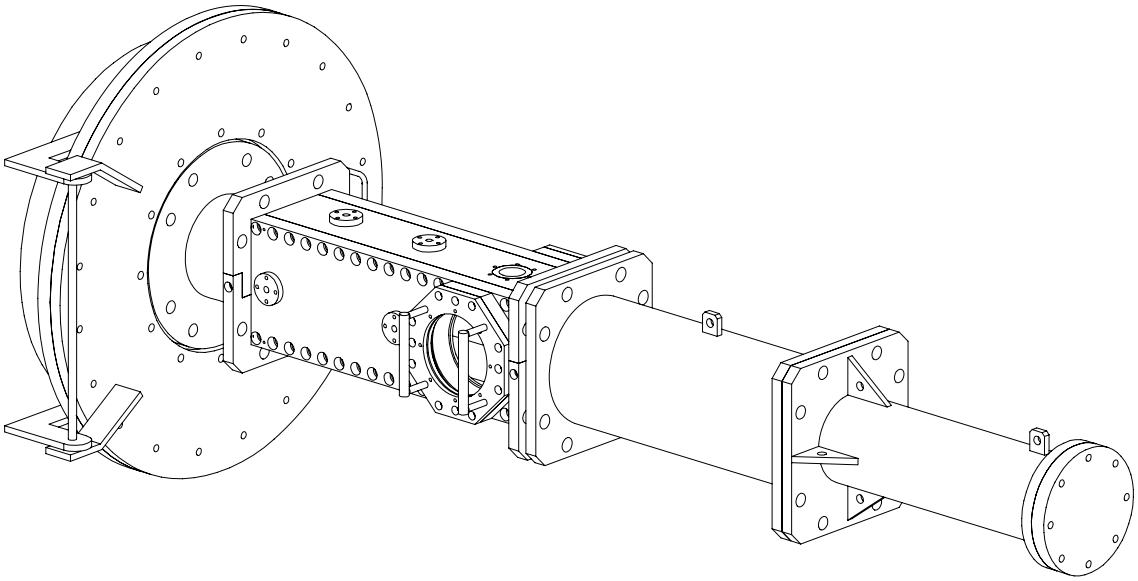

Figure 5.3: Diagram of test station assembly.

Before each shot, the test section volume was isolated from the evacuated dump tank and from the target section by 0.001-inch thick mylar diaphragms. In cases where the mixture pressure was greater than about 1.5 bar, two mylar diaphragms were used at each station. During series I, the target section contained air at ambient conditions, but the blast wave and debris generated by the projectile impact wore heavily on the test section (particularly the windows). In later experiments, the target section was evacuated before the test, and the effects of the impact were significantly reduced.

Test Section

A number of constraints and goals influenced the design of the test section. A square internal cross section, with the ability to optically view wall interactions, led to a bolted-plate construction, rather than a simpler round tube. It was also designed to be used in conjunction with the GALCIT Detonation Tube, described by Akbar [3]. AISI 304 stainless steel was used for the major components to avoid corrosion, since it was designed to be disassembled, and because highly corrosive gases were anticipated in experiments with the detonation tube.

Figure C.2 shows a test section assembly schematic. The inside of the test section was 152 mm x 152 mm (6 inch x 6 inch) square in cross section and 76.2 cm (30 inch) long. The top and bottom plates were 50.8 mm (2 inch) thick, and locked into the 38.1-mm (1.5-inch) thick side plates through keyways. Longitudinal o-rings in these keyways provided a vacuum seal between the four plates, which were fastened together by SAE Grade 8 or stronger bolts. 19-mm (3/4-inch) thick stainless steel end plates covered both ends of the test section. Rectangular o-ring face seals under each end

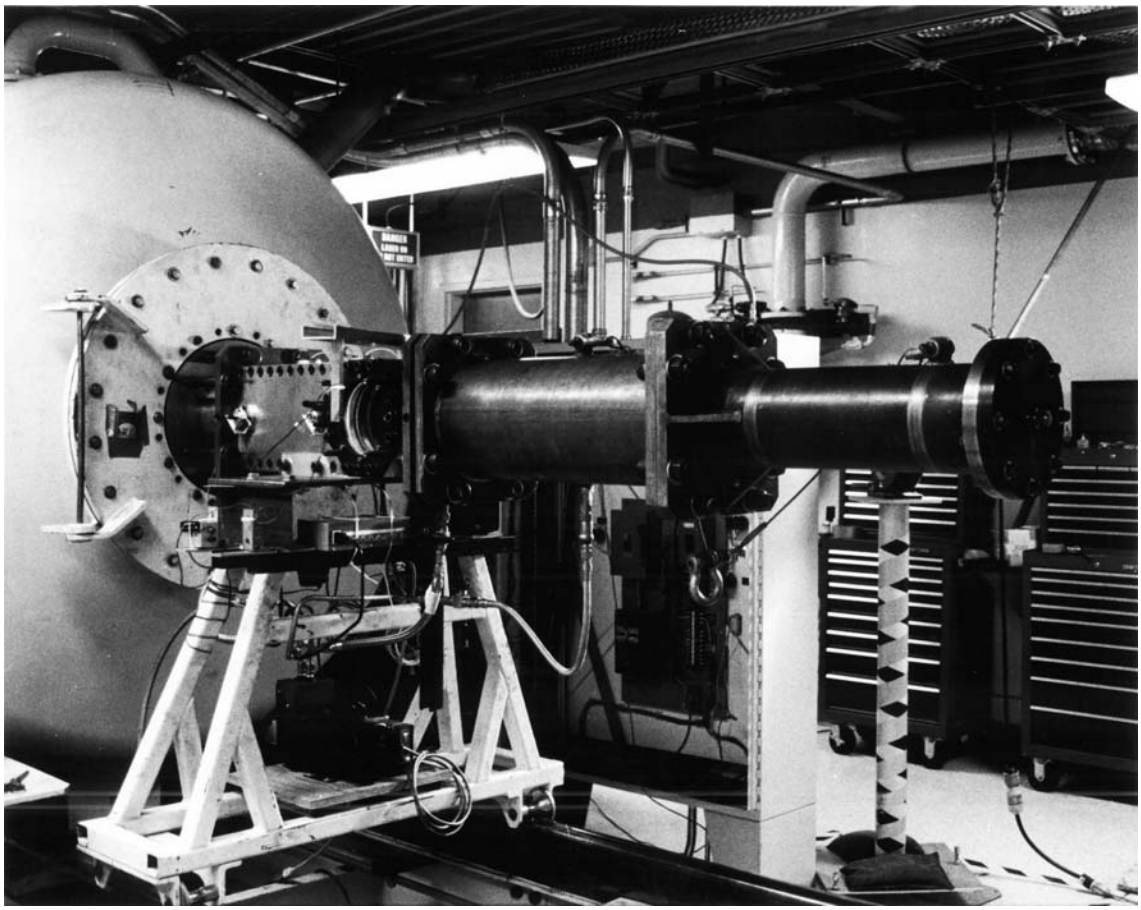

Figure 5.4: Photograph of test station assembly.

plate mated with the longitudinal o-rings. Access for the projectile was provided by a 76.2-mm (3-inch) diameter opening in each end plate. These openings were sealed by mylar diaphragms which were clamped in place by additional, smaller plates. O-rings on both sides of each diaphragm provided a firm grip and vacuum seal. The test section was structurally connected to the dump tank and target section by flanges and bolts. Because the test section was square and designed to be disassembled, the flanges connected to the test section by keyways. Each flange consisted of two halves which fit around the end of the test section like a collar.

Instrumentation ports were provided on the sides, top, and bottom of the test section. Two ports on the bottom were used for gas feed and circulation. Two pairs of ports on the sides were used for laser triggers. One large and two small ports on the top were used for pressure transducers. All instrumentation mounts were manufactured from aluminum 6061-T6.

The optical windows presented a challenging design problem. Estimating the maximum allowable loads on the glass was complicated by the imprecise nature of glass strength data, the transient and nonuniform loading, and the complicated mounting. To avoid metal-glass contact, known to greatly reduce the effective glass strength, the window assemblies were designed with three o-rings cushioning

the glass in front, back, and around the outside. The rear o-ring was eventually replaced with a Teflon ring. In order to allow the glass to sit flush with the inside wall of the test section, the front edge of the glass had a step where the front o-ring and the frame supported it. Because the viewing aperture was larger than the inside cross section of the test section, the front of the glass was exposed to a small area of metal at the top and bottom. Under dynamic loading during an experiment, the intentionally compliant supports allowed the glass to impact this metal, and cracking in this area was experienced in early experiments. The problem was solved by inserting a thin layer of compliant material (Teflon or silicone sealant) between the glass and metal, and tightening the glass firmly (to prevent movement). The glass windows were made from BK-7 optical glass. The frames were manufactured from carbon steel and aluminum 6061-T6. The diameter of the viewing area was 165.1 mm (6.5 inch).

To investigate the effect of projectile travel distance in the combustible mixture, i.e., distance from the entrance of the test chamber, an extension was built for the upstream end of the test section (Fig. C.3). This tube had a 152-mm (6-inch) inside diameter, 6.4-mm (1/4-inch) wall thickness, and 99.1-cm (39-inch) length. When this tube was installed, the test section upstream end plate was removed, so that the inside area transitioned directly from the 152-mm diameter of the extension tube to the 152-mm square of the test section. The upstream end of the extension tube was sealed in the same manner as the normal test section openings. The extension tube was fastened to the test section and inserted into the dump tank.

Because the extension tube and test section did not have the same inside dimensions, an area change occurred at the transition. The ratio of the extension tube area to the test section area was 0.785. This complicates analysis of the results somewhat, and introduces the possibility of phenomena caused by the area change. Nonetheless, the extension tube allowed identification of some results that had depended on the specific test section length, and in other cases allowed observation of steady results at conditions that had previously resulted in unsteady phenomena because of the short travel distance.

Target Section

After passing through the dump tank and test section, the projectile came to rest in the target section (Fig. C.4). Its energy and momentum were absorbed by a stack of aluminum honeycomb separated by aluminum and steel plates. Since the honeycomb collapses under a predictable load, it limits the force exerted on the end plate of the target section. The amount of honeycomb required was estimated by equating the energy absorbed by the honeycomb (crush force times collapse length) with the kinetic energy of the projectile ($mv^2/2$). However, this proved to be very conservative because most of the energy of the projectile is dissipated by the cratering of the first solid plate and the destruction of the projectile. A more significant problem was debris ejected from the target

impact striking the windows. Pitting of the windows was caused by aluminum (or aluminum oxide) fragments, and the optical quality tended to degrade over a number of shots.

Because of this, for series II and III, an additional buffer section was added to the assembly, between the target section and the test section. This chamber increased the separation of the impact from the windows, and was equipped with a fitting to allow the target sections to be evacuated before each shot. This reduced window damage, but did not eliminate it.

5.3.3 Safety

Before any experiments were performed, an assessment of safety concerns and procedures was performed and documented, and reviewed by the faculty of GALCIT. This document is reproduced, with minor editing, as Appendix E.

Because the safety assessment was written before experiments were performed, a few remarks should be made, in reflection:

1. As noted above, leaving air in the target section was found to be a problem, so most experiments were performed with the target evacuated.

2. The evacuation sequence was changed. To detect leaks between the test section and the dump tank, which could result in combustible gases filling the dump tank, the dump tank was evacuated before the test section, and the test section pressure was monitored. All vessels were evacuated before any were filled.

3. The checklist included in the safety assessment was the earliest version. It was developed to make the experiments safer and more efficient.

4. Prior to any experiments, the test section was hydrotested. This test did not include the BK7 windows, which were replaced with aluminum versions. The maximum pressure achieved in this test was 160 bar (2300 psi). Since the hydrotest was to be at 150% of the maximum allowable working pressure, the test section pressure rating was 106 bar. For the sake of detonation experiments, this rating was applied by estimating the pressure behind a normally reflected detonation in the proposed mixture. The experiment was allowed if this estimated pressure was less than the rating.

5. The proposed alignment procedure for the launch tube, using a laser beam, was unsuccessful because of reflections on the inside of the tube. The procedure adopted was a more crude, but very sensitive, visual technique. A diffuse light source was placed in the T5 shock tube just upstream of the launch tube, and the assembly was closed. With the test section mounted in place on the dump tank, cross hairs were strung across the downstream opening in the test

section. By sighting down the launch tube and comparing with the cross hairs, the offset of the launch tube centerline could be seen.

5.4 Diagnostics

5.4.1 Pressure Transducers, Laser Triggers, and Wire Triggers

Three pressure transducers were mounted along the centerline of one wall of the test section for all tests. These transducers were evenly spaced 21.4 cm (8-7/16 inch) apart. In addition, for some tests, a transducer was mounted at the exit of the launch tube. These transducers were all PCB Piezotronics piezoelectric dynamic pressure transducers, model numbers 113A24 or 113A26. These models have 500 kHz resonant frequency and 1 μs rise time. The pressure sensitive area is 5.54 mm (.218 inch) in diameter. Generally the faces of the transducers were covered with a layer of silicone rubber to protect them from high heat flux, which causes the signal to drop, often below zero pressure.

Laser beams were used to detect the projectile during its flight for velocity measurement. In all experiments, two pairs of windows on the sides of the test section were used for this purpose. In addition, a third laser trigger was mounted on the test section, with the beam passing obliquely through the optical imaging windows and through the center of the test section, for series II and III. Laser triggers at the exit of the launch tube and the entrance of the extension tube were used for some series III tests, although the launch tube trigger proved to be unusable.

At each laser detector station, the beam from a diode laser (650-680 nm) passed across the path of the projectile, through an interference filter (except during series I) which eliminated background light from combustion, and into a photodetector. Without the interference filter, the combustion emission detected by the photodetector was greater than the initial laser signal, making projectile detection impossible.

In some tests, the arrival of the projectile just upstream of the test section (inside the dump tank) was detected by a trip wire. The wire used was .10-.15 mm (.004-.006 inch) in diameter copper. When this wire broke, the increase of resistance was detected as a decrease in voltage across a series resistor. While a number of good results were obtained with this arrangement, it proved to be unreliable overall. Oddly, the voltage drop would not always occur when the wire broke (see Section 5.4.6). For this reason, for series III, the wire was replaced with a laser trigger, which exhibited marginally better reliability. Finally, a new wire mounting scheme was developed to address the reliability problems of both systems. However, this was only used for two shots.

The relative locations of some detector stations changed between tests as a result of design changes and equipment modifications. Figure 5.5 shows the nomenclature used to describe the various stations and distances between them. Not all the stations and distances shown are relevant

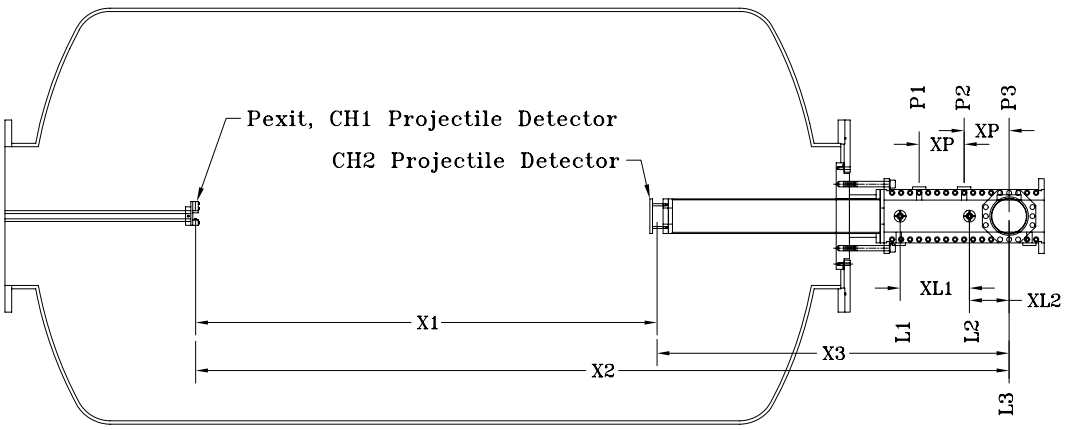

Figure 5.5: Schematic of apparatus showing detector stations and nomenclature.

for all tests performed. For instance, for tests without a launch tube exit detector (CH1), $X1$ and $X2$ are irrelevant, but $X3$ is relevant. In tests with a CH1 detector, $X1 = X2 - X3$.

The relevant distances are reported in Table 5.2. As shown, the distances between test section laser triggers and pressure transducers did not change. The test section distances ($XL1$, $XL2$, XP) were fixed, and known to high precision (within 1 mm). The uncertainty of $X3$ was determined by the precision to which the CH2 break wire or laser trigger could be located, generally within a few millimeters. $X1$ and $X2$ were much less precise, however, first because of the longer distances involved and the difficulty of measuring them, and second because the relative position of the launch tube and test section was not fixed since the shock tube and dump tank could move independently. Therefore, $X1$ and $X2$ were known to within about 1 cm.

Table 5.2: Distances (m) between detector and sensor stations.

Shots	$X1$	$X2$	$X3$	$XL1$	$XL2$	XP
857–860	-	-	1.034	0.3302	0.1889	0.2143
861–862	-	-	1.018	″	″	″
863–865	-	-	1.014	″	″	″
1003–1032	-	-	1.027	″	″	″
1800–1838	2.169	3.865	1.696	″	″	″
1839–1840	2.235	3.865	1.630	″	″	″

5.4.2 Shadowgraph and Differential Interferometer Setup

For imaging density fields in the flow around the projectile, two techniques were used: shadowgraphy and differential interferometry. The physical arrangement is shown in Fig. 5.6.

The arrangement shown in Fig. 5.6 is representative of the physical setup used, although the distances are not to scale, and in fact varied some between experiments. The standard T5 setup was used but modified because of the different location of the test field, i.e., on the downstream end

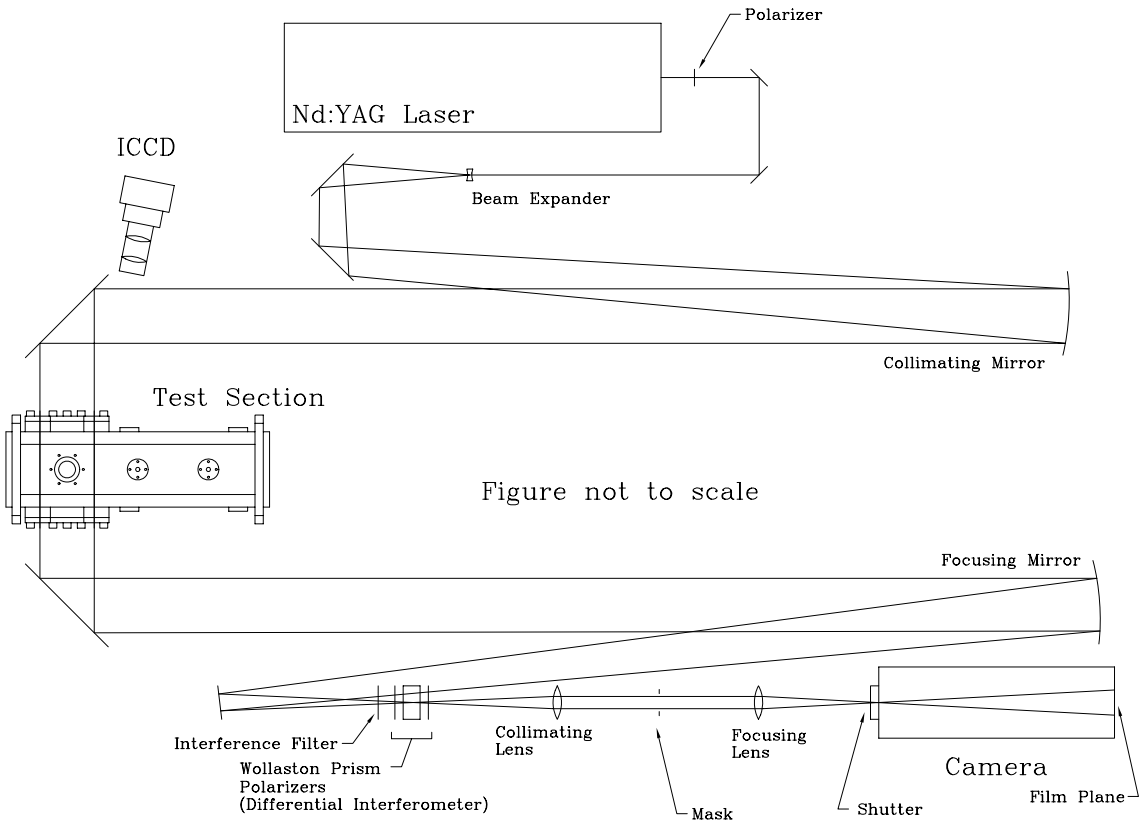

Figure 5.6: Optical system arrangement.

of the dump tank instead of the upstream end. For series I, the optical tables holding the source and receiving optics were moved adjacent to the detonation test section. For series II and III, the optical tables were left in their normal position, and only the turning mirrors were moved.

The laser used in series I and II was a Continuum YG 660B Nd:YAG. In series III, a Spectra Physics GCR-150-10 Nd:YAG was used. Both were pulsed lasers with maximum repetition rate of about 10 Hz, and pulse widths around 7 ns, emitting at 532 nm.

Shadowgraph

A focused shadowgraph system was used for most of the photographs. Discussion of this type of setup is given by Beams [8] and Soule and Sabol [104]. Detailed review of the analytical theory of the shadowgraph technique will be omitted here, but it is worth noting that the recorded intensity represents the Laplacian of the density field, integrated along the line of sight across the test section. To focus the receiving optics, a collimated beam was first obtained after the collimating lens. The spacing between the focusing lens and the camera shutter was fixed by the requirement that the collimated beam should be focused at the shutter. The position of this pair was adjusted to bring the image of an object in the test section into sharp focus on the film plane. Another image of

the test section was formed between the collimating lens and the focusing lens, and a mask (spatial filter) was placed at this location to block scattered light outside the desired field-of-view. Because a shadowgraph focused on a two-dimensional phase object will yield no information (the deflected rays are returned by the focusing process), the action of the focused shadowgraph is due only to the depth of the test section and possibly some schlieren effect at one or more of the apertures, mostly the camera shutter. Thus, the focused shadowgraph is fairly insensitive, but flow features such as shock waves are very sharp. This was desirable in the present experiments because the density variations were very strong, and a more sensitive system would be grossly unresolved. Generally, quantitative density field interpretation of the shadowgraphs is not useful.

Differential Interferometer

The differential interferometer arrangement differed from the shadowgraph only by the addition of the Wollaston prism and polarizers. Discussion of the differential interferometer is given by Merzkirch [87]. In principle, the differential interferometer is more easily analyzed quantitatively than the shadowgraph, because it is sensitive (its fringe shift is proportional) to density gradients. The main drawback is the unavoidable double image of objects or disturbances in the test field. The interferograms shown in Appendix B exhibit a couple of different orientations of the Wollaston prism (and therefore fringe alignment and density gradient sensitivity). Again, quantitative density information has not been extracted from the photographs, and is largely not useful.

5.4.3 Intensified CCD Imaging

For series III shots, an intensified CCD (ICCD) camera was used to image natural fluorescence emitted by the flow. As illustrated in Fig. 5.6, the ICCD viewed the test section windows at an angle (about 9.5°) relative to the shadowgraph beam. This resulted in a reduced field of view, and precluded exact correspondence between shadowgraph images and ICCD images, but was considered the most practical arrangement.

The camera was a Princeton Instruments ITE/CCD-576. This model is a sealed unit consisting of an 18-mm diameter Gen II intensifier with enhanced UV and NIR photocathode, fiber-optically coupled to a CCD array. Minimum gating time of the intensifier was 5 ns. The detector array was an EEV 86230, with 576x384 resolution, and multi-pin phasing (reduces dark charge accumulation). A Nikon 105-mm UV lens was mated to the camera. Computer interface for the CCD array was provided by a Princeton Instruments ST-133 controller, which controlled the detector temperature (thermoelectrically cooled down to about -30° C to reduce dark charge accumulation) and CCD readout. Control and high-voltage gating of the intensifier was performed by a Princeton Instruments PG-200 programmable pulse generator. This device generated the high-voltage pulses used by the intensifier, and performed various timing operations related to intensifier gating. The controller

was connected to a Dell Optiplex GXi Pentium computer running Microsoft Windows NT 4.0 and Princeton Instruments' Winview/32 software. The setup is illustrated in Fig. 5.7.

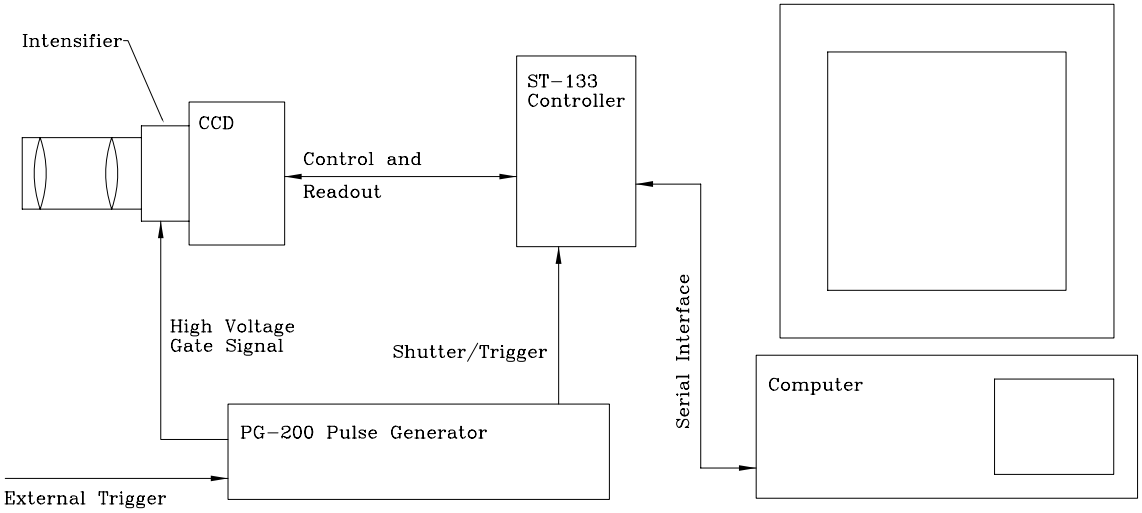

Figure 5.7: Intensified CCD camera setup.

In the single-shot mode used during T5 experiments, the timing of the ICCD was controlled by the PG-200. Prior to the experiment, the CCD was cleared and set to accumulate charge (armed), while the intensifier was off. An external trigger to the PG-200, taken usually from a pressure transducer, and other times from a laser trigger, started the acquisition sequence. After separate programmable delays, a high-voltage gate pulse was sent to the intensifier, and the controller was signaled to read the image out of the CCD. The intensifier gate pulse width, typically 300 ns, represented the exposure time.

The physical principles and characteristics of multi-channel plate (MCP) image intensifiers are beyond the scope of this discussion, but are discussed by Biberman and Nudelman [14], Biberman and Nudelman [15], and Rose [97]. Applications of intensified CCD cameras to combustion imaging are discussed by Kychakoff et al. [70] and Hanson et al. [46]. The purpose of the ICCD in the present investigation was to supplement the shadowgraph data. The use of the ICCD was somewhat speculative, in that little was known about what to expect, but it was anticipated that natural fluorescence might be used to identify reaction zones. Although selective imaging of OH emission, a common marker for combustion, was not feasible because the BK7 windows blocked most UV radiation, hydrocarbon combustion products were visible. Quantitative analysis of the intensity data was not attempted. The intensifier was essential for acquiring fast-exposure natural-fluorescence images. By acting as a very fast shutter, it allowed the high-speed projectile to be imaged without blurring. By amplifying the image, it compensated for the very short exposure time.

Several sources of noise were encountered in the ICCD images. In cases where strong emission occurred, noise of any type was not a problem, but when a detonation was not observed, the signal-

to-noise ratio deteriorated. First, CCD cameras, intensified or not, accumulate charge even when not exposed to light. This "dark charge" noise accumulates over time and is removed each time the CCD array is read out, so that long delays between arming the camera and acquiring an image are to be avoided. Dark charge can also be reduced by cooling the CCD array, and the Princeton Instruments camera was equipped with thermoelectric cooling. Leakage currents within the CCD array create a reproducible dark charge pattern characteristic of the individual chip that can therefore be subtracted from the acquired image. The intensifier adds some relatively random and diffuse dark charge noise that can not generally be subtracted, but this is usually weaker than the CCD contribution. Second, background noise results from leakage directly through the intensifier, when it is off. This results in a faint image of whatever the camera is focused on. Background noise can generally be subtracted from the final image, also. Background and dark charge noise are both removed by acquiring a null image with the same accumulation time as the final image, and subtracting it. However, a third noise source that was encountered was actually a distortion of the other two that made their subtraction difficult or impossible. The cause was not an inherent property of ICCD cameras but apparently a malfunction during the read-out process, possibly attributable to the beta-version control software. The symptom was a horizontal shift of the background and dark charge patterns. Thus, it appears as if the CCD was partially read out just prior to the intensifier gate (exposure). Read out is done by shifting the rows of pixels sequentially across the chip, and after each step, shifting the last row vertically into a special read-out pixel. Fortunately, the effect of noise on the ICCD images was limited to cases with low signal levels, and therefore only a few images were affected (see Fig. B.49).

5.4.4 Data Acquisition System

Primary data acquisition was performed by a CAMAC-based system, linked to a Sun Sparcstation computer by an IEEE 488 (GPIB) bus. DSP Technologies model 2612 transient recorders were used to record diagnostic data from T5. Two DSP TRAQ systems were used to record data from the detonation diagnostics. Low-level signals from optical detectors were, in some cases, amplified by DSP 1402 amplifiers. All channels were triggered simultaneously, generally from a laser or wire trigger. Detonation diagnostics were sampled at 500 kHz or 1 MHz.

The TRAQ systems were supplemented by a Tektronix 640A digital storage oscilloscope. Four channels were recorded on the scope to provide additional timing information, and to verify the CAMAC data.

5.4.5 Timing Control

Precise timing control was crucial to successful acquisition of images of the projectiles. At 2300 m/s, the projectile was completely visible in the optical windows for 61 μs, and precision of less than

10 μs was necessary to catch the projectile and associated waves at a particular position.

Timing of the ICCD exposure was relatively simple, because it could be triggered almost instantaneously from a pressure transducer or laser trigger signaling the arrival of the projectile or pressure wave in the optical window. The only complication occurred when the projectile did not arrive in the window near the same time as the shock/detonation reflection on the wall. This happened either because the detonation was faster than the projectile and outran it, or because the bow wave was a shock with a very shallow angle. If one of these cases was expected, either the projectile and vicinity, or the wave interaction at the wall could be imaged, but not both.

The Nd:YAG laser used in the shadowgraphy and differential interferometry required more elaborate timing. Two sequential signals were required, the first to discharge the laser flash lamps, and the second to trigger the q-switch. The ideal interval between these signals was about 190 μs, with a tolerance of about $\pm$30 μs. As the delay varied from the ideal, the laser energy decreased. The Continuum laser required a somewhat longer delay (about 250 μs) because of internal delays on the flash lamp discharge. Both lasers could be configured with a fixed delay, or with independent flash lamp and q-switch inputs. In either case, the timing system had to produce a signal a fixed interval prior to the desired exposure time. This was accomplished by two methods, described as passive and active.

Passive

The simplest system for timing the flash lamp signal was to detect the arrival of the projectile well ahead of the test section and trigger the laser flash lamps after a fixed delay. The fixed delay was based on an assumed projectile velocity. This system was used for all tests in series I and II and a few in series III. A fixed q-switch delay was used in most of these cases, although an independent q-switch signal, based on a laser trigger, was used in some series III tests. The major drawback of this method is that the uncertainty of the projectile speed directly affects the laser timing. With the q-switch delay fixed, the laser intensity was consistent, but the q-switch time was highly variable. With an independent q-switch signal, the q-switch time would be virtually guaranteed, but the laser intensity would be variable.

Active

In order to remove the projectile speed assumption from the timing system, the control system for the laser had to determine the speed in real time and use the result to determine the proper flash-lamp discharge time. A system suitable for this purpose, although used somewhat differently, was described by Chernyavskii et al. [20]. That system used two sensors upstream of the photographic station to determine the proper time to discharge a photographic spark light source. The sensors triggered function generators that produced monotonically increasing functions of the form $u =$

$f(kt)$. By setting the coefficients k_1 and k_2 such that $k_2/k_1 = 1 + l_1/l_2$, where l_1 and l_2 were the distances from the first sensor to the second sensor and to the photographic station, respectively, the voltages produced by the function generators would cross when the projectile was in the photographic window. The spark light source was triggered off this crossing event.

A similar system was built to control the laser flash-lamp timing, except that the time of arrival of the projectile at a particular location was not the desired output, but a fixed period prior to that. This system is described in Appendix F, and was used in most series III experiments.

5.4.6 Problems and Errors

The projectile experimental apparatus was in almost constant development throughout the course of the experiments. Modifications and additions were made on each new series. Some of these developments were in response to particular problems, and in some cases, they created new problems. Several chronic problems are discussed below. This is necessary, in the case of data acquisition system timing, to explain certain systematic errors that reduce confidence in some of our data, while the other two problems are presented mostly for the sake of technology development.

Data Acquisition Timing

During the third set of experiments, an error in one of the data acquisition modules was discovered. All experimental data were recorded through one of two DSP Technologies TRAQ systems. Each system consists of a TRAQ controller (model 4012 or 4032), one memory module (model 5200), and a number of digitizers (model 2860). The 4-channel digitizers convert the analog inputs to digital numbers at a rate determined by the controller. Transfer of the digital samples over the TRAQ bus is controlled by the TRAQ controller and occurs at a maximum throughput of 8 million samples per second (MS/s). All analog – digital conversion channels sample simultaneously, and then the digital samples are transferred over the TRAQ bus serially. The TRAQ controller passes the samples into the memory module, and reads them back out during data download.

In normal T5 operation, a large number of digitizer channels are used in each TRAQ system, at a relatively low sampling frequency ($\leq$ 200 kHz), such that the total TRAQ throughput is less than the maximum allowable 8 MS/s (e.g., 6.4 MS/s). Accuracy of the sampling frequency is rarely questioned or checked. In our configuration, 8 channels were configured at 1 MHz sampling rate, i.e., at the maximum TRAQ throughput. In the course of diagnosing an unrelated problem, it was found that not all data points were being recorded by the TRAQ system, resulting in inaccurate time base information. For instance, during some tests, every fourth sample was dropped, resulting in a timing error of 25%. The system manufacturer, DSP Technologies, was able to find one miscalibration in the affected TRAQ controller, but could not explain all of the observed symptoms. For the rest of series III, the experimental data were split among the two TRAQ controllers and were acquired at a

slower rate to avoid the timing errors. Some channels were also recorded on an independent digital storage oscilloscope (Tektronix 640A) to allow double checking of the TRAQ system timing.

Because all experimental data in series I and II were taken in the same way, serious doubt was cast on the accuracy of the projectile velocities measured in those experiments. DSP Technologies was unable to specifically explain the observed errors nor produce a rational strategy for recovering these corrupted data. Fortunately, the data themselves contained clues that were useful for reconstructing the actual time bases.

During series I and II, photograph timing was accomplished by assuming a projectile speed (based on previous shots) and firing the laser an appropriate delay after detection of the projectile by a laser trigger or break wire. The delay and laser control was accomplished with the T5 laser controller, which is a custom-built CAMAC module. The primary function of the T5 laser controller is to maintain a constant pulsing frequency prior to the experiment to keep the Nd:YAG laser thermally stable, and to switch to single-shot mode upon receipt of a preliminary signal (generally taken from an accelerometer mounted on the T5 compression tube). After being switched to single-shot mode, it was triggered by a projectile detector via a DSP 1024 trigger generator. The delay was programmed through the data acquisition software, and the programmed value was recorded for each shot. This delay was typically on the order of 170 μs. After receiving a fire signal, the laser discharged its flash lamps and, after another delay, generated a pulse by q-switching its cavity. The q-switch delay was approximately 250 μs ($\pm$10 μs), and was set by a potentiometer on the laser. Tests of the laser and laser controller have shown that the timing of each component is accurate and repeatable within 1 μs. Therefore, the actual time between projectile detection and laser pulse for each experiment can be determined within about 10 μs.

In all experiments, the time of initial projectile detection and the time of the laser pulse were both recorded along with the other data. Comparing the delay from projectile detection to laser pulse measured by the data acquisition system with that expected from the above analysis yields a correction factor for the time base of the TRAQ system data. The computed correction factor (recorded time / actual time) averaged 0.895 with a standard deviation of 0.002 for all shots for which data were available (28 cases), assuming the nominal q-switch delay of 250 μs. The uncertainty in the q-switch delay leads to a range of correction factor from 0.875 to 0.916. In other words, the true projectile velocities from series I and II were about 0.895 as great as the originally measured values. Velocity data (and derived quantities) reported by Bélanger et al. [11] and Kaneshige and Shepherd [64] were the original, uncorrected values.

Break Wire Trigger

Different triggering mechanisms were used to detect approach of the projectile to the test section, and these devices were a chronic source of problems. An electrical break wire was used for series I

and II. The benefit of this system was simplicity. Figure 5.8 shows the circuit used to monitor the state of the break wire. The wire itself was approximately 38 AWG (0.1-mm diameter) copper, and was stretched about 80 mm across the launch tube – test section centerline.

Initially, the break wire detector performed well, but after a number of shots, it began giving spurious output. Examples of a clean break wire signal and an anomalous signal are shown in Figs. 5.9(a) and 5.9(b), respectively. Apparently the accumulation of soot on the wire supports, combined with the vacuum environment of the dump tank, provided a current leak path between the wire terminals such that the current did not stop flowing when the wire broke. Measures were taken to remove the soot from critical insulating surfaces and to increase the amount of insulation, but the failure rate did not improve during the second experiment series. For this reason, an optical trigger was used at this station, for most of series III. Inevitably, this optical trigger experienced its own problems, and a modified form of break wire was used for the last two shots.

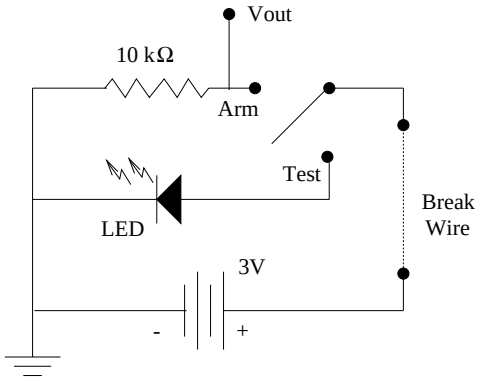

Figure 5.8: Break wire control circuit.

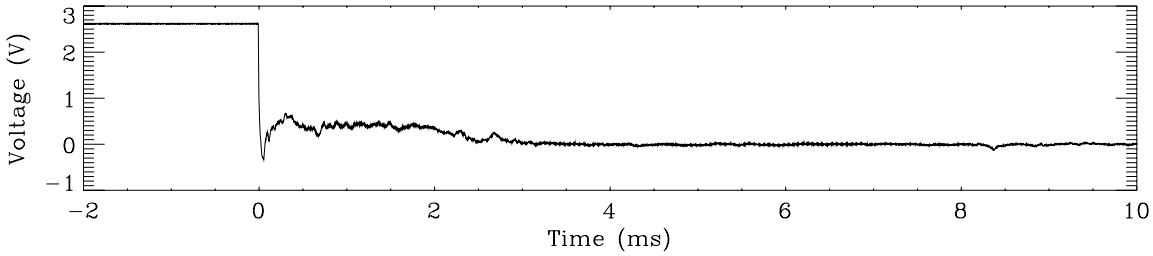

(a) Shot 1007

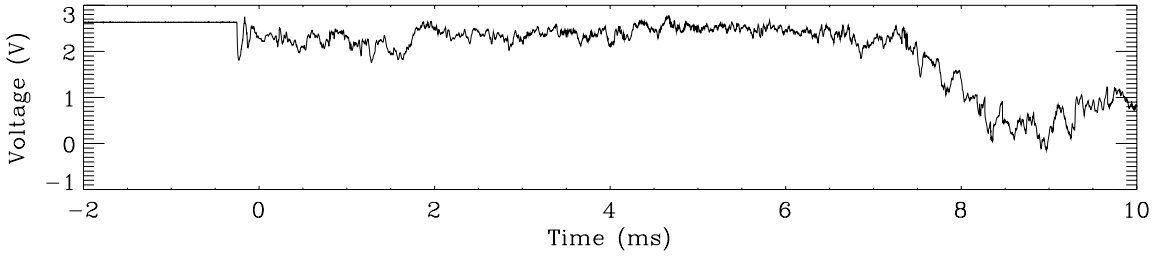

(b) Shot 1009

Figure 5.9: Example break wire signals showing (a) a good trigger and (b) a malfunction.

Optical Triggers

Optical detectors were used with great success at three locations on the test section during series I and II. Therefore, to eliminate the problems with break wire failures and the need to replace a wire after each shot, optical detectors were installed at two positions within the dump tank for series III. Each of these detectors used a collimated diode laser beam aimed at a photodiode, with an interference filter in front of the photodiode to block luminosity from the gases around the projectile. Interference filters were added to the test section laser detectors after series I after the detectors were found to be useless with combusting mixtures during the first series. Both the transmitting and receiving elements were suitably protected from the flow and subsequent soot by glass windows. As seen in series I and II, the expected signal from the laser triggers was a steady and stable level interrupted by an abrupt and fast drop indicating passage of the projectile. However, the optical triggers in the dump tank were significantly less successful.

One laser trigger was mounted on the end of the launch tube, since this was the beginning of the constant velocity phase of the projectile trajectory. This trigger never provided a useful signal. Instead, its output drifted slowly down to zero starting well before the projectile exited the launch tube. The cause of this behavior was not determined, but possibilities include a compression wave in front of the projectile, and stress waves in the launch tube generated by the shock reflection in the T5 shock tube. This trigger was replaced by a PCB pressure transducer, which worked successfully from then on. In fact, the pressure transducer did not show any effects of stress waves, even though it should have been more sensitive to them, suggesting that they were not responsible for failure of the laser trigger.

The laser trigger mounted on the end of the extension tube was more successful than the original break wire, but still experienced trouble. Protecting the optics from high energy debris proved challenging, and led to the use of a mirror to keep the sensitive components as shielded as possible. Even so, filters, windows, and lasers required occasional replacement, and cleaning and realignment was necessary after each shot. This nullified the intended advantage of not replacing a wire for each shot. Even with an apparently functional system, this trigger failed perhaps 1/4 of the time by registering a trigger ahead of the actual projectile arrival. Again, the cause of this malfunction was not conclusively determined, but one possibility was debris or gas ahead of the projectile.

Chapter 6 Discussion of Experimental Results

This chapter describes the results of the experimental program carried out in the T5 laboratory. Raw data are presented in Appendix B. The discussion of results is divided into four parts. Section 6.1 gives a description of the raw data and some specific interpretation, by mixture. The data are summarized, along with data from other sources, in the form of initiation and failure transition maps in Section 6.2. In Section 6.3, wave angle data are compiled and compared with simple predictions. Section 6.4 discusses observations of the unique phenomenon of stabilized delayed initiation.

6.1 Interpretation and Discussion of Raw Data

This section presents interpretation of the images and other raw data presented in Appendix B. The photographic results are discussed in groups divided by mixture.

6.1.1 Inert - N_2

Figure B.3 (shot 861) shows an example of an inert mixture useful as a baseline (no combustion) case. The picture shows the double-image effect of the differential interferometer, particularly at the window and projectile edges, and also along the shock wave where it is nearly aligned with the fringes. Also visible behind and in front of the projectile are conical bow shocks created by debris particles. The bow shock at the nose has been disturbed by broken pieces of the projectile, causing the apparent shock stand-off distance to be about twice the expected value (Eq. 6.2).

A large spike visible in the P3 signal (Fig. B.4) about 500 μs after the projectile bow shock is a blast wave caused by the projectile impact in the target section. This effect was seen in all cases in which the target section was not evacuated and a detonation was not promptly initiated in the test section. After test series I, the target section was evacuated before each test to eliminate this blast effect.

6.1.2 $2H_2+O_2+N_2$

The $2H_2+O_2+N_2$ mixture is characterized as having a CJ velocity very close to the projectile velocity ($\sim$2300 m/s). The cell size is relatively small, however, and detonations were initiated in a number of shots. Although the projectile velocity was sometimes higher than the CJ speed, it was not high enough to lead to a truly stabilized wave in the travel distance provided.

Comments and Interpretation of Raw Data

Shot 1810, 0.080 bar, Fig. B.5: A piece of the projectile is seen separating and perturbing the bow shock. Otherwise, the shock shows no difference from an ordinary unreactive bow shock. The shock locus (as discrete points) is plotted in Fig. 6.1 along with data from similar shots (1819 and 1021), and compared with a correlation given by Billig [16]. This correlation, given as Eq. (6.1) (with changed sign to fit the coordinate system of Fig. 6.1), is a hyperbola fit to experimental data from projectile shots in air, constrained to match separate correlations for the stand-off distance (6.2) and radius of curvature at the nose (6.3), and the Mach wave angle at large distance ($\mu = \sin^{-1}(1/M_\infty)$).

$$-x = R + \Delta - R_c \cot^2 \mu \left[\left(1 + \frac{y^2 \tan^2 \mu}{R_c^2} \right)^{1/2} - 1 \right] \tag{6.1}$$

$$\frac{\Delta}{R} = 0.143 \exp(3.24/M_\infty^2) \tag{6.2}$$

$$\frac{R_c}{R} = 1.143 \exp[0.54/(M_\infty - 1)^{1.2}] \tag{6.3}$$

This correlation was developed for blunt-nosed conical bodies, of which a blunt-nosed cylinder is a special case. By applying it to spheres, the effect of the cylindrical portion of the body is ignored. Of course, Eqs. (6.1-6.3) contain only Mach number as a parameter, and are not generally valid for gases with $\gamma \neq 1.4$.

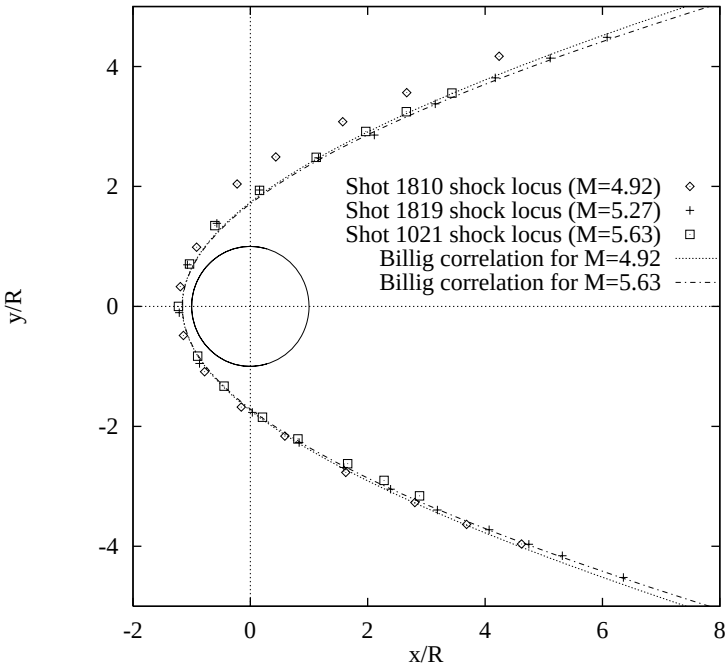

Figure 6.1: Comparison of shock loci for non-reactive shots with hyperbola correlation.

In Fig. 6.1, the experimental data were taken from shots with $\gamma = 1.4$ and M_∞=4.92 – 5.63. Equation (6.1) is plotted for the two extreme Mach numbers, and the variation over this range is seen to be small. The experimental shock loci agree well with the correlation, except where the upper branch of the shot 1810 shock is shifted up by the large projectile fragment. Also, the observed stand-off distance appears slightly larger than that predicted by Eq. (6.2). This may be an effect of combustion

in the stagnation region, although the generally good agreement with the non-reactive correlation elsewhere indicates that this effect is local.

The wall pressure signals in Fig. B.6 show a train of strong pressure waves behind the bow wave. This suggests an explosion occurring in the shock-heated gases behind the projectile.

Shot 865, 0.100 bar, Fig. B.7: The quality of the image is poor, because the optical system had deteriorated during the test series, and also because of debris particles interfering with the projectile bow wave. Nothing in the interferogram or the pressure signals indicate any effect of combustion on the bow wave. However, large pressure waves behind the bow wave in the P3 signal of Fig. B.8 suggest an explosion starting in the shocked gases behind the projectile.

Shot 1811, 0.100 bar, Fig. B.9: Even though the conditions of shot 1811 were almost identical to those of shot 865, the result was remarkably different. The bow wave, which otherwise shows no clear effects of combustion, appears straight after decaying to about 37° (40° on the top, 34° on the bottom). A normal detonation wave is seen about one diameter behind the projectile. The pressure signals indicate that although the apparent velocity of the wave fluctuated, the amplitude, which was consistent with an overdriven detonation at about 2500 m/s, remained roughly constant. Two differences between the conditions of shots 1811 and 865 are notable. The projectile velocity in shot 1811 was about 300 m/s lower, and the travel distance was 1 m longer. The velocity difference, although relatively small, could be important, since the projectile velocity was very close to the CJ velocity in both shots. The difference in travel distance is probably more important, however. The explosion observed behind the projectile in the shot 865 pressure signals apparently developed in shot 1811 into an unsteady overdriven detonation that is seen overtaking the projectile in Fig. B.9.

Shot 1809, 0.120 bar, Fig. B.11: In shot 1809, the overdriven detonation observed in shot 1811 has overtaken the projectile and approached the CJ state, as indicated by the wall pressure signals. Slightly increasing the initial pressure caused the normal detonation wave to overtake the projectile earlier by causing the explosion behind the projectile to occur earlier. The differences in projectile and CJ speeds in shots 1811 and 1809 were too small to account for the observed difference. Since the projectile is traveling at very close to the CJ speed, the detonation may be marginally coupled to the projectile. The detonation wave shows up faintly in the ICCD image because radiation from hydrogen combustion is primarily ultraviolet and the BK7 windows blocked most UV. However, the numerous debris particles visible in the shadowgraph, mostly consisting of nylon, left trails of hydrocarbon combustion products visible in the ICCD image.

Shot 1808, 0.180 bar, Fig. B.13: The shadowgraph and pressure plots look very similar to those of shot 1809. Although not well-defined, some transverse waves are visible behind the detonation

wave.

Shots 1012, 1801, and 1806, 0.250 bar, Figs. B.15, B.17, and B.19: Shots 1012, 1801, and 1806 were performed with the same mixture and initial pressure, but exhibit some strong differences. These differences can be attributed only to projectile velocity, travel distance, and inherent randomness. A shorter travel distance of 0.6 m was used in shot 1012, whereas the other shots were done with a travel distance of about 1.6 m. Figure B.15 shows a bow shock with decoupling reaction zone, and a curved wave behind the projectile. The second wave is interesting, but difficult to interpret. The asymmetry was probably due to a slight offset ($\sim$5 mm) of the projectile below the test section centerline. The pressure plots show the apparent wave speed increasing dramatically, suggesting that the second wave was traveling much faster than the projectile and overtook the bow wave in the vicinity of the second pressure transducer. Clearly, the observed phenomena were not steady.

The longer travel distance (1.6 m) was used in both shots 1801 and 1806, so any differences in the results should be related to the slightly different projectile velocity. The general appearance of the images is very different, because the shot 1801 shadowgraph was not focused, resulting in a blurred image of the projectile, but more pronounced density variations. The highly contrasted striations appear to represent the cellular detonation structure, and in fact, the observed spacing of about 7 mm is reasonably close to the 8.9-mm cell size of the mixture. Striations are only barely visible in the more focused shadowgraph from shot 1806.

Aside from differences in image quality, readily apparent is the difference in spacing between the detonation wave and the projectile, and the slight curvature of the wave in shot 1801 that is absent in shot 1806. This was due to the higher projectile velocity in shot 1801. In both cases, the projectile velocity was very close to the CJ speed of 2340 m/s, but it was apparently just fast enough to keep up with the wave in shot 1801 and not in shot 1806. The pressures and apparent wave speeds in 1801 were consistent with a near-CJ detonation (the P2 signal suffered from a bad electrical connection). The lower projectile velocity of 2290 m/s in shot 1806 resulted in the detonation wave decoupling from the projectile and propagating away from it. The pressure plots from shot 1806 are very similar to those from shot 1801.

Shot 1818, 0.410 bar, Fig. B.21: The results of shot 1818 are consistent with the results of shot 1806. An approximately CJ normal detonation is propagating ahead of the projectile. The pressures and apparent wave speed is consistent with a CJ wave.

Shot 1010, 0.500 bar, Fig. B.23: The interferogram from shot 1010 shows a normal detonation leading the projectile, similar to shots 1818 and 1806. However, the travel distance was shorter and the initial pressure was higher. As a result, the unsteady initiation process is more apparent. The

pressure traces show a faster, more overdriven detonation. The distance between the detonation and the projectile was relatively small. Since the wave speed was much higher than the projectile speed, the separation between them was increasing when the interferogram was taken. Visible between the projectile and the detonation is a curved shock wave that suggests that the flow approaching the projectile was weakly supersonic. Somewhat speculatively, this may be due to acceleration of the flow by the expansion wave following the detonation.

Shots 862 and 863, 1.000 bar, Figs. B.25 and B.27: Some of the features observed in the shot 862 and 863 data are easily explained; others are not. The pressure traces show the detonation wave moving faster than the projectile but decelerating, consistent with the hypothesis that it was initiated by an unsteady explosion behind the projectile which overtook the projectile as a decaying overdriven detonation. However, the measured detonation pressure of ∼18 bar is more consistent with a CJ detonation than an overdriven wave propagating at 2700 m/s (∼33 bar). Particularly interesting are the shock waves visible between the projectile and the detonation, especially in Fig. B.25. The shape and appearance of these waves is different from the wave observed in shot 1010, although they are probably related. Figures B.25 and B.27 appear to be snapshots of the same process at different times, although the sequence is not clear. Because Fig. B.25 was taken later and the projectile was traveling slower, it might be considered to be the later frame. However, the lens-shaped shock wave in Fig. B.25 would seem more likely to develop into the larger, less defined waves visible in Fig. B.27. Despite the apparent differences between Figs. B.25 and B.27, the pressure traces in Fig. B.26 and Fig. B.28 are virtually identical.

Also striking about Figs. B.25 and B.27 are the narrow horizontal striations behind the projectile that represent the transverse waves characteristic of detonations, and which lead to the familiar cellular structure. The spacing, based on averaging a number of striations, is 2.0 mm for shot 862 and 1.8 mm for shot 863. This is reasonably close to the expected cell width for a CJ detonation of 2.3 mm. However, overdriven detonations exhibit smaller cells than CJ waves, so smaller cells would be expected for a wave propagating at 2700 m/s. Assuming that cell width is proportional to ZND reaction zone thickness, the expected cell size for a detonation traveling at 2700 m/s is 0.38 times the CJ cell size. The agreement of the striation spacing with the cell width for a CJ wave is another example of the likeness of these waves to a CJ wave despite their higher apparent velocities.

Discussion

Figure 6.2 summarizes the results of tests with the $2H_2+O_2+N_2$ mixture. Results from test series I and II are discriminated from test series III results to indicate possible effects of the longer travel distance in the latter.

Because all of the tests with this mixture were performed with near-CJ velocities, no clearly

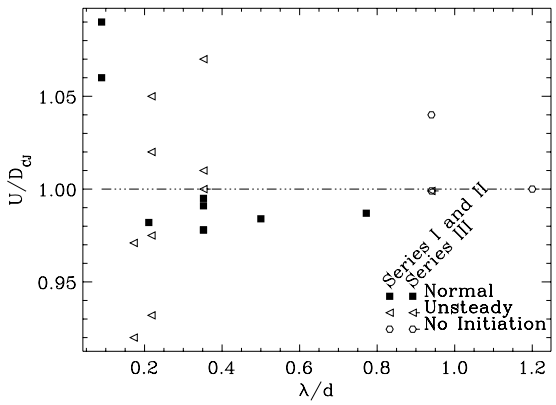

Figure 6.2: Summary of results with $2H_2$+O_2+N_2, in terms of U/D_{CJ} and λ/d.

stabilized detonations were observed, although a number appeared to be marginally stabilized, in that the apparent detonation wave speed was not significantly different from the projectile velocity. In fact, a number of "normal" detonation points are shown below the $U = D_{CJ}$ line. The marginal stabilization at sub-CJ projectile velocities may be because the normal detonations exhibited a velocity deficit, although this would not be expected for mixtures with cell sizes so much smaller than the confinement. For the most part, the results with this mixture were either unsteady initiations or failures.

6.1.3 $2H_2$+O_2+$2N_2$

Increasing the nitrogen content from 25% to 40% decreases the CJ velocity significantly, while not increasing the cell size too much, so that stabilized detonations can be observed.

Comments and Interpretation of Raw Data

Shot 1819, 0.110 bar, Fig. B.29: The results of shot 1819 are very similar to those of shot 1810 (Fig. B.5), and the discussion of Section 6.1.2 is applicable here.

Shot 1814, 0.557 bar, Fig. B.31: Figure B.31 shows an example of a disintegrated projectile. The P2 signal in Fig. B.32 also shows pathological behavior, unrelated to the disintegration of the projectile. An error in the data acquisition system caused a vertical shift, accompanied by a period of high-amplitude noise.

Shot 1815, 0.557 bar, Fig. B.33: Shot 1815 resulted in a clearly stabilized detonation. The shadowgraph in Fig. B.33 shows the detonation decay to very close to the expected CJ wave angle, and form a Mach reflection from the walls. The Mach stem blends smoothly into the incident wave, so that no reflected shock is visible. The intersection of the conical detonation with the

square test section walls causes the reflection to occur slightly more forward in the center of each wall (and window) than at the corners. This gives the wave some apparent thickness at the top and bottom, and causes the apparent curvature near the projectile and thickness at the top and bottom. The double lines at the rear are interpreted as the reflections from the windows not being exactly coincident. The strong emission behind the projectile in the ICCD image is believed to result from combustion of hydrocarbons ablated from the projectile. Possibly, the bright plume signals separation of the flow on the back of the projectile. Particularly notable about the shadowgraph and ICCD images is the complete lack of wake structures in the shadowgraph, where the wake is the most prominent feature of the ICCD image. Apparently, the source of light emission in the wake, whether hydrocarbon combustion or not, is not accompanied by a significant density variation. Figure B.34, although exhibiting some extraneous noise pulses, shows the apparent wave speed to be very steady.

The similarity of the results (ICCD image and pressure traces) of shots 1815 and 1814, despite the disintegration of the projectile in shot 1814, demonstrates the insensitivity of the detonation to the shape of the projectile.

6.1.4 $2H_2+O_2+3N_2$

Comments and Interpretation of Raw Data

Shots 1022, 1023, and 1813, 0.831 bar, Figs. B.35, B.37, and B.39: Three shots were performed with the $2H_2+O_2+3N_2$ mixture at the same condition. Two were done without the extension tube (0.6-m travel distance) and the third was done with it (1.6 m), and the velocity in all cases was approximately 2300 m/s. Therefore, the only systematic difference should result from the change in travel distance.

The shadowgraph from shot 1022 (Fig. B.35) was taken early, so only part of the bow wave is visible. The part that is visible is similar to the bow wave in Fig. B.37 (shot 1023), but a little wider. The pressure plots in both cases show changes in apparent wave speed and in the shape of the profile, indicating that the waves were unsteady. The shot 1023 P3 signal, which was measured on the top wall of the test section, adjacent to the center of the window, shows an amplitude of 40 bar, which is consistent with an overdriven detonation propagating at the apparent wave speed of 2780 m/s. Since this is faster than the projectile speed, the Mach stem visible at the top of the window must have been traveling forward relative to the projectile, and the top part of the bow wave would probably look the same as the lower part, eventually. The Mach reflection on the bottom wall is similar to that observed in shot 1815 (Fig. B.33), except that a reflected shock is visible. Since the Mach stem blends smoothly into the incident wave, the reflected shock must form from a distributed compression wave. In contrast, the Mach reflection at the top shows a sharp bend, and the reflected shock appears stronger. Assuming the top Mach stem formed later than the one on the

bottom, this is consistent with the observation by Akbar [3] that detonation Mach reflections seem to begin sharp, but evolve into smooth transitions. Although small, the slight offset of the projectile about 3.5 mm below the test section centerline may be responsible for the asymmetry of Fig. B.37.

The stabilized detonation in Fig. B.39 looks similar to that from shot 1815 (Fig. B.33) except that the wave bends further around the projectile, because the CJ speed was lower. Also, the Mach reflections generate visible reflected shocks. The ICCD images also look similar except that the wake seems to separate further back on the projectile in Fig. B.39. The pressure traces from shot 1813 (Fig. B.40) indicate less unsteadiness than those from shots 1022 and 1023, suggesting that the phenomena observed in the shorter travel distance cases have stabilized. The P1 trace shows the effects of a bad electrical contact.

Discussion

Figure 6.3 shows combined results from the $2H_2+O_2+2N_2$ and $2H_2+O_2+3N_2$ mixtures, since relatively few experiments were done with these mixtures.

Except for the single failure result on the right of the plot, all of the tests were intentionally performed at a single λ/d value. Therefore, the only apparent variation between these shots was the U/D_{CJ} value, although this variation was minimal. Thus, the appearance of steady and unsteady initiations in the same region is probably not significant.

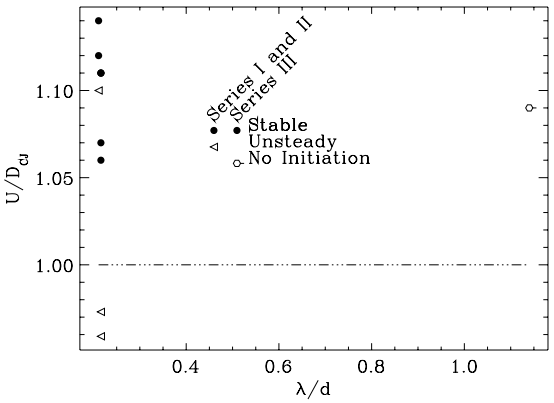

Figure 6.3: Summary of results with $2H_2+O_2+2N_2$ and $2H_2+O_2+3N_2$, in terms of U/D_{CJ} and λ/d.

6.1.5 $2H_2+O_2+3.76N_2$

The stoichiometric hydrogen-air mixture, having an even lower CJ speed than the previous mixtures, exhibited relatively stable waves, and because of the larger cell sizes, required higher pressures to establish detonations.

Comments and Interpretation of Raw Data

Shot 1021, 0.100 bar, Fig. B.41: The results of shot 1021 are very similar to those of shot 1810 (Fig. B.5), and the discussion of Section 6.1.2 is applicable here.

Shot 1015, 0.421 bar, Fig. B.43: Figure B.43 shows a good example of shock-induced combustion, in which the reaction zone completely decouples from the bow shock. Some structures

reminiscent of the "large-disturbance" quasi-periodic structures of Alpert and Toong [4] are visible between the decoupled reaction zone and the bow shock, along with the interconnecting waves discussed by McVey and Toong [86].

Fortuitously, a debris particle present just ahead of the bow shock, in the region where the reaction zone has fully decoupled, serves as a crude diagnostic tool in the shadowgraph. Where the gas was shock heated by the particle bow shock, it is seen to react immediately behind the projectile bow shock. At the corresponding region above the projectile, the reaction zone is receding from the shock wave. This supports the contention that the boundary seen separating from the bow shock is in fact a reaction front, or contact surface between unreacted and reacted gases. Also, McVey and Toong [86] demonstrated that similar boundaries in their experiments were reaction fronts, by probing the flow around the projectile with an ionization probe.

Shot 1016, 0.853 bar, Fig. B.45: Shot 1016 gave results similar to shot 1015, at about twice the initial pressure. Although the shadowgraph was taken too late to see the nose of the projectile and bow shock, the reaction zone appears to have decoupled from the shock later than in Fig. B.43. The reflection of the shock from the bottom wall is visible, although the top reflection is not, because of a small offset of the projectile below the test section centerline ($\sim$3.5 mm).

Shot 1807, 1.000 bar, Fig. B.47: The bow shock and decoupling reaction zone of shot 1807 look much like those of shots 1015 and 1016. The shock appears to be wider than at the lower pressures, but the reaction zone appears to decouple from the shock sooner than in shot 1016. The pressure plots show a wave of greater strength than the bow shock following it. This may indicate that a detonation was stabilized by the reflection of the bow shock (see Section 6.1.6).

Shot 1817, 1.120 bar, Fig. B.49: The ICCD image from shot 1817 shows low light levels from a non-detonative event, superimposed with a noise pattern (see Section 5.4.3). The shock heated and compressed gases in the stagnation region of the projectile are barely visible, but significant emission is seen from the hot projectile nose and from the wake.

As discussed in Section 5.4.3, the noise pattern consists of dark charge and background noise, shifted by an inexplicable read-out error. The dark charge appears as intermittent vertical stripes. The large circular area on the right side of the image that appears slightly brighter than the background is actually a shifted background image of the window, accumulated before the shot. It is not an image of the reaction zone.

Shot 1816, 1.200 bar, Fig. B.51: The ICCD image from shot 1816 is similar to Fig. B.49, except taken at a later time. The wake emission was strong enough to make the noise almost negligible. Both Fig. B.51 and Fig. B.49 are most notable for what they do not show. No signs of combustion

are visible outside of the wake. The pressure traces show signs of slow combustion, but only 300 μs or so behind the bow shock. The P2 signal in Fig. B.52 was corrupted by a bad electrical connection, although the bow shock arrival time is clear.

Shot 1812, 1.700 bar, Fig. B.53: Figure B.53 shows a stabilized detonation very similar to that observed in shot 1813 (Fig. B.39). The wake visible in the ICCD image is seen to expand suddenly, at about the same location as where part of the Mach disk is visible in the shadowgraph ($\sim$2 projectile diameters behind the projectile). Otherwise, the most noticeable feature of the ICCD image, the wake, is completely absent from the shadowgraph. The pressure plots show a stabilized detonation, although the maximum pressure is less than expected for an overdriven detonation traveling at 2200 m/s.

Shot 1018, 1.707 bar, Fig. B.55: Shot 1018 demonstrates a transitional case similar to shot 1023 (Fig. B.37). A pseudo-stabilized oblique detonation is visible above the projectile, with a small but well-defined Mach reflection. Below the projectile, the bow shock with decoupling reaction zone curves continuously backward. The reflection of the curved bow wave from the window is visible as a backward-concave arc. The pressure traces show the pressure wave rapidly changing from a non-detonative wave to an overdriven detonation propagating faster than the projectile. This is consistent with the transition of an initially non-detonative bow shock reflection to an overdriven detonation Mach reflection. Since shots 1018 and 1812 were done with almost identical initial pressures, the significant differences in results can be attributed to the difference in travel distance, with Fig. B.55 being an early snapshot of the evolution toward Fig. B.53.

Shot 1821, 1.900 bar, Fig. B.57: The detonation seen in Fig. B.57 appears to be completely stabilized. The pressure traces show a roughly constant apparent wave speed, although the maximum pressure is less than expected for an overdriven detonation traveling at 2300 m/s ($\sim$60 bar), like shot 1812. In both cases, the pressure plots exhibit a sharp initial spike, so the maximum pressure may only occur for a very short time, less than the time resolution of the transducers.

Shot 1820, 2.000 bar, Fig. B.59: An example of the delayed initiation phenomenon is seen in shot 1820. In the shadowgraph, the bow wave is seen to decay beyond the CJ point (59.7°) and appears as if the reaction zone has decoupled from the bow shock. However, immediately behind the projectile is a second, approximately normal wave that curves backward outside the decoupled shock and then forward in a Mach reflection. The minimum angle of this wave ($\sim$65°) is somewhat larger than the CJ angle (59.7°), although the measurement error is large because of the small distances involved.

The superimposed waves of Fig. B.59 are similar to other, completely unsteady, situations involving an overdriven detonation overtaking a non-detonative bow shock, e.g., shots 1012 and 1811 (Figs. B.15 and B.9). In this case, transient events would not be expected because of the long travel distance, and the pressure traces indicate that the pressure wave was roughly steady. This suggests that the secondary wave was in fact stabilized behind the projectile. If so, the stabilization was apparently marginal, since shot 1821, at almost identical in conditions, resulted in a prompt initiation and stabilization.

Shot 1020, 2.560 bar, Fig. B.61: While the shadowgraph in Fig. B.61 appears to show a fully stabilized detonation, the pressure traces in Fig. B.62 show significant change in the apparent wave speed. However, the apparent wave speed dropped to near the projectile speed, so it was probably approximately steady when the shadowgraph was taken. Again, the maximum pressure expected for an overdriven detonation traveling at the projectile speed (∼86 bar) was not observed, probably because the pressure spike was too narrow and fast to be resolved by the transducers.

Discussion

Figure 6.4(b) shows the results of tests with hydrogen-air mixtures, in terms of the ratio of projectile velocity to CJ speed and the ratio of cell size to projectile diameter. λ/d is plotted on a log scale because the data span a wide range but are concentrated at lower values. Initiation and failure points are seen in the same area, along with the delayed-initiation case from shot 1820. However, these were not simply randomly distributed events.

Figure 6.4(a) shows the same data plotted versus initial pressure instead of cell size ratio. Since the initial pressure was the only variable in the experiments (aside from travel distance), it should be inversely equivalent to the cell size ratio. However, the data are seen to segregate much more when plotted versus pressure, with the single exception of the shot 1820 delayed initiation. This is due to a peculiarity about the chemistry of hydrogen combustion. Normally, the cell size and reaction zone thickness decrease monotonically with initial pressure.

As seen in Fig. 6.5(a), the reaction zone thickness of hydrogen detonations exhibits a local minimum with increasing pressure. This effect is known as the second explosion limit and results from the varying importance of the reactions $H + O_2 \rightarrow OH + O$ and $H + O_2 + M \rightarrow HO_2 + M$, as noted by Viguier et al. [119] and Ju and Sasoh [61]. Ju and Sasoh [61] predicted a local minimum of critical projectile velocity for detonation initiation because of this effect. Calculations performed with two reaction mechanisms are shown in Fig. 6.5(a), and although some shift in the existence and location of the minimum are apparent, they approximately agree. The local minimum is responsible for concentrating the data in Fig. 6.4(a) even though they are evenly distributed in Fig. 6.4(b). It also suggests a reason for the occurrence of the shot 1820 delayed initiation amongst prompt initiation

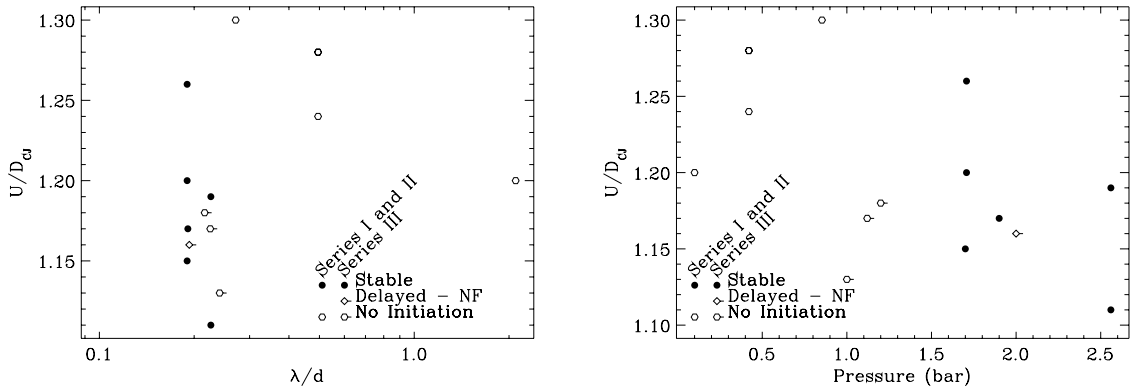

(a) U/D_{CJ} versus λ/d

(b) U/D_{CJ} versus initial pressure

Figure 6.4: Summary of results with hydrogen-air

cases, since the reaction zone thickness minimum occurs roughly at the pressure of shot 1820. This possibility is merely speculation at present, as the exact mechanism responsible for the delayed initiation is not clear. The details of the variation of the reaction zone thickness minimum are presumably important, but as Fig. 6.5(a) shows, the existing reaction mechanisms are not very precise in the relevant regime. Also, if detonation initiation is more directly related to cell size than to reaction zone thickness, the translation of the reaction zone thickness minimum to cell width variation could further distort the relationship. Unfortunately, cell size data for hydrogen-air detonations at such pressures are not available.

6.1.6 C_2H_4+3O_2+5N_2

Not all of the shots in this series used exactly the same mixture. In some shots, the nitrogen concentration was varied, in order to explore phenomena around the initiation transition. The standard mixture was somewhat less dilute than a stoichiometric ethylene-air mixture, and was selected to allow investigation of the transition to detonation initiation. A stoichiometric ethylene-air mixture would have been too insensitive, while an ethylene-oxygen mixture would have resulted in excessive pressures.

The series using the standard mixture followed an unusual progression, with a very stable normal detonation behind the projectile at lower pressure transitioning suddenly to a stable prompt initiation at higher pressure.

Comments and Interpretation of Raw Data

Shot 1829, 0.300 bar, Fig. B.63: The ICCD image in Fig. B.63 shows a detonation wave following the projectile. Most of the bow shock is not visible, except close to the nose where the

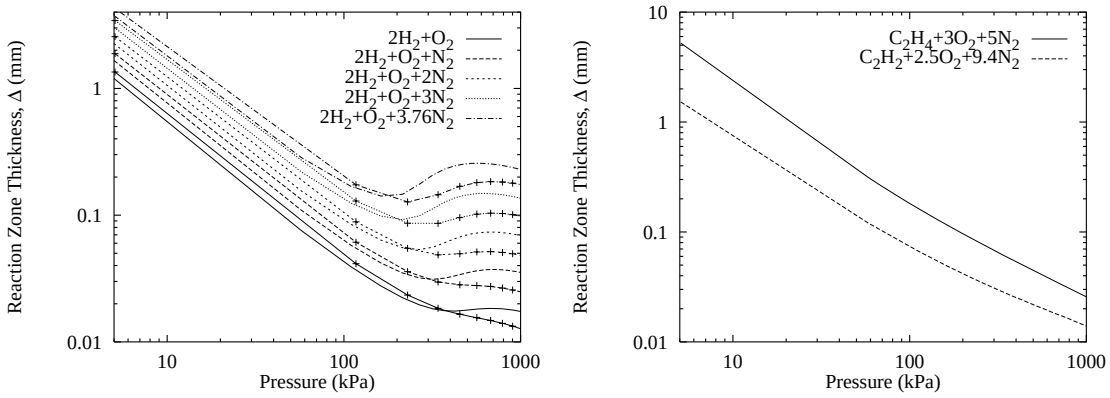

(a) H_2-O_2-N_2 mixtures

(b) C_2H_4+$3O_2$+$5N_2$ and C_2H_2+$2.5O_2$+$9.4N_2$ mixtures

Figure 6.5: Variation of CJ detonation reaction zone thickness with initial pressure. In (a), smooth curves were computed with the mechanism of Lutz et al. [82] and curves with marks were computed with the mechanism of Frenklach et al. [39]. Only the Lutz et al. [82] mechanism was used for (b).

temperature and density were highest. Just in front of the detonation, a region of emission is visible inside the bow shock. Whether this is related to the shock or reaction front is not clear. Since the detonation seems to be completely normal, there is no sign of coupling between it and the projectile, so some relative velocity would be expected. However, the pressure traces show a relatively stable wave propagating at the same speed as the projectile. Unfortunately, the CCD saturated in the region behind the detonation, so no structure can be seen there.

Shot 1823, 0.350 bar, Fig. B.65: The results of shot 1823 are very similar to those of shot 1829. The normal detonation appears to be the same distance behind the projectile (2.7 diameters, from the viewpoint of the ICCD), and the pressure plots show it to be steady. Except for the detonation, the shadowgraph looks like previous shock-induced combustion cases, such as shot 1015.

Shot 1832, C_2H_4+$3O_2$+$4.3N_2$, 0.350 bar, Fig. B.67: The results of shot 1832 appear very similar to those of shot 1820 (Fig. B.59), in which a stabilized delayed initiation was observed. The ICCD image is brighter, primarily because carbon compounds in the products fluoresce more in the visible range than hydrogen compounds (e.g., in shot 1820). Clearly visible in the image are the wave reflections from the front and back windows, the non-detonative bow shock, and the curved detonation immediately behind the projectile. The intersection of the bow shock and the detonation on the far side of the projectile is visible as a somewhat distorted arc. The pressure traces in Fig. B.68 confirm, as in shot 1820, that the waves are roughly steady, and the observed phenomenon was probably stable.

Shot 1824, 0.400 bar, Fig. B.69: The results of shot 1824 are virtually identical to those of shots 1829 and 1823 (Figs. B.63 and B.65). The distance between the detonation and the projectile in the ICCD image is about 2.7 diameters. In the more precise shadowgraph, the distance is about 3.3 diameters, the same as in shot 1823. These results strongly suggest that the detonation following the projectile is stabilized there, probably by the reflection of the bow shock.

Shots 1828 and 1834, 0.400 bar, Figs. B.70 and B.73: The results of shots 1828 and 1834 are similar, but with some interesting differences. The images were deliberately timed to catch the normal detonation observed in shots 1823, 1824, and 1829, except the ICCD image of shot 1828 was timed to observe the flow around the nose of the projectile.

The shadowgraph of shot 1828 (Fig. B.70) does not show the flow near the projectile, which had left the window when the photograph was taken, but shows a trapezoidal wave pattern in the vicinity of the bow wave wall reflection. The decoupled reaction zone is seen on the left, near the top and bottom, with a normal wave spanning the area in between. Oblique waves are seen in the area outside the reaction front. These oblique waves terminate in short Mach stem-like vertical waves. Also barely visible in the shadowgraph at the top and bottom, adjacent to the oblique waves, are the regular reflections of the projectile bow shock from the top and bottom walls.

The shot 1828 pressure traces show the reflection of the bow shock, followed after a decreasing delay by the secondary wave. While the bow shock reflection appears to be decelerating slightly, the secondary wave was accelerating, from 2490 m/s between P1 and P2, to 2610 m/s between P2 and P3. From its amplitude, around 40 bar, it was clearly a detonation (as opposed to a shock), and the apparent acceleration suggests that it was not overdriven, since an unsupported overdriven detonation would decelerate. The acceleration may have been due to the unsteady expansion behind the projectile, which would make the absolute speed of the detonation higher as it approached the projectile. Also, any slow combustion occurring in the flow behind the projectile would tend to make the CJ speed decrease with distance.

However, these conclusions are complicated by certain differences between shot 1828 and similar shots. First, the pressure traces of shot 1834 and similar shots such as 1823, 1824, and 1829 show the detonation stabilized relative to the projectile. The corresponding photographs show the detonation stabilized near where the bow shock would reflect from the wall. This pattern suggests that the results of shot 1828 show a transitional event prior to stabilization of the detonation by the wall reflection. Second, the trapezoidal wave pattern seen in the shot 1828 shadowgraph is not observed in the shot 1834 shadowgraph. The shadowgraphs of other, similar shots do not show the entire detonation, and the ICCD images are obscured by the oblique viewing angle, so they do not reveal either configuration. However, since the shot 1828 pressure traces are distinct from the others, the trapezoidal wave pattern was probably unique, and characteristic of the transitional process. The

oblique waves in Fig. B.70 suggest that the normal wave spanning the reaction zone boundary was propagating faster than the corresponding waves outside the boundary. However, if these waves were detonations, the opposite would be expected. The CJ speed inside the reaction zone boundary would be lower than outside, because the equivalent heat release would be lower (due to partial combustion and higher temperature) and the fluid velocity (at least across the contact surface) would be higher. The observed pattern is consistent with an unsteady shock or overdriven detonation, in which case the wave speed inside the boundary might be higher than outside.

The projectile and some of the flow around it are visible in the shot 1828 ICCD image. The luminous region around the projectile may be the reaction zone, or simply the shock-heated region, although the bow wave is clearly non-detonative.

As in the similar shots (1823, 1824, and 1829), the ICCD image of shot 1834 shows the normal detonation wave near the center of the window. However, the ICCD gain (specifically multi-channel plate voltage and gate width) was set lower, so that emission from the detonation products did not saturate the CCD, and some structure is visible. The intersection of the bow shock with the normal detonation is visible as a thin ellipse. Bright areas at the top and bottom of the intersection correspond to dark areas in the other ICCD images, due to the saturation effect discussed in Section B.4. The intersection of the detonation with the front window is visible as a nearly straight vertical boundary between lighter and darker regions.

Shot 1833, C_2H_4+3O_2+5.2N_2, 0.420 bar, Fig. B.74: The shadowgraph, ICCD image, and pressure traces from shot 1833 show the bow shock reflecting from the test section walls without initiating a detonation. The decoupled reaction front is visible in the shadowgraph and ICCD image. Following the bow shock reflection by about 250 μs in the pressure traces is a large pressure spike possibly indicating a detonation.

Shot 1830, 0.450 bar, Fig. B.77: In contrast to the normal detonations stabilized behind the projectile at lower pressures, the results of shot 1830 resembled a promptly initiated and stabilized detonation. The shadowgraph shows a familiar configuration, with the bow wave decaying to approximately the CJ angle and ending in Mach reflections at the walls, with the reflected shocks and a Mach disk visible behind the detonation. However, the bow wave shows a number of kinks and disturbances, which show up strongly in the ICCD image. In the ICCD image, the bow wave appears to consist of three steps, with the third much brighter than the first two. This may represent an intermediate case between prompt and delayed initiation (see shots 1820 and 1832). The bow wave in the shadowgraph displays several different angles, and the steepest portion in the lower branch is roughly the CJ angle. The pressure traces indicate that the waves were stable.

Shot 1831, C_2H_4+3O_2+5.5N_2, 0.450 bar, Fig. B.79: By increasing the nitrogen concentration, the prompt initiation of shot 1830 was suppressed in shot 1831. The ICCD image shows a detonation following the projectile almost outside the window. The detonation seems to protrude upstream along the projectile wake. Like shot 1828 (Fig. B.70), the pressure plots show the detonation overtaking the projectile bow shock. Possibly, the protrusion observed on the detonation was similar in nature to the trapezoidal wave pattern observed in shot 1828.

Shot 1822, 0.500 bar, Fig. B.81: The results of shot 1822 were similar to those of shot 1830, except that the disturbances on the bow wave were smaller, corresponding to a decrease in detonation cell width. However, the disturbances do not directly represent cells, which would have a width around 5.8 mm.

Shots 1825 and 1826, 1.000 bar, Figs. B.83 and B.85: Doubling the initial pressure resulted in smoother stabilized detonations in shots 1825 and 1826. Most of the area behind the detonation in Fig. B.83 was saturated in the ICCD image, although the Mach stems and the wake are visible because of over-saturation (see Section B.4). The ICCD gain was reduced in shot 1826 so that Fig. B.85 resolves the projectile, its wake, and the wave reflections from the windows.

Discussion

Figure 6.6 shows the results of all tests performed with C_2H_4-O_2-N_2 mixtures. Over the narrow range of U/D_{CJ} shown, prompt detonation initiation appears to occur at a λ/d value around 0.25. A number of delayed initiation cases are plotted. "Delayed - NF" refers to initiation in the near field of the projectile, away from the test section wall. "Delayed-WR" indicates initiation and apparent stabilization of a normal detonation at the bow shock wall reflection. In these cases, transition from failure to prompt initiation occurred gradually, with the two types of delayed initiation as intermediate steps.

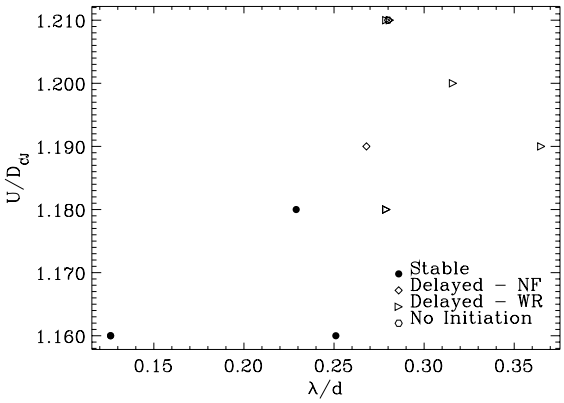

Figure 6.6: Summary of results with C_2H_4-O_2-N_2 mixtures, in terms of U/D_{CJ} and λ/d.

In contrast to the hydrogen mixtures, the ethylene and acetylene mixtures used do not exhibit a second explosion limit, as shown in Fig. 6.5(b). This suggests that the initiation criteria should be clearer.

6.1.7 C_2H_2+2.5O_2+9.4N_2

A stoichiometric mixture of acetylene and air was chosen because it provided appropriate sensitivity, detonation speed, and pressure characteristics to explore critical conditions for detonation initiation. The mixture was not varied.

Comments and Interpretation of Raw Data

Shot 1836, 0.500 bar, Fig. B.87: The results of shot 1836 were similar to those of shot 1833 (Fig. B.74), with a non-detonative bow shock reflecting from the walls without initiating a detonation. A pressure wave possibly representing a transition to detonation followed the bow shock by about 250 μs.

Shot 1837, 0.800 bar, Fig. B.88: Shot 1837 resulted in a normal detonation following the projectile at a roughly stable distance, similar to shots 1829, 1823, 1824, 1828, and 1834 (see Section 6.1.6). The quality of the shadowgraph is poor because of a timing malfunction in the Nd:YAG laser trigger circuit. The flash-lamp trigger occurred too early, but the q-switch trigger occurred at a proper time, resulting in a very long q-switch delay, and a severely under-exposed negative. An image was recovered from the resulting negative through filtering during enlargement and digital image processing.

Visible in the ICCD image are the reaction zone around the projectile and the normal detonation wave. Where the projectile wake intersects the detonation, a particularly bright region is visible at the right edge of the window. The ICCD was triggered off the P3 signal, and since it shows the detonation to the right of the center of the window, it must have been triggered by the bow shock, which was not visible in front of the detonation. Therefore, the faint glow in the region around the projectile must have been due to the reaction zone, rather than the shock.

In contrast to the previous cases of detonations stabilized behind the projectile by the bow shock reflection, the pressure plots from shot 1837 seem to show the detonation falling behind the bow shock. This may be related to the lower CJ speed of the acetylene mixture (relative to the ethylene mixture), and suggests that the observed normal detonation was initiated unsteadily and would eventually decouple from the projectile entirely, or settle into a position further behind it.

Shot 1840, 0.820 bar, Fig. B.91: Shot 1840 seems to represent a transitional case between the delayed normal detonation behavior of shot 1837 and prompt initiation. The bow wave looks like a non-detonative shock with decoupling reaction zone, except that the reaction zone is not clearly visible, and a number of disturbances are apparent on the shock surface. The ICCD image has been processed to enhance some of the more faint features, and some disturbances can be correlated between the shadowgraph and ICCD image. The most prominent feature in the ICCD image is the

partially visible detonation, which appears asymmetric, probably because the projectile was about 12.4 mm above the test section centerline. As in shot 1837, the pressure plots show the detonation separating from the bow shock reflection and falling behind it.

Shot 1839, 0.850 bar, Fig. B.93: Shot 1839 resulted in a stabilized detonation similar to shot 1822 (see Fig. B.81).

Shot 1838, 0.900 bar, Fig. B.95: The stabilized detonations shown in Fig. B.95 are straighter than those in Fig. B.93, with smaller corrugations consistent with the smaller mixture cell size.

Shot 1835, 1.000 bar, Fig. B.97: The results of shot 1835 are consistent with the progression of shots 1839 and 1838 toward straighter stabilized detonations with smaller disturbances.

Discussion

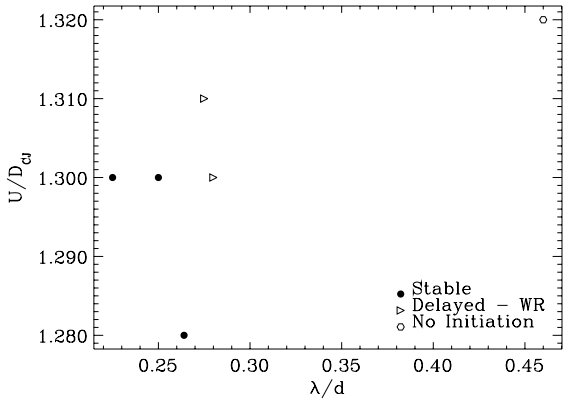

Figure 6.7: Summary of results with C_2H_2-O_2-N_2 in terms of U/D_{CJ} and λ/d.

Figure 6.7 summarizes results of all tests performed with the acetylene mixture. As with the ethylene mixtures, stabilized prompt initiations occur at λ/d less than about 0.25, and transition from failure to prompt initiation appears to occur gradually, with delayed initiations in between.

6.2 Initiation and Failure Transition Maps

A large amount of data on detonation initiation by projectiles is available from the present experiments and work by other investigators. To make sense of these results, a natural approach is to consider different mixtures separately, and within each mixture, to consider the effect of initial pressure. The results presented in Appendix B and discussed in the preceding sections of this chapter are organized in this fashion.

Figure 6.8 shows most of the available data plotted together on the U/D_{CJ} vs λ/D plane. The data are sorted by source organization and roughly by observed phenomena. Different shapes identify data from different sources, while variations of each shape identify the results. Also plotted are the boundary curves between initiation and failure predicted by the Lee-Vasiliev model for γ=1.4 (solid) and γ=1.556 (dashed). Most of the data are from mixtures of hydrogen, oxygen, and nitrogen, for which γ=1.4 is valid. γ=1.4 is also roughly valid for the mixtures with ethylene and acetylene as fuels since they were mostly oxygen and nitrogen. To be precise, γ=1.37 for C_2H_4+3O_2+5N_2 and γ=1.38 for C_2H_2+2.5O_2+9.4N_2. For the University of Washington (UW) data, generated with 2H_2+O_2+7Ar, γ=1.556 is more appropriate. The result categories are somewhat simplified. Gen-

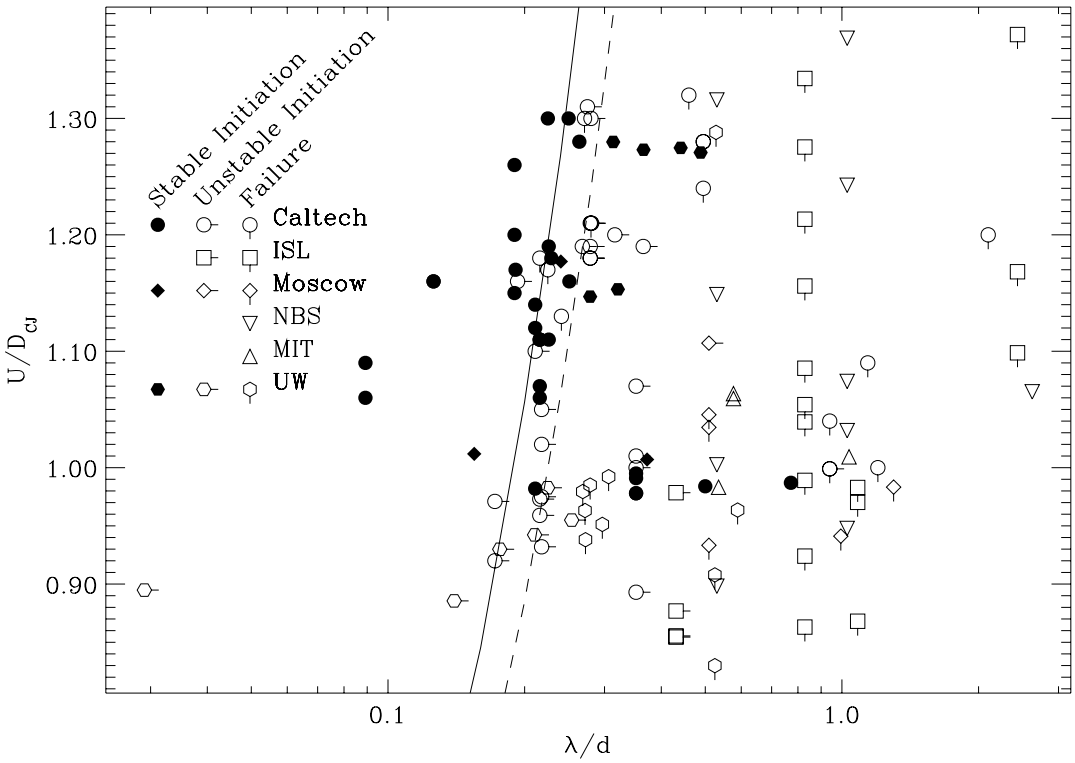

Figure 6.8: Projectile-initiated detonation transition map.

erally, "unstable initiation" represents detonation initiation in cases where the observed detonation was clearly transient, so that a stabilized or a failed detonation could eventually result. For the purpose of Fig. 6.8, failure represents anything other than detonation initiation, although a variety of phenomena can be observed in this case. Non-reactive shocks, steady shock-induced combustion, and distinct regimes of pulsating shock-induced combustion, as studied in detail by other researchers, can occur where detonation is absent.

As expected, Fig. 6.8 shows initiation occurring at small λ/D and large U/D_{CJ}, although at some

values of λ/D, detonation was not observed at any value of U/D_{CJ}, within the range investigated. The upper-left quadrant, where stabilized initiation is expected, is relatively unpopulated because of the dual requirements of high velocity and small cell size. Given the velocity limitations of a facility, the ratio U/D_{CJ} can be increased by decreasing the CJ velocity, typically by diluting the mixture. This has a negative effect on the cell size, however, causing the condition to move to larger λ/D simultaneously.

Unequivocal (photographic) evidence of stabilized detonations have been obtained by only two other groups: at Moscow State University and Nagoya University. Detonation initiation over a range of conditions was observed at the University of Washington, but no flow visualization was performed. Also, most work was performed with sub-CJ projectile velocities, leading inevitably to non-stabilized detonations. Most of the data from the University of Washington are not shown, because they were performed at low values of U/D_{CJ}, whereas Fig. 6.8 concentrates on projectile speeds above the CJ speed.

Although some overlap occurs between initiation and failure points, the presence of a border between the two cases is apparent. The Lee-Vasiljev prediction crosses the observed border near $U = D_{CJ}$. While a number of objections were raised to this model in Section 2.2.3, some amount of flexibility, relating to the choice of critical energy model used, is present in the constant of proportionality. However, adjusting this constant causes the curve to shift up and down, but does not rotate it. This indicates a more substantial weakness of the Lee-Vasiljev model.

Figure 6.9 shows that the various fuels did not produce significantly different results.

6.3 Wave Angles

The hydrodynamic model of detonations predicts that a detonation initiated by and stabilized on a projectile will decay to the CJ state in the far field. This leads to a simple prediction of the wave angle. That is, where β_{CJ} is the angle between the wave and the axis of flight for a CJ wave,

$$\beta_{CJ} = \sin^{-1} \frac{D_{CJ}}{U} \tag{6.4}$$

Table 6.1 shows angles measured from photographs in Appendix B along with values of β_{CJ} predicted from Eq. (6.4). Separate values from film images and ICCD images are given. Only waves that were not continuously concave toward the projectile were measured, and the angles reported in Table 6.1 were taken as half of the total angle between the top and bottom surfaces of the waves. These surfaces were identified as the straightest part of the wave, where there was a clear straight section, or the region of minimum slope, where the wave showed an inflection point. In cases where the wave was heavily corrugated, an average across several corrugations was taken.

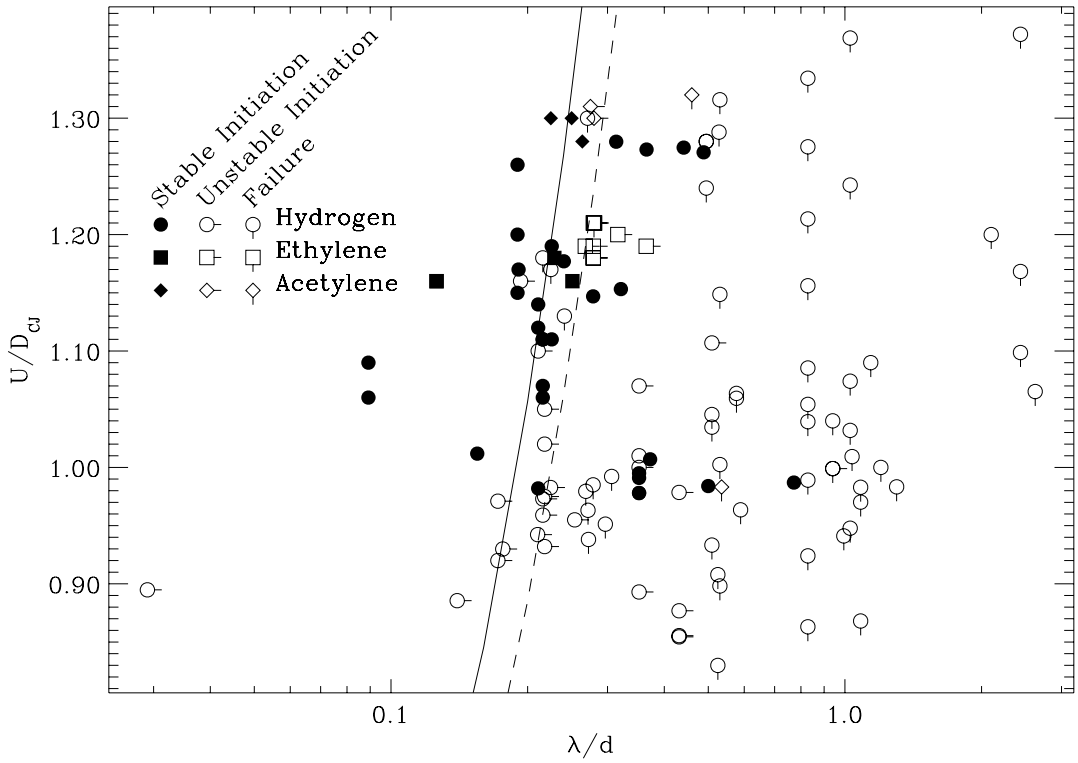

Figure 6.9: Projectile-initiated detonation transition map - sorted by fuel.

Generally, the angles measured from ICCD images are slightly larger than those measured from film images. This is explained by two effects. First, the ICCD camera was not aligned perpendicular to the axis of flight, because it would have interfered with the shadowgraph laser beam, which was aligned perpendicular to the flight axis. The obliqueness of the ICCD camera was about 9.5°. An angle, such as that of a conical wave on a projectile, that is in the vertical plane parallel to the flight axis, would appear larger when viewed obliquely. The second reason is that when viewed at an angle, less of the outer part of the bow wave is visible, and the inner part, which usually has a larger angle, is more prominent.

Table 6.1 shows that in most cases, the β_{CJ} angles, though slightly larger, agree well with the measured angles. Measured angles larger than β_{CJ} indicate that the wave was overdriven, while smaller angles indicate a velocity deficit. Either case can also be caused by unsteadiness of the flow.

Note that the CJ wave angle is very sensitive to the projectile speed and CJ speed. For instance, shots 1023 and 1813 used the same mixture and pressure, and had very similar projectile velocities: 2300 m/s and 2350 m/s. This difference is enough to change the CJ angle from 60° to 62.8°, well within the measurement uncertainty.

Table 6.1: Wave angles comparison.

Shot Number	β (deg)	β_{ICCD} (deg)	β_{CJ} (deg)	λ mm
1018	50.0		55.9	4.84
1020	62.5		56.7	5.73
1023	55.0		60.5	5.36
1812	59.8	62.5	60.4	4.84
1813	56.5	59.3	62.8	5.36
1815	70.3	70.5	71.2	5.48
1820			59.7	4.90
1821		56.8	58.4	4.85
1822	51.0	51.8	58.1	5.81
1825		63.5	59.9	3.21
1826		63.5	59.9	3.21
1830	52.5	50.5	59.5	6.38
1835		46.8	50.5	5.71
1838	45.4	46.5	50.4	6.34
1839		50.5	51.5	6.69

6.4 Stabilized Delayed Initiation

Not all stabilized detonations were initiated and maintained at the nose of the projectile. Two kinds of stabilized delayed initiation were observed. In the first, and less common type, the detonation was stabilized adjacent to or immediately behind the projectile, and had a curved shape that satisfied boundary conditions on the bow shock and at the wall. The second type involved a normal detonation far behind the projectile, stabilized in the vicinity of the reflection of the bow shock from the walls. Both types may be related to reflection of the bow shock from the test section walls.

Delayed initiation has also been reported by Chernyi and Chernyavskii [23] and Endo et al. [36] (see Chapter 2). Chernyi and Chernyavskii [23] observed pulsating shock-induced combustion around the projectile, which transitioned to an oblique detonation immediately behind the projectile. The projectile was a spherically blunt 12.7-mm diameter cylinder travelling at 2890 m/s in $2H_2$+O_2 at 186 torr (24.8 kPa) initial pressure. Endo et al. [36] observed a similar configuration on a 45° conical, 10-mm diameter projectile travelling at 2860 m/s in $2H_2$+O_2 at 0.33 atm (33.4 kPa). In both cases, the photographic records were unclear and difficult to interpret. Higgins [51] reported observing delayed initiation in wall pressure records, but the specific interpretation or further analysis of those results is even more tenuous without flow visualization. In particular, the events observed by Higgins [51] were inherently unsteady, whereas the phenomena reported by Chernyi and Chernyavskii [23] and Endo et al. [36] appeared to be steady.

The near-field initiation was observed in shot 1820 (Fig. B.59, $2H_2$+O_2+$3.76N_2$ at 2.000 bar) and shot 1832 (Fig. B.67, C_2H_4+$3O_2$+$4.3N_2$ at 0.350 bar). Possibly, the detonations were originally initiated by the bow shock wall reflection, and propagated forward along the bow wave until some

type of equilibrium was reached. This equilibrium could stem from the curvature of the detonation front. The overdriven parts of the wave are influenced by expansions from behind, while satisfying the boundary condition at the wall and continuity along the wave. The intersection with the bow wave provides another boundary condition for the detonation.

The wall-reflection initiation was observed in a number of C_2H_4 tests. This phenomena was observed in the basic C_2H_4+$3O_2$+$5N_2$ mixture at pressures of 0.300-0.400 bar, and in C_2H_4+$3O_2$+-$5.5N_2$ at 0.450 bar. The initiation of detonations at the wall is not surprising, but stability of normal detonations at the wall-reflection position is interesting. At least it indicates the importance of flow visualization for interpretation of results, since in most cases the wall pressure records do not suggest the observed phenomena.

In a steady flow, analysis of detonation initiation is usually approached with the assumption that the normal portion of the bow wave represents an overdriven detonation. Initiation of the fully stabilized detonation occurs if the wave decays to the CJ state without quenching. Thus, the possibility of a quenched wave re-initiating downstream, in a steady flow, is not considered. Indeed, since the quenched wave would tend to decay monotonically downstream, re-initiation would seem to be unlikely. Also, it is unclear if a detonation initiated behind the projectile would be stable there. The detonation would presumably propagate along the bow shock in the direction of the gradient of shock strength, that is, toward the nose. Any mechanism retarding upstream propagation of the detonation would have to be related to the flow away from the shock, for instance in the recirculation zone behind the projectile.

An analogous flow that does exhibit this delayed-onset behavior is blast initiation. Numerical simulations of spherical blast waves in detonating gases have been observed to decay to a velocity below the CJ speed for a period of time before re-accelerating and eventually acquiring a constant CJ velocity [34]. Similar behavior has been observed experimentally with detonation transition from a tube to an unconfined space (critical tube experiments) [33]. To the extent that cylindrical blast-initiated detonations are expected to behave similarly, and to the extent that projectile initiation is similar to cylindrical blast initiation (see Chapter 3), delayed onset is not surprising in projectile initiation.

Chapter 7 Conclusions and Recommendations

7.1 Conclusions

Initiation and stabilization of detonations by projectiles was demonstrated in mixtures of hydrogen-oxygen-nitrogen, ethylene-oxygen-nitrogen, and acetylene-oxygen-nitrogen. Although projectile-initiated and stabilized detonations have been observed previously, the present results are unique in several ways. For the first time, initiation and stabilization have been observed with fuels other than hydrogen. While previous researchers have presented either photographic or wall-pressure data, the current study has generated both, including natural fluorescence images. Interaction of the shock and detonation waves with the walls of the containment vessel, acknowledged to be an important factor in initiating detonations, have been observed directly, photographically. Previously unreported phenomena were observed, namely wall-reflection stabilized normal detonations.

Initiation and failure of hydrogen-air segregate strongly with variation of initial pressure, but not in terms of normalized cell width (λ/d) or reaction zone thickness. Since these length scales are taken to be unique functions of the initial pressure for a particular mixture, this effect is entirely due to the non-monotonic variation of reaction length scale with pressure. It is unclear if this indicates that these length scales are the wrong parameters for determining initiation and failure, or if the separation by pressure is accidental.

The Lee-Vasiliev model presents a reasonable approach to estimating the scales responsible for initiation and failure. However, the simplifications, approximations, and reliance on unproven sub-models inherent in it are significant compared to the sensitivity of the initiation phenomena to real effects such as initial and boundary conditions.

As noted by previous researchers, initiation is sensitive to confinement and other effects of non-ideal test conditions. Results are seen to vary even at apparently constant test conditions. Some evidence suggests that under some conditions that may lead to failure in a truly unconfined space may lead to initiation in a large but finite containment vessel. If this is true, confinement issues are essential to the definition of the problem, and not an experimental effect that can be eliminated. Furthermore, practical applications of the models applied to this problem almost always require consideration of confinement, and the models must therefore handle confinement accurately.

The shock curvature approach to analyzing detonation failure on projectiles travelling at super-CJ speeds illustrates the important physical effects, and shows promise as a predictive tool. Shock curvature can strongly affect the reaction zone, causing it to quench before the detonation can

stabilize at the CJ angle. Some preliminary results of this analysis show agreement with experimental observations with hydrogen-air, but not with the ethylene and acetylene mixtures studied.

7.2 Recommendations

7.2.1 Further Experiments

A number of variations and extensions to the experimental program would be useful for dispelling some questions about the data and providing support for modeling efforts.

Wider ranges of test conditions would permit more robust testing of proposed models and theories. Particularly, projectile speeds significantly faster than the CJ speed would allow investigation of more firmly stabilized detonations and steeper oblique detonations.

To achieve higher speeds, improvements could be made to the launcher. The technique used to launch projectiles in T5 was very inefficient. Performance could be improved significantly by using an isentropic compression process instead of the shock compression achieved in the T5 shock tube. This complicates the design and operation somewhat because either a strong diaphragm or a fast-acting valve would be needed at the projectile station to isolate it from the second stage until the desired pressure is reached.

Future projectiles should be fabricated from Lexan instead of nylon, since additional tests have found Lexan to be more durable under the conditions experienced by the projectile.

Additional diagnostics could illuminate some of the more interesting aspects of the experiments that can only be indirectly surmised at present. For instance, use of a high-speed framing camera or multi-frame electronic camera would allow direct observation of transient phenomena or verify that the observed phenomena are steady. Planar laser-induced fluorescence or similar flow visualization techniques would precisely identify reaction zones in the flow. Data of this sort would be especially useful for validating detailed models.

Variation of the projectile shape and size would introduce another means of exploring new phenomena. Changing the projectile size would offer valuable corroborating evidence for global scaling relationships that were explored only by varying the inherent mixture length scales so far. Conical and flat-nosed projectiles have been used by previous researchers, providing established data for comparison. Likewise, blunt projectiles with different nose profiles could offer useful data for comparison with models based on the nose curvature.

7.2.2 Extensions to Theory

The two main theoretical approaches to describing and predicting detonation initiation by projectiles could both benefit from further development.

The primary shortcoming of the Lee-Vasiliev model is the assumed critical energy model. All current critical energy models include some arbitrary factors that are used to fit experimental data. While this approach has been marginally successful with spherical critical energy, very little data are available for the cylindrical case, and the models are therefore much less certain. As further experiments and analysis lead to greater understanding of critical energy phenomena, the uncertainty in the Lee-Vasiljev model will decrease.

In contrast, most aspects of the shock-curvature model have been developed already. Further deveopment can be achieved through further implementation of the existing concepts and use of modern computational methods and chemical kinetics data. For application to specific conditions, coupling to a numerical solution is necessary. Another avenue for investigation is the issue of uniqueness. The shock-curvature model predicts failure of the detonation as a result of shock curvature, where the shock shape is determined assuming a particular (e.g., hyperbolic) type of wave. If this assumption is relaxed, the solution method may lead to non-unique results, in which case the boundary conditions may become increasingly important.

Bibliography

[1] S. Abid, G. Dupre, and C. Paillard. Oxidation of gaseous unsymmetrical dimethylhydrazine at high temperatures and detonation of UDMH/O_2 mixtures. In *Dynamic Aspects of Detonations*, volume 153 of *Progress in Astronautics and Aeronautics*, pages 162–181. AIAA, 1991. Technical Papers from the Thirteenth International Colloquium on Dynamics of Explosions and Reactive Systems, Nagoya, Japan.

[2] J.K. Ahuja, A. Kumar, D.J. Singh, and S.N. Tiwari. Simulation of shock-induced combustion past blunt projectiles using shock-fitting technique. *Journal of Propulsion and Power*, 12(3): 518–526, 1996.

[3] Raza Akbar. *Mach Reflection of Gaseous Detonations.* PhD thesis, Rensselaer Polytechnic Institute, 1997.

[4] R.L. Alpert and T.Y. Toong. Periodicity in exothermic hypersonic flows about blunt projectiles. *Astronautica Acta*, 17:539–560, 1972.

[5] J.D. Anderson. *Hypersonic and High Temperature Gas Dynamics.* McGraw-Hill, Inc., New York, 1989.

[6] H.O. Barthel. Predicted spacings in hydrogen-oxygen-argon detonations. *Physics of Fluids*, 17(8):1547–1553, 1974.

[7] J.B. Bdzil, T.D. Aslam, and D.S. Stewart. Curved detonation fronts in solid explosives: collisions and boundary interactions. In *Proceedings of the 20th International Symposium on Shock Waves*, volume 1, pages 97–106, 1995.

[8] J.W. Beams. Shadow and schlieren methods. In *Physical Measurements in Gas Dynamics and Combustion*, volume IX of *High Speed Aerodynamics and Jet Propulsion*, pages 26–46. Princeton University Press, 1954.

[9] H. Behrens, H. Lehr, W. Struth, and F. Wecken. Shock-induced combustion by high speed shots in explosive gas mixtures. In *New Experimental Techniques in Propulsion and Energetics Research*, number 38 in AGARD Conference Proceedings, pages 151–163, Munich, 1970.

[10] H. Behrens, W. Struth, and F. Wecken. Studies of hypervelocity firings into mixtures of hydrogen with air or with oxygen. In *10th Symposium (International) on Combustion*, pages 245–252, Cambridge, England, 1964.

[11] J. Bélanger, M. Kaneshige, and J.E. Shepherd. Detonation initiation by hypervelocity projectiles. In *Proceedings of the 20th International Symposium on Shock Waves*, volume 2, pages 1119–1124, Pasadena, California, 1995. World Scientific.

[12] W.B. Benedick. Review of large scale fuel-air explosion tests and techniques. In J.H.S. Lee and C.M. Guirao, editors, *Fuel-Air Explosions*, pages 507–552. University of Waterloo Press, 1982.

[13] Robert E. Berggren and Robert M. Reynolds. The light-gas-gun model launcher. In T.N. Canning, A. Seiff, and C.S. James, editors, *Ballistic-Range Technology*, AGARDograph AGARD-AG-138-70, chapter 2, pages 11–96. North Atlantic Treaty Organization, 1970.

[14] Lucien M. Biberman and Sol Nudelman, editors. *Photoelectronic Imaging Devices. Devices and Their Evaluation*, volume 2. Plenum Press, New York, 1971.

[15] Lucien M. Biberman and Sol Nudelman, editors. *Photoelectronic Imaging Devices. Physical Processes and Methods of Analysis*, volume 1. Plenum Press, New York, 1971.

[16] F.S. Billig. Shock-wave shapes around spherical- and cylindrical-nosed bodies. *Journal of Spacecraft and Rockets*, 4(6):822–823, 1967.

[17] D.W. Bogdanoff. Ram accelerator direct space launch system: New concepts. *Journal of Propulsion and Power*, 8(2):481–490, 1992.

[18] A.P. Bruckner. The ram accelerator: overview and state of the art. In *Ram Accelerators*, pages 3–23, 1997. Proceedings of the Third International Workshop on Ram Accelerators Held in Sendai, Japan, 16-18 July.

[19] M.W. Chase, C.A. Davies, J.R. Davies, D.J. Fulrip, R.A. McDonald, and A.N. Syverud. *JANAF Thermochemical Tables*. American Chemical Society, third edition, 1986. Journal of Physical and Chemical Reference Data, 14, Supplement 1.

[20] S.Yu. Chernyavskii, N.N. Baulin, and A.S. Mkrtumov. High-speed flow of a mixture of hydrogen and oxygen over blunt bodies. *Combustion, Explosion, and Shock Waves*, 9(6):687–690, 1973. Translated from Fizika Goreniya i Vzryva, 9(6):786–791, 1973.

[21] G.G. Chernyi. Supersonic flow around bodies with formation of detonation and deflagration fronts. *Astronautica Acta*, 13:467–480, 1968. In Russian.

[22] G.G. Chernyi. Supersonic flow past bodies with formation of detonation and combustion fronts. In *Problems of Hydrodynamics and Continuum Mechanics*, pages 145–169. Society for Industrial and Applied Mathematics, 1969.

[23] G.G. Chernyi and S.Yu. Chernyavskii. Motion of blunt bodies with high velocity in mixtures of hydrogen and oxygen. *Soviet Physics Doklady*, 18(9):596–597, 1974. Translated from Doklady Akademii Nauk SSSR 212(2):316–319, 1973.

[24] G.G. Chernyi, S.Yu. Chernyavskii, and N.N. Baulin. High-velocity motion of bodies in a hydrogen-air mixture. *Soviet Physics Doklady*, 31:706–707, 1986. Translated from Doklady Akademii Nauk SSSR 290:44-47, 1986.

[25] G.G. Chernyi and S.M. Gilinski. High speed motion of a body in chemically active gases. In W. Fiszdon, P. Kucharczyk, and W.J. Prosnak, editors, *Fluid Dynamics Transactions*, volume 4, pages 485–500, 1969.

[26] G.G. Chernyi and S.M. Gilinskii. High velocity motion of solid bodies in combustible gas mixtures. *Astronautica Acta*, 15:539–545, 1970.

[27] B. Pat Denardo. Measurements of momentum transfer from plastic projectile to massive aluminum targets at speeds up to 25,600 feet per second. Technical Note D-1210, NASA Ames Research Center, 1962.

[28] Yu.N. Denisov and Ya.K. Troshin. Structure of gaseous detonation in tubes. *Soviet Physics. Technical Physics*, 5(4):419–431, 1960.

[29] Charles E. DeRose and Peter F. Intrieri. Model and sabot design and launching techniques. In T.N. Canning, A. Seiff, and C.S. James, editors, *Ballistic-Range Technology*, AGARDograph AGARD-AG-138-70, chapter 3, pages 97–154. North Atlantic Treaty Organization, 1970.

[30] D. Desbordes. Transmission of overdriven plane detonations: Critical diameter as a function of cell regularity and size. In *Dynamics of Explosions*, volume 114 of *Progress in Astronautics and Aeronautics*, pages 170–185. AIAA, Warsaw, Poland, 1987. Technical Papers Presented from the Eleventh International Colloquium on Dynamics of Explosions and Reactive Systems.

[31] D. Desbordes. *Aspects stationnaires et transitoires de la detonation dans les gaz: relation avec la structure cellulaire du front.* PhD thesis, Universite de Poitiers, 1990.

[32] D. Desbordes, C. Guerraud, L. Hamada, and H.N. Presles. Failure of the classical dynamic parameters relationships in highly regular cellular detonation systems. In *Dynamics Aspects of Detonations*, volume 153 of *Progress in Astronautics and Aeronautics*, pages 347–359. AIAA, Nagoya, Japan, 1991. Technical Papers from the Thirteenth International Colloquium on Dynamics of Explosions and Reactive Systems.

[33] D. Desbordes and M. Vachon. Critical diameter of diffraction for strong plane detonations. In *Dynamics of Explosions*, volume 106 of *Progress in Astronautics and Aeronautics*, pages

131–143. AIAA, Berkeley, California, 1985. Technical Papers Presented from the Tenth International Colloquium on Dynamics of Explosions and Reactive Systems.

[34] C.A. Eckett, J.J. Quirk, and J.E. Shepherd. An analytical model for direct initiation of gaseous detonations. In *Proceedings of the 21st International Symposium on Shock Waves*, volume 1, pages 383–388, Great Keppel Island, Australia, 1997.

[35] C.A. Eckett, J.J. Quirk, and J.E. Shepherd. The role of unsteadiness in direct initiation of gaseous detonations. Technical Report FM97-19, GALCIT, 1997.

[36] T. Endo, J. Kasahara, A. Takeishi, and T. Fujiwara. Experiments on oblique detonation waves around hypersonic cone-nosed projectiles. Presented at the 16th International Colloquium on the Dynamics of Explosions and Reactive Systems, Cracow, Poland, 1997.

[37] Wildon Fickett and William C. Davis. *Detonation*. University of California Press, 1979.

[38] David A. Frank-Kamenetskii. *Diffusion and Heat Transfer in Chemical Kinetics*. Plenum Press, 2nd edition, 1969. Translated from Russian.

[39] M. Frenklach, H. Wang, C.T. Bowman, R.K. Hanson, G.P. Smith, D.M. Golden, W.C. Gardiner, and V. Lissianski. An optimized kinetics model for natural gas combustion. Technical report, Gas Research Institute, 1995. For more information, see HTTP://www.gri.org.

[40] S.M. Gilinskii. Combustible mixture flow ahead of a blunt body. *Fluid Dynamics*, 3(2):47–51, 1968. Translated from Izvestiia Akademii Nauk SSSR. Mekhanika Zhidkosti i Gaza, 3(2):75–81.

[41] S.M. Gilinskii. Calculation of hydrogen-air combustion behind detached shock wave for supersonic flow past a sphere. *Fluid Dynamics*, 4(4):60–66, 1969. Translated from Izvestiia Akademii Nauk SSSR, Mekhanika Zhidkosti i Gaza, 4(4):97–106.

[42] S.M. Gilinskii and G.G. Chernyi. Supersonic flow of combustible gas mixture past sphere with account for ignition delay time. *Fluid Dynamics*, 3(1):12–19, 1968. Translated from Izvestiia Akademii Nauk SSSR. Mekhanika Zhidkosti i Gaza, 3(1):20–32.

[43] S.M. Gilinskii and Z.D. Zapryanov. Transition of supersonic flow of combustible gas mixture to the Chapman-Jouguet regime. *Fluid Dynamics*, 2(3):90–92, 1967. Translated from Izvestiia Akademii Nauk SSSR. Mekhanika Zhidkosti i Gaza, 2(3):137–140.

[44] S.M. Gilinskii, Z.D. Zapryanov, and G.G. Chernyi. Supersonic flow of a combustible gas mixture past a sphere. *Fluid Dynamics*, 1(5):4–8, 1966. Translated from Izvestiia Akademii Nauk SSSR. Mekhanika Zhidkosti i Gaza, 1(5):8–13.

[45] R.A. Gross and W. Chinitz. A study of supersonic combustion. *Journal of the Aerospace Sciences*, 27(7):517–524, 1960.

[46] Ronald K. Hanson, Jerry M. Seitzman, and Phillip H. Paul. Planar laser-fluorescence imaging of combustion gases. *Applied Physics B: Photo-physics and Laser Chemistry*, 50:441–454, 1990.

[47] Wallace D. Hayes and Ronald F. Probstein. *Hypersonic Flow Theory.* Academic Press, 1959.

[48] A. Hertzberg, A.P. Bruckner, and D.W. Bogdanoff. Ram accelerator: A new chemical method for accelerating projectiles to ultrahigh velocities. *AIAA Journal*, 26(2):195–203, 1988.

[49] A. Hertzberg, A.P. Bruckner, and C. Knowlen. Experimental investigation of ram accelerator propulsion modes. *Shock Waves*, 1:17–25, 1991.

[50] A. Hertzberg, E.A. Burnham, and J.B. Hinkey. Recent advances in ram accelerator technology. In *Combustion in High-Speed Flows*, pages 309–344. Kluwer Academic Publishers, 1994.

[51] A.J. Higgins. *Investigation of Detonation Initiation by Supersonic Blunt Bodies.* PhD thesis, University of Washington, 1996.

[52] A.J. Higgins. The effect of confinement on detonation initiation by blunt projectiles. In *33rd AIAA/ASME/SAE/ASEE Joint Propulsion Conference and Exhibit*, number AIAA-97-3179, Seattle, WA, 1997.

[53] A.J. Higgins and A.P. Bruckner. Detonation initiation by supersonic blunt bodies. In *15th International Colloquium on the Dynamics of Explosions and Reactive Systems*, 1995.

[54] A.J. Higgins and A.P. Bruckner. Experimental investigation of detonation initiation by hypervelocity blunt projectiles. In *34th Aerospace Sciences Meeting and Exhibit*, number AIAA-96-0342, Reno, NV, 1996.

[55] A.J. Higgins, M.I. Radulescu, and J.H.S. Lee. Initiation of cylindrical detonation by rapid energy deposition along a line. In *Proceedings of the 27th Symposium (International) on Combustion*, Boulder, Colorado, 1998. In Press.

[56] T. Horii, J. Kasahara, T. Endo, and T. Fujiwara. Experimental studies on supersonic combustion phenomena of CO-O_2-H_2 premixed gases around hypersonic projectiles. *JSME International Journal. Series B, Fluids and Thermal Engineering*, 41(2):316–321, 1998. Translated from Jpn. Soc. Mech Eng. B 63(607):917–924, 1997.

[57] H. Hornung. Performance data of the new free-piston shock tunnel at GALCIT. In *AIAA 17th Aerospace Ground Testing Conference*, Nashville, 1992.

[58] H.G. Hornung. Some aspects of hypersonic flow over power law bodies. *Journal of Fluid Mechanics*, 30:143–162, 1969.

[59] H.G. Hornung. Non-equilibrium ideal-gas dissociation after a curved shock wave. *Journal of Fluid Mechanics*, 74:143–159, 1976.

[60] H.G. Hornung. Gradients at a curved shock in reacting flow. *Shock Waves*, 8:11–21, 1998.

[61] Y. Ju and A. Sasoh. Numerical study of detonation initiation by a supersonic sphere. *Transactions of the Japan Society for Aeronautical and Space Sciences*, 40(127):19–29, 1997.

[62] M.R. Kamel, C.I. Morris, M.C. Thurber, S.D. Wehe, and R.K. Hanson. Use of an expansion tube for imaging studies of hypersonic reactive flows around blunt bodies. In *Proceedings of the 20th International Symposium on Shock Waves*, volume 1, pages 275–280, Pasadena, 1996. World Scientific.

[63] M.J. Kaneshige and H.G. Hornung. Corrigendum: Gradients at a curved shock in reacting flow. *Shock Waves*, 1999. Correction to Hornung [60] to be published.

[64] M.J. Kaneshige and J.E. Shepherd. Oblique detonation stabilized on a hypervelocity projectile. In *26th Symposium (International) on Combustion*, pages 3015–3022, Naples, Italy, 1996.

[65] J. Kasahara, T. Horii, T. Endo, and T. Fujiwara. Experimental observation of unsteady H_2-O_2 combustion phenomena around hypersonic projectiles using a multiframe camera. In *26th Symposium (International) on Combustion*, pages 2903–2908, Naples, Italy, 1996.

[66] J. Kasahara, A. Takeishi, H. Kuroda, M. Horiba, K. Matsukawa, J.E. Leblanc, T. Endo, and T. Fujiwara. Experimental observation of oblique detonation waves around hypersonic free projectiles. In *Ram Accelerators*, pages 263–270, 1997. Proceedings of the Third International Workshop on Ram Accelerators Held in Sendai, Japan, 16-18 July.

[67] R. Knystautas, J.H. Lee, and C.M. Guirao. The critical tube diameter for detonation failure in hydrocarbon-air mixtures. *Combustion and Flame*, 48(1):63–83, 1982.

[68] D.L. Kruczynski, F. Liberatore, and M.J. Nusca. Experimental flow visualization for a large-scale ram accelerator. *Journal of Propulsion and Power*, 12(1):206–210, 1996.

[69] D.L. Kruczynski and D.M. Verbus. Continued experiments with high performance ram acceleration. In *33rd AIAA/ASME/SAE/ASEE Joint Propulsion Conference and Exhibit*, number AIAA-97-2651, Seattle, WA, 1997.

[70] George Kychakoff, Robert D. Howe, and Ronald K. Hanson. Quantitative flow visualization technique for measurements in combustion gases. *Applied Optics*, 23(5):704–712, 1984.

[71] S. Laberge, R. Knystautas, and J.H.S. Lee. Propagation and extinction of detonation waves in tube bundles. In *Dynamic Aspects of Detonations*, volume 153 of *Progress in Astronautics and Aeronautics*, pages 381–396. AIAA, 1991. Technical Papers from the Thirteenth International Colloquium on Dynamics of Explosions and Reactive Systems, Nagoya, Japan.

[72] J.H. Lee. Initiation of gaseous detonation. *Annual Review of Physical Chemistry*, 28:75–104, 1977.

[73] J.H.S. Lee. Dynamic parameters of gaseous detonations. *Annual Review of Fluid Mechanics*, 16:311–336, 1984.

[74] J.H.S. Lee. Initiation of detonation by a hypervelocity projectile. In *Advances in Combustion Science: in honor of Ya. B. Zel'dovich*, volume 173 of *Progress in Astronautics and Aeronautics*, chapter 18, pages 293–310. AIAA, Reston, Virginia, 1997.

[75] J.H.S. Lee, R. Knystautas, and C. Guirao. The link between cell size, critical tube diameter, initiation energy and detonability limits. In *Fuel-Air Explosions*, pages 157–187. University of Waterloo Press, 1982.

[76] M.H. Lefebvre and T. Fujiwara. Numerical modeling of combustion processes induced by a supersonic conical blunt body. *Combustion and Flame*, 100:85–93, 1995.

[77] Hartmuth F. Lehr. *Experimente zur stossinduzierten Verbrennung in Wasserstoff / Luft- und Wasserstoff / Sauerstoff- Gemischen*. Doktor-ingenieurs, Universität Karlsruhe, 1971. English Title: Experiments on shock-induced combustion in hydrogen / air and hydrogen / oxygen mixtures.

[78] H.F. Lehr. Experiments on shock-induced combustion. *Astronautica Acta*, 17:589–597, 1972.

[79] V.A. Levin. Transition of plane overdriven detonation wave to the chapman-jouguet regime. *Fluid Dynamics*, 3(2):31–34, 1968. Translated from Izvestiia Akademii Nauk SSSR. Mekhanika Zhidkosti i Gaza, 3(2):50–55.

[80] Bernard Lewis and Guenther von Elbe. *Combustion, Flames, and Explosions of Gases*. Academic Press, New York, 2nd edition, 1961.

[81] A.E. Lutz. A numerical study of thermal ignition. Technical Report SAND88-8228, Sandia National Laboratories, 1988.

[82] A.E. Lutz, R.J. Kee, J.A. Miller, H.A. Dwyer, and A.K. Oppenheim. Dynamic effects of autoignition centers for hydrogen and $C_{1,2}$-hydrocarbon fuels. In *22nd Symposium (International) on Combustion*, pages 1683–1693, 1988.

[83] V.I. Manzhalei, V.V. Mitrofanov, and V.A. Subbotin. Measurement of inhomogeneities of a detonation front in gas mixtures at elevated pressures. *Combustion, Explosion, and Shock Waves (USSR)*, 10(1):89–95, 1974.

[84] A. Matsuo and K. Fujii. Computational study of large-disturbance oscillations in unsteady supersonic combustion around projectiles. *AIAA Journal*, 33(10):1828–1835, 1995.

[85] A. Matsuo and K. Fujii. Flow features of shock-induced combustion around projectile traveling at hypervelocities. *AIAA Journal*, 33(6):1056–1063, 1995.

[86] J.B. McVey and T.Y. Toong. Mechanism of instabilities of exothermic hypersonic blunt-body flows. *Combustion Science and Technology*, 3:63–76, 1971.

[87] Wolfgang Merzkirch. *Flow Visualization*. Academic Press, Inc. Harcourt Brace Jovanovich, Publishers, Orlano, 2nd edition, 1987.

[88] J.A. Miller, R.E. Mitchell, M.D. Smooke, and R.J. Kee. Toward a comprehensive chemical kinetic mechanism for the oxidation of acetylene: Comparison of model predictions with results from flame and shock tube experiments. In *19th Symposium (International) on Combustion*, pages 181–196, 1982.

[89] C.I. Morris, M.R. Kamel, and R.K. Hanson. PLIF and schlieren imaging of oblique detonation waves. In *Proceedings of the 21st International Symposium on Shock Waves*, Great Keppel Island, Australia, 1997.

[90] S.B. Murray and J.H. Lee. The influence of physical boundaries on gaseous detonation waves. In *Dynamics of Explosions*, volume 106 of *Progress in Astronautics and Aeronautics*, pages 329–355, Berkeley, California, 1985. AIAA. Technical Papers Presented from the Tenth International Colloquium on Dynamics of Explosions and Reactive Systems.

[91] A technique for studying supersonic combustion in the vicinity of a hypersonic missile. *Technical News Bulletin of the National Bureau of Standards*, 44(11):181–182, 1960.

[92] D.T. Pratt, J.W. Humphrey, and D.E. Glenn. Morphology of standing oblique detonation waves. *Journal of Propulsion*, 7(5):837–845, 1991.

[93] J.J. Quirk. Godunov-type schemes applied to detonation flows. In *Combustion in High-Speed Flows*, pages 575–596. Kluwer Academic Publishers, 1994.

[94] W.C. Reynolds. The element potential method for chemical equilibrium analysis: Implementation in the interactive program STANJAN. Technical report, Department of Mechanical Engineering, Stanford University, 1986.

[95] J. Rom. Analysis of detonation on a hypervelocity projectile in the in-tube chemical accelerator. In *Proceedings of the 20th International Symposium on Shock Waves*, volume 2, pages 1149–1154, Pasadena, California, 1995. World Scientific.

[96] J. Rom. Performance limits for projectile flight in the ram and external propulsion accelerators. *Journal of Propulsion and Power*, 13(5):583–591, 1997.

[97] Albert Rose. *Vision: Human and Electronic*. Plenum Press, New York, 1973.

[98] F.W. Ruegg and W.W. Dorsey. A missile technique for the study of detonation waves. *Journal of Research of the National Bureau of Standards - C. Engineering and Instrumentation*, 66C (1):51–58, 1962.

[99] F.W. Ruegg and W.W. Dorsey. Untitled discussion. In *9th Symposium (International) on Combustion*, pages 476–477, 1963.

[100] Leonid I. Sedov. *Similarity and Dimensional Methods in Mechanics*. Academic Press, New York, 1959. Translated from Russian.

[101] F. Seiler, G. Patz, G. Smeets, and J. Srulijes. Gasdynamic limits of ignition and combustion of a gas mixture in ISL's RAMAC 30 scram accelerator. In *Proceedings of the 20th International Symposium on Shock Waves*, volume 2, pages 1057–1062, Pasadena, CA, 1995. World Scientific.

[102] J.E. Shepherd. Pressure loads and structural response of the BNL high-temperature detonation tube. Technical Report A-3991, Brookhaven National Laboratory, 1992.

[103] J.E. Shepherd. Detonation waves and propulsion. In *Combustion in High-Speed Flows*, pages 373–421. Kluwer Academic Publishers, 1994.

[104] Harold V. Soule and Alexander P. Sabol. Development and preliminary investigation of a method of obtaining hypersonic aerodynamic data by firing models through highly cooled gases. Technical Note 2120, NACA, Langley Aeronautical Laboratory, VA, 1950.

[105] J. Srulijes, G. Smeets, G. Patz, and F. Seiler. Accelerating hydrogen/air mixtures to superdetonative speeds using an expansion tube. In *RAMAC III Workshop*, Sendai, Japan, 1997.

[106] D.W. Stamps and S.R. Tieszen. The influence of initial pressure and temperature on hydrogen-air-diluent detonations. *Combustion and Flame*, 83(3):353–364, 1991.

[107] D.S. Stewart, T.D. Aslam, and J. Yao. On the evolution of cellular detonation. In *26th Symposium (International) on Combustion*, pages 2981–2989, Naples, Italy, 1996.

[108] R.A. Strehlow. Transverse waves in detonations: II. structure and spacing in H_2-O_2, C_2H_2-O_2, C_2H_4-O_2 and CH_4-O_2 systems. *AIAA Journal*, 7(3):492–496, 1969.

[109] Roger A. Strehlow. *Combustion Fundamentals*. McGraw-Hill, 1984.

[110] W. Struth. Kurzzeitaufnahmen von schüssen mit hyperschallgeschwindigkeit in reagierende gase. In *Proceedings of the Sixth International Congress on High-Speed Photography*, pages 443–449, The Hague / Scheveningen (Netherlands), 1962. English title: High Speed Photographs of Shots at Hypersonic Velocity in Reacting Gases.

[111] G.I. Taylor. The formation of a blast wave by a very intense explosion. *Proceedings of the Royal Society of London. Series A: Mathematical and Physical Sciences*, 201:159–174, 1950.

[112] P.A. Thibault, J.D. Penrose, A. Sulmistras, S.B. Murray, and J.L.D.S. Labbé. Studies on detonation driven hollow projectiles. In J. Buckmaster, T.L. Jackson, and A. Kumar, editors, *Combustion in High-Speed Flows*, pages 421–443. Kluwer Academic Publishers, 1994.

[113] Philip A. Thompson. *Compressible-Fluid Dynamics*. McGraw-Hill, 1972.

[114] N.A. Tonello, M. Sichel, and C.W. Kauffman. Mechanisms of detonation transmission in layered H_2-O_2 mixtures. *Shock Waves*, 5:225–238, 1995.

[115] Tau-Yi Toong. Instabilities in reacting flows. *Acta Astronautica*, 1(3-4):317–344, 1974.

[116] Tau-Yi Toong. *Combustion Dynamics: the Dynamics of Chemically Reacting Fluids*. McGraw-Hill, New York, 1983.

[117] A.A. Vasil'ev, B.I. Kulakov, V.V. Mitrofanov, V.V. Sil'vestrov, and V.M. Titov. Initiation of explosive gaseous mixtures by a rapidly moving body. *Physics - Doklady*, 39(9):653–654, 1994. Translated from Doklady Akademii Nauk, 338(2):188–190.

[118] A.A. Vasiljev. Initiation of gaseous detonation by a high speed body. *Shock Waves*, 3:321–326, 1994.

[119] C. Viguier, L.F. Figueira Da Silva, D. Desbordes, and B. Deshaies. Onset of oblique detonation waves: Comparison between experimental and numerical results for hydrogen-air mixtures. In *26th Symposium (International) on Combustion*, pages 3023–3031, Naples, Italy, 1996.

[120] B.V. Voitsekhovskii, V.V. Mitrofanov, and M.E. Topchian. The structure of a detonation front in gases. Technical Report FTD-MT-64-527 (AD 633821), Wright-Patterson AFB, 1966.

[121] H.Gg. Wagner. Gaseous detonations and the structure of a detonation wave. In A. Ferri, editor, *Fundamental data obtained from shock tube experiments*, number 41 in AGARDograph AGARD-AG-41-61, pages 320–385. Advisory Group for Aeronatical Research and Development, North Atlantic Treaty Organization, 1961.

[122] J. Yao and D.S. Stewart. On the normal detonation shock velocity-curvature relationship for materials with large activation energy. *Combustion and Flame*, 100:519–528, 1995.

[123] S. Yungster, S. Eberhardt, and A.P. Bruckner. Numerical simulation of hypervelocity projectiles in detonable gases. *AIAA Journal*, 29(2):187–199, 1991.

[124] J. Zeldovich and O. Leipunsky. A study of chemical reactions in shock waves - theory of the method and results of preliminary experiments. *Acta Physicochimica URSS*, 18(2-3):167–171, 1943.

[125] R. Zitoun, D. Desbordes, C. Guerraud, and B. Deshaies. Direct initiation of detonation in cryogenic gaseous H_2-O_2 mixtures. *Shock Waves*, 4(6):331–337, 1995.

Appendix A Experimental Conditions

A.1 Test Section Conditions and Results

Table A.1 summarizes the conditions and results of each test. It is organized chronologically, as the tests were performed. The projectile speed was computed from the best data available in each case, i.e., the arrival times with the greatest spatial separation. Usually these were one of the dump tank triggers and the imaging station. The Mach number, Ma, and Chapman-Jouguet speed, D_{CJ}, were computed with STANJAN [94], as described in Chapter 4. Reaction zone thickness, Δ, was computed, also as described in Chapter 4, using the reaction mechanism of Lutz et al. [82]. Cell width, λ, was estimated from Δ using correlations with experimentally measured cell widths.

Results in parentheses were determined from pressure traces and other indirect evidence only because flow visualization results were not obtained. All other results were determined primarily from images. Descriptions and abbreviations in the results column are as follows:

shock - Bow shock with no significant effect from combustion.

shock-induced combustion (SIC) - Non-detonative bow shock with clear signs of combustion behind the shock. In some cases, the pressure traces showed a detonation develop far behind the projectile.

normal detonation (ND) - A normal detonation was observed in front of the projectile. It is described as "unsteady" if the change in the apparent wave speed, or the difference between the apparent wave speed and the projectile speed, was greater than 150 m/s.

unsteady initiation - A detonation was observed overtaking the projectile.

prompt initiation - Stabilized detonation with initiation taking place at the nose of the projectile.

delayed initiation (DI) - Stabilized detonation with initiation taking place behind the projectile. The delayed initiation occurred either at the wall reflection of the bow wave, or immediately behind the projectile, in the "near field."

The photographic and pressure data in Appendix B are referenced by Figure number in the last column.

Table A.1: Summary of test section conditions and results.

Shot	Speed (m/s)	Ma	Δ (mm)	λ (mm)	D_{CJ} (m/s)	Mixture	Press. (bar)	Result	Fig.
857	1110	3.19				Air	1.000	shock	
858	1790	5.06				N_2	0.250	shock	
859	2570	7.27				N_2	0.200	shock	
860	2600	7.35				N_2	0.250	shock	
861	2610	7.38				N_2	0.250	shock	B.3
862	2550	5.45	0.063	2.26	2398	$2H_2+O_2+N_2$	1.000	ND	B.25
863	2610	5.58	0.063	2.26	2398	$2H_2+O_2+N_2$	1.000	ND	B.27
864	2300	4.92	0.753	23.9	2303	$2H_2+O_2+N_2$	0.100	(SIC)	
865	2400	5.13	0.753	23.9	2303	$2H_2+O_2+N_2$	0.100	SIC	B.7
1003						N_2	1.000	shock	
1004	2370	6.70				N_2	1.000	shock	
1005	2390	6.76				N_2	0.250	shock	
1006						N_2	0.250	shock	
1007	2500	7.07				N_2	0.250	shock	
1008			0.126	4.37	2370	$2H_2+O_2+N_2$	0.500	(unsteady ND)	
1009	2180	4.66	0.126	4.37	2370	$2H_2+O_2+N_2$	0.500	unsteady ND	
1010	2300	4.92	0.126	4.37	2370	$2H_2+O_2+N_2$	0.500	unsteady ND	B.23
1011	2360	5.05	0.268	8.94	2341	$2H_2+O_2+N_2$	0.250	(unsteady ND)	
1012	2500	5.35	0.268	8.94	2341	$2H_2+O_2+N_2$	0.250	unsteady initiation	B.15
1013	2500	6.11	0.384	12.6	1952	$2H_2+O_2+3.76N_2$	0.421	SIC	
1014	2500	6.11	0.384	12.6	1952	$2H_2+O_2+3.76N_2$	0.421	(SIC)	
1015	2430	5.94	0.384	12.6	1952	$2H_2+O_2+3.76N_2$	0.421	SIC	B.43
1016	2560	6.25	0.203	6.87	1968	$2H_2+O_2+3.76N_2$	0.853	SIC	B.45
1017	2490	6.08	0.140	4.84	1982	$2H_2+O_2+3.76N_2$	1.707	(prompt initiation)	
1018	2370	5.79	0.140	4.84	1982	$2H_2+O_2+3.76N_2$	1.707	prompt initiation	B.55
1019	2210	5.40	0.168	5.73	1990	$2H_2+O_2+3.76N_2$	2.560	prompt initiation	
1020	2360	5.77	0.168	5.73	1990	$2H_2+O_2+3.76N_2$	2.560	prompt initiation	B.61
1021	2300	5.62	1.751	53.2	1918	$2H_2+O_2+3.76N_2$	0.100	shock	B.41
1022	2260	5.40	0.156	5.36	2046	$2H_2+O_2+3N_2$	0.831	SIC	B.35
1023	2330	5.57	0.156	5.36	2046	$2H_2+O_2+3N_2$	0.831	prompt initiation	B.37
1024	2400	5.50	0.160	5.48	2168	$2H_2+O_2+2N_2$	0.557	(prompt initiation)	
1025	2110	4.84	0.160	5.48	2168	$2H_2+O_2+2N_2$	0.557	(unsteady initiation)	
1026	2080	4.77	0.160	5.48	2168	$2H_2+O_2+2N_2$	0.557	(unsteady initiation)	
1027	2400	5.50	0.160	5.48	2168	$2H_2+O_2+2N_2$	0.557	(prompt initiation)	
1028	2400	5.50	0.160	5.48	2168	$2H_2+O_2+2N_2$	0.557	(prompt initiation)	
1029	2480	5.30	0.162	5.55	2360	$2H_2+O_2+N_2$	0.395	unsteady ND	
1030	2400	5.13	0.162	5.55	2360	$2H_2+O_2+N_2$	0.395	(unsteady ND)	
1031	2200	4.70	0.162	5.55	2360	$2H_2+O_2+N_2$	0.395	(unsteady ND)	
1032	2300	4.92	0.162	5.55	2360	$2H_2+O_2+N_2$	0.395	(unsteady ND)	
1800			0.268	8.94	2341	$2H_2+O_2+N_2$	0.250	(ND)	
1801	2330	4.98	0.268	8.94	2341	$2H_2+O_2+N_2$	0.250	ND	B.17
1802	2340	5.00	0.268	8.94	2341	$2H_2+O_2+N_2$	0.250	(unsteady ND)	
1803	(2090)	4.47	0.268	8.94	2341	$2H_2+O_2+N_2$	0.250	(ND)	
1804	2320	4.96	0.268	8.94	2341	$2H_2+O_2+N_2$	0.250	(ND)	
1805	2290	4.90	0.268	8.94	2341	$2H_2+O_2+N_2$	0.250	(ND)	
1806	2290	4.90	0.268	8.94	2341	$2H_2+O_2+N_2$	0.250	ND	B.19
1807	2230	5.45	0.180	6.13	1971	$2H_2+O_2+3.76N_2$	1.000	SIC	B.47
1808	2290	4.90	0.387	12.7	2327	$2H_2+O_2+N_2$	0.180	ND	B.13
1809	2280	4.87	0.612	19.6	2310	$2H_2+O_2+N_2$	0.120	ND	B.11
1810	2300	4.92	0.970	30.4	2294	$2H_2+O_2+N_2$	0.080	shock	B.5

Shot	Speed (m/s)	Ma	Δ (mm)	λ (mm)	D_{CJ} (m/s)	Mixture	Press. (bar)	Result	Fig.
1811	2300	4.92	0.753	23.9	2303	$2H_2+O_2+N_2$	0.100	unsteady initiation	B.9
1812	2280	5.57	0.140	4.84	1982	$2H_2+O_2+3.76N_2$	1.700	prompt initiation	B.53
1813	2300	5.50	0.156	5.36	2046	$2H_2+O_2+3N_2$	0.831	prompt initiation	B.39
1814	2320	5.32	0.160	5.48	2168	$2H_2+O_2+2N_2$	0.557	prompt initiation	B.31
1815	2290	5.25	0.160	5.48	2168	$2H_2+O_2+2N_2$	0.557	prompt initiation	B.33
1816	2330	5.69	0.160	5.48	1975	$2H_2+O_2+3.76N_2$	1.200	SIC	B.51
1817	2310	5.64	0.167	5.71	1974	$2H_2+O_2+3.76N_2$	1.120	SIC	B.49
1818	2320	4.96	0.156	5.35	2362	$2H_2+O_2+N_2$	0.410	ND	B.21
1819	2300	5.27	0.927	29.1	2113	$2H_2+O_2+2N_2$	0.110	shock	B.29
1820	2300	5.62	0.142	4.9	1985	$2H_2+O_2+3.76N_2$	2.000	DI - near field	B.59
1821	2330	5.69	0.141	4.85	1984	$2H_2+O_2+3.76N_2$	1.900	prompt initiation	B.57
1822	2350	6.88	0.368	5.81	1994	$C_2H_4+3O_2+5N_2$	0.500	prompt initiation	B.81
1823	2370	6.94	0.539	8.02	1983	$C_2H_4+3O_2+5N_2$	0.350	DI - wall reflection	B.65
1824	2340	6.85	0.466	7.09	1987	$C_2H_4+3O_2+5N_2$	0.400	DI - wall reflection	B.69
1825	2330	6.82	0.182	3.21	2016	$C_2H_4+3O_2+5N_2$	1.000	prompt initiation	B.83
1826	2330	6.82	0.182	3.21	2016	$C_2H_4+3O_2+5N_2$	1.000	prompt initiation	B.85
1827	2360	6.91	0.466	7.09	1987	$C_2H_4+3O_2+5N_2$	0.400		
1828	2350	6.88	0.466	7.09	1987	$C_2H_4+3O_2+5N_2$	0.400	DI - wall reflection	B.70
1829	2350	6.88	0.639	9.26	1978	$C_2H_4+3O_2+5N_2$	0.300	DI - wall reflection	B.63
1830	2310	6.77	0.411	6.38	1991	$C_2H_4+3O_2+5N_2$	0.450	prompt initiation	B.77
1831	2380	6.96	0.470	7.15	1972	$C_2H_4+3O_2+5.5N_2$	0.450	DI - wall reflection	B.79
1832	2400	7.05	0.444	6.81	2012	$C_2H_4+3O_2+4.3N_2$	0.350	DI - near field	B.67
1833	2400	7.02	0.467	7.1	1981	$C_2H_4+3O_2+5.2N_2$	0.420	SIC	B.74
1834	2410	7.06	0.466	7.09	1987	$C_2H_4+3O_2+5N_2$	0.400	DI - wall reflection	B.73
1835	2420	6.98	0.074	5.71	1867	$C_2H_2+2.5O_2+9.4N_2$	1.000	prompt initiation	B.97
1836	2440	7.03	0.140	11.7	1850	$C_2H_2+2.5O_2+9.4N_2$	0.500	SIC	B.87
1837	2420	6.98	0.090	7.12	1861	$C_2H_2+2.5O_2+9.4N_2$	0.800	DI - wall reflection	B.88
1838	2420	6.98	0.081	6.34	1864	$C_2H_2+2.5O_2+9.4N_2$	0.900	prompt initiation	B.95
1839	2380	6.86	0.085	6.69	1863	$C_2H_2+2.5O_2+9.4N_2$	0.850	prompt initiation	B.93
1840	2430	7.00	0.088	6.98	1862	$C_2H_2+2.5O_2+9.4N_2$	0.820	DI - wall reflection	B.91

A.2 T5 Run Conditions

Table A.2 lists T5 run parameters used for the experiments, chronologically, in the order the experiments were performed. DT1 and DT2 are the total and remaining thickness of the indented stainless steel diaphragm. ST gas is the gas used in the shock tube, helium in all cases except shot 857. P_{ST} and P_{CT} are the initial gas pressures in the shock tube and compression tube, respectively. % He is the fraction of helium used in the compression tube, the balance being Ar. P_{2R} is the air pressure in the secondary reservoir. Values reported for P_4 and P_0 represent averages of the outputs of the two transducers where both signals were usable, and a single transducer otherwise. The shock velocity, V_s, is based on the transit time of the shock between shock timing stations ST3 and ST4, as is standard T5 practice. V_{proj} was determined as described in Appendix A.1.

Table A.2: Summary of T5 conditions.

Shot	DT1 (in)	DT2 (in)	ST gas	P_{ST} (kPa)	P_{CT} (kPa)	% He	P_{2R} (psi)	P_4 (MPa)	V_S (m/s)	P_0 (MPa)	V_{proj} (m/s)
857	0.187	0.125	N_2	75	46	60	285	0.0		0.0	1110
858	0.187	0.125	He	200	70	96.3	450	31.0	3993	22.6	1790
859	0.215	0.157	He	250	73	98	600	51.5	4554	33.1	2570
860	0.215	0.167	He	250	73	97.9	575	54.5	4701	33.8	2600
861	0.215	0.167	He	200	73	97.9	575	53.1	5025	32.6	2610
862	0.215	0.167	He	200	73	97.9	575	51.4	5025	31.8	2550
863	0.215	0.167	He	200	73	97.9	575	52.5	5114	32.5	2610
864	0.215	0.167	He	200	73	97.9	575	52.5	5114	33.0	2300
865	0.215	0.167	He	200	73	97.9	575	53.5	5205	32.1	2400
1003	0.215	0.164	He	200	73	97.9	575	52.5	3658	21.1	
1004	0.215	0.164	He	200	73	97.9	575	49.5	5357	14.9	2370
1005	0.215	0.164	He	200	73	97.9	575	52.6	5263	16.8	2390
1006	0.216	0.164	He	200	73	97.9	575	48.9	5263	13.6	
1007	0.216	0.164	He	200	73	97.9	575	51.2	5405	13.8	2500
1008	0.216	0.164	He	200	73	97.9	575	50.5		14.2	
1009	0.217	0.164	He	200	73	97.9	575	50.9	5504	15.7	2180
1010	0.217	0.164	He	200	73	97.9	575	52.2	5555	14.8	2300
1011	0.217	0.164	He	200	73	97.9	575	52.0	5555	14.8	2360
1012	0.215	0.164	He	200	73	97.9	575	52.5	5807	15.2	2500
1013	0.213	0.164	He	200	73	97.9	575	51.8	5504	15.4	2500
1014	0.218	0.164	He	200	73	97.9	575	51.6	5454	16.8	2500
1015	0.218	0.164	He	200	73	97.9	575	51.3	5172	31.4	2430
1016	0.211	0.164	He	200	73	97.9	575	52.2	5405	33.8	2560
1017	0.211	0.165	He	200	73	97.9	575	51.4	5555	32.5	2490
1018	0.211	0.164	He	200	73	97.9	575	52.8	5454	33.3	2370
1019	0.213	0.164	He	225	73	100	510	48.5	5172	26.7	2210
1020	0.213	0.164	He	250	73	100	525	49.9	5172	31.4	2360
1021	0.212	0.161	He	250	73	100	525	49.8	5172	30.1	2300
1022	0.215		He	250	73	100	520	49.8	5172	30.5	2260
1023	0.215		He	250	73	100	520	50.8	5309	30.9	2340
1024	0.222		He	250	73	100	520	50.6	5263	31.4	2400
1025	0.222	0.167	He	250	73	100	520	50.1	5263	31.2	2110
1026	0.206	0.166	He	250	73	100	520	50.8	5357	31.9	2080

Shot	DT1 (in)	DT2 (in)	ST gas	P_{ST} (kPa)	P_{CT} (kPa)	% He	P_{2R} (psi)	P_4 (MPa)	V_S (m/s)	P_0 (MPa)	V_{proj} (m/s)
1027	0.206	0.162	He	250	73	100	520	53.7	5357	32.4	2400
1028	0.206	0.162	He	250	73	100	520	50.5	5263	32.0	2400
1029	0.205		He	250	73	100	520	49.8	5263	30.7	2480
1030	0.206		He	250	73	100	520	53.1	5309	32.1	2400
1031	0.205		He	250	73	100	520	53.7	5454	33.1	2200
1032	0.205		He	250	73	100	520	53.1	5454	32.5	2300
1800	0.187	0.134	He	250	73	100	520	64.1	5042	0.0	
1801	0.187	0.136	He	250	73	100	520	63.0	5217	28.8	2330
1802	0.188	0.135	He	250	73	100	520	66.0	5309	28.9	2340
1803	0.188	0.135	He	250	60	100	480	66.1	5309	27.6	(2090)
1804	0.188	0.135	He	250	60	100	480	66.0	5309	28.0	2320
1805	0.187	0.131	He	250	60	100	480	64.0	5309	27.3	2290
1806	0.188	0.135	He	250	60	100	480	68.8	5263	28.3	2290
1807	0.188	0.133	He	250	60	100	480	63.2	5263	26.8	2230
1808	0.188	0.134	He	250	60	100	480	66.7	5405	26.9	2290
1809	0.188	0.135	He	250	60	100	480	63.9	5309	27.4	2280
1810	0.188	0.134	He	250	60	100	480	62.9	5309	27.3	2300
1811	0.188	0.134	He	250	60	100	480	67.8	5357	27.6	2300
1812	0.187	0.134	He	250	60	100	480	66.9	5357	27.6	2280
1813	0.188	0.134	He	250	60	100	480	65.5	5405	27.3	2300
1814	0.188	0.137	He	250	60	100	480	65.0	5309	27.8	2320
1815	0.188	0.136	He	250	60	100	480	64.3	5405	26.5	2290
1816	0.188	0.134	He	250	60	100	480	64.8	5357	27.6	2330
1817	0.187	0.133	He	250	60	100	480	65.9	5454	27.8	2310
1818	0.187	0.135	He	250	60	100	480	64.5	5454	27.6	2320
1819	0.188	0.135	He	250	60	100	480	67.5	5454	27.7	2300
1820	0.187	0.135	He	250	60	100	480	67.5	5504	28.0	2300
1821	0.188	0.135	He	250	60	100	480	64.8	5357	28.1	2330
1822	0.188	0.135	He	250	60	100	480	63.1	5357	27.7	2350
1823	0.188	0.134	He	250	60	100	480	65.1	5405	28.1	2370
1824	0.188	0.135	He	250	60	100	480	63.5	5504	27.4	2340
1825	0.188	0.135	He	250	60	100	480	67.2	5504	27.4	2330
1826	0.189	0.136	He	250	60	100	480	63.1	5357	27.5	2330
1827	0.188	0.134	He	250	60	100	480	65.8	5405	28.4	2360
1828	0.188	0.134	He	250	60	100	480	65.8	5405	28.0	2350
1829	0.188	0.134	He	250	60	100	480	67.4	5504	27.6	2350
1830	0.188	0.134	He	250	60	100	480	63.0	5405	26.7	2310
1831	0.188	0.135	He	250	60	100	480	63.1	5405	28.1	2380
1832	0.188	0.135	He	250	60	100	480	65.2	5454	28.8	2400
1833	0.187	0.134	He	250	60	100	480	65.3	5504	28.6	2400
1834	0.188	0.132	He	250	60	100	480	65.6	5454	28.8	2410
1835	0.188	0.134	He	250	60	100	480	68.1	5504	29.4	2420
1836	0.188	0.135	He	250	60	100	480	67.5	5504	29.9	2440
1837	0.188	0.135	He	250	60	100	480	66.0	5405	30.1	2420
1838	0.188	0.135	He	250	60	100	480	66.2	5504	29.9	2420
1839	0.187	0.135	He	250	60	100	480	62.3	5504	28.8	2380
1840	0.188	0.135	He	250	60	100	480	64.9	5555	29.9	2430

Appendix B Raw Data

This appendix contains raw data in the form of photographs, time history plots, and tabulated arrival times. A summary of the conditions and results of each test is given in Appendix A. All of the useful image data (differential interferogram, shadowgraph, and intensified CCD) are presented here. Although pressure signals were recorded for almost all shots, only those corresponding to useful images are included. Except for a few examples, other recorded time history data that contain essentially a single piece of information (i.e., time of arrival) are not presented, but are summarized in Tables B.1 and B.2. The nomenclature used to identify stations and signals is explained in Section 5.4.1.

B.1 Example Plots

Fig. B.1 shows examples of P_{exit} pressure transducer and CH2 laser trigger plots from two shots. These plots are fairly typical, for shots in which they were recorded (most of series III), and show several important features. The launch tube exit pressure transducer (P_{exit}) was used as the primary trigger source after a laser trigger at the launch tube exit was found to be useless. The precursor waves visible on the P_{exit} signals starting at around -1.6 ms correspond to the reflection of the shock wave from the end of the T5 shock tube, delayed by the time of propagation of sound waves along the steel launch tube. The beginning of these precursor waves also correspond to the time at which false triggers were generated by the original laser detector, suggesting that the laser triggers were sensitive to stress waves. The exit pressure transducer generated a reliable trigger, but direct exposure to the launch tube exit subjected it to high heat flux loads. To protect the transducer and reduce the effect of temperature change on the signal, a layer of silicone sealant (RTV) was applied to the face of the transducer. Over time, the silicone was eroded, and the effect on the transducer output is apparent between shots 1808 and 1828 in Fig. B.1(a) and B.1(b). The apparent pressure drop in Fig. B.1(b) was actually caused by heat transfer to the transducer.

The laser detector at the entrance to the test chamber extension tube used in series III (CH2) was not influenced by stress waves from the T5 shock reflection as was the launch tube exit laser trigger because it was mounted to the dump tank, which was not rigidly connected to the shock tube. However, the CH2 laser detector was subject to another source of false triggers. The CH2 signals shown in Fig. B.1 both exhibit a dip around 0.4 ms, prior to the true projectile signal (a narrow, sharp drop around 0.95 ms). In order to trigger correctly and avoid the premature dip, the trigger threshold was set very low. However, the amplitude of the dip varied significantly between

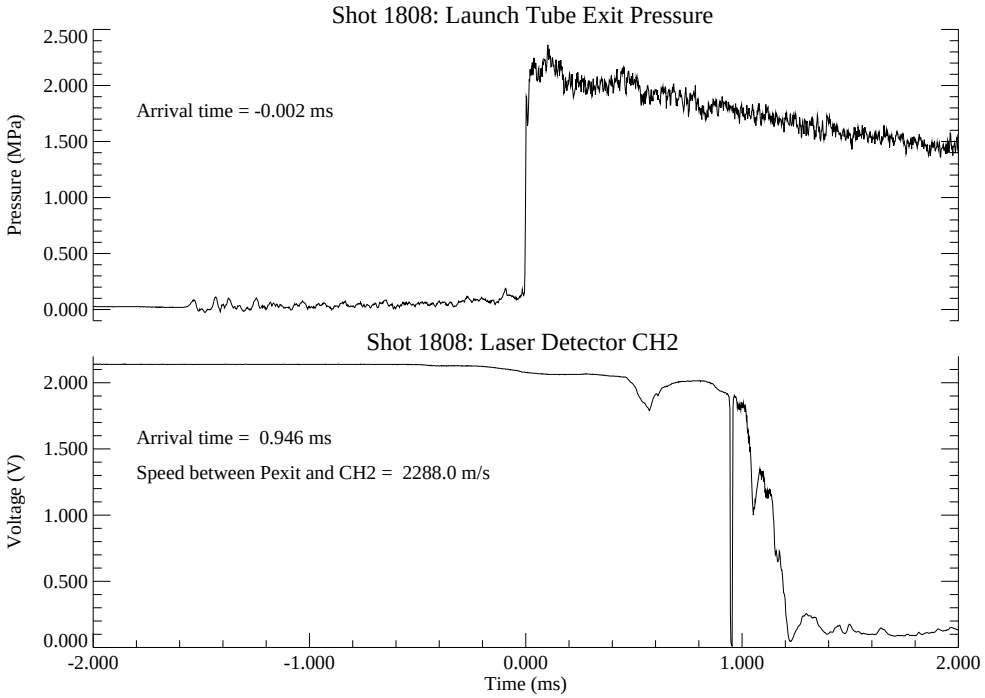

(a) Shot 1808

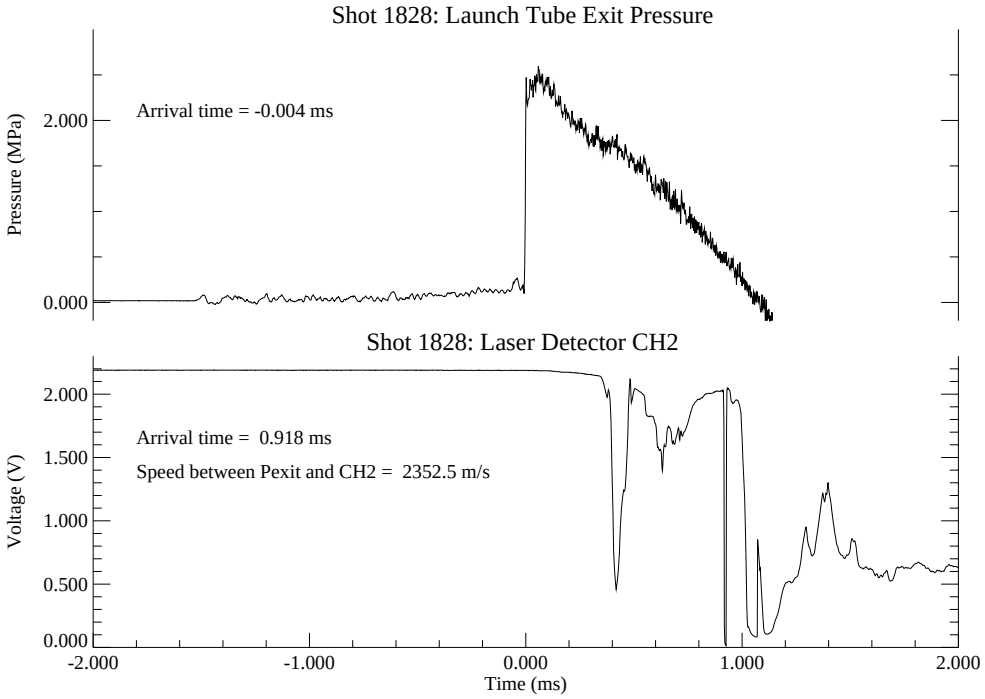

(b) Shot 1828

Figure B.1: Example P_{exit} and CH2 laser detector plots.

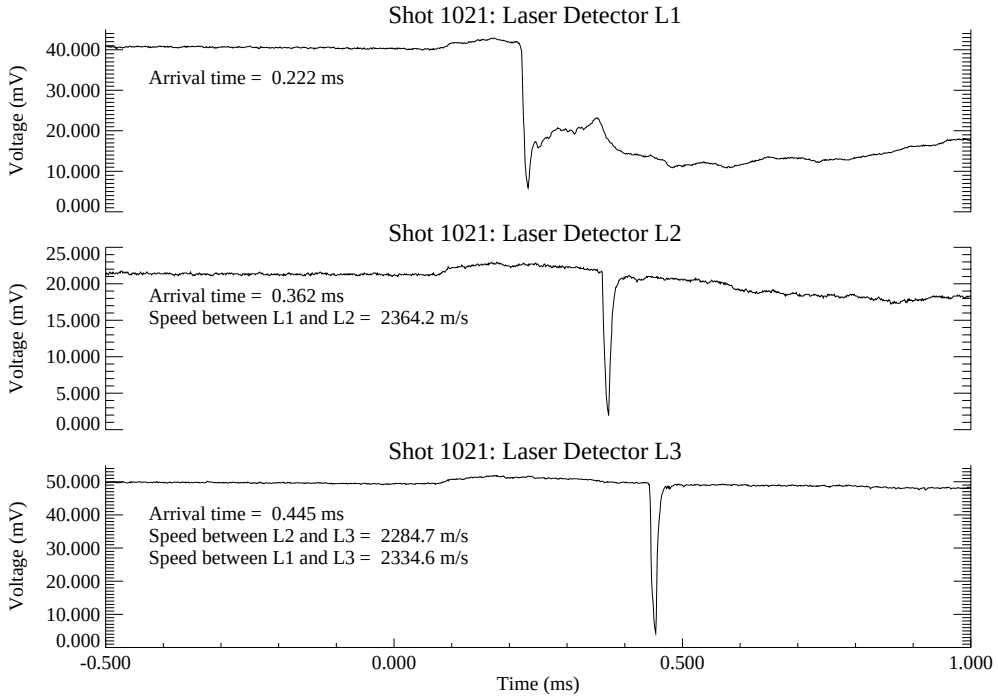

(a) Shot 1021

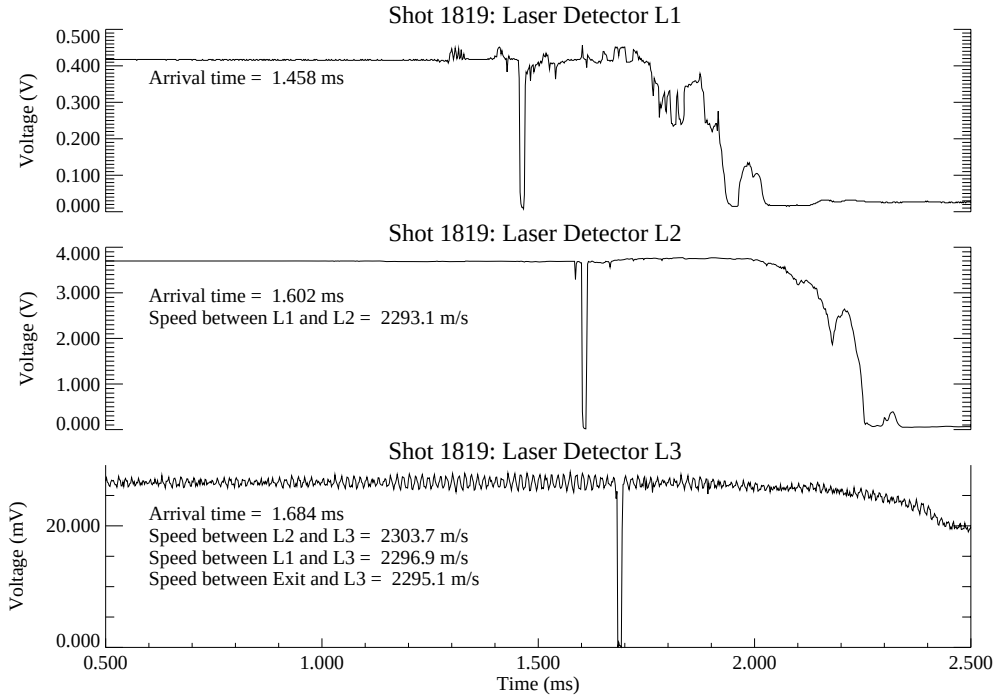

(b) Shot 1819

Figure B.2: Example of test section laser detector plots.

tests, so that the success of the trigger was somewhat random. The cause of the false triggers was never conclusively identified, although a possibility is debris and/or blow-by gases ejected from the launch tube before the projectile. The effect of blow-by gases was expected to be minimal because of the 2 m distance between the launch tube exit and test chamber entrance, and the intermediate vacuum.

In test series I and II, a break wire trigger (also CH2) was used to detect the projectile inside the dump tank, just before it entered the test section, as described in Section 5.4. Examples of recorded break wire signals are shown in Fig. 5.9. In contrast to the premature triggers experienced by the laser systems, the break wire sometimes provided a late signal.

Fig. B.2 shows examples of test section laser detector signals from two shots. The third laser detector, looking at an angle through the main optical windows, was not used in series I and some of series II. During series II, the third laser detector was added. The intended use of these detectors was projectile velocimetry, but a number of difficulties prevented them from being used reliably and independently. The first problem encountered was interference from combustion-generated light emission. During series I, the laser beams were used unfiltered, so that in cases involving combustion, the photodetection signal actually increased when the projectile crossed the laser beam. To prevent this, interference filters were introduced during series II. These filters effectively blocked combustion-generated emission, but also reduced the signal level, and created a new problem of matching laser and filter wavelengths. A poor match seriously degraded the signal.

Window conditions, laser alignment, performance of the lasers, photodetectors, and photodetector driver circuits, and even mounting design changed between tests and affected the signal quality and time response. The plots from shots 1021 and 1819 in Fig. B.2 show relatively clean signals, although a difference in time response is apparent, in this case due to a change in the photodetector circuits. The non-instantaneous drop in the signal caused uncertainty in the arrival time depending on the detection threshold used. This uncertainty was compounded, in the velocity calculation, by the short distances between laser detector stations. In practice, the L1 and L2 signals were not used for velocimetry. L3 was used in conjunction with earlier signals such as P_{exit} and CH2. In that case, the longer travel distance reduced the effect of uncertainty in any single arrival time value.

B.2 Tabulated Arrival Time Data

Tables B.1 and B.2 report arrival time information obtained from various sources. Table B.1 summarizes arrival time data taken by postprocessing the recorded (analog) sensor signals. In some cases, these signals were used to generate real-time triggers, but were recorded for post-test analysis and debugging. Not all signals were generated or recorded during all shots. For instance, the launch tube exit pressure transducer, P_{exit}, was only used during series III. Except for the last two columns,

QSW and X_{T-Q}, the time values reported were determined from the data acquisition system records. Because of variation of the signals between shots, arrival times were determined using time windows and level thresholds subjectively selected for each case. Since the real-time triggers operated off preset thresholds, they did not necessarily coincide with the times reported in Table B.1. In general, the P_{exit}, CH2, and P1-3 signals were well defined and the reported values were not sensitive to the thresholds used. The test section laser triggers L1-3 were very sensitive, however, and they have been used only as backups for the other signals. The CH2 (break wire) signal was used to trigger the data acquisition system and laser timing circuit for series I and II, whereas P_{exit} was used for most of series III, explaining the difference in zero point. Shots 1800 through 1805 were triggered off a laser trigger at the P_{exit} station, although this system was not reliable. The QSW and X_{T-Q} columns report the time and position of the projectile obtained from shadowgraphs and interferograms. The q-switch time of the Nd:YAG laser, QSW, was obtained from a photodiode monitor in series I and II, and a laser output q-switch sync signal in series III. The distance from the trigger station to the projectile at the time of the laser flash, X_{T-Q}, was determined by measuring the position of the nose of the projectile in the photograph and adding the known distance from the trigger station. This information provided the most accurate velocity values.

Omitted entries indicate that the data were not taken, while dashes (-) indicate that the signal was unusable for some reason.

Table B.1: Summary of timing signals (times in milliseconds).

Shot	P_{exit}	CH2	L1	L2	L3	P1	P2	P3	QSW	X_{T-Q} (m)
857		0.000	0.449	0.746		0.647	0.839	-		
858		0.000	0.289	0.472		0.434	0.556	0.679		
859		0.000	-	-		0.369	0.451	0.535		
860		0.000	-	0.335		0.284	0.368	0.447	0.419	
861		0.000	0.190	0.316		0.295	0.379	0.461	0.419	1.093
862		0.000	-	-		0.232	0.311	0.391	0.419	1.070
863		0.000	-	-		0.228	0.306	0.385	0.404	1.053
864		0.000	-	-		0.292	0.387	0.480	0.406	0.932
865		0.001	-	-		0.288	0.389	0.464	0.415	0.994
1004		-0.001	0.212	0.353		0.342	0.441	0.540		
1005		-0.002	0.216	0.349		0.356	0.438	0.524		
1007		-0.008	0.196	0.327		0.323	0.409	0.497	0.456	
1009		-0.250	-0.006	0.126	0.221	0.053	0.123	0.202	0.426	
1010		-0.006	0.213	0.353	0.436	0.269	0.345	0.427	0.426	0.994
1011		-0.003	0.215	0.355	0.431	0.282	0.355	0.434		
1012		0.000	0.206	0.337	0.410	0.276	0.369	0.444	0.426	1.063
1013		-0.003	0.242	0.374	0.449	0.315	0.409	0.499	0.425	0.979
1014		0.000	0.263	0.397	0.472	0.341	0.437	0.527	0.439	
1015		-0.001	0.206	0.342	0.419	0.298	0.392	0.482	0.439	1.069
1016		-0.001	0.193	0.324	0.398	0.275	0.359	0.446	0.439	1.126
1017		-0.002	0.269	0.407	0.483	0.345	0.415	0.499	0.438	
1018		-0.002	0.212	0.352	0.427	0.289	0.366	0.447	0.439	1.047
1019		-0.001	0.229	0.379	0.464	0.309	0.381	0.473	0.439	0.970

Shot	P_{exit}	CH2	L1	L2	L3	P1	P2	P3	QSW	X_{T-Q} (m)
1020		-0.001	0.209	0.350	0.430	0.279	0.354	0.444	0.439	1.040
1021		-0.001	0.222	0.363	0.445	0.280	0.422	0.516	0.440	1.012
1022		0.000	0.235	0.374	0.449	0.313	0.393	0.484	0.439	0.993
1023		-	0.204	0.345	0.426	0.277	0.368	0.445	0.455	1.092
1024		-	0.179	0.318	0.393	0.244	0.323	0.406	0.453	
1025		0.059	0.313	0.461	0.546	0.389	0.467	0.549	0.453	
1026		-0.003	0.269	0.400	0.491	0.346	0.416	0.497	0.453	
1027		-0.002	0.241	0.378	0.457	0.305	0.381	0.466		
1028		-0.001	0.283	0.419	0.497	0.345	0.421	0.505		
1029		0.000	0.202	0.336	0.415	0.258	0.330	0.411	0.453	1.117
1030		-0.004	0.291	0.428	0.506	0.342	0.419	0.501	0.445	
1031		-0.237	-0.003	0.126	0.212	0.057	0.130	0.206	0.448	
1032		-0.181	-0.040	0.095	0.179	0.013	0.089	0.171	0.447	
1800		0.000	-	-	-	0.545	0.635	0.730		
1801		2.447	-	-	3.173	2.988	3.080	3.173	3.177	1.703
1802		1.468	-	2.100	2.192	2.008	2.097	2.192		
1804		2.290	-	2.930	3.022	2.836	2.926	3.018	3.024	
1805	1.560	2.506	-	3.116	3.246	3.050	3.138	3.250		
1806	0.000	0.944	1.426	1.540	1.684	1.492	1.582	1.676	1.690	3.875
1807	0.000	0.958	1.492	1.642	1.728	1.574	1.680	1.776	1.732	3.870
1808	0.002	0.946	1.454	1.594	1.688	1.502	1.592	1.686	1.694	3.872
1809	0.000	0.950	1.464	1.608	1.698	1.514	1.604	1.700	1.702	3.872
1810	0.000	0.944	1.456	1.602	1.682	1.560	1.646	1.744	1.686	3.869
1811	0.000	0.942	1.456	1.600	1.682	1.540	1.620	1.706	1.684	3.870
1812	0.000	0.936	1.436	1.592	1.694	1.516	1.612	1.710	1.696	3.870
1813	0.000	0.938	1.450	1.596	1.684	1.512	1.604	1.702	1.684	3.868
1814	0.000	0.930	1.418	1.566	1.664	1.490	1.582	1.678	2.294	
1815	0.002	0.942	1.450	1.598	1.688	1.506	1.600	1.696	1.690	3.873
1816	-	0.928	1.430	1.576	1.656	1.516	1.610	1.708		
1817	0.000	0.934	1.444	1.586	1.670	1.530	1.624	1.724	1.688	
1818	0.000	0.934	1.428	1.566	1.668	1.472	1.564	1.658	1.672	
1819	0.002	0.942	1.458	1.602	1.684	1.566	1.660	1.760	1.700	3.900
1820	0.000	0.930	1.446	1.574	1.680	1.510	1.606	1.704	1.698	3.898
1821	0.000	0.918	1.426	1.568	1.656	1.484	1.578	1.676	1.674	
1822	0.000	0.918	1.420	1.558	1.644	1.480	1.572	1.668	1.660	3.902
1823	0.000	0.912	1.414	1.554	1.632	1.498	1.588	1.682	1.648	3.901
1824	0.002	0.924	1.428	1.568	1.654	1.512	1.606	1.702	1.670	3.902
1825	0.000	0.922	1.412	1.558	1.658	1.486	1.580	1.678	2.590	
1826	0.002	0.918	1.396	1.550	1.660	1.484	1.580	1.678	2.850	
1827	0.000	0.918	1.412	1.554	1.638	-	-	-		
1828	0.000	0.918	1.422	1.564	1.646	1.508	1.598	1.696		
1829	0.000	0.922	1.426	1.568	1.648	1.520	1.606	1.698	1.698	
1830	0.000	0.934	1.430	1.582	1.672	1.504	1.598	1.696	1.696	3.925
1831	-	0.906	-	1.540	1.624	1.490	1.582	1.676		
1832	0.000	0.900	1.382	1.528	1.612	1.452	1.542	1.636	1.638	
1833	0.000	0.898	1.392	1.532	1.612	1.472	1.566	1.658	1.662	
1834	0.002	0.896	1.386	1.520	1.604	1.472	1.562	1.656	1.658	
1835	0.000	0.886	-	1.512	1.598	1.440	1.530	1.624	1.624	
1836	0.000	0.884	1.368	1.506	1.584	1.450	1.542	1.636	1.640	
1837	0.002	0.890	1.378	1.514	1.598	1.460	1.552	1.646	1.602	3.876
1838	0.000	0.888	1.376	1.514	1.598	1.438	1.528	1.620	1.602	3.878
1839	0.002	-	1.400	1.538	1.624	1.462	1.554	1.650	1.628	
1840	0.000	0.902	1.370	1.512	1.588	1.444	1.532	1.626	1.594	3.876

Table B.2 summarizes the recorded auxiliary (digital) timing signals from test series III, since they were only recorded for those tests. These signals differed from those summarized in Table B.1 in that they were analog records of TTL trigger outputs, so that interpretation of the results was much simpler. These signals were recorded on two systems: the main T5 data acquisition system, and a Tektronix digital storage oscilloscope used as a backup and for timing verification. In addition, the ICCD gate pulse was triggered and delayed (by a dedicated pulse generator) from one of the recorded timing signals, so it provides an additional independent timing source. The values in Table B.2 verify the accuracy of the data acquisition system time base and assist interpretation of the photographs, particularly when shadowgraph and ICCD images were both recorded during one shot.

B.3 Uncertainty Estimation

Sources of uncertainty in the arrival time data, and hence the projectile and pressure wave velocities, came from a number of sources and varied between test series. The most serious contributor was the data acquisition time base error discussed in Section 5.4.6, because the accuracy of each signal could not be determined by comparison with the other signals. Otherwise, comparison of different signals helped reduce and estimate uncertainty.

Fortunately, timing information independent of the data acquisition system was available for the series I and II shots, in the form of recorded laser pulses. As discussed in Section 5.4.6, a correction factor for the series I and II time (and velocity) data was determined to range between 0.875 and 0.916. All arrival time and velocity data in Appendices A and B from those tests have been corrected by the nominal value of 0.895. For a projectile velocity of 2300 m/s, the uncertainty in the correction factor leads to a velocity uncertainty of about ± 50 m/s.

In all cases, the precision of the velocity measurements was limited by the precision of the arrival time measurements, although the effect varied depending on the distance between detection stations. The most uncertain arrival times were the laser detectors, especially those mounted on the test section. In cases in which a shadowgraph or interferogram was obtained, the position of the projectile in the picture and the recorded laser pulse (or q-switch sync output) time provided the most precise information, so these data were used to compute the projectile velocity in those cases. When a photograph was not obtained, the L3 laser trigger was used. Because of the time response of the photodetector, the uncertainty of the arrival time was up to ± 5 μs, which led to a velocity uncertainty of about ± 25 m/s. This value is conservative because median L3 arrival times were found to agree with velocities computed from photographic data to within 16 m/s. Therefore, for series I and II, the velocity uncertainty was dominated by the data acquisition timing error, i.e., ± 50 μs. Series III projectile velocities, on the other hand, were more precise, because of the longer distance between detector stations, so that L3 and photographic data agreed to within 10 m/s.

Table B.2: Data acquisition system and oscilloscope timing signals (times in milliseconds).

	DAS			Oscilloscope			ICCD
Shot	CH2	FL	QSW	CH2	FL	QSW	Gate
1801	-	2.952	3.177				
1802	-	1.972					
1804	-	2.006	3.024				
1805	2.110	2.692	3.250				
1806	0.950	1.432	1.690	0.960	1.440	1.688	
1807	0.962	1.502	1.732	0.960	1.504	1.728	
1808	0.952	1.498	1.694	0.952	1.496	1.688	
1809	0.954	1.502	1.702	0.960	1.504	1.704	1.701
1810	0.948	1.492	1.686	0.952	1.496	1.688	
1811	0.946	1.488	1.684	0.944	1.488	1.688	
1812	0.940	1.480	1.696	0.944	1.480	1.696	1.711
1813	0.942	1.482	1.684	0.944	1.480	1.688	1.703
1814	0.934	1.468	2.294	0.936	1.472	2.296	1.679
1815	0.946	1.488	1.690	0.944	1.488	1.688	1.697
1816	-	-	-	0.560	0.840	1.656	1.709
1817	0.598	0.916	1.688	0.600	0.920	1.688	1.670
1818	0.938	1.474	1.672	0.936	1.472	1.672	1.668
1819	0.948	1.504	1.700	0.944	1.504	1.696	
1820	0.934	1.482	1.698	0.936	1.480	1.696	1.704
1821	0.586	0.894	1.674	0.584	0.896	1.672	1.676
1822	0.920	1.462	1.660	0.920	1.464	1.664	1.668
1823	0.918	1.456	1.648	0.928	1.456	1.648	1.682
1824	0.928	1.474	1.670	0.928	1.472	1.672	1.702
1825	0.924	1.468	2.590	0.928	1.472	2.592	1.678
1826	0.660	1.024	2.850	0.664	1.024	2.848	1.678
1827	0.920	-	-	0.928	1.424	-	
1828	0.922	1.464	-	0.928	1.464	1.720	1.661
1829	0.652	0.998	1.698	0.656	1.000	1.696	1.686
1830	0.936	1.472	1.696	0.936	1.472	1.696	1.678
1831	-	-	-	0.688	1.000	1.680	1.662
1832	0.536	1.506	1.638	0.536	1.504	1.640	1.643
1833	0.902	1.506	1.662	0.904	1.504	1.664	1.606
1834	0.900	1.508	1.658	0.896	1.504	1.656	1.663
1835	0.890	1.506	1.624	0.888	1.504	1.624	1.631
1836	0.512	1.458	1.640	0.512	1.464	1.640	1.643
1837	0.522	1.458	1.602	0.520	1.456	1.600	1.646
1838	0.890	1.458	1.602	0.888	1.464	1.600	1.620
1839	-	-	1.628	-	-	1.624	1.650
1840	0.900	1.424	1.594	0.904	1.424	1.584	1.626

Of course, the velocity computed between two distant points is only an average value. At least in the test chamber, drag will cause the velocity to vary. However, a simple calculation shows that the drag force on the projectile, and hence the drop in velocity along its path, are small. For the sake of the estimation, the drag is assumed to be unchanged by combustion. This is not generally true, as other researchers have found combustion to reduce the drag on a spherical projectile. Therefore, ignoring the effect of combustion is conservative.

The basic relation for the motion of the projectile is:

$$D = \frac{1}{2}\rho V^2 C_D A = m \cdot a \tag{B.1}$$

Applying the ideal gas law and rearranging derivatives, we get

$$\frac{dv}{dx} = \frac{\pi}{8}\frac{\gamma P M^2 C_D d^2}{mV} \tag{B.2}$$

Inserting conservative values from Table A.1,

$$\begin{aligned} \frac{df}{dx} &= \frac{\pi}{8}\frac{1.4(1\text{ bar})7^2(0.912)(25.4\text{ mm})^2}{(10\text{ g})(2300\text{ m/s})} \\ &= 58\text{ m/s} \end{aligned} \tag{B.3}$$

B.4 Photographs and Pressure Plots

Virtually all of the photographs taken are presented here, along with the corresponding pressure plots. They are grouped by fuel and dilution ratio, and sorted by increasing initial pressure. Table A.1 is sorted chronologically (by shot number) and lists the figure numbers of the photographic images. These results are discussed in detail in Chapter 6. Note also the following general comments:

1. Photographic images consist of a shadowgraph or differential interferogram, an ICCD image, or both, depending on which systems were used and functioned correctly on each shot. The pressure plots for each shot are given immediately after the photographic results.

2. The alignment of the shadowgraph and interferogram images was determined manually, using cues present in the images, such as the top and bottom surfaces of the test section. The alignment of the ICCD images was controlled by the alignment of the camera, which was determined manually during pre-experiment tests. The precision of these alignments (with respect to the axis of the test section) is estimated at better than 1.5° and 1° for the film and ICCD images, respectively.

3. Times of arrival of the pressure waves are listed in Table B.1. The absolute pressure levels behind the wave, along the wall, can be taken from the plots similarly, but such measurements are

much less precise and therefore have not been tabulated. In detonation cases, the actual peak pressure measured by each transducer can vary significantly because of the three-dimensional and temporal structure of the detonation. Since the PCB gauges are dynamic transducers, the plots give the pressure relative to the initial pressure. To recover the absolute pressure, the initial value must be added. No correction for zero offset due to signal conditioning or digitizing has been performed, and in some cases this offset is significant.

4. The apparent wave speeds along the wall were computed from the arrival times of the shock or detonation at each test section pressure transducer, and these values are printed on the pressure plots. The two values often differ by 100 m/s or more. The series III shots in particular show a fairly consistent drop in apparent wave speed of about 100 m/s. This was probably due to the area change upon passage from the extension tube to the test section. Larger changes were common in series I and II shots, and these were attributed to significant unsteadiness over the length of the test section, since the extension tube was not used in those shots.

5. Vasiljev [118] observed features that look much like debris particles seen in some of our images, but he attributed them to "jets." No other observation of jet-like phenomena has been made in projectile-initiated detonation experiments, suggesting that this interpretation is incorrect.

6. The shadowgraph/interferogram system was set up in a typical arrangement with the collimated laser beam perpendicular to the test section windows. The ICCD camera was focused on the windows from a position outside the laser beam path, so that its view was necessarily oblique. In most of the ICCD images, the top and bottom surfaces of the test section, the edges of the window, and some bolt heads around the outside of the window can be seen illuminated by light emission from inside the test section. A dark rectangular shape on the right side of the window is a mount for the L3 laser trigger diode laser, and the small bright circle on the left side of the window is the receiving photodetector illuminated by the laser.

7. The images obtained from the ICCD camera had a 12-bit dynamic range, giving 4096 gray levels (0-4095). The intensifier, lens aperture, and preamplifier gain were set to make the best use of this range, but saturation of the CCD did occur sometimes. Normally, pixels in a saturated region took the highest value (4095). In some cases, however, the controller software saved saturated pixels at the lowest value (0). Therefore, some areas of high intensity, such as the reflective top and bottom surfaces of the test section appear black in some ICCD images.

8. The main optical windows were damaged to varying degrees during the tests. Pitting and scratching by debris particles was a persistent problem that required replacement or repolishing of the windows between series. The transient pressure loads, combined with the compliant glass mount and surrounding metal parts resulted in some fracturing of the inside surface at the top

and bottom. During series II, in particular, a sizable "clamshell" fracture formed that appears in some of the photographs as a dark circular region (cf. Fig. B.35).

9. All of the stable initiations obtained with the extension tube (series III), with the exception of some low dilution H_2-O_2-N_2 cases, exhibited a series of several large pressure waves following the bow wave in the P1 trace and decaying in P2 and P3. Therefore, these waves must have been related to the extension tube - test section area change (see Section 5.3.2). This phenomenon has not been observed in shots without the extension tube. Also, the amplitude of the waves was greatest with the smoothest (smallest disturbances) detonations.

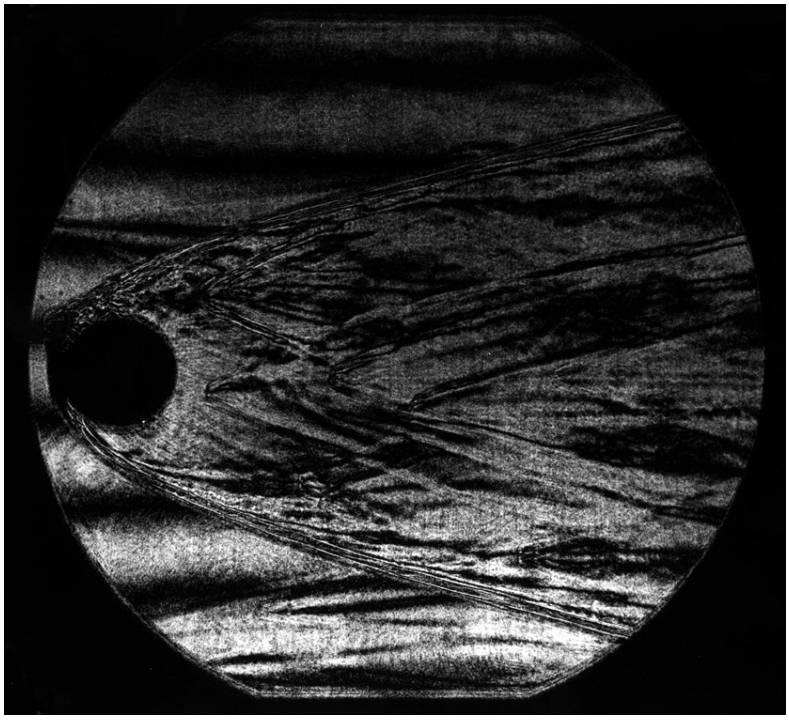

Figure B.3: Shot 861 Interferogram: N_2 at 0.250 bar, 2610 m/s.

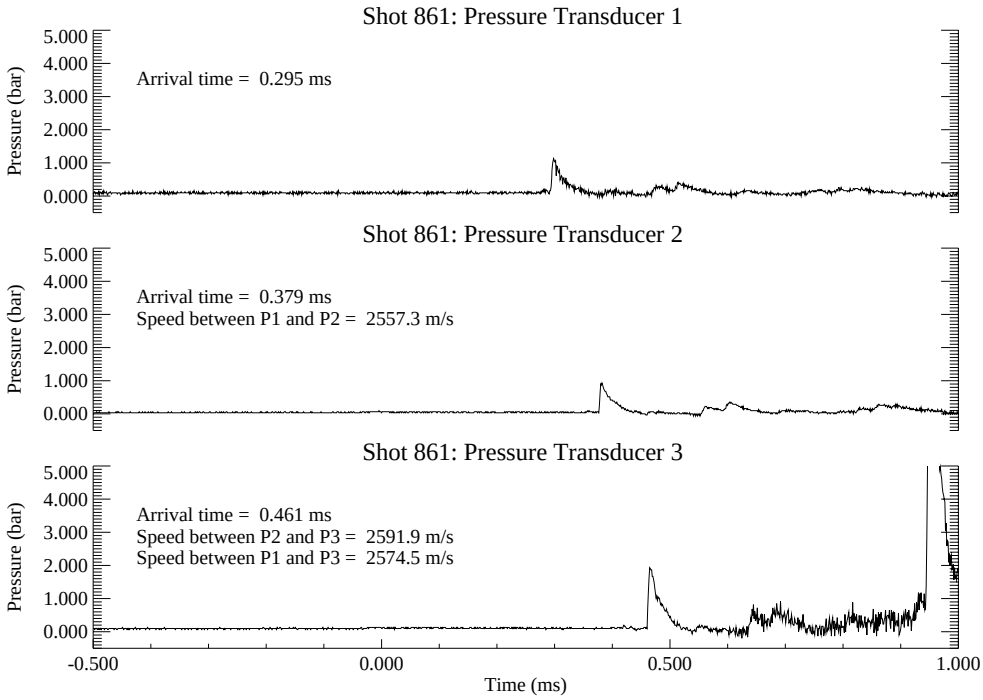

Figure B.4: Shot 861 pressure traces.

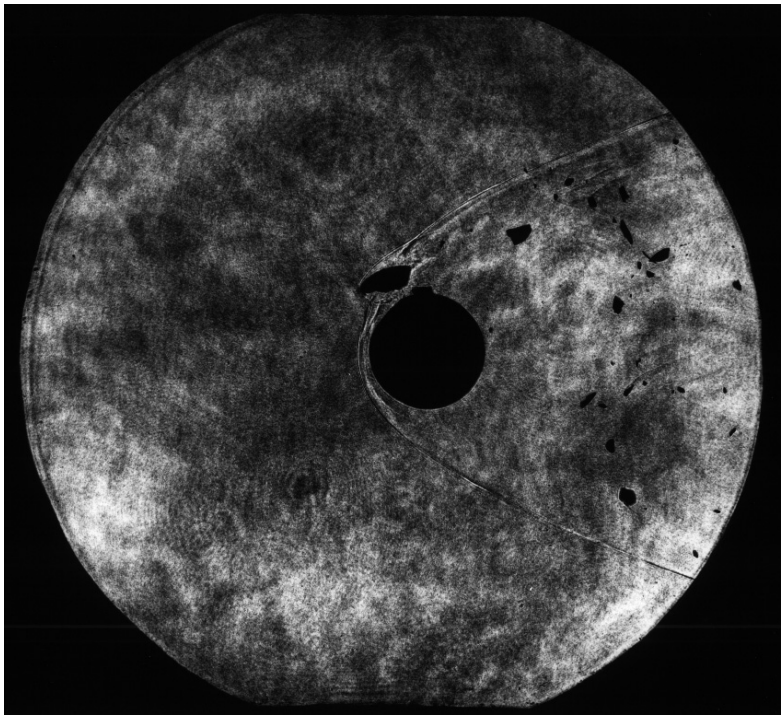

Figure B.5: Shot 1810 Shadowgraph: $2H_2+O_2+N_2$ at 0.080 bar, 2300 m/s.

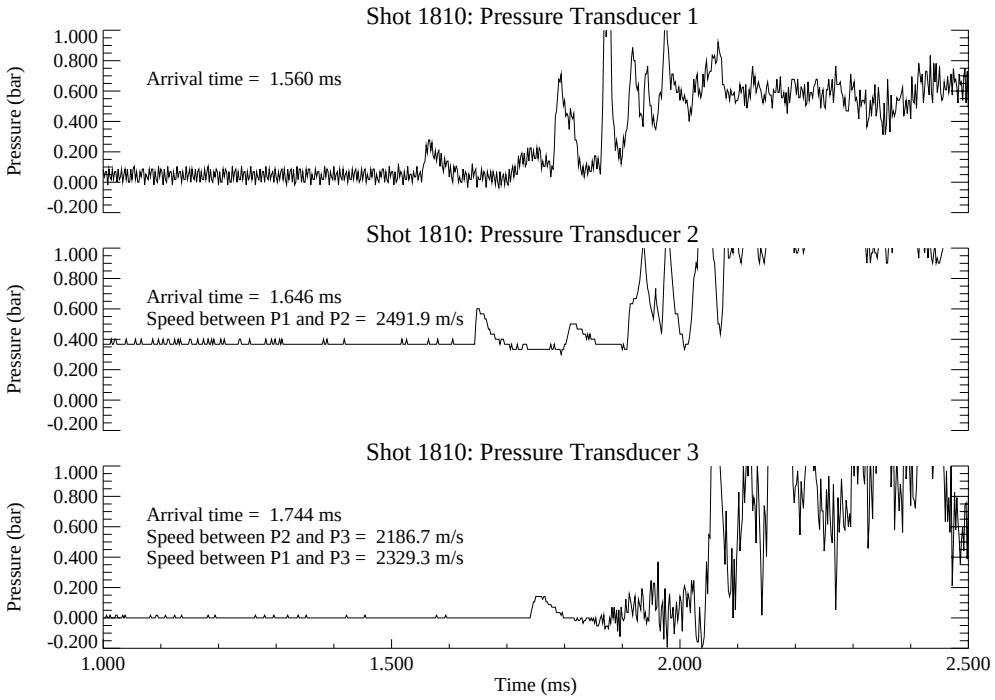

Figure B.6: Shot 1810 pressure traces.

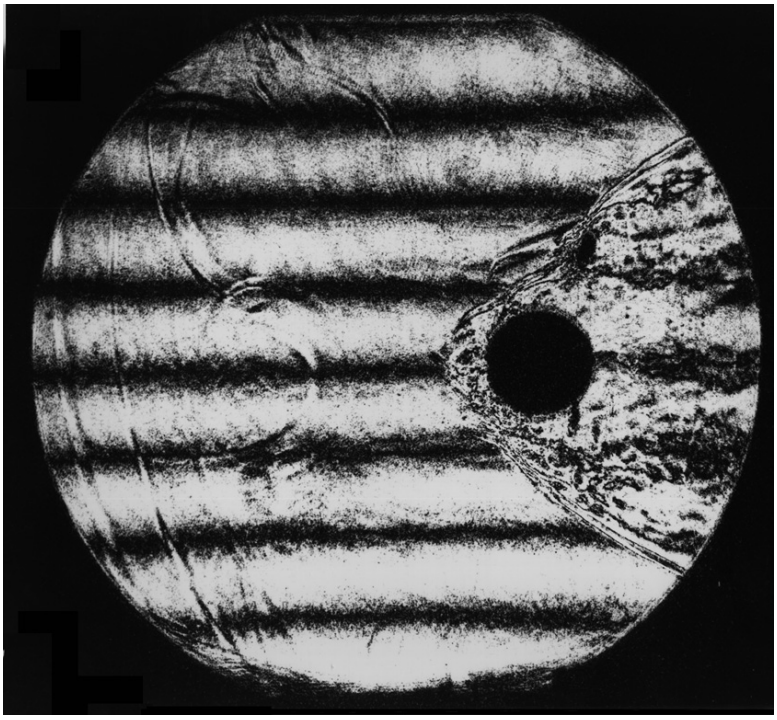

Figure B.7: Shot 865 Interferogram: $2H_2+O_2+N_2$ at 0.100 bar, 2400 m/s.

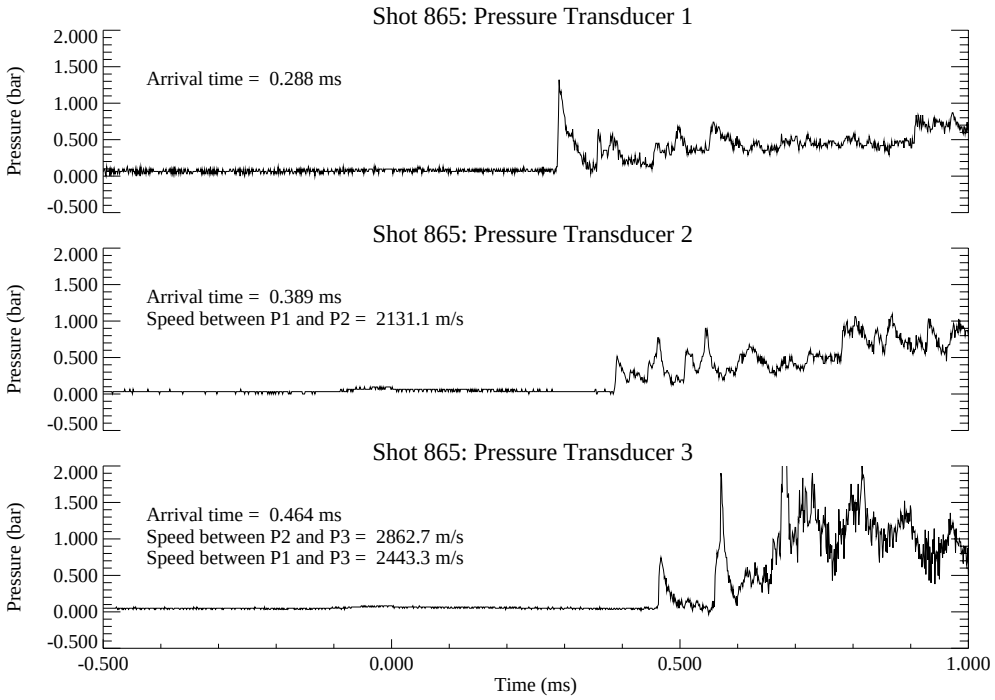

Figure B.8: Shot 865 pressure traces.

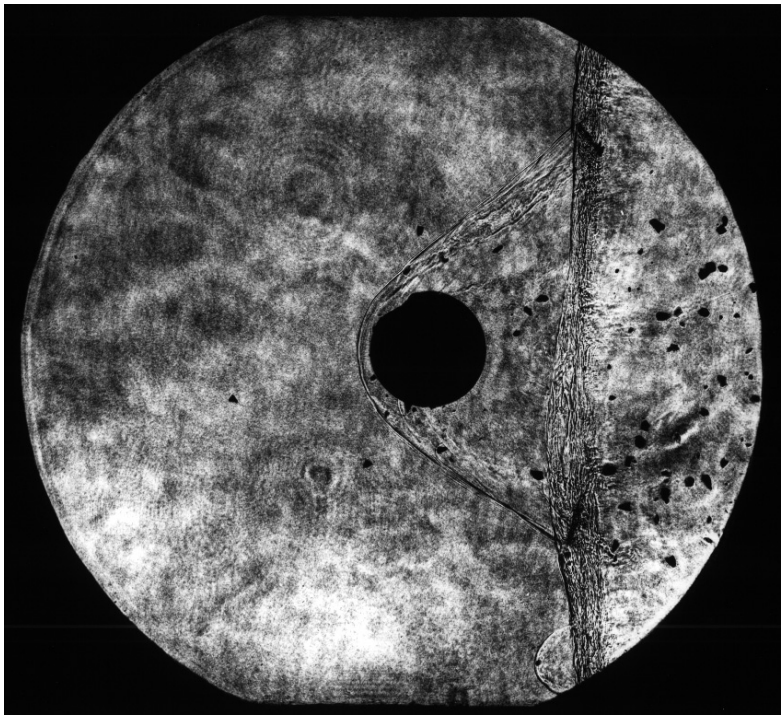

Figure B.9: Shot 1811 Shadowgraph: $2H_2+O_2+N_2$ at 0.100 bar, 2300 m/s.

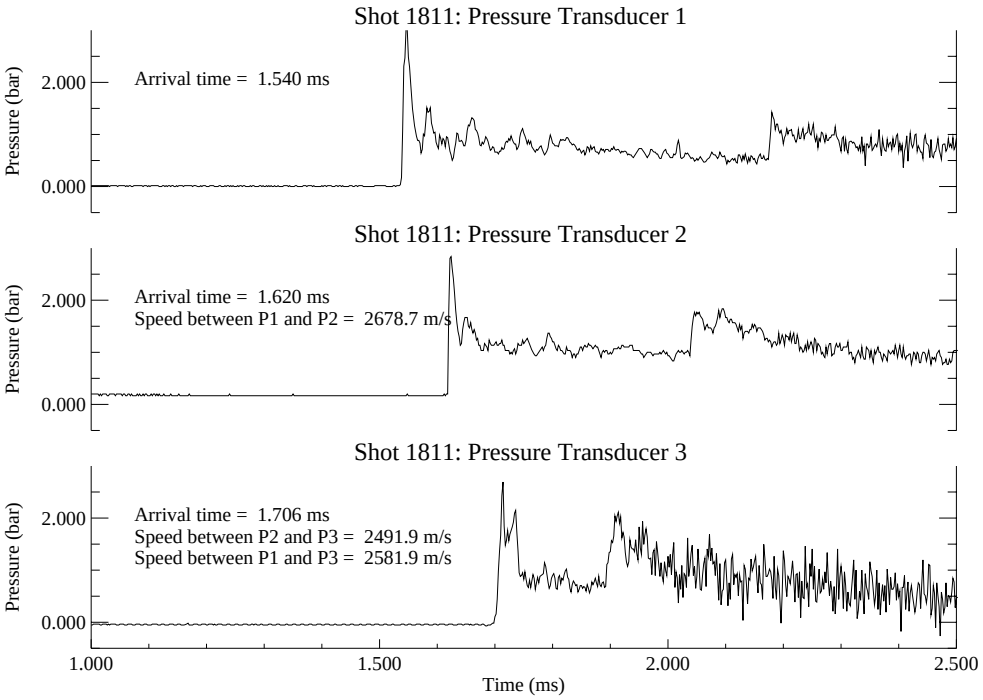

Figure B.10: Shot 1811 pressure traces.

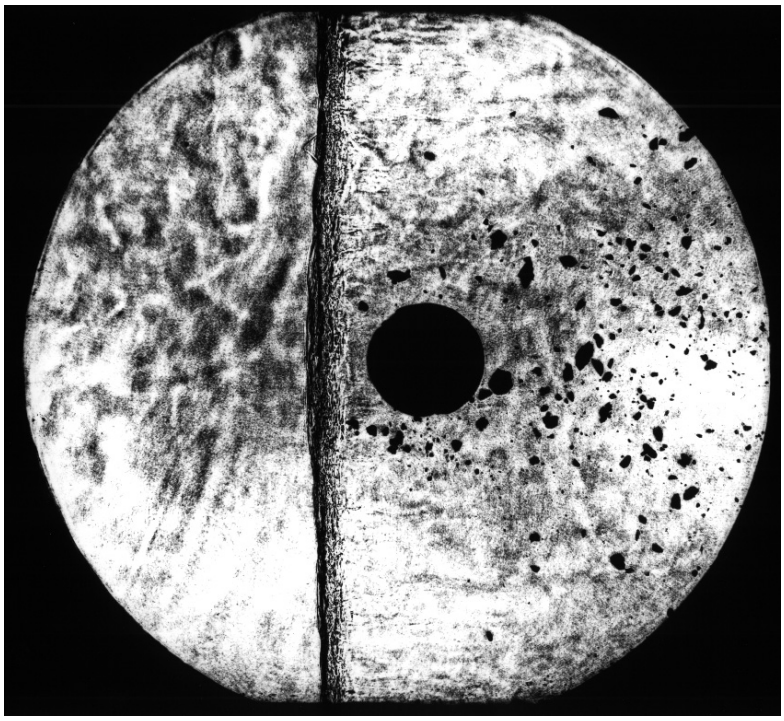

(a) Shadowgraph

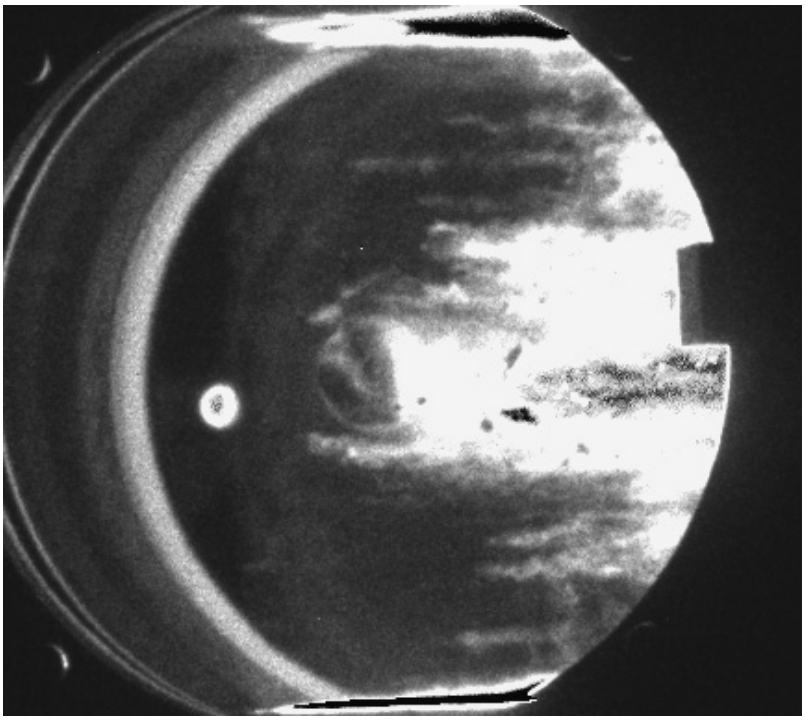

(b) ICCD

Figure B.11: Shot 1809: $2H_2+O_2+N_2$ at 0.120 bar, 2280 m/s.

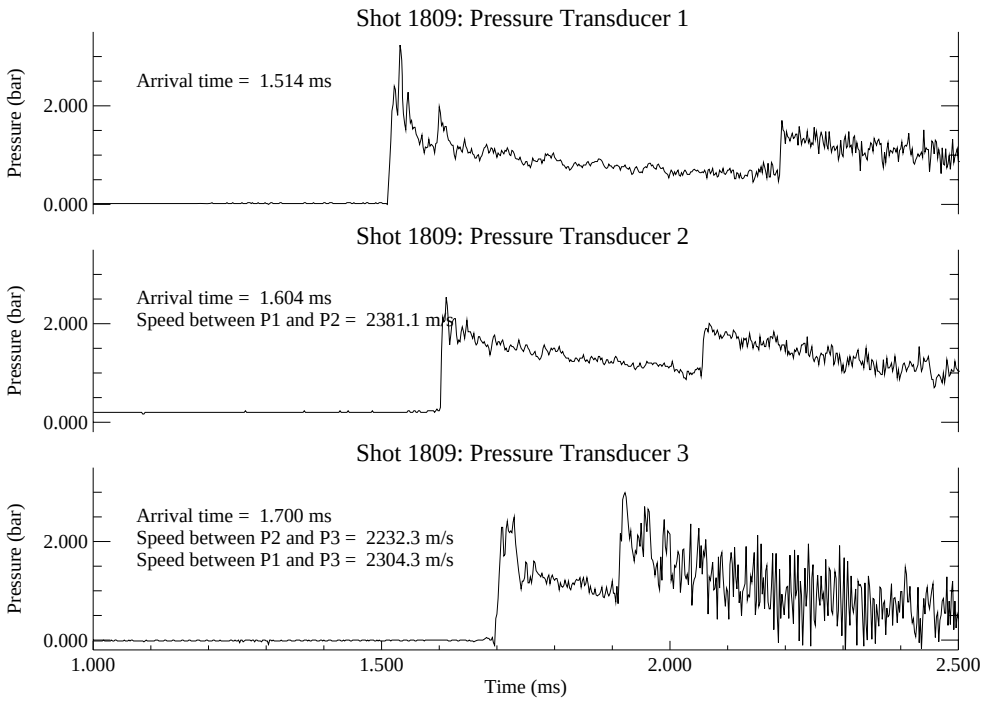

Figure B.12: Shot 1809 pressure traces.

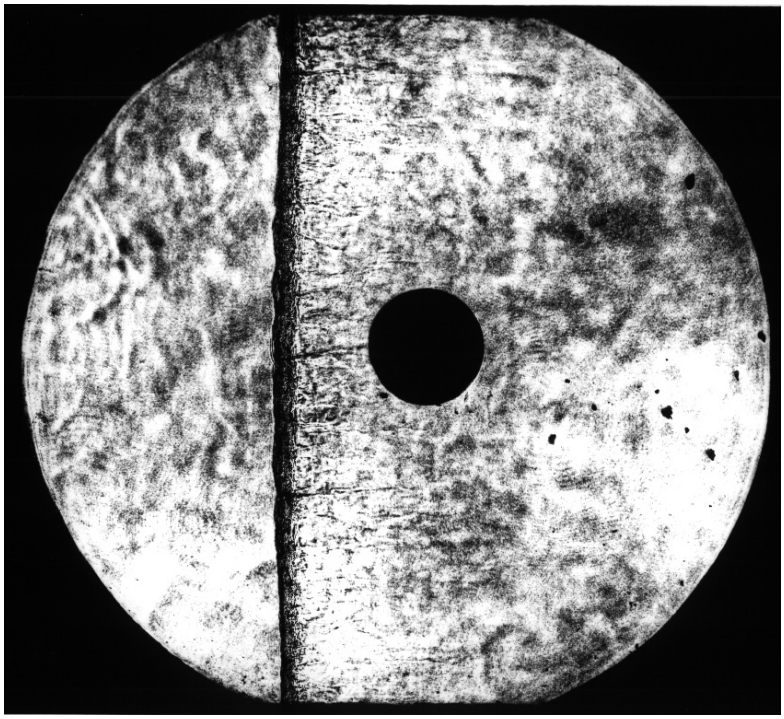

Figure B.13: Shot 1808 Shadowgraph: $2H_2+O_2+N_2$ at 0.180 bar, 2290 m/s.

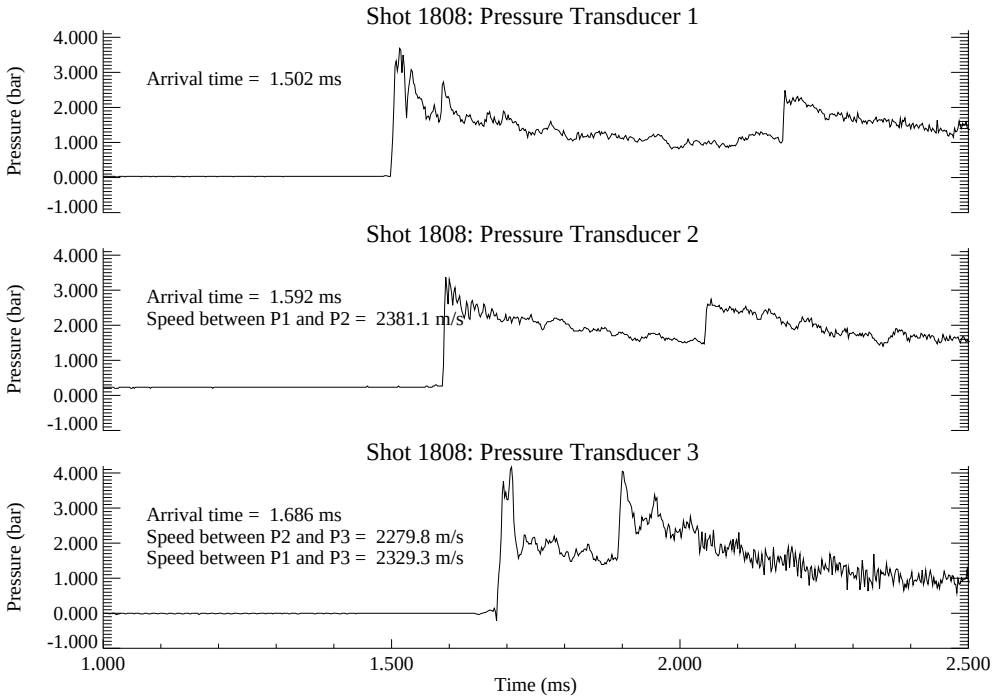

Figure B.14: Shot 1808 pressure traces.

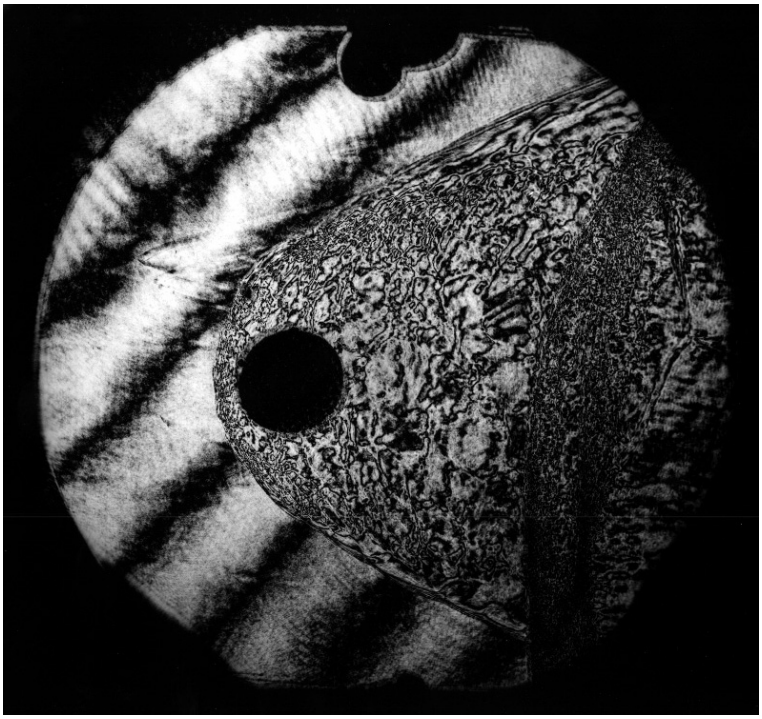

Figure B.15: Shot 1012 Interferogram: $2H_2+O_2+N_2$ at 0.250 bar, 2500 m/s.

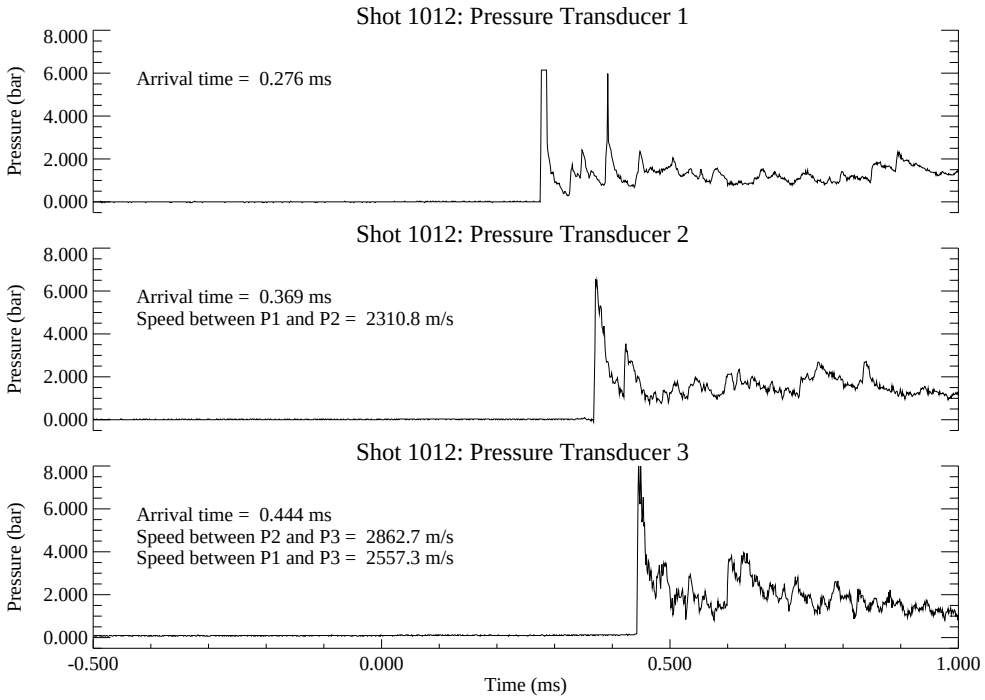

Figure B.16: Shot 1012 pressure traces.

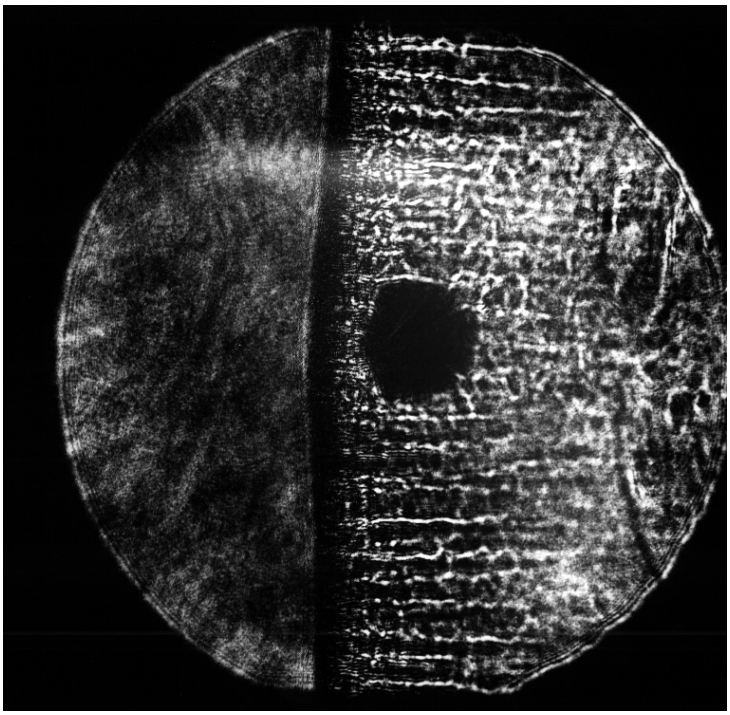

Figure B.17: Shot 1801 Shadowgraph: $2H_2+O_2+N_2$ at 0.250 bar, 2330 m/s.

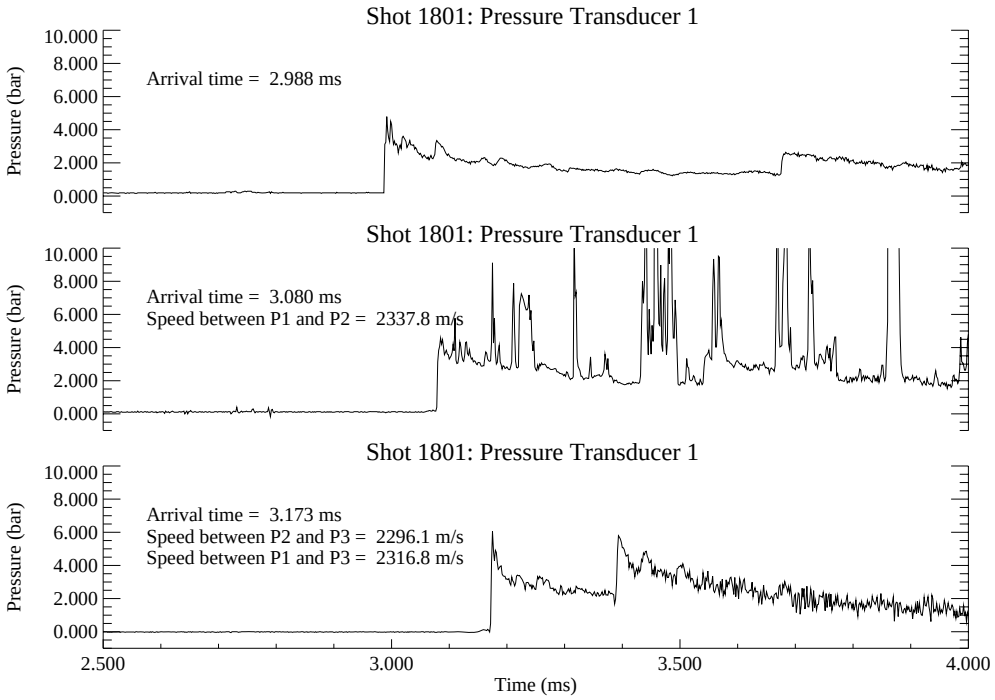

Figure B.18: Shot 1801 pressure traces.

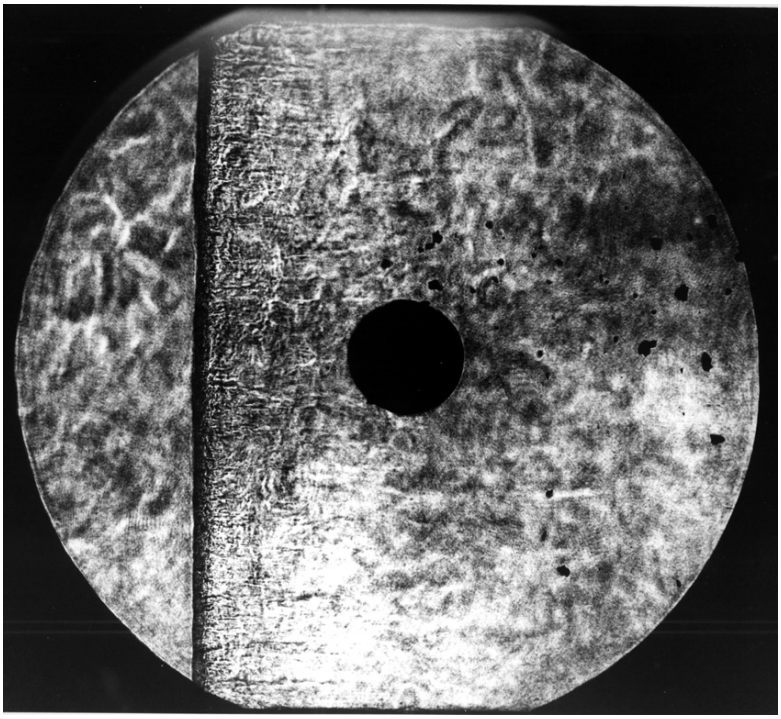

Figure B.19: Shot 1806 Shadowgraph: $2H_2+O_2+N_2$ at 0.250 bar, 2290 m/s.

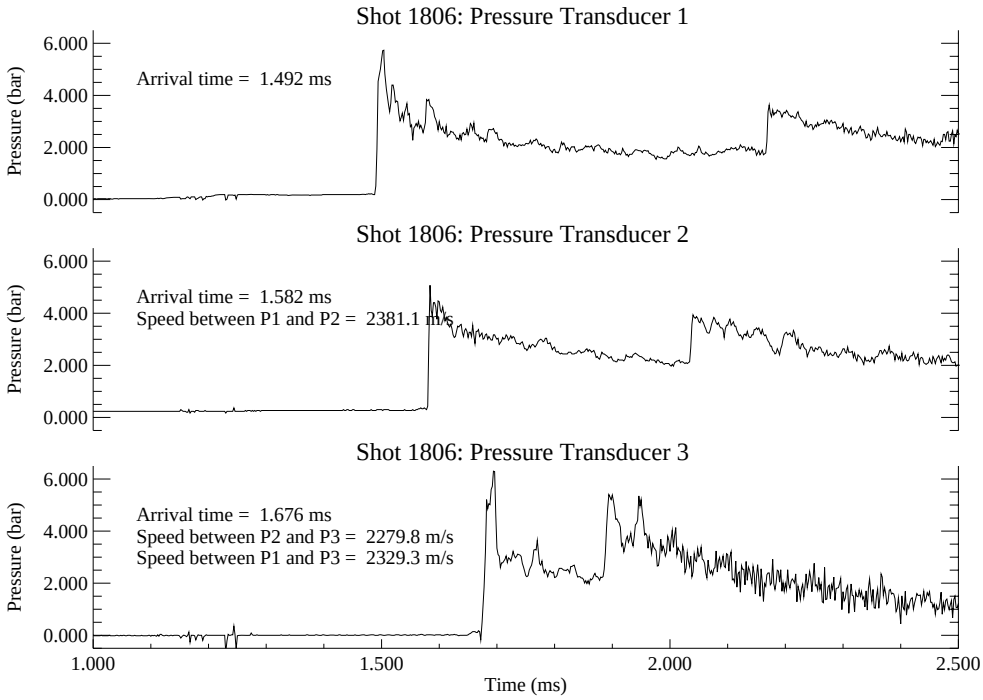

Figure B.20: Shot 1806 pressure traces.

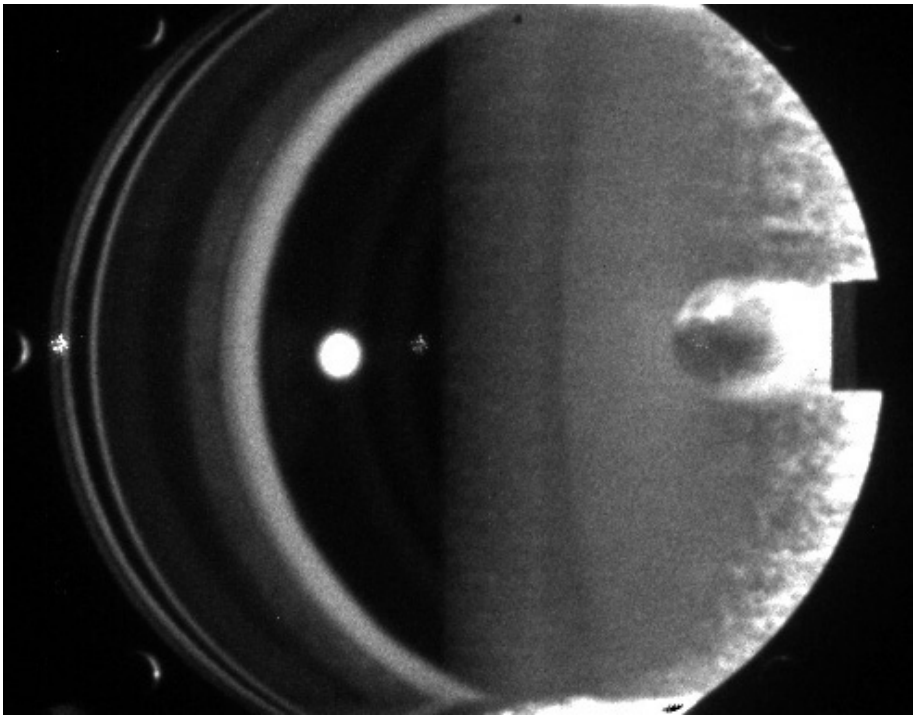

Figure B.21: Shot 1818 ICCD: $2H_2+O_2+N_2$ at 0.410 bar, 2320 m/s.

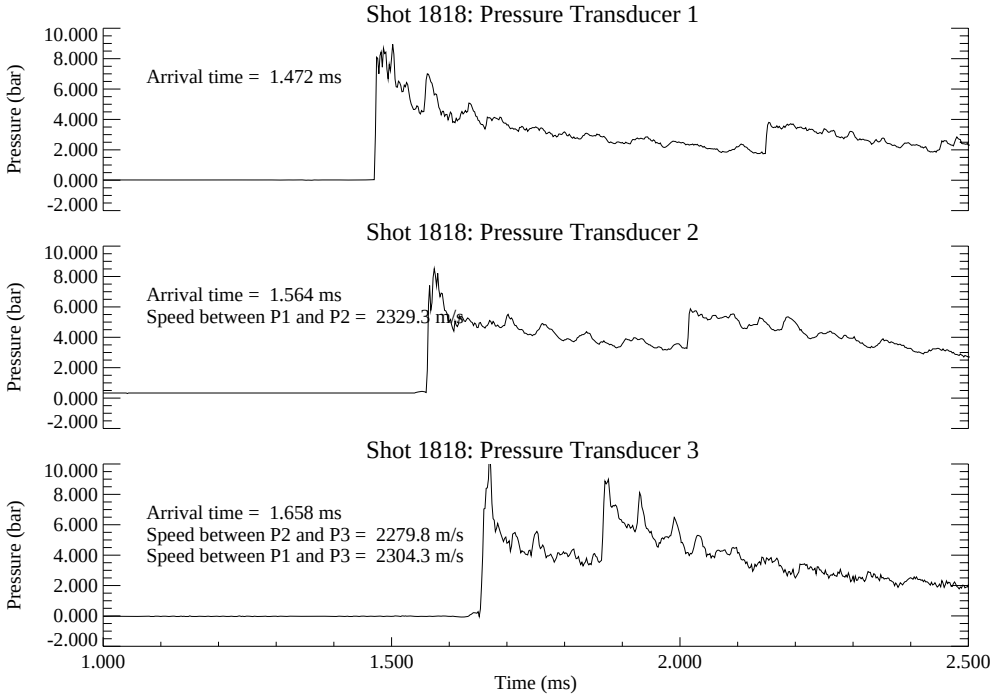

Figure B.22: Shot 1818 pressure traces.

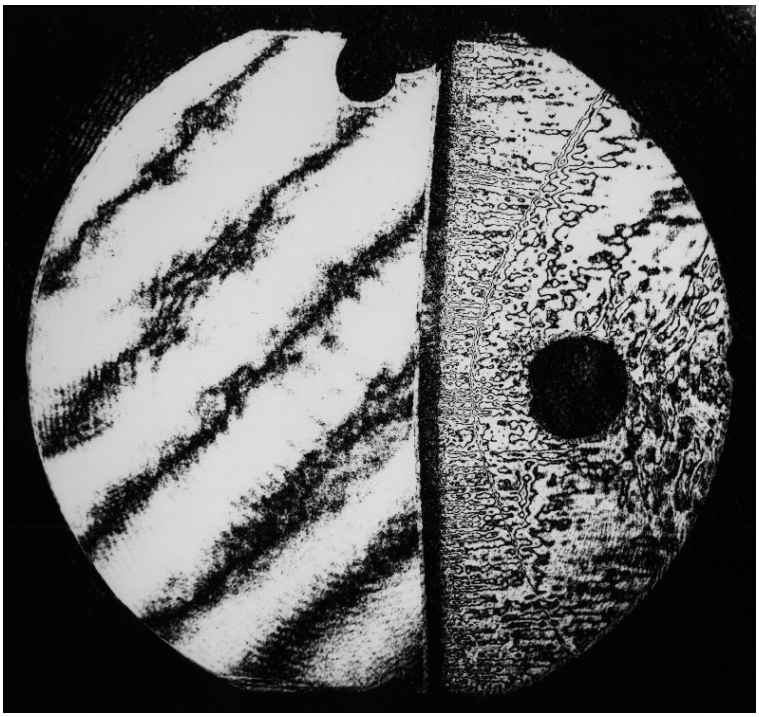

Figure B.23: Shot 1010 Interferogram: $2H_2+O_2+N_2$ at 0.500 bar, 2300 m/s.

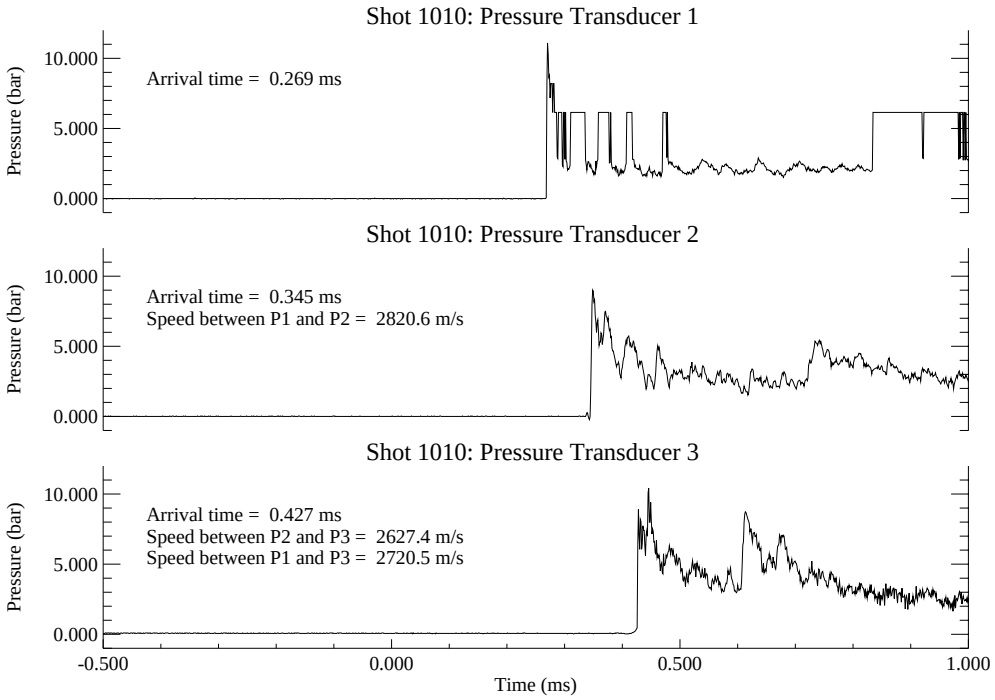

Figure B.24: Shot 1010 pressure traces.

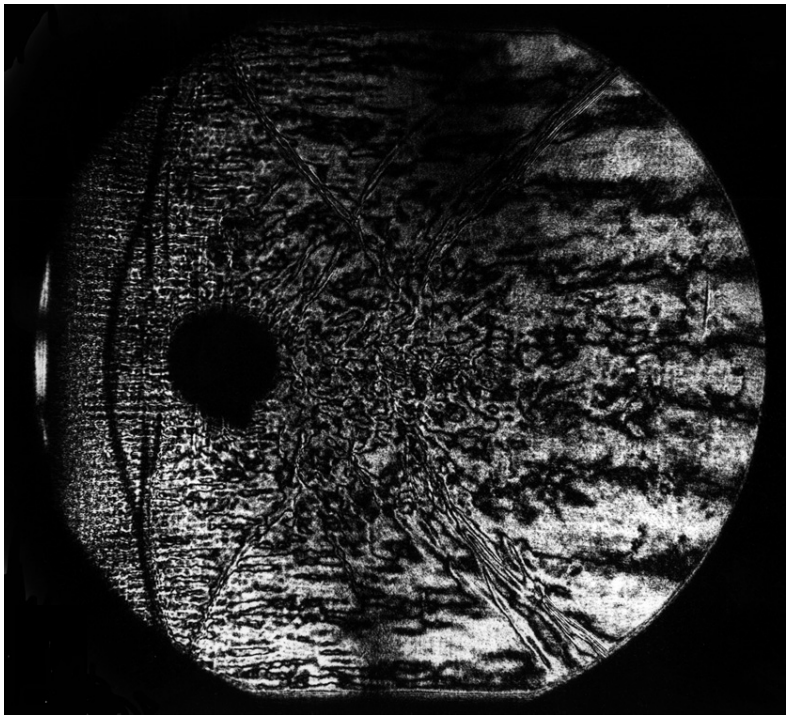

Figure B.25: Shot 862 Interferogram: $2H_2+O_2+N_2$ at 1.000 bar, 2550 m/s.

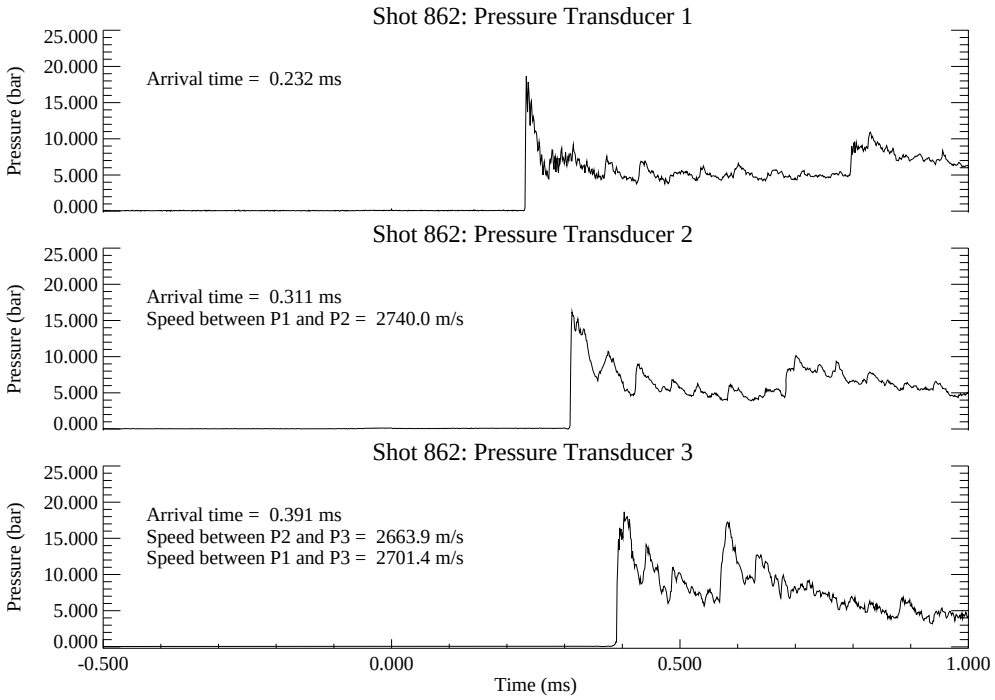

Figure B.26: Shot 862 pressure traces.

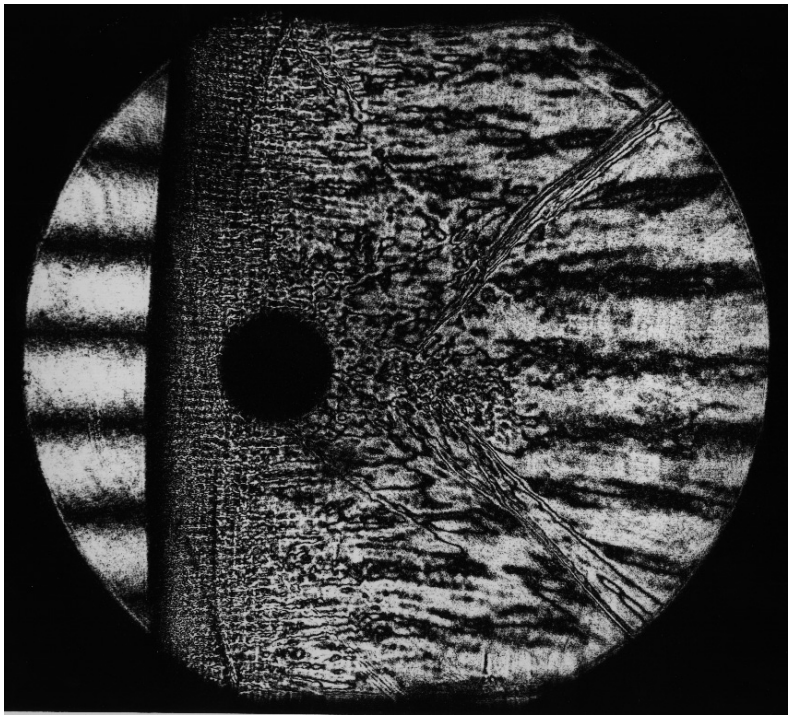

Figure B.27: Shot 863 Interferogram: $2H_2+O_2+N_2$ at 1.000 bar, 2610 m/s.

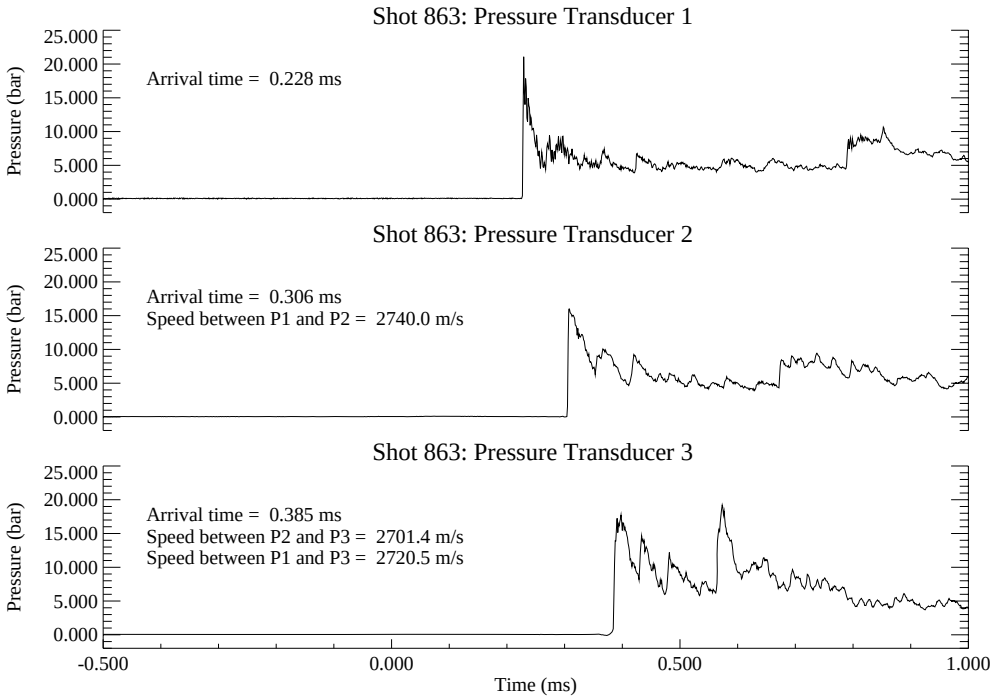

Figure B.28: Shot 863 pressure traces.

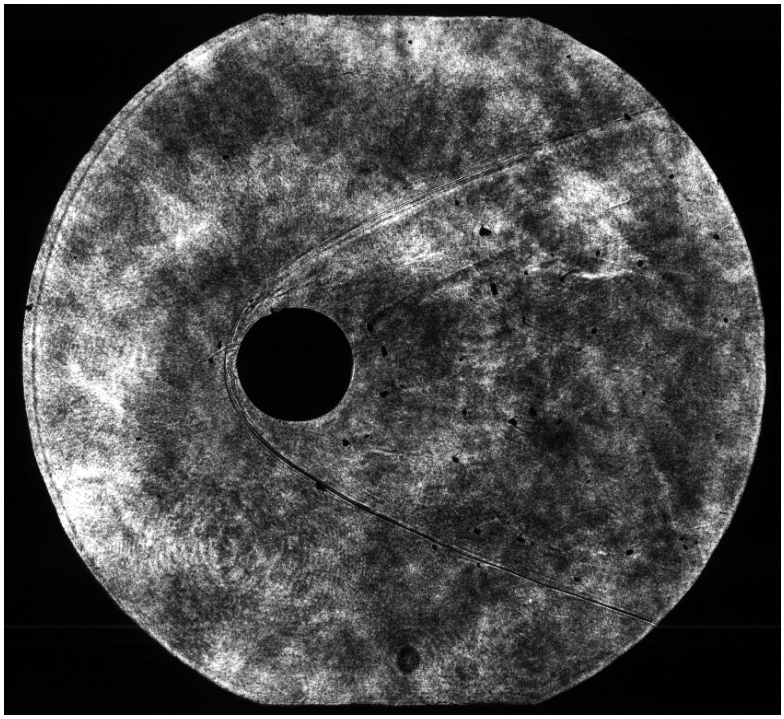

Figure B.29: Shot 1819 Shadowgraph: $2H_2+O_2+2N_2$ at 0.110 bar, 2300 m/s.

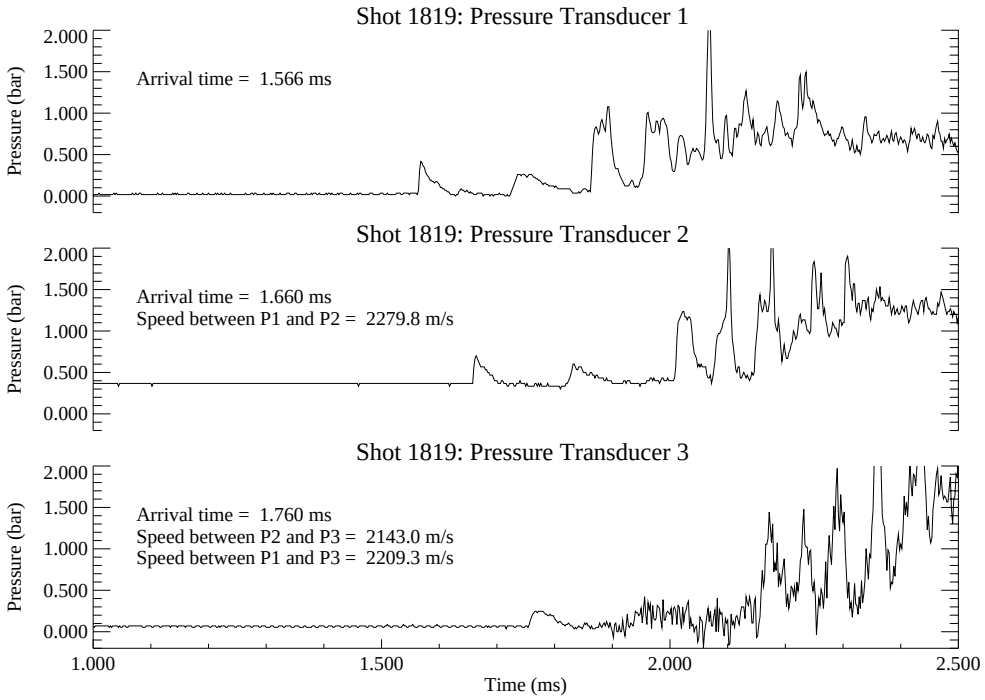

Figure B.30: Shot 1819 pressure traces.

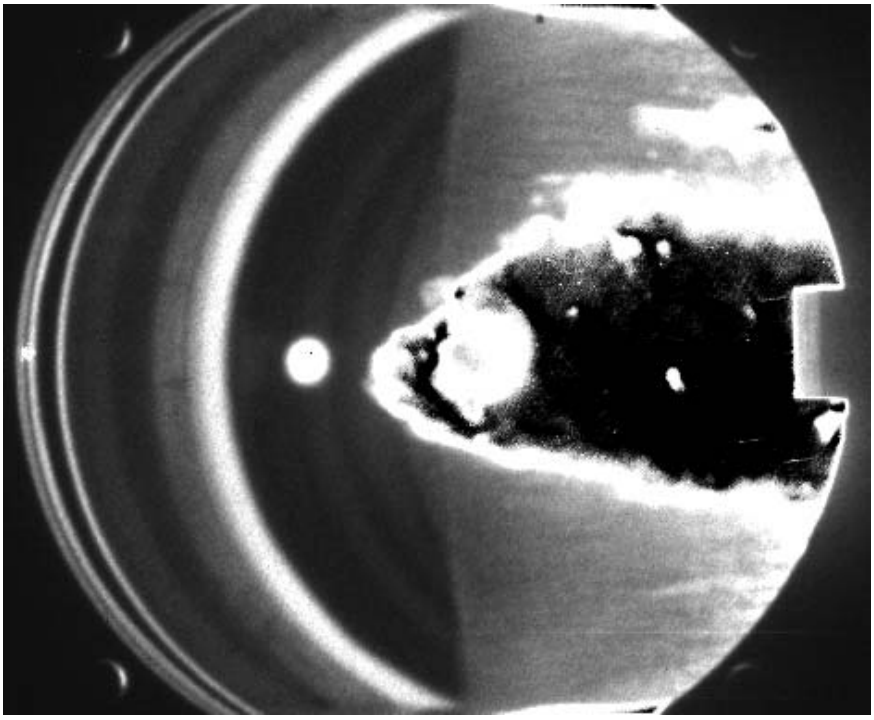

Figure B.31: Shot 1814 ICCD: $2H_2+O_2+2N_2$ at 0.557 bar, 2320 m/s.

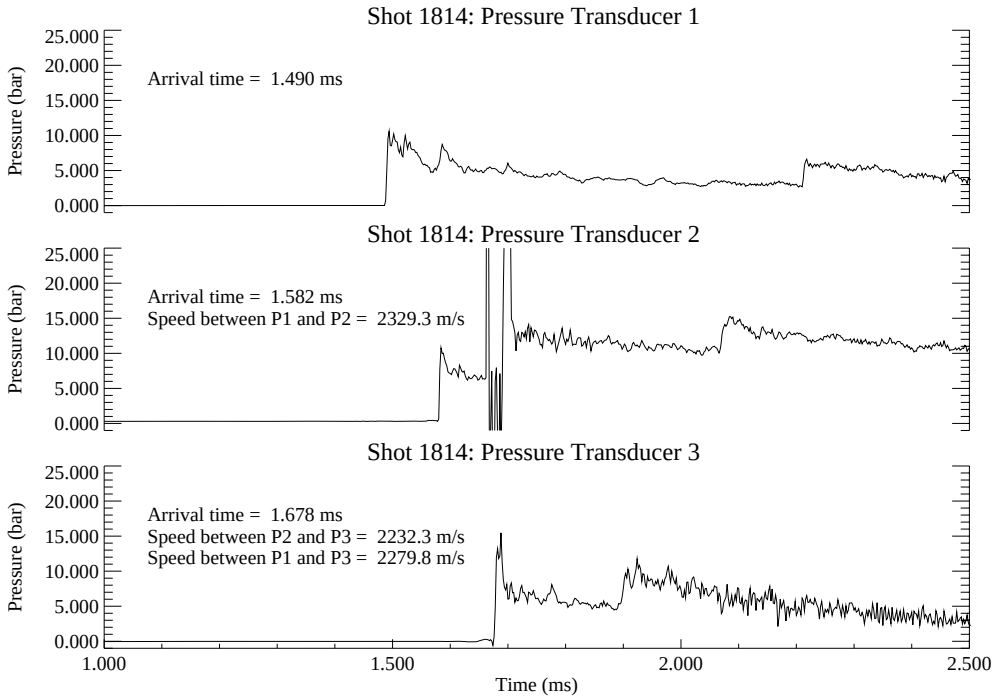

Figure B.32: Shot 1814 pressure traces.

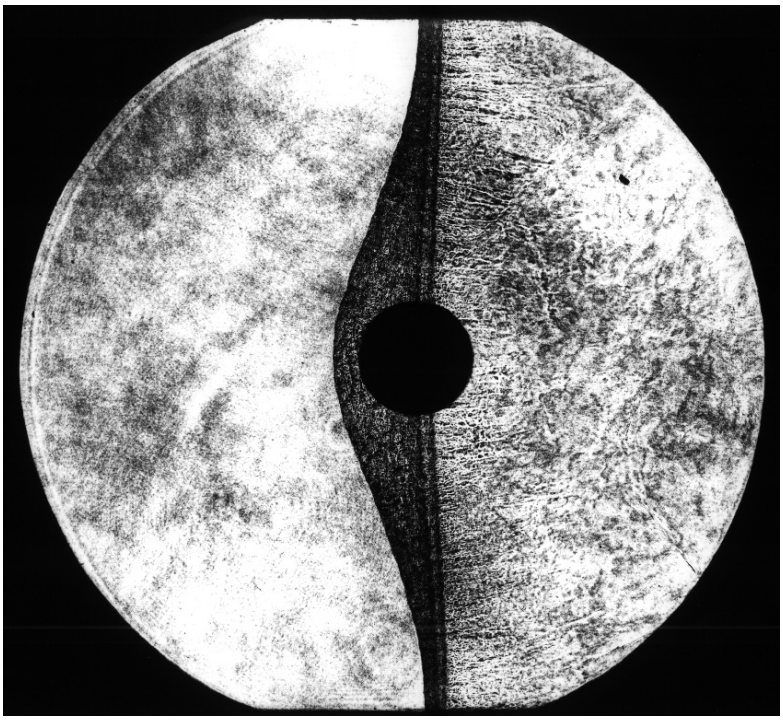

(a) Shadowgraph

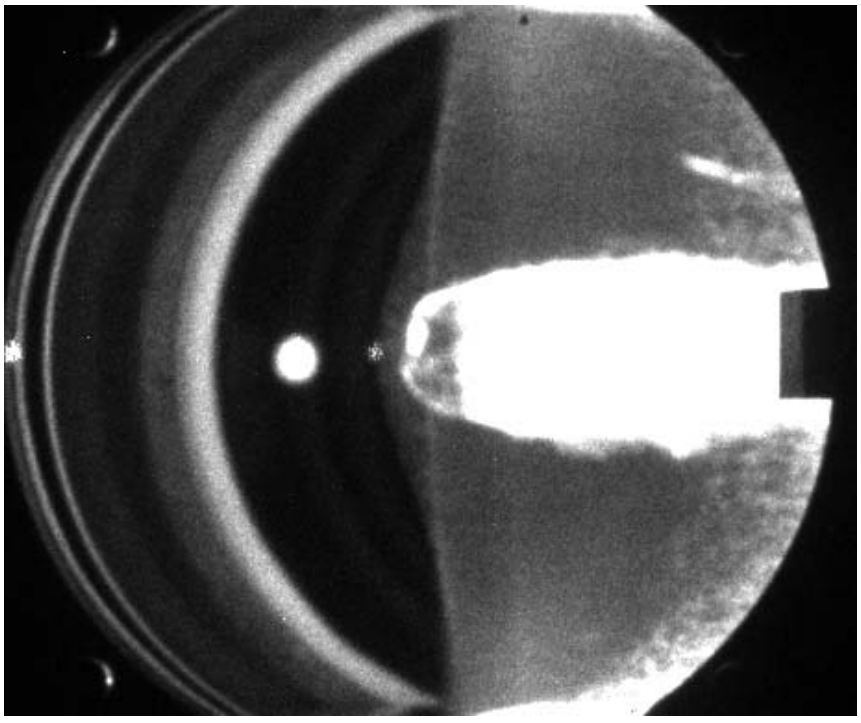

(b) ICCD

Figure B.33: Shot 1815: $2H_2+O_2+2N_2$ at 0.557 bar, 2290 m/s.

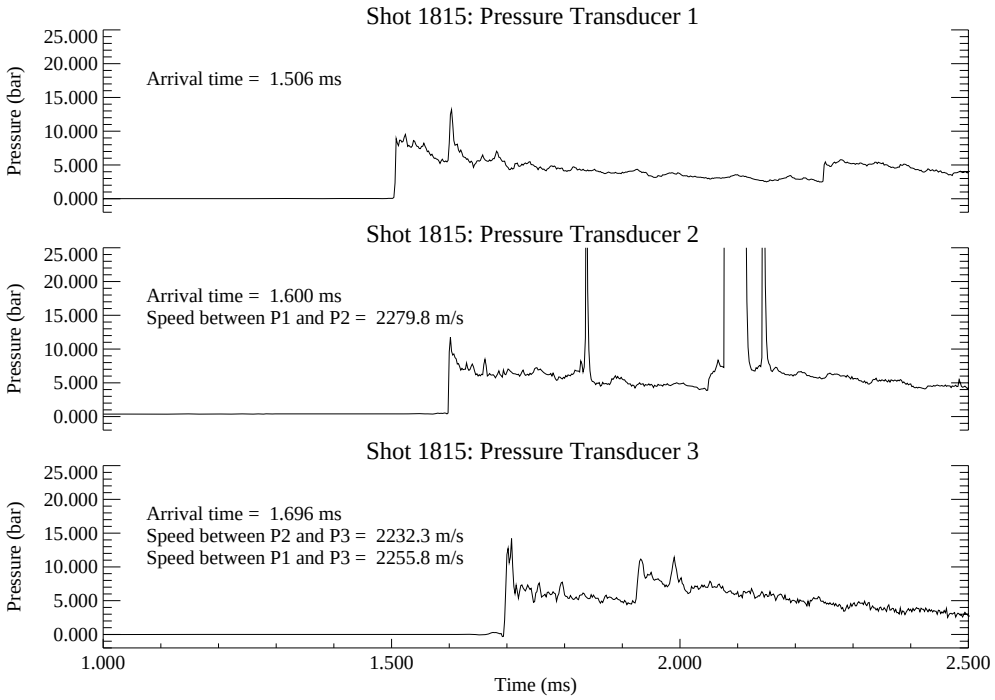

Figure B.34: Shot 1815 pressure traces.

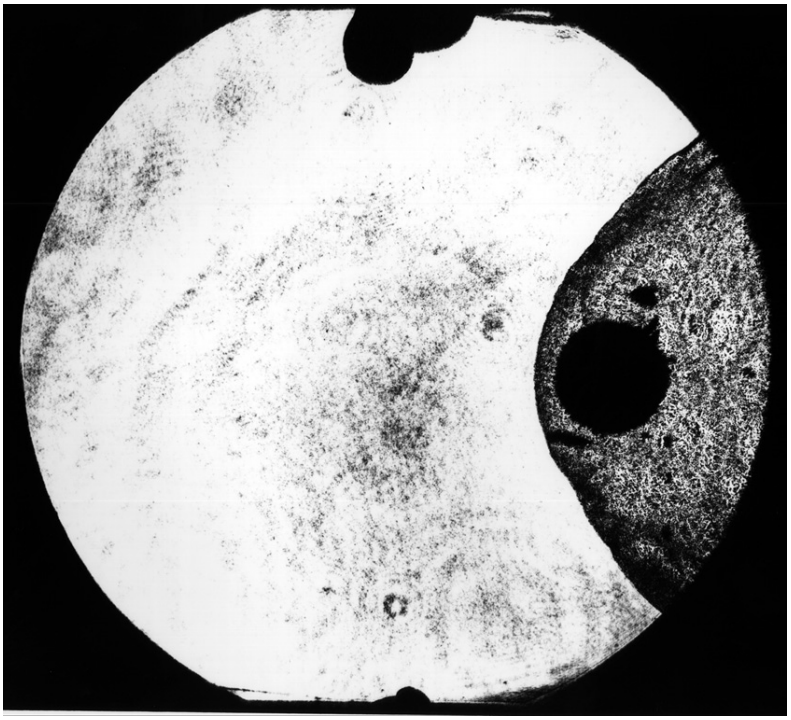

Figure B.35: Shot 1022 Shadowgraph: $2H_2+O_2+3N_2$ at 0.831 bar, 2260 m/s.

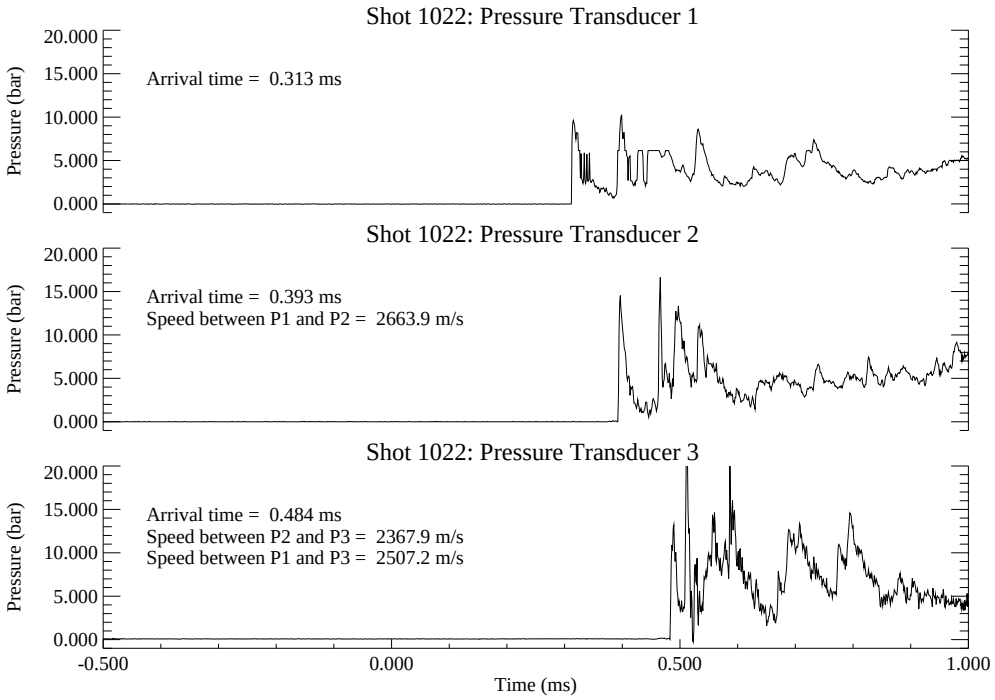

Figure B.36: Shot 1022 pressure traces.

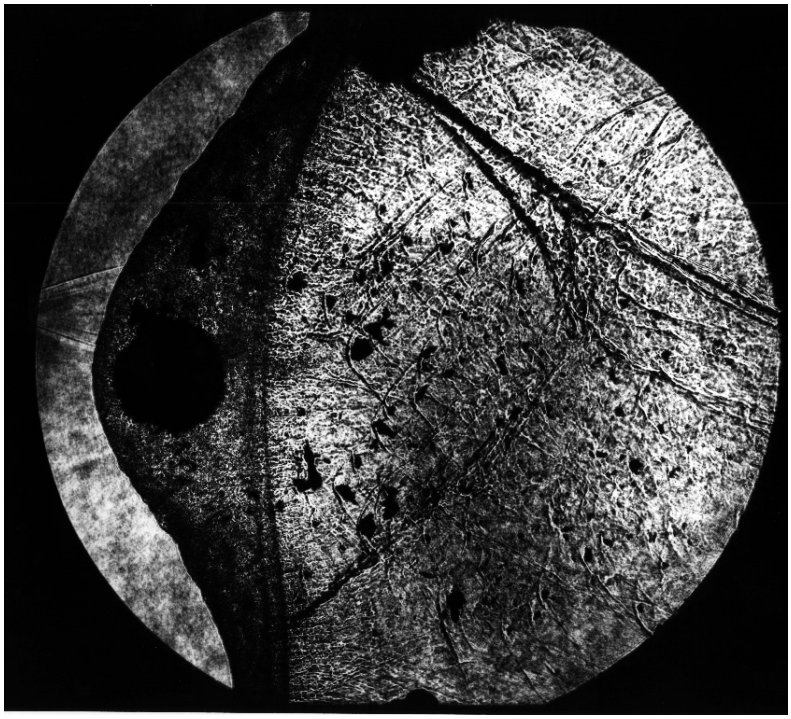

Figure B.37: Shot 1023 Shadowgraph: $2H_2+O_2+3N_2$ at 0.831 bar, 2330 m/s.

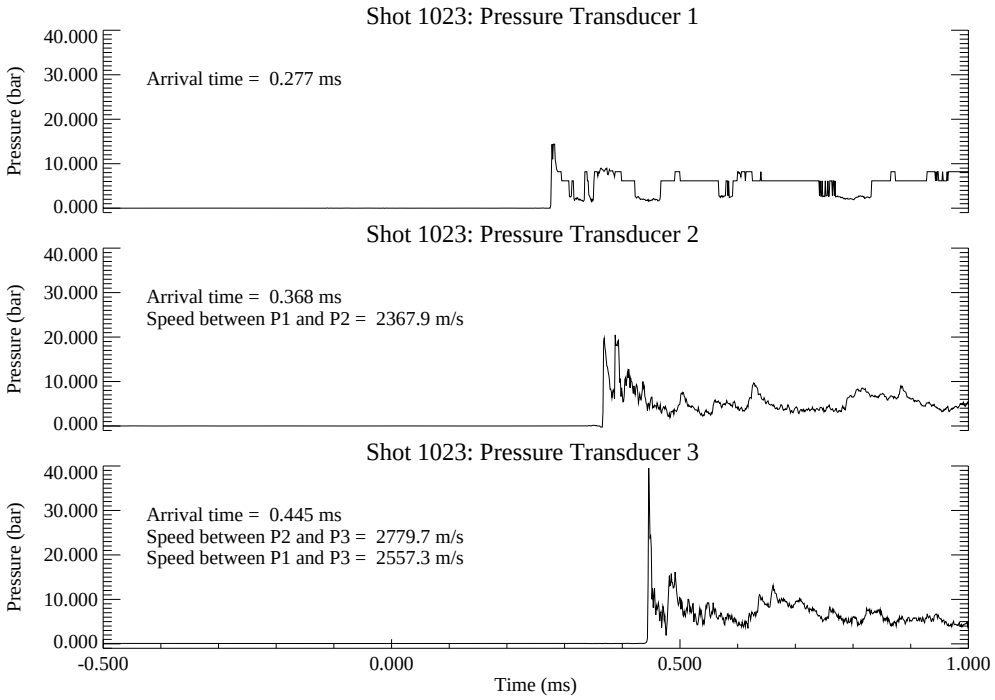

Figure B.38: Shot 1023 pressure traces.

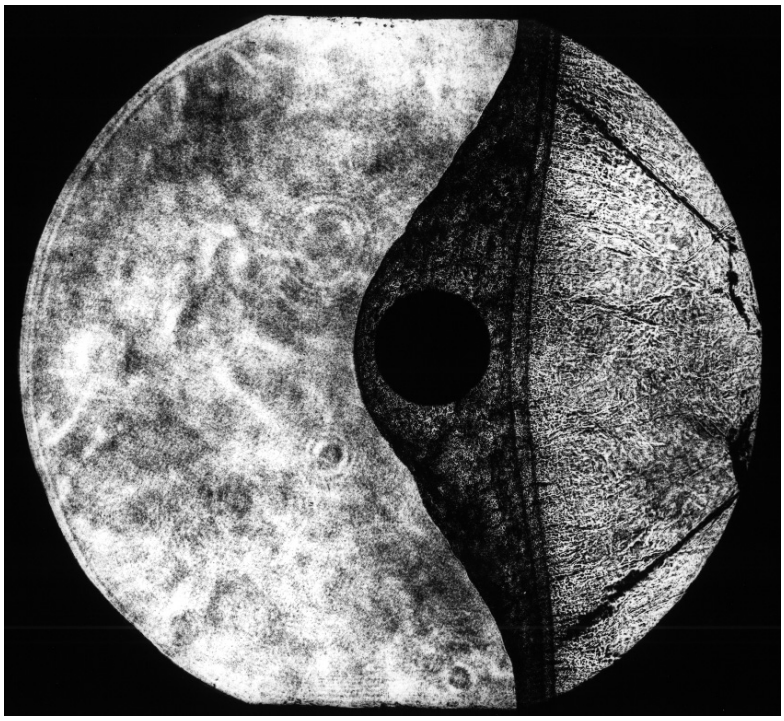

(a) Shadowgraph

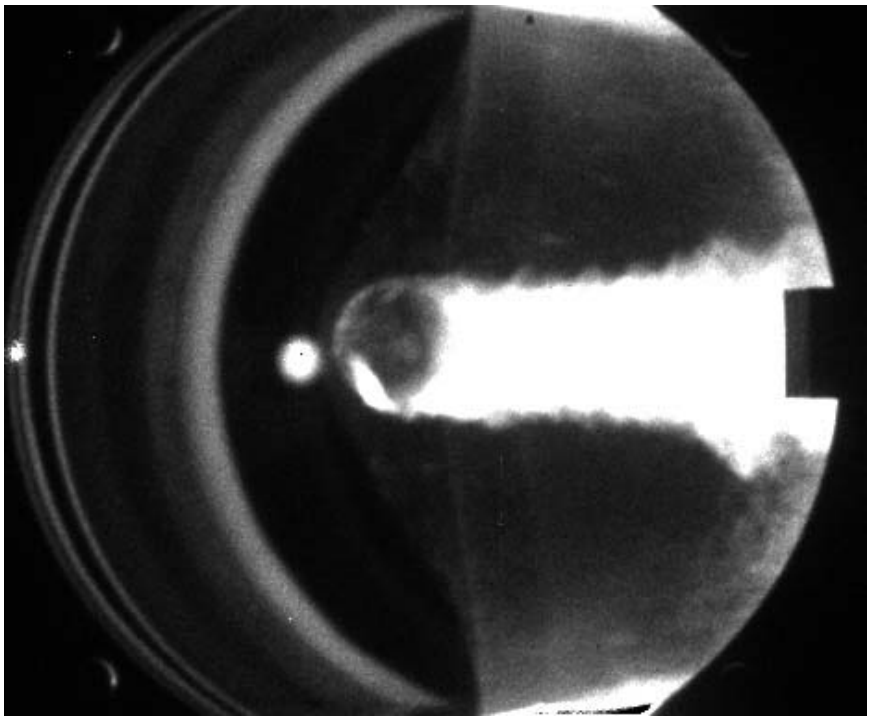

(b) ICCD

Figure B.39: Shot 1813: $2H_2+O_2+3N_2$ at 0.831 bar, 2300 m/s.

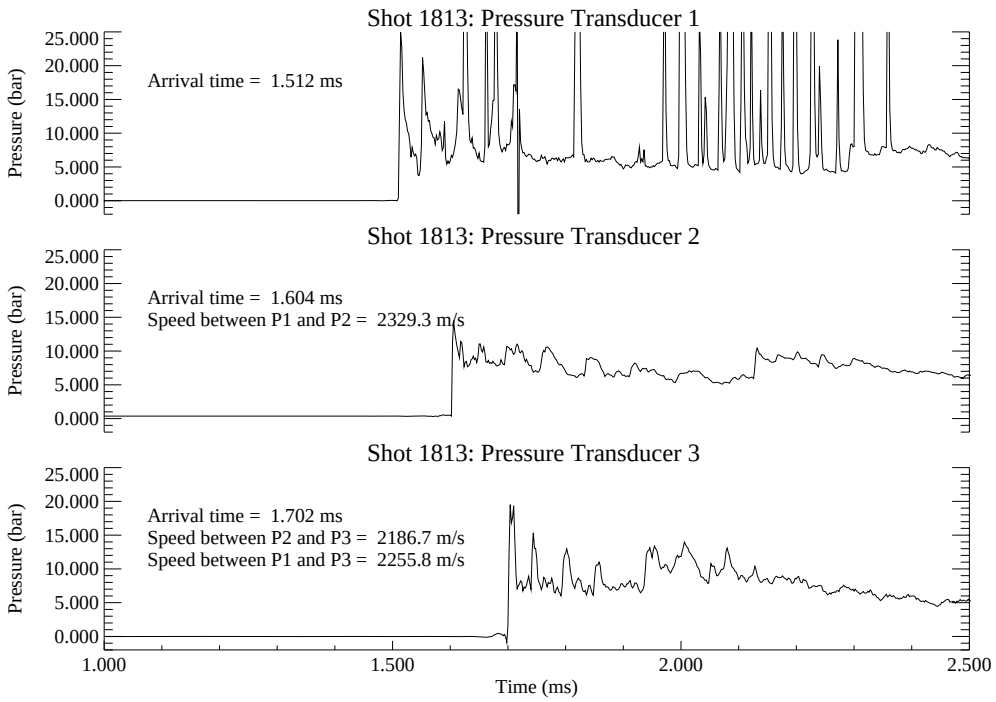

Figure B.40: Shot 1813 pressure traces.

Figure B.41: Shot 1021 Shadowgraph: $2H_2+O_2+3.76N_2$ at 0.100 bar, 2300 m/s.

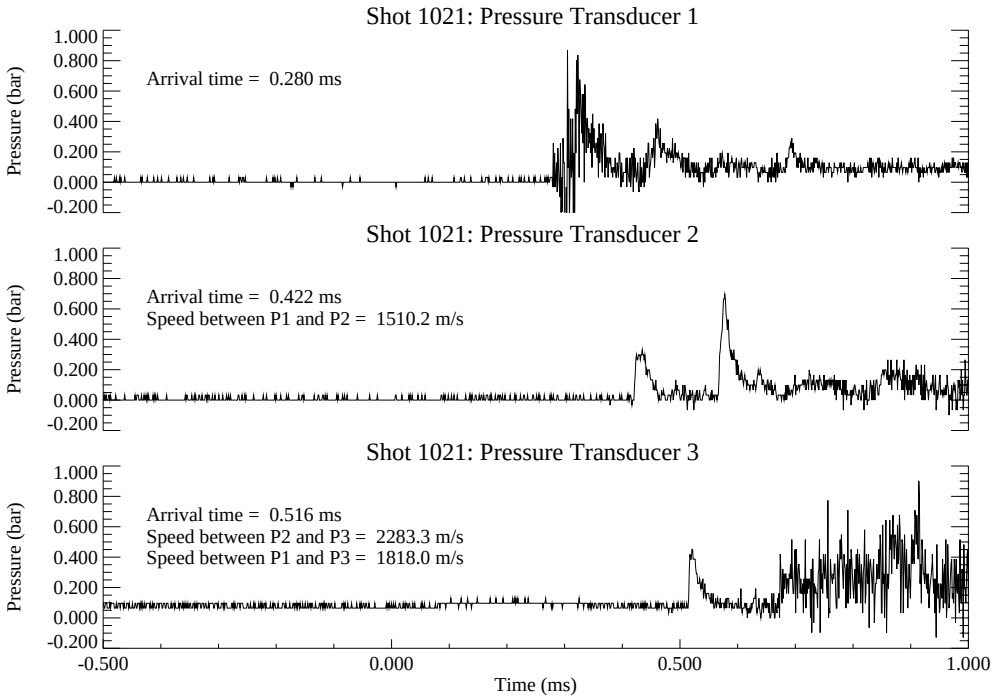

Figure B.42: Shot 1021 pressure traces.

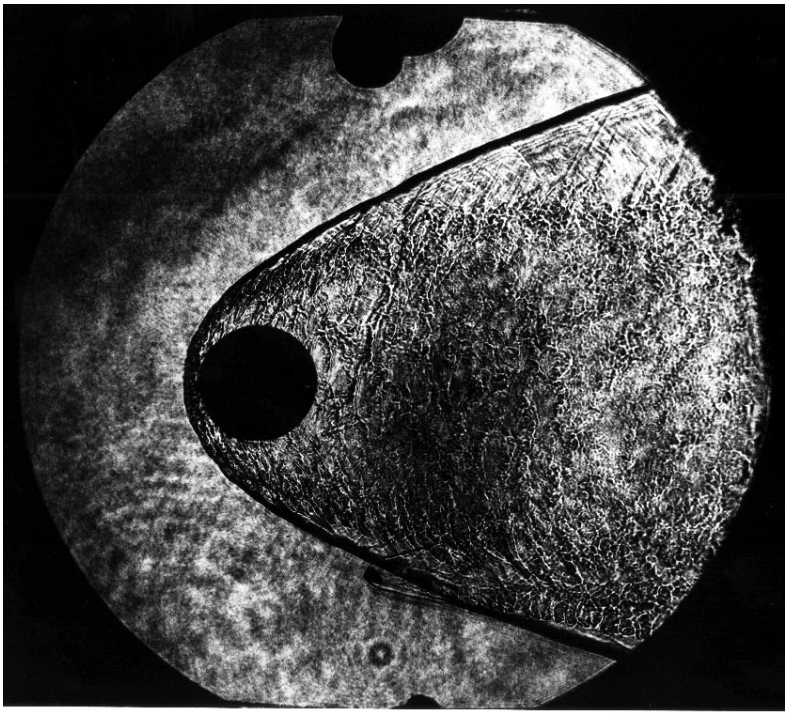

Figure B.43: Shot 1015 Shadowgraph: $2H_2+O_2+3.76N_2$ at 0.421 bar, 2430 m/s.

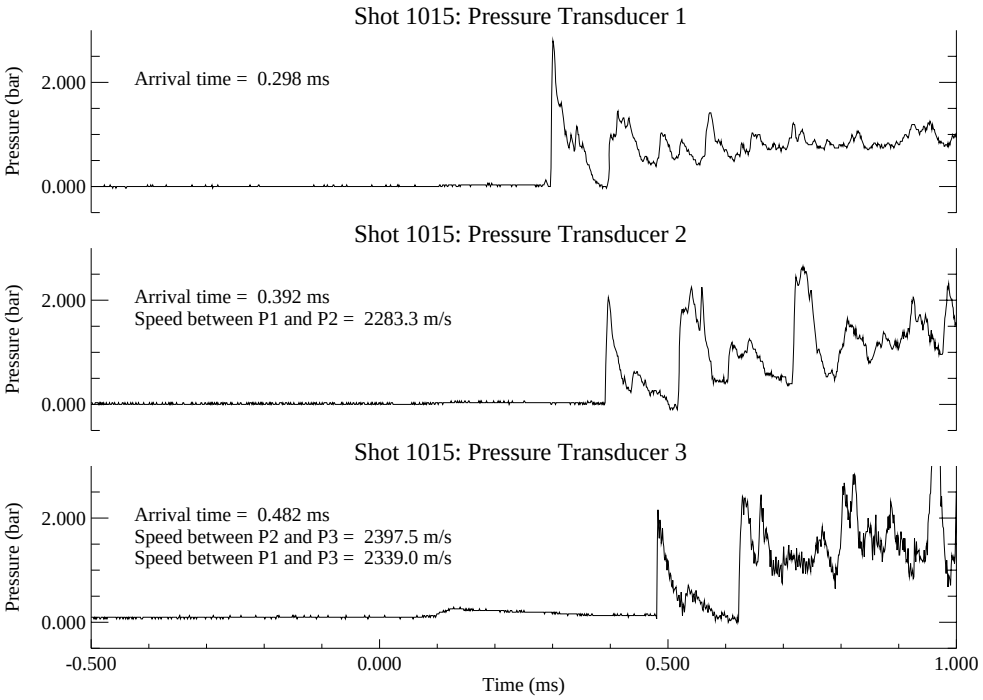

Figure B.44: Shot 1015 pressure traces.

Figure B.45: Shot 1016 Shadowgraph: $2H_2+O_2+3.76N_2$ at 0.853 bar, 2560 m/s.

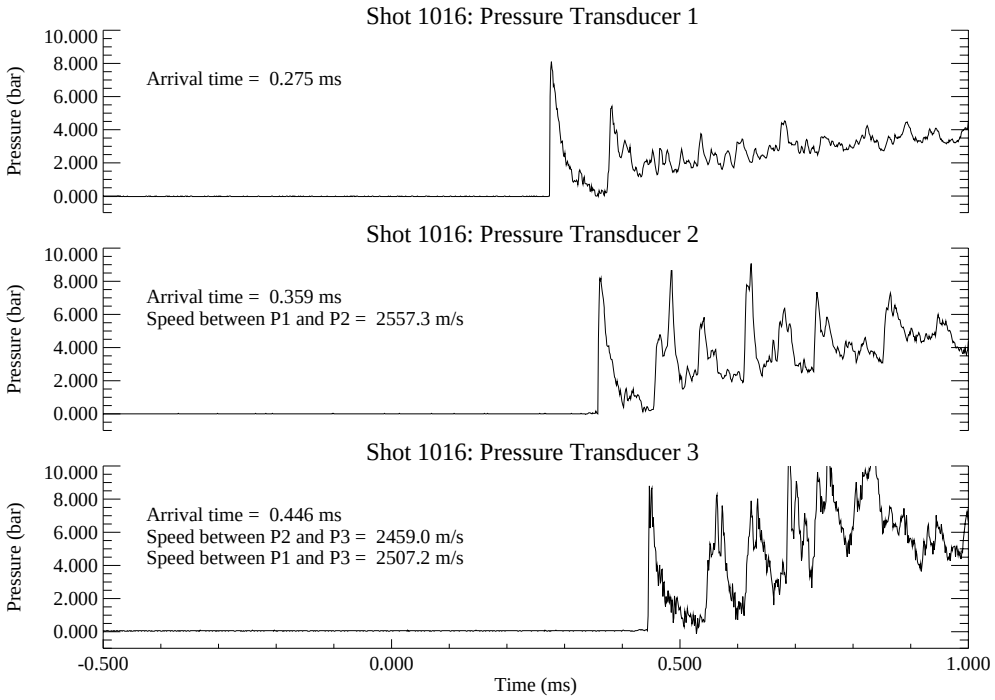

Figure B.46: Shot 1016 pressure traces.

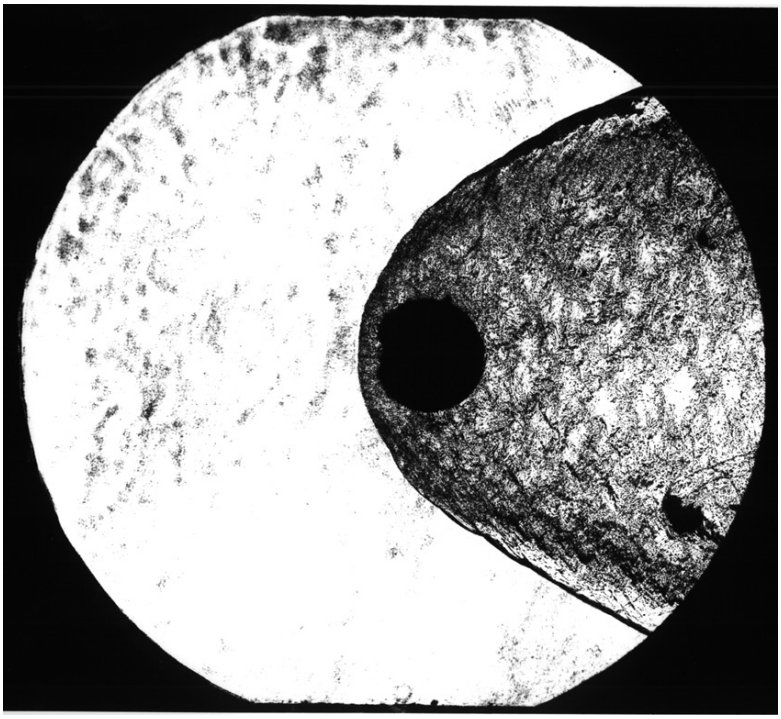

Figure B.47: Shot 1807 Shadowgraph: $2H_2+O_2+3.76N_2$ at 1.000 bar, 2230 m/s.

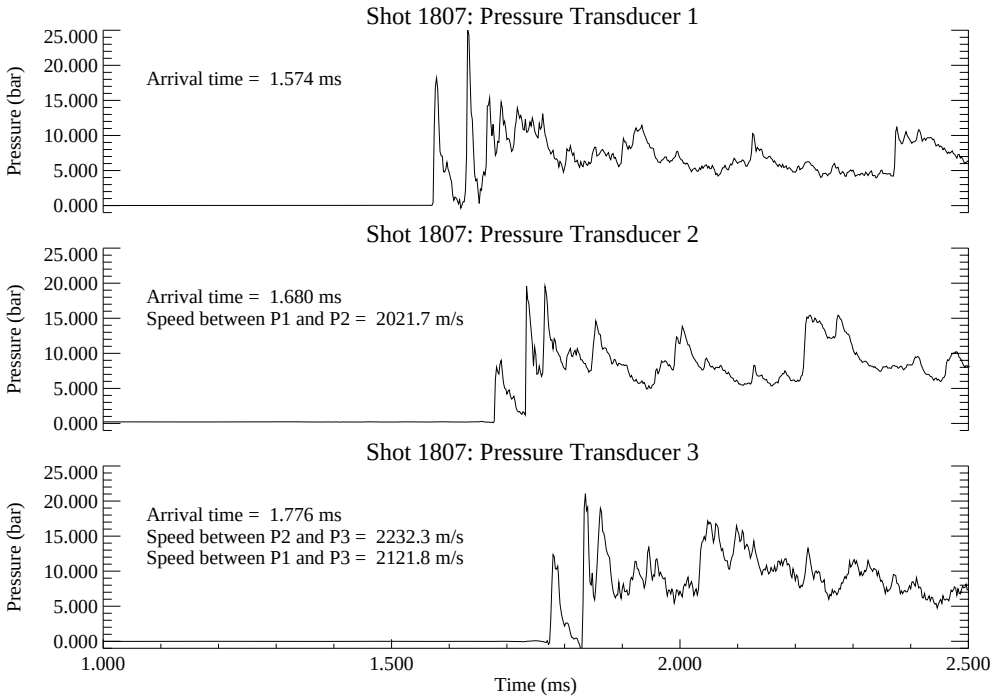

Figure B.48: Shot 1807 pressure traces.

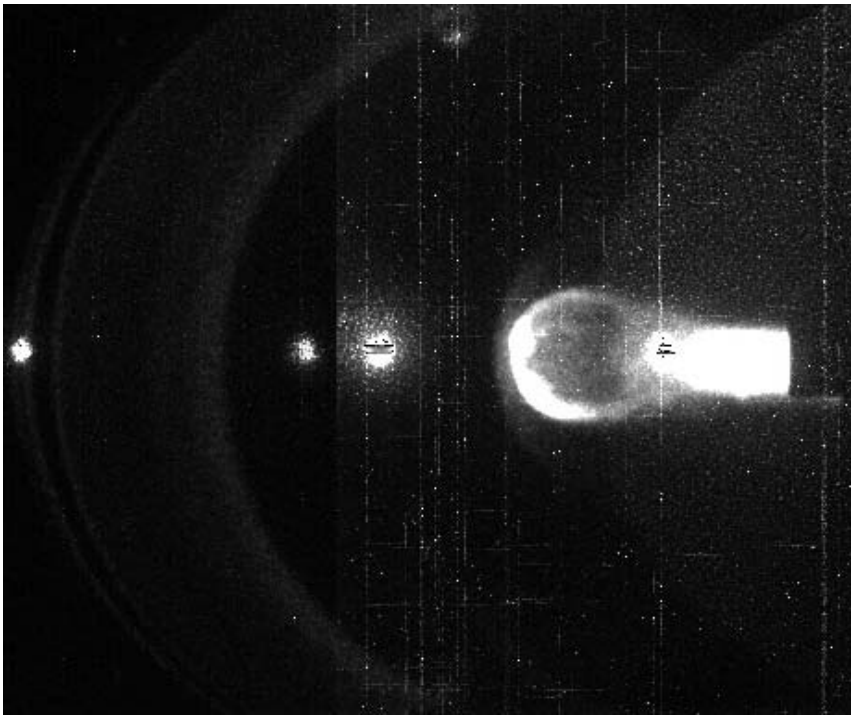

Figure B.49: Shot 1817 ICCD: $2H_2+O_2+3.76N_2$ at 1.120 bar, 2310 m/s.

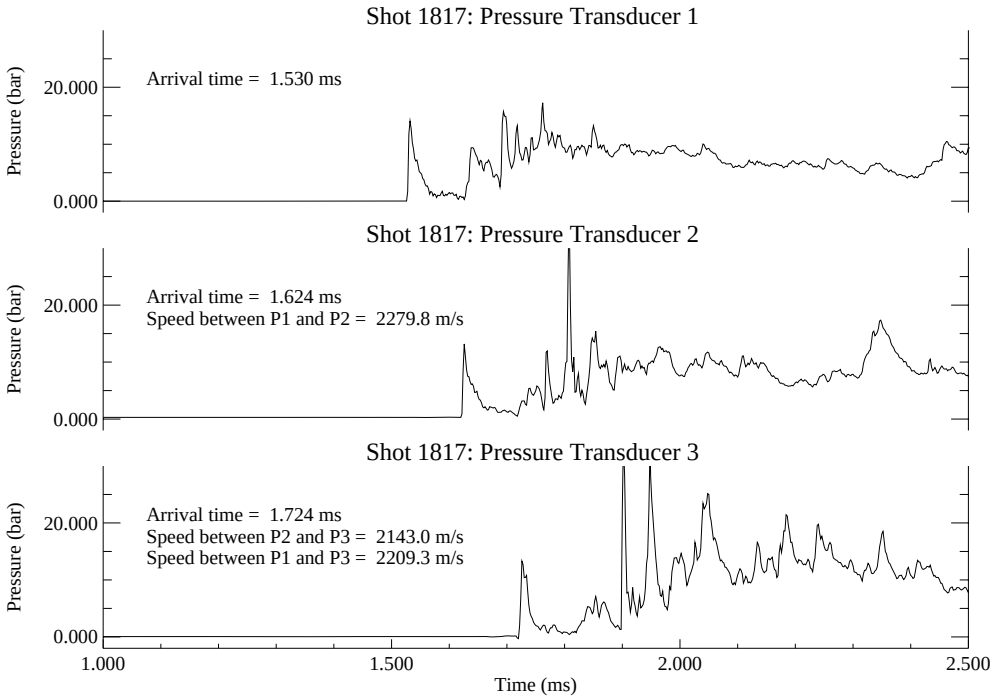

Figure B.50: Shot 1817 pressure traces.

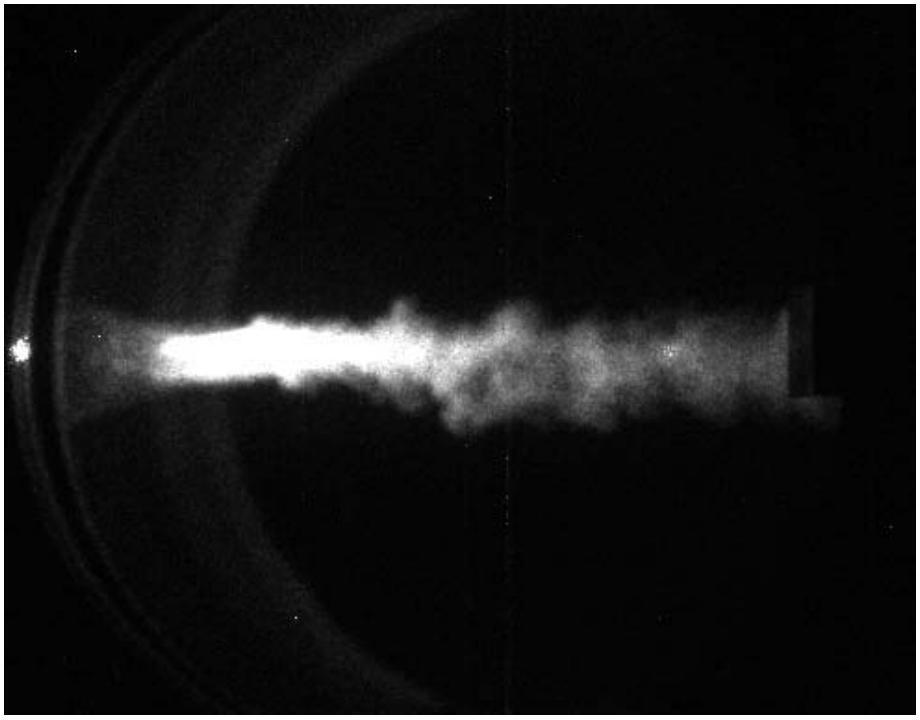

Figure B.51: Shot 1816 ICCD: $2H_2+O_2+3.76N_2$ at 1.200 bar, 2330 m/s.

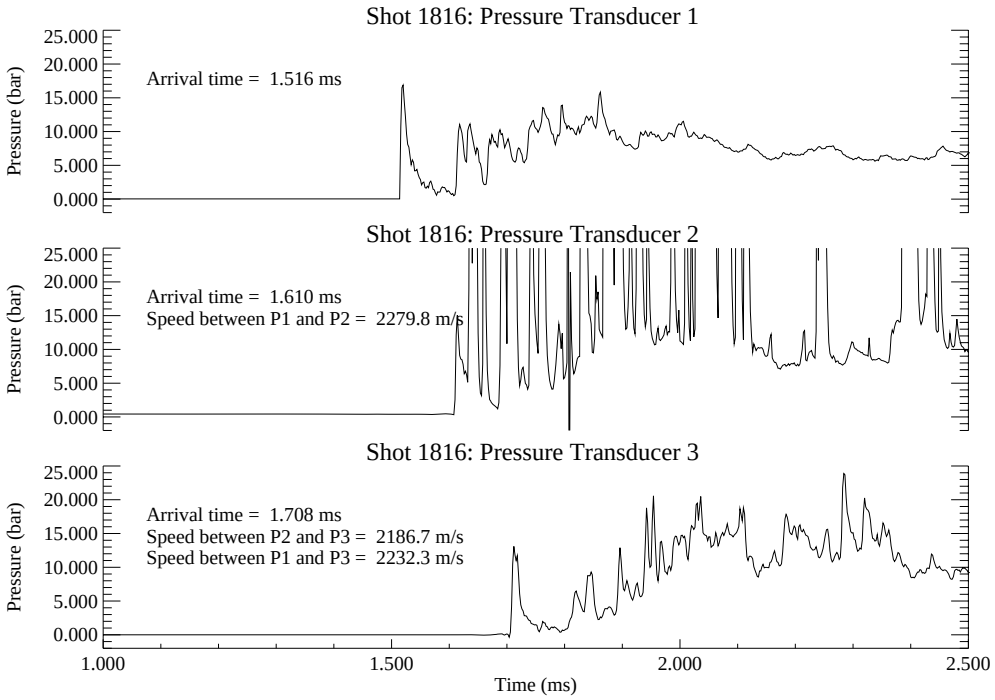

Figure B.52: Shot 1816 pressure traces.

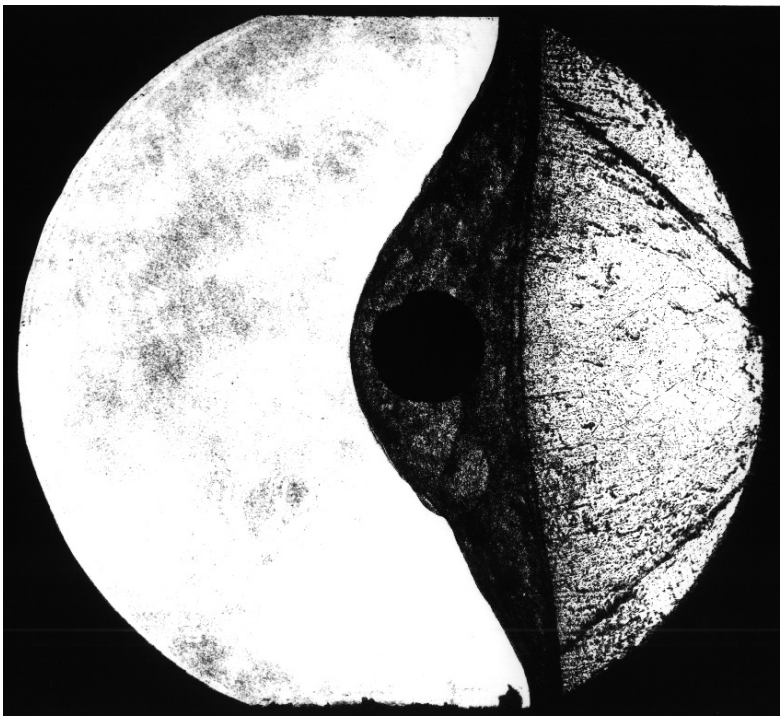

(a) Shadowgraph

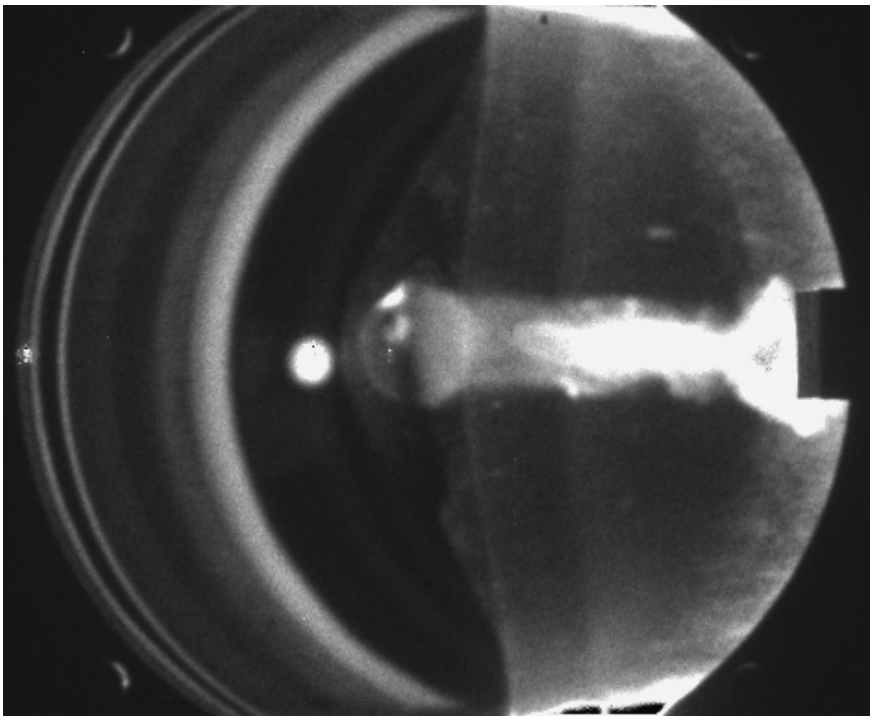

(b) ICCD

Figure B.53: Shot 1812: $2H_2+O_2+3.76N_2$ at 1.700 bar, 2280 m/s.

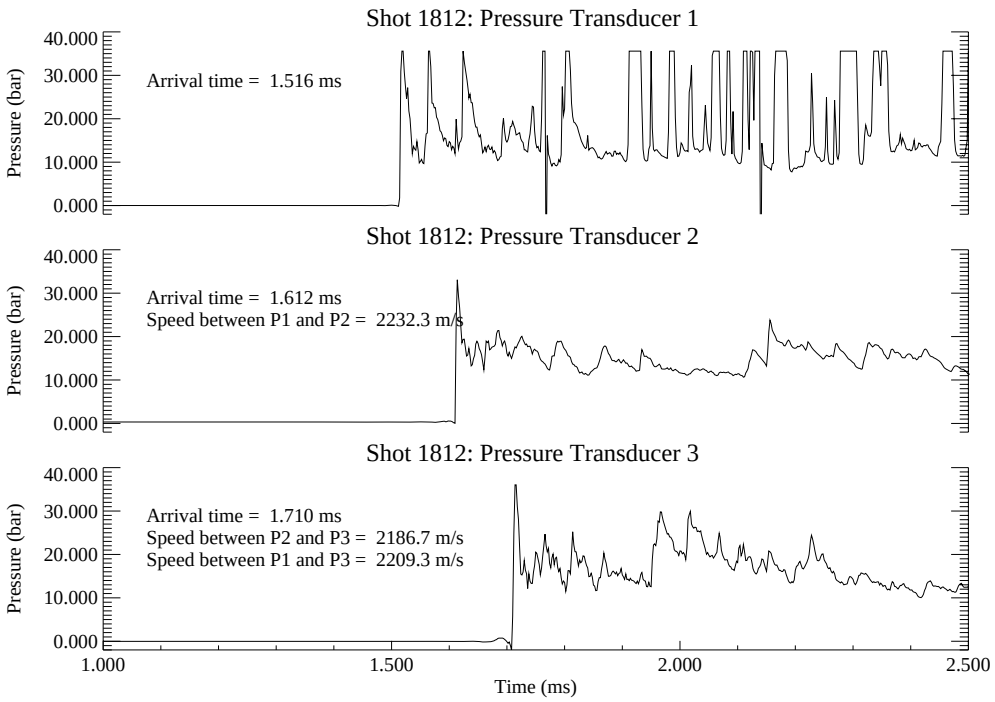

Figure B.54: Shot 1812 pressure traces.

Figure B.55: Shot 1018 Shadowgraph: $2H_2+O_2+3.76N_2$ at 1.707 bar, 2370 m/s.

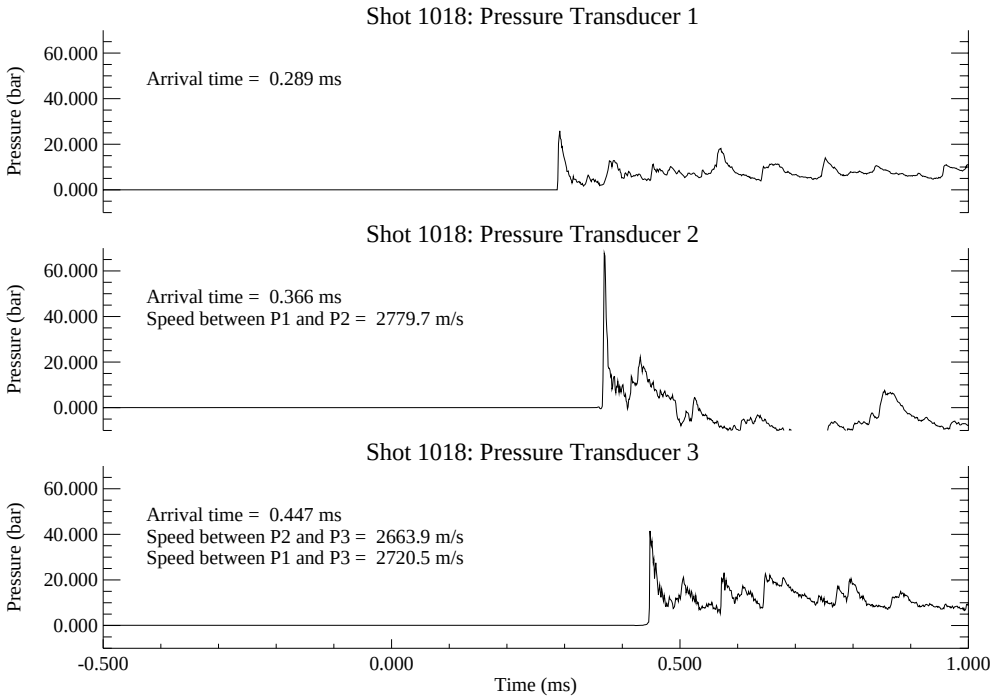

Figure B.56: Shot 1018 pressure traces.

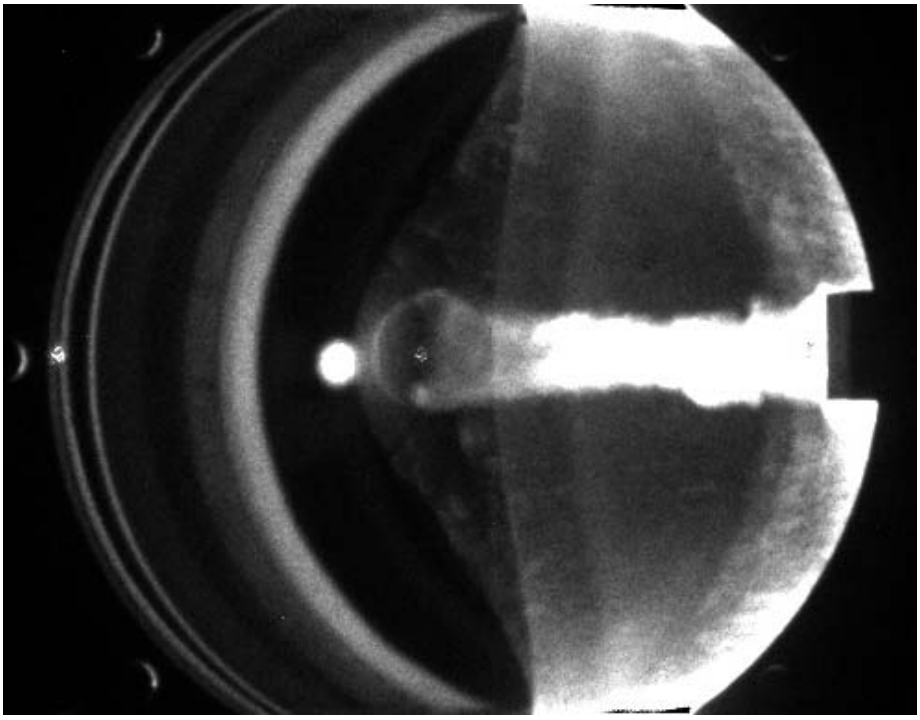

Figure B.57: Shot 1821 ICCD: $2H_2+O_2+3.76N_2$ at 1.900 bar, 2330 m/s.

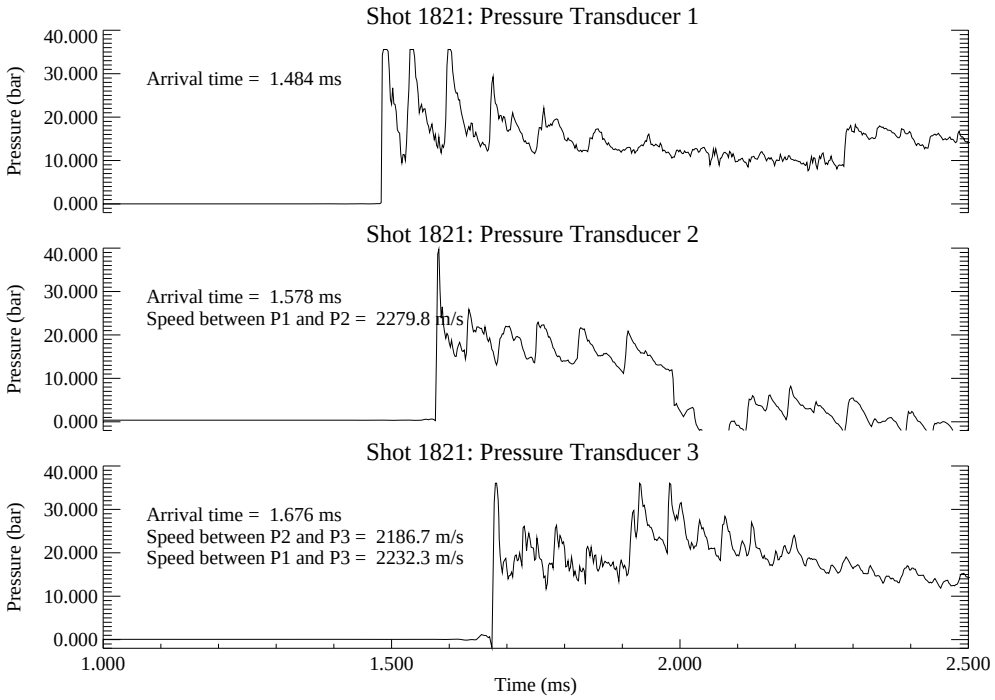

Figure B.58: Shot 1821 pressure traces.

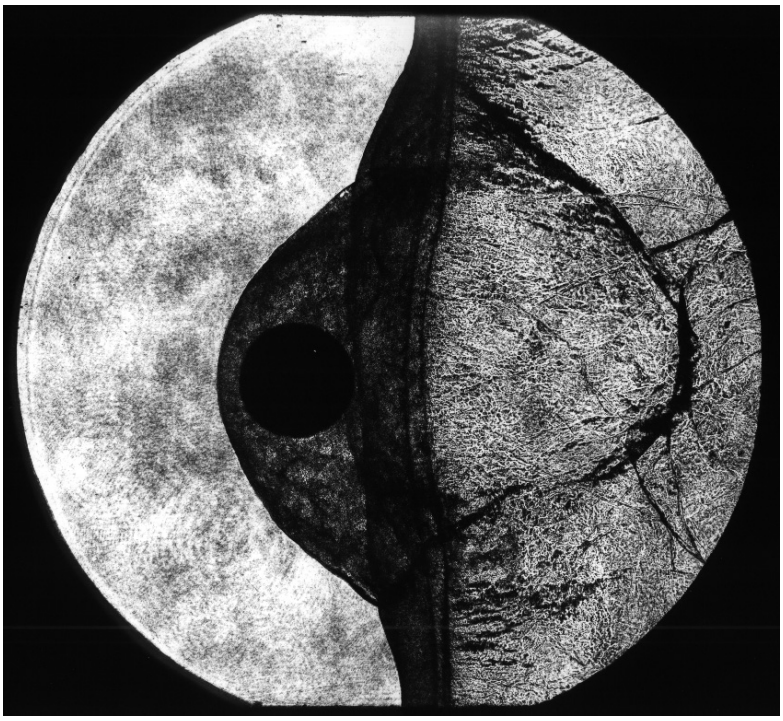

(a) Shadowgraph

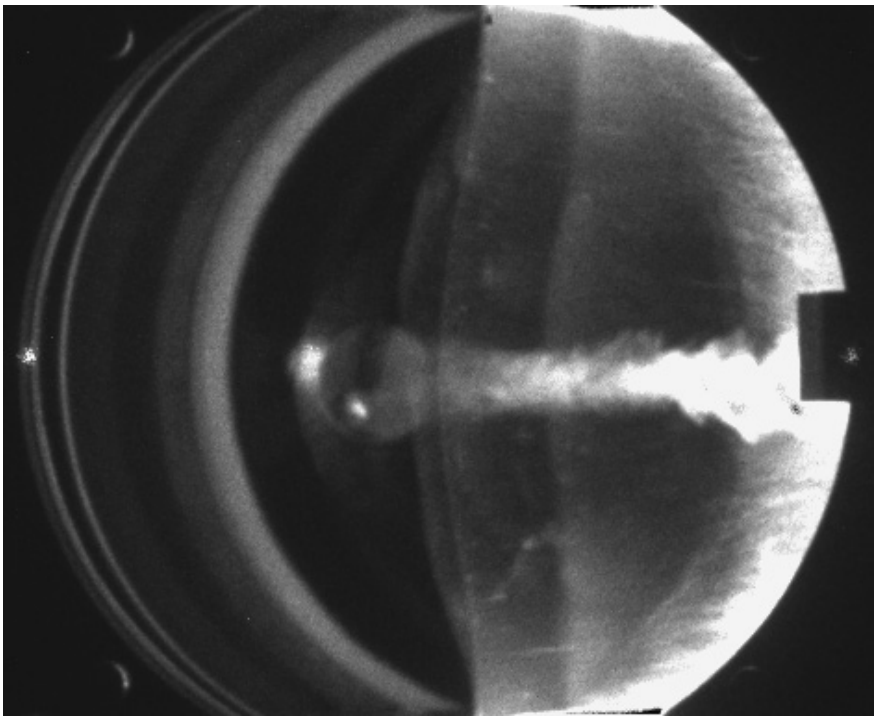

(b) ICCD

Figure B.59: Shot 1820: $2H_2+O_2+3.76N_2$ at 2.000 bar, 2300 m/s.

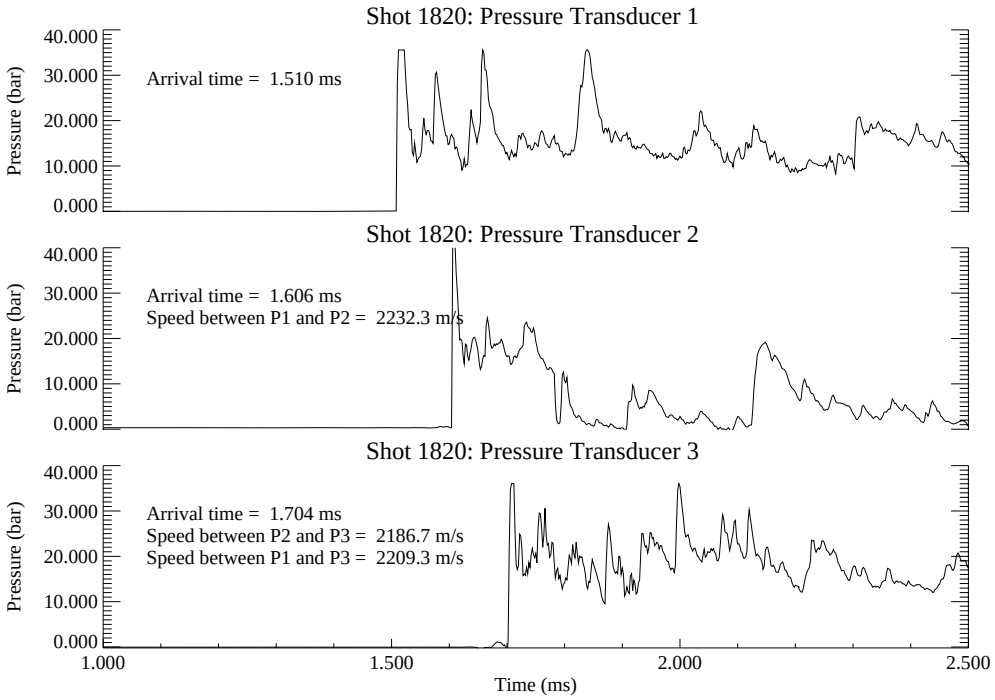

Figure B.60: Shot 1820 pressure traces.

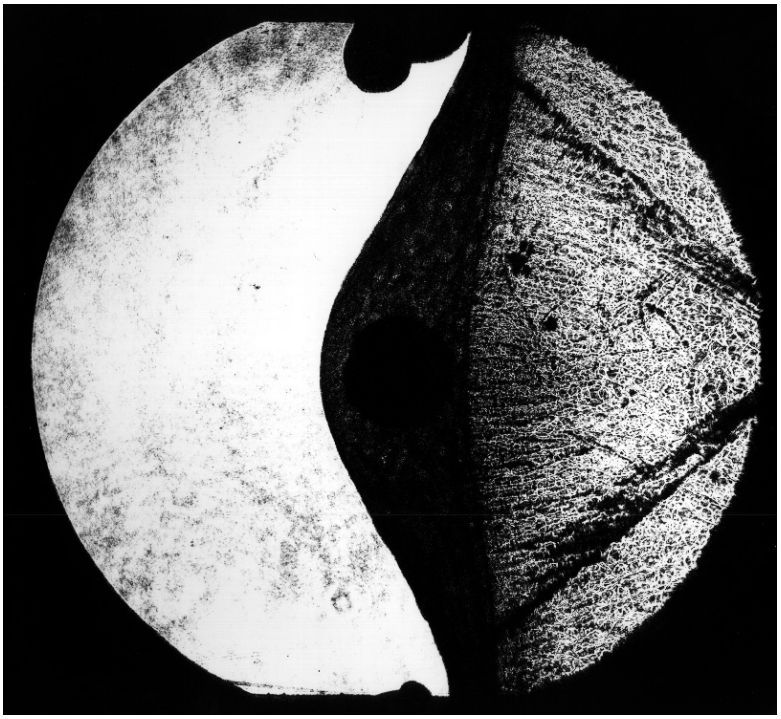

Figure B.61: Shot 1020 Shadowgraph: $2H_2+O_2+3.76N_2$ at 2.560 bar, 2360 m/s.

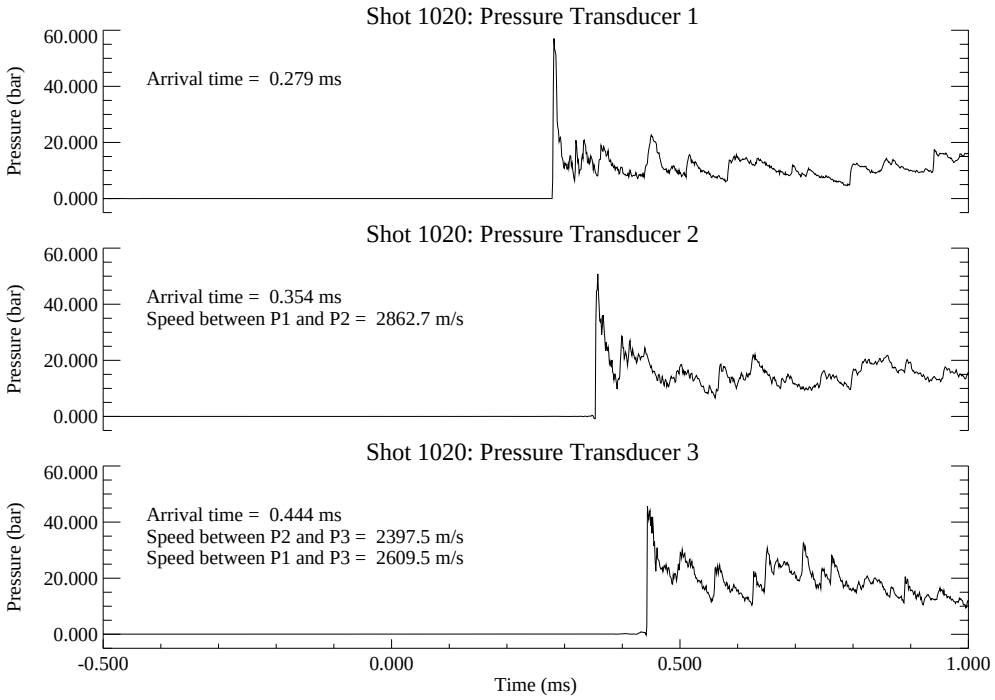

Figure B.62: Shot 1020 pressure traces.

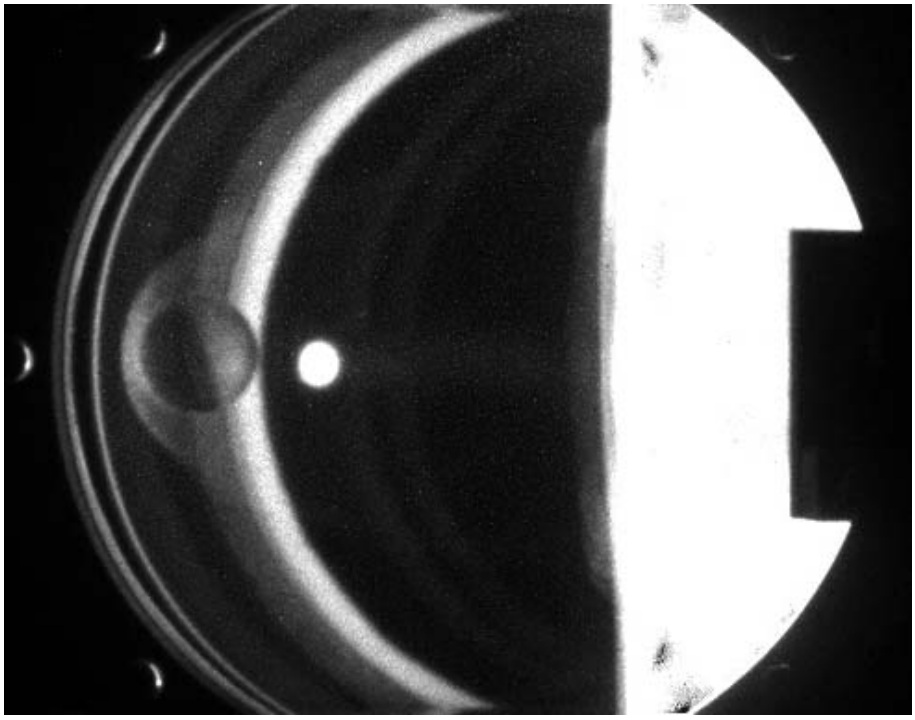

Figure B.63: Shot 1829 ICCD: $C_2H_4+3O_2+5N_2$ at 0.300 bar, 2350 m/s.

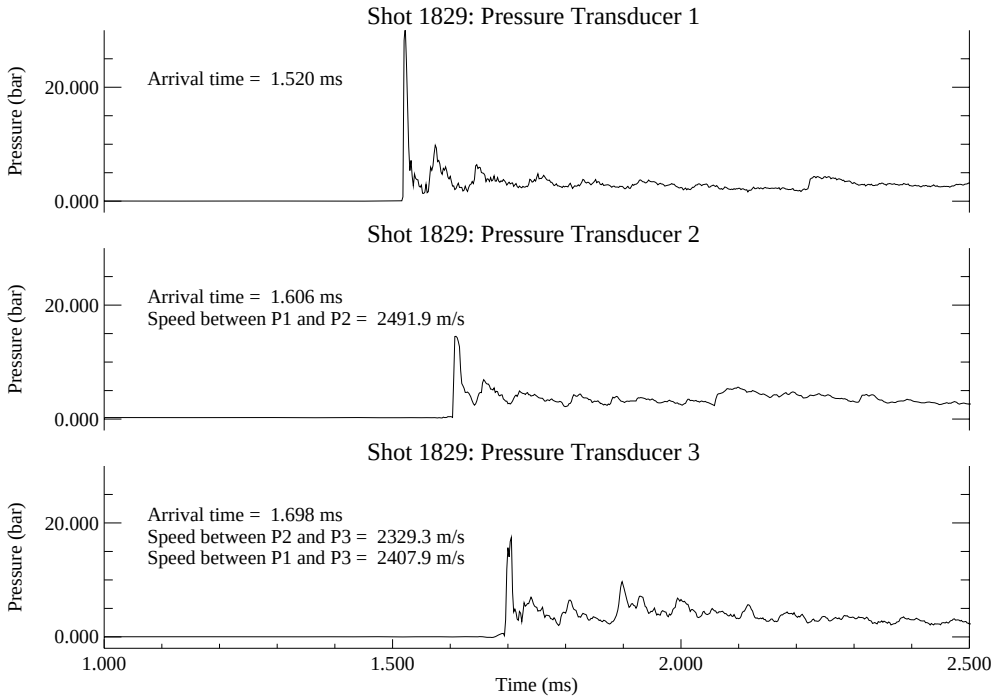

Figure B.64: Shot 1829 pressure traces.

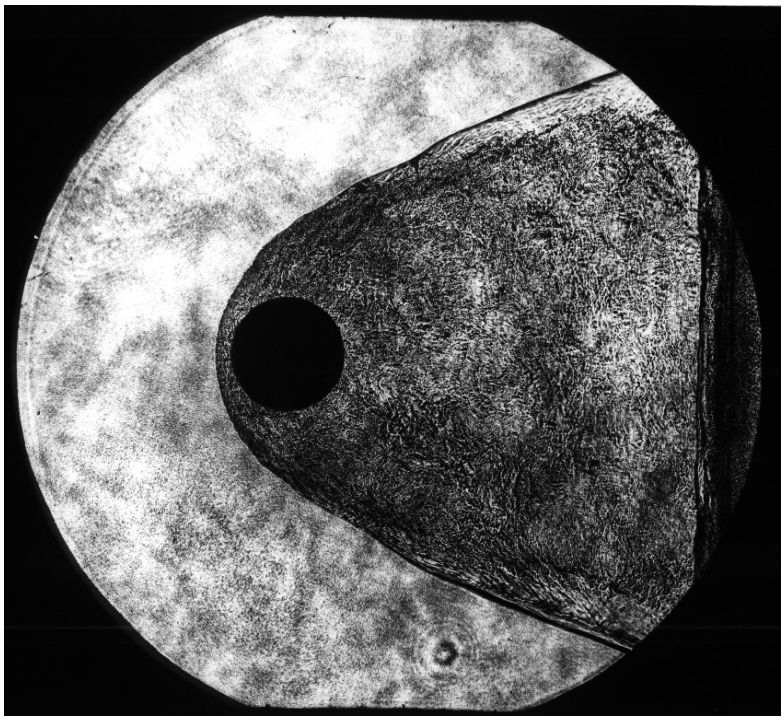

(a) Shadowgraph

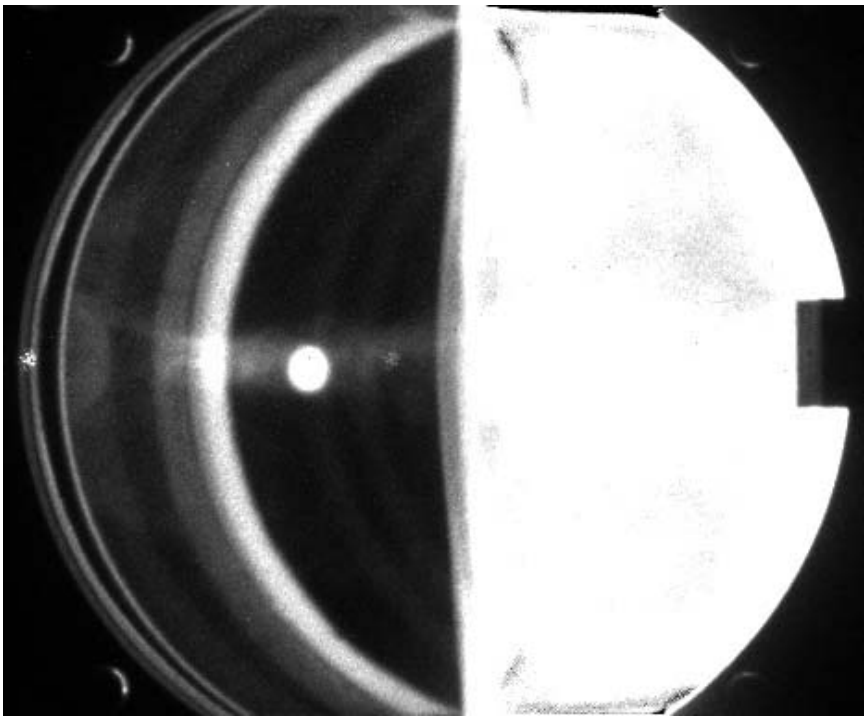

(b) ICCD

Figure B.65: Shot 1823: C_2H_4+$3O_2$+$5N_2$ at 0.350 bar, 2370 m/s.

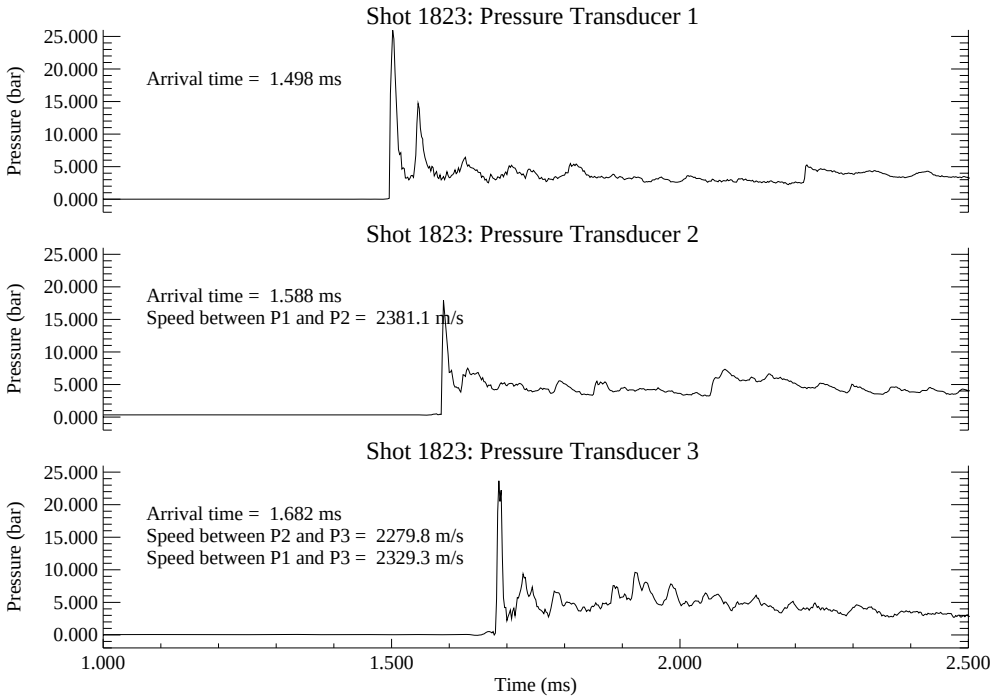

Figure B.66: Shot 1823 pressure traces.

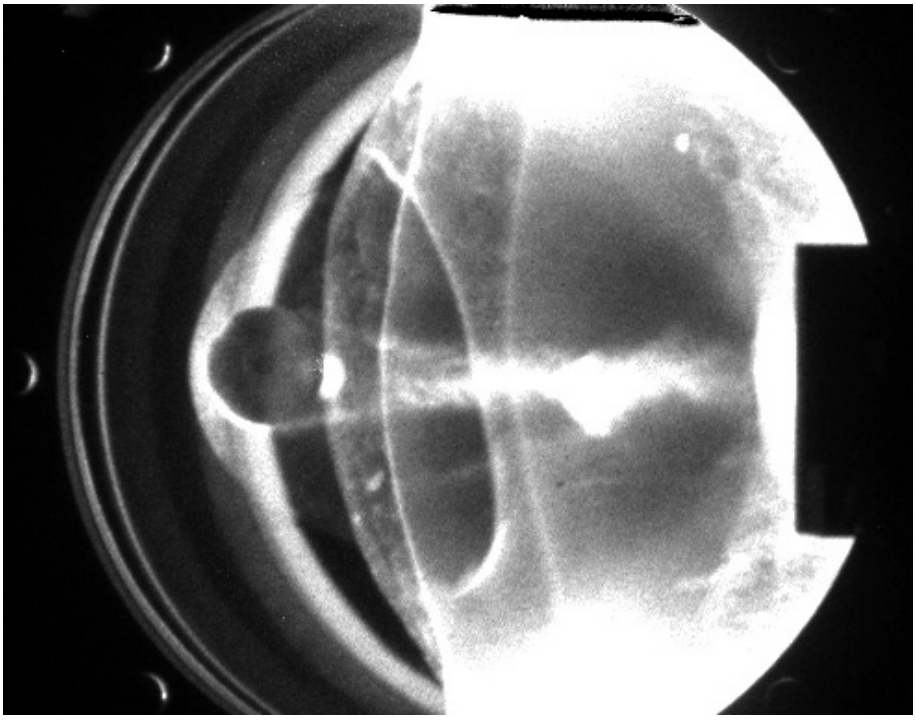

Figure B.67: Shot 1832 ICCD: C_2H_4+3O_2+4.3N_2 at 0.350 bar, 2400 m/s.

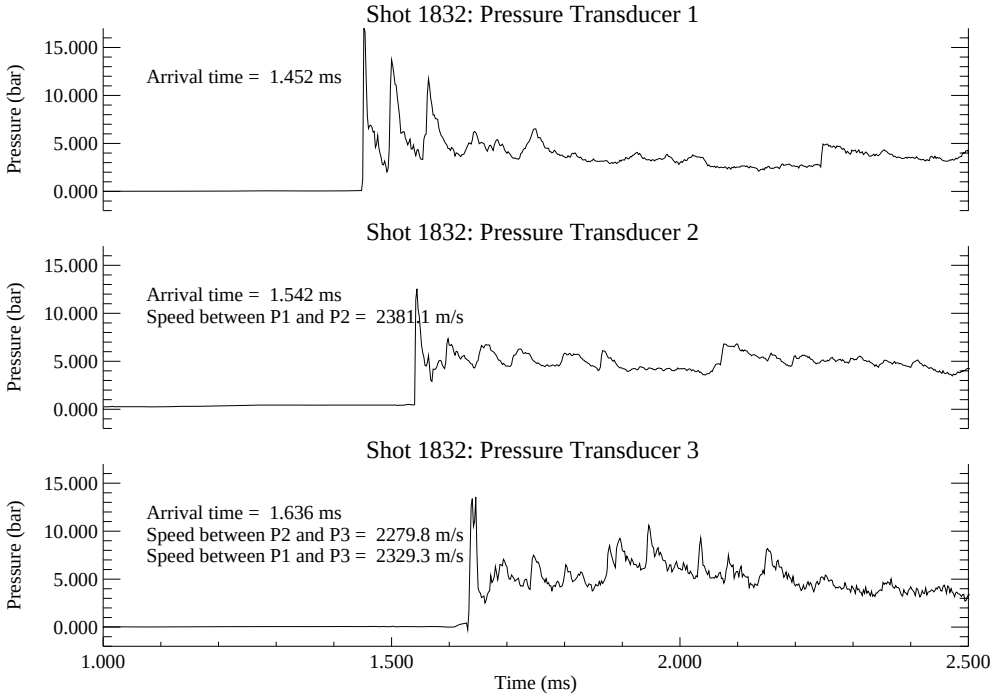

Figure B.68: Shot 1832 pressure traces.

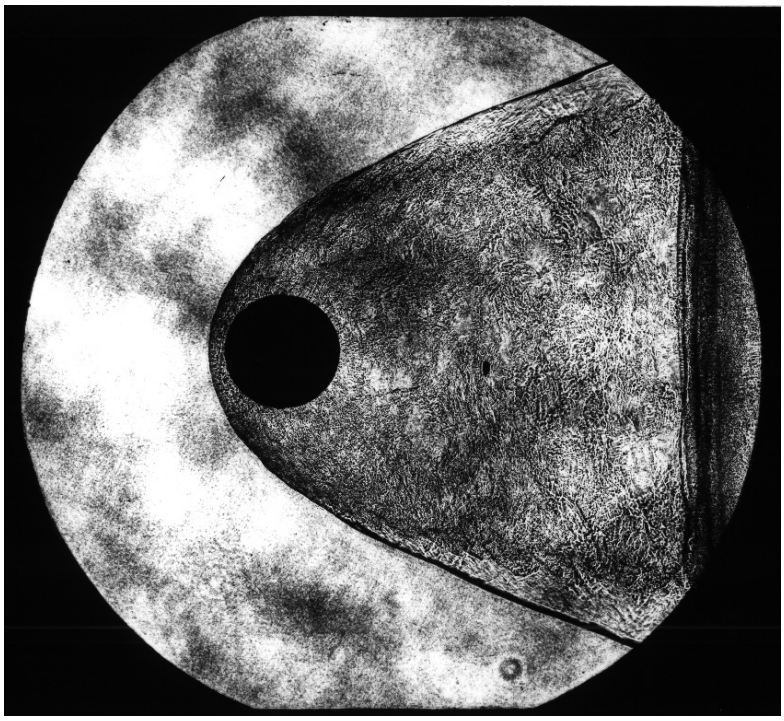

(a) Shadowgraph

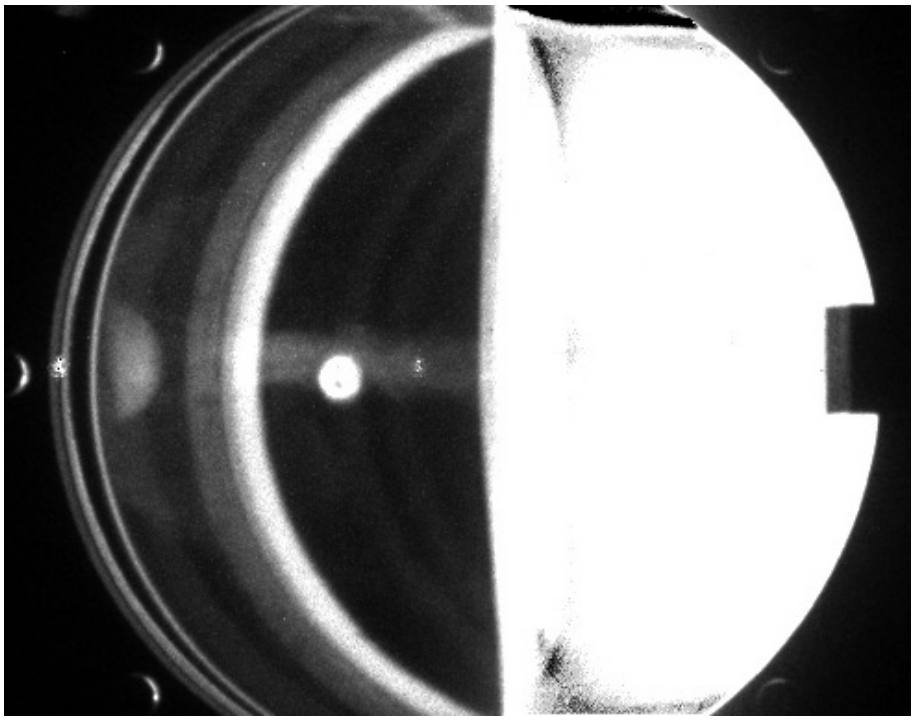

(b) ICCD

Figure B.69: Shot 1824: C_2H_4+$3O_2$+$5N_2$ at 0.400 bar, 2340 m/s.

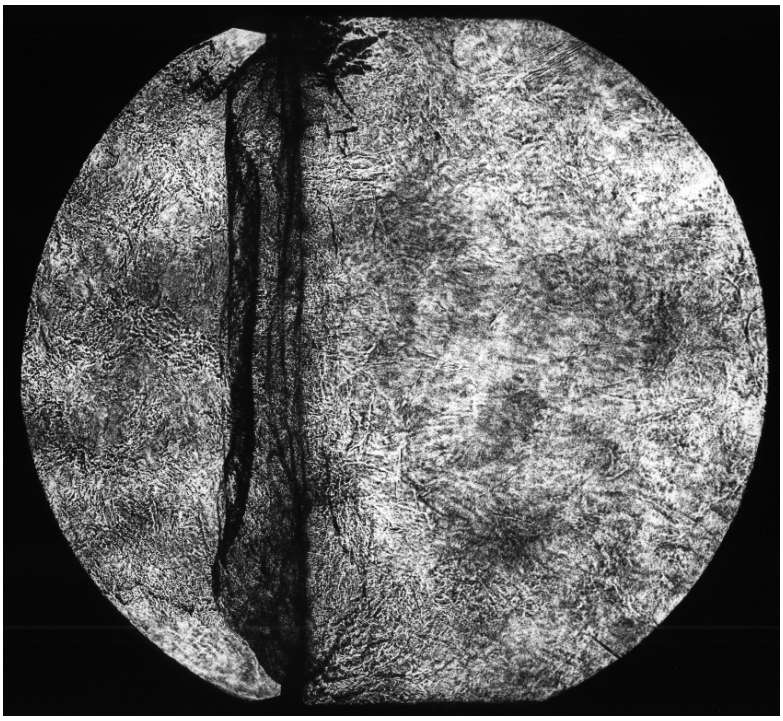

(a) Shadowgraph

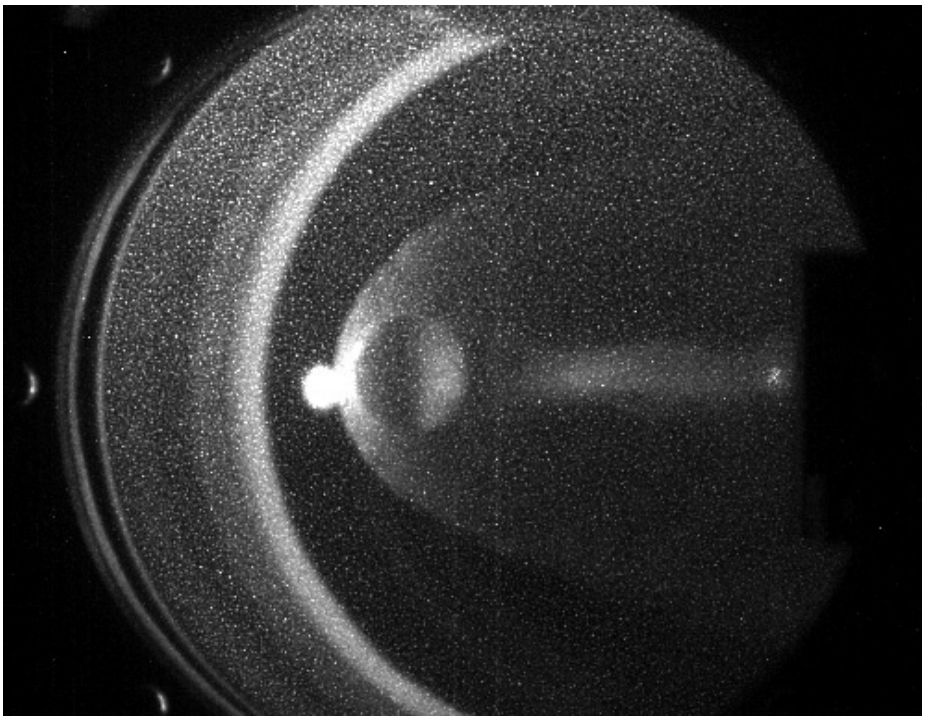

(b) ICCD

Figure B.70: Shot 1828: C_2H_4+$3O_2$+$5N_2$ at 0.400 bar, 2350 m/s.

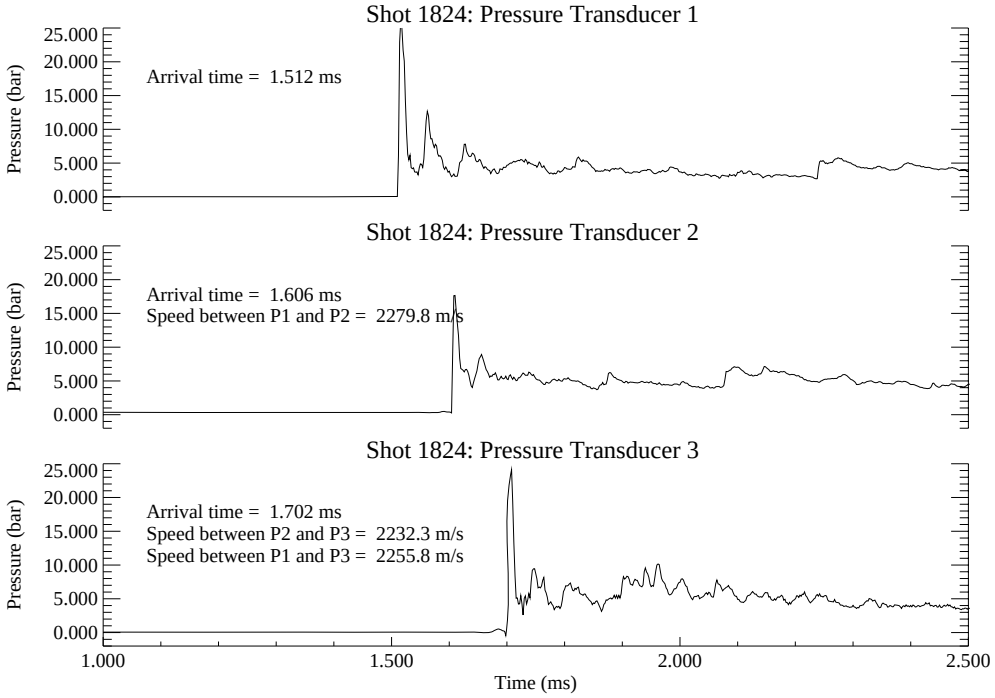

Figure B.71: Shot 1824 pressure traces.

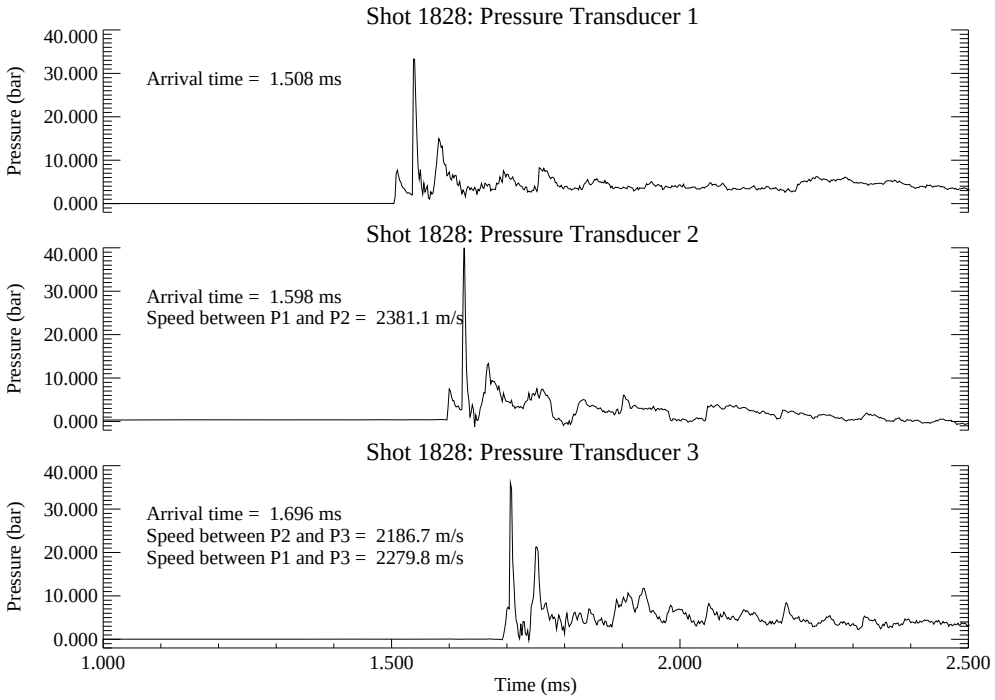

Figure B.72: Shot 1828 pressure traces.

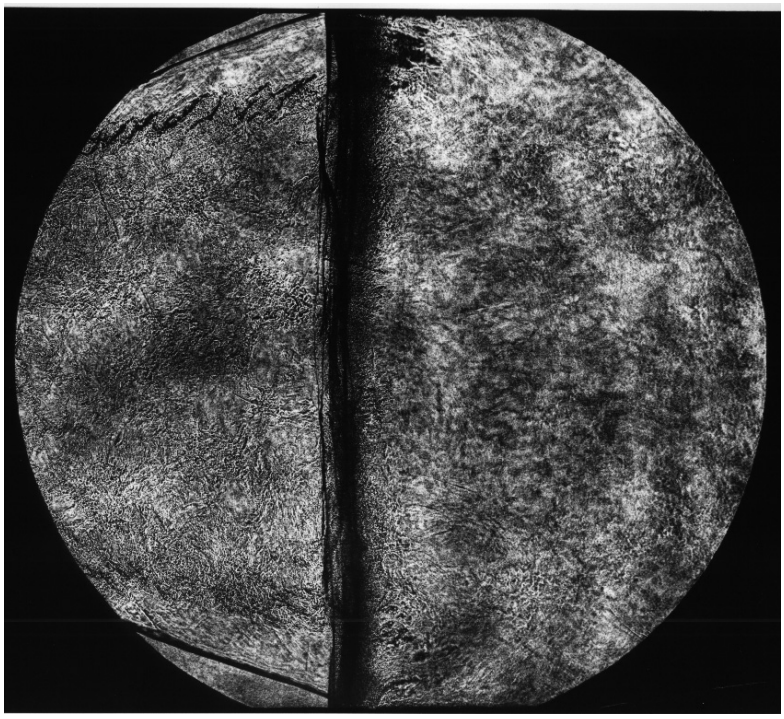

(a) Shadowgraph

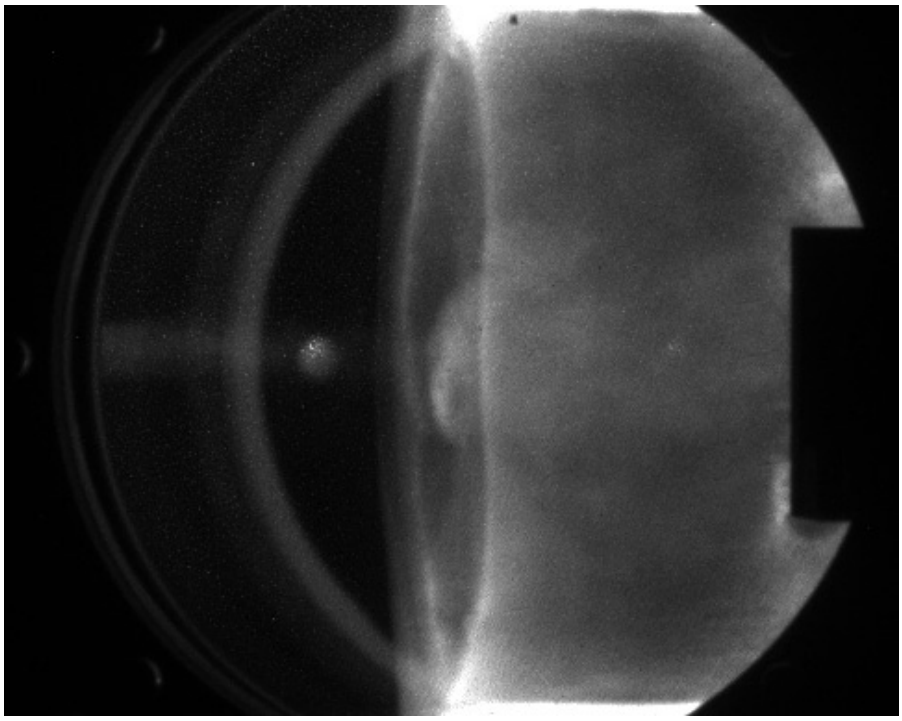

(b) ICCD

Figure B.73: Shot 1834: C_2H_4+$3O_2$+$5N_2$ at 0.400 bar, 2410 m/s.

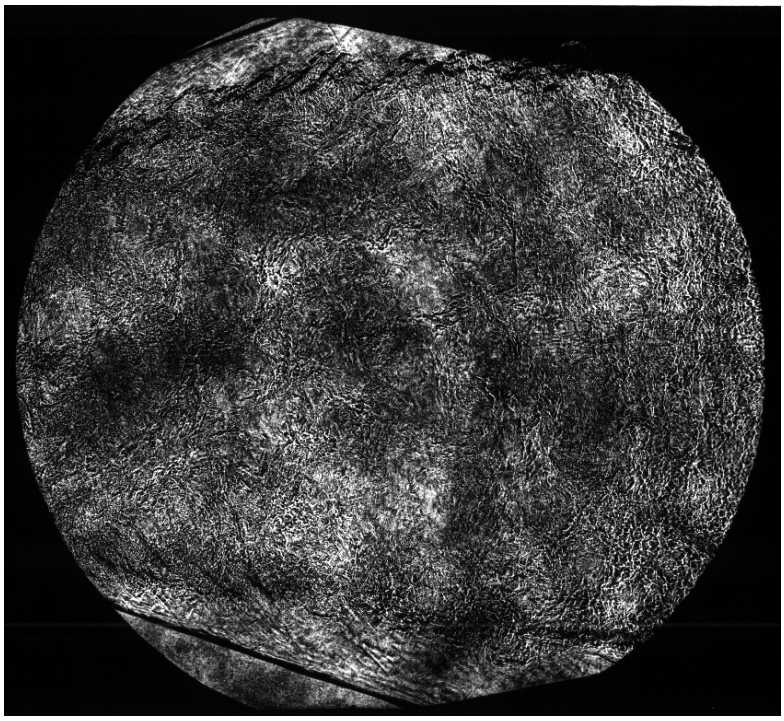

(a) Shadowgraph

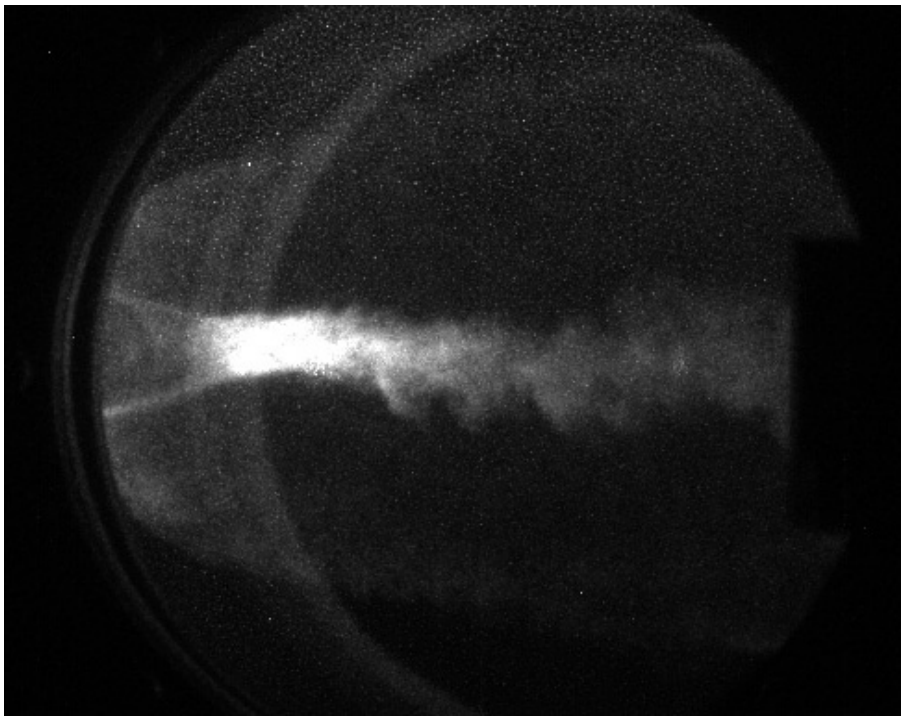

(b) ICCD

Figure B.74: Shot 1833: C_2H_4+$3O_2$+$5.2N_2$ at 0.420 bar, 2400 m/s.

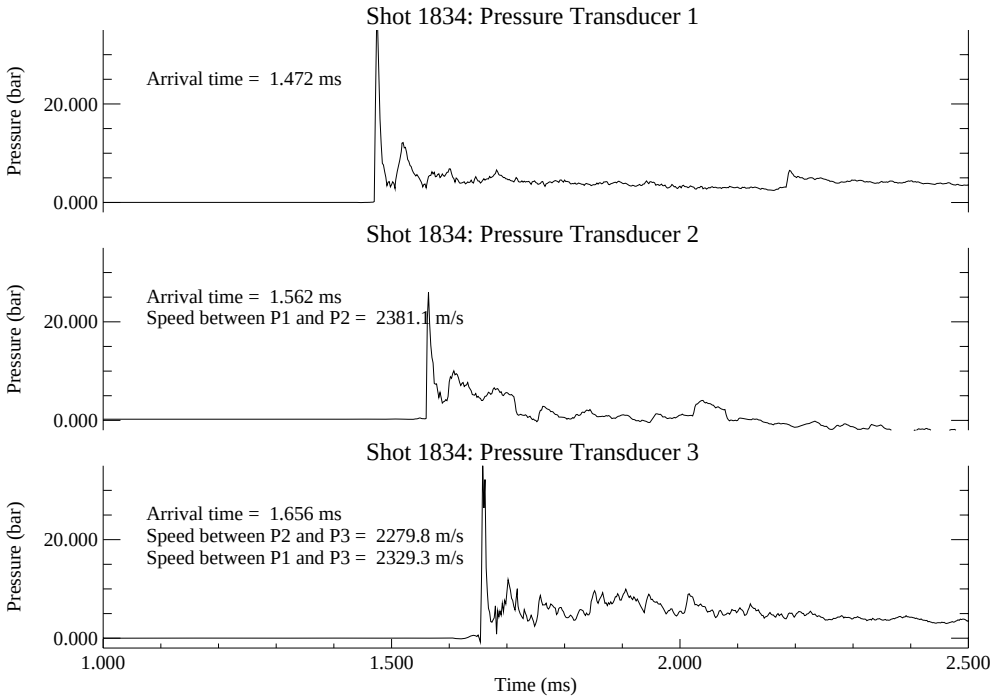

Figure B.75: Shot 1834 pressure traces.

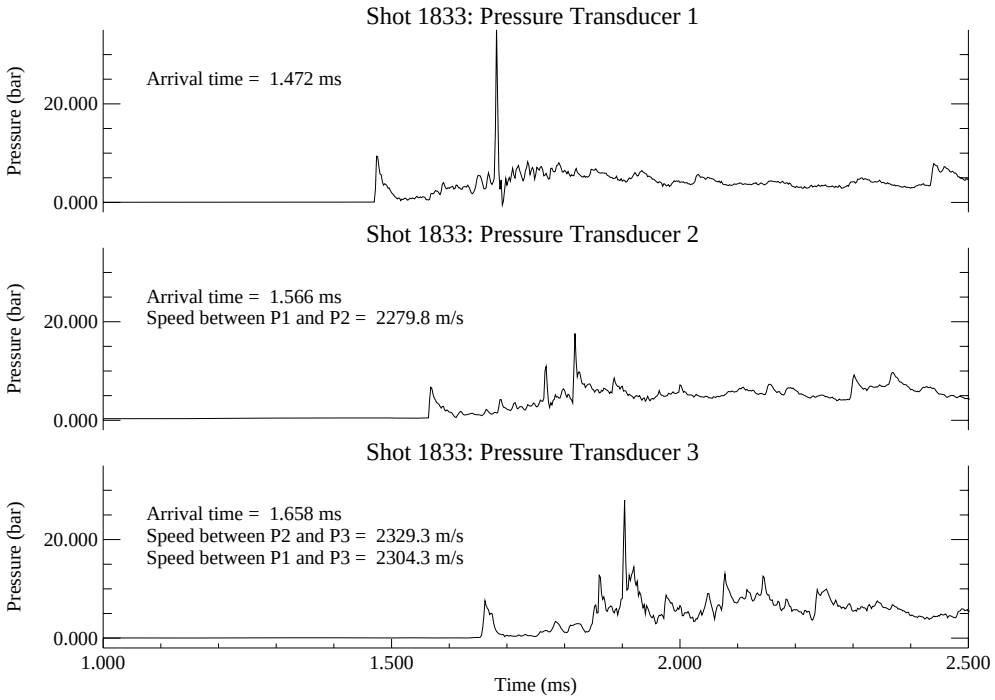

Figure B.76: Shot 1833 pressure traces.

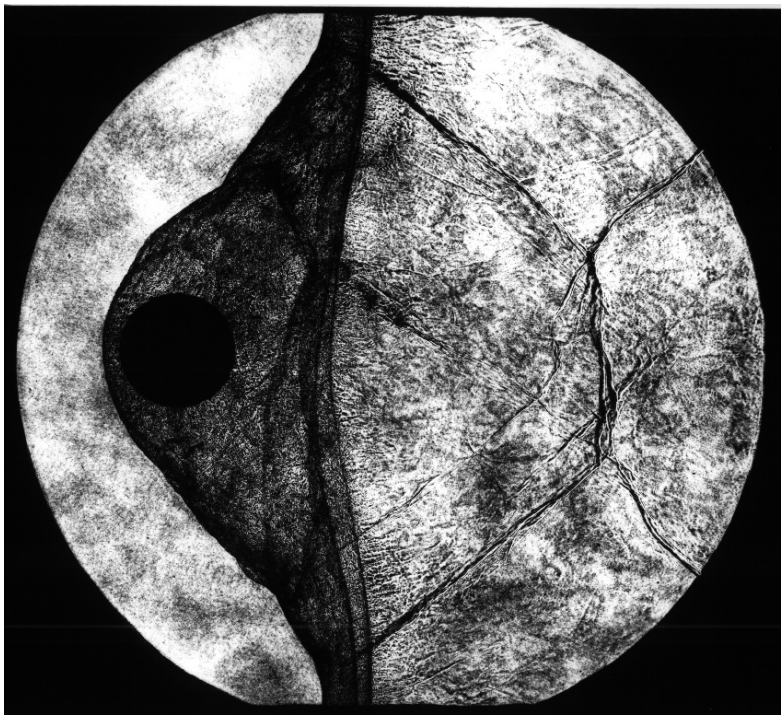

(a) Shadowgraph

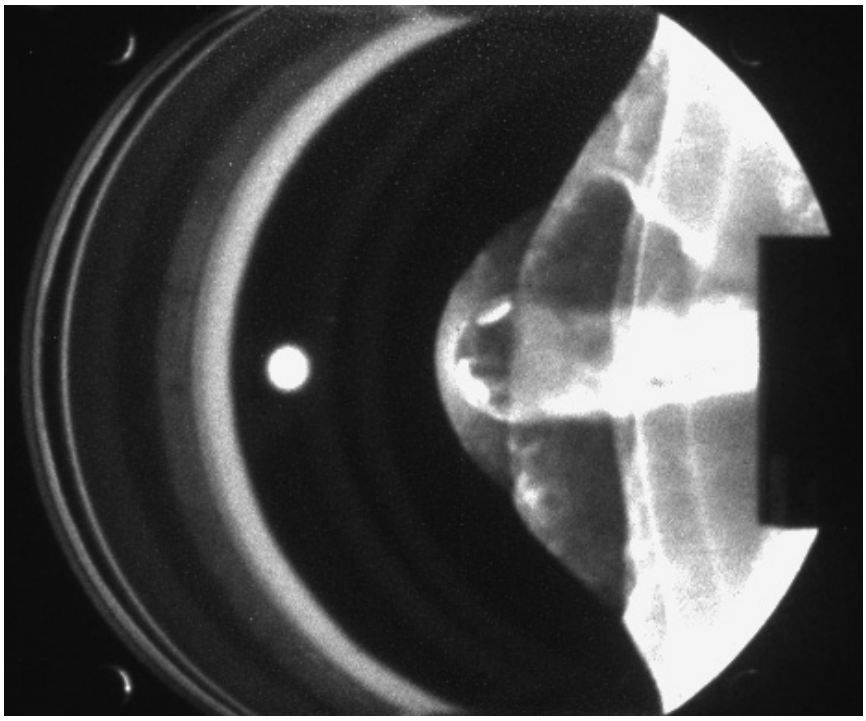

(b) ICCD

Figure B.77: Shot 1830: C_2H_4+$3O_2$+$5N_2$ at 0.450 bar, 2310 m/s.

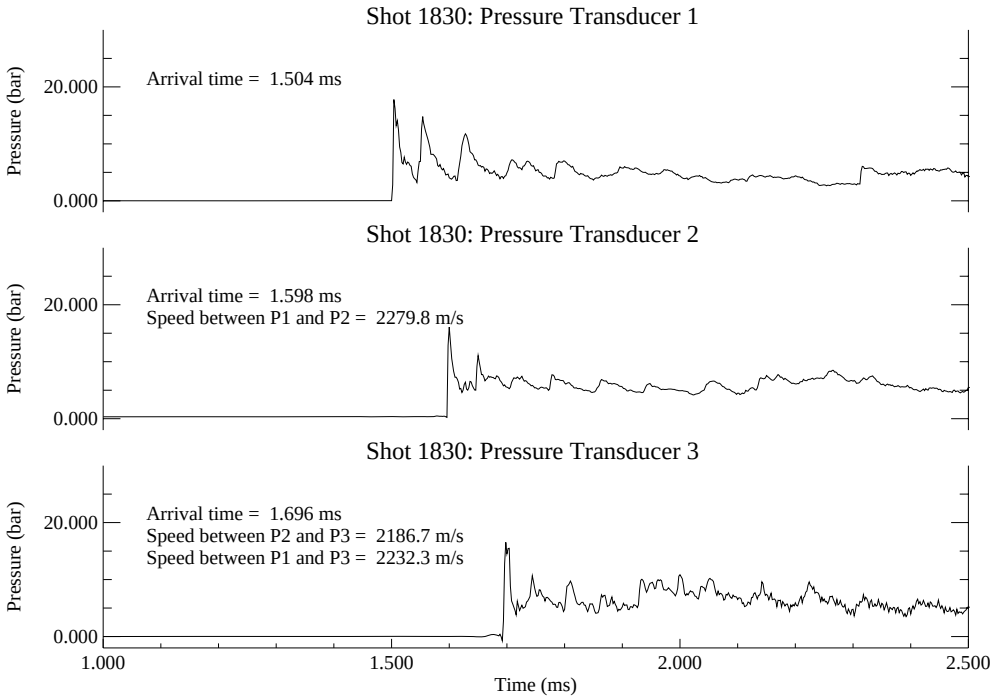

Figure B.78: Shot 1830 pressure traces.

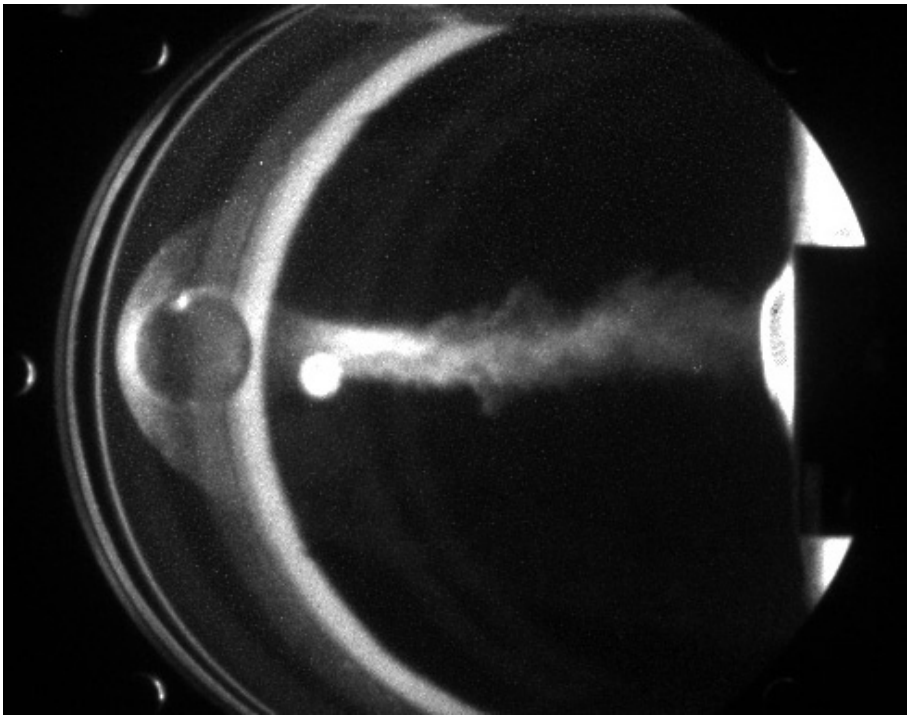

Figure B.79: Shot 1831 ICCD: C_2H_4+$3O_2$+$5.5N_2$ at 0.450 bar, 2380 m/s.

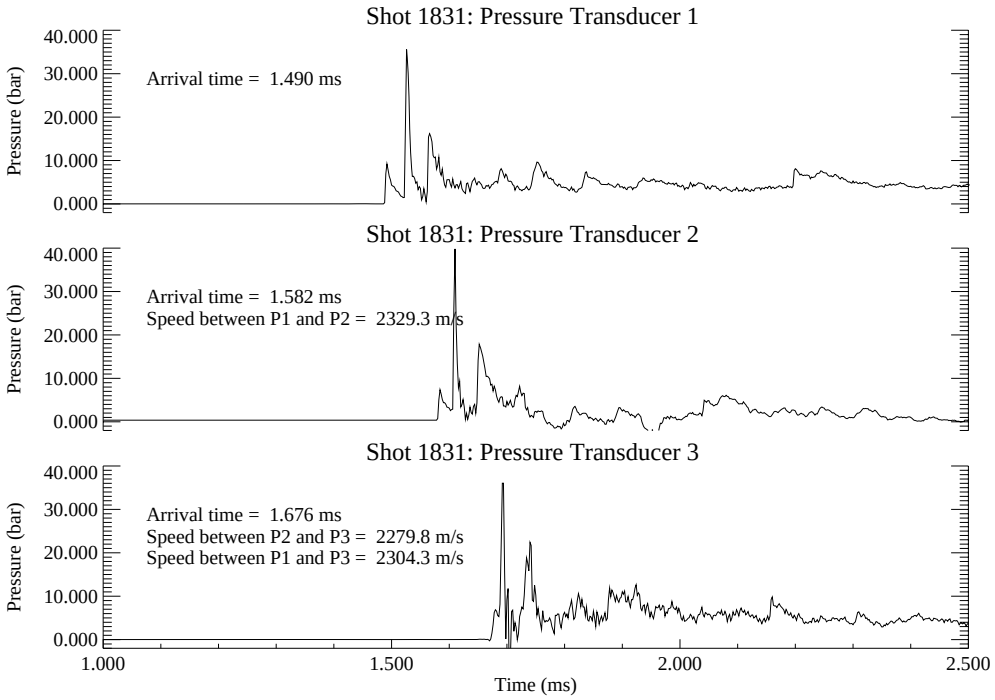

Figure B.80: Shot 1831 pressure traces.

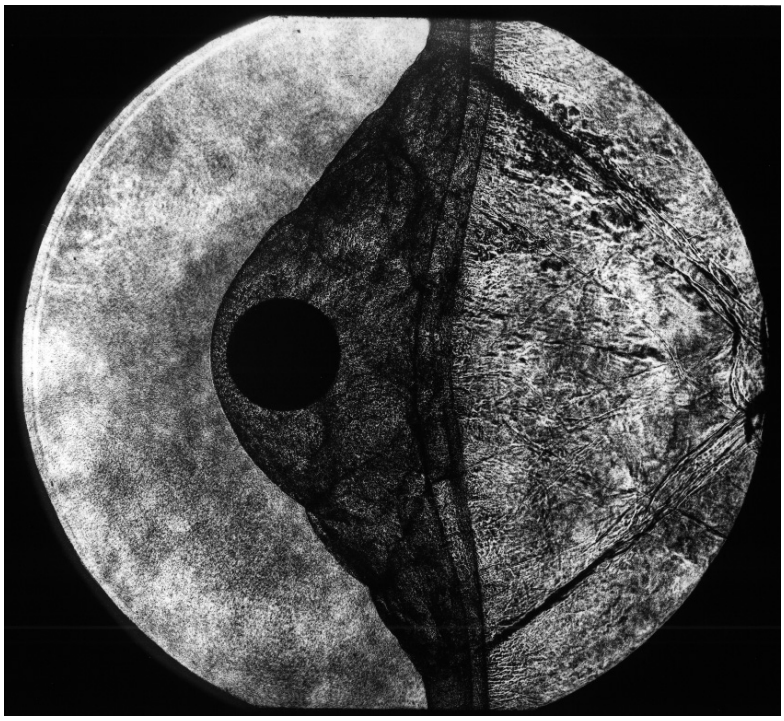

(a) Shadowgraph

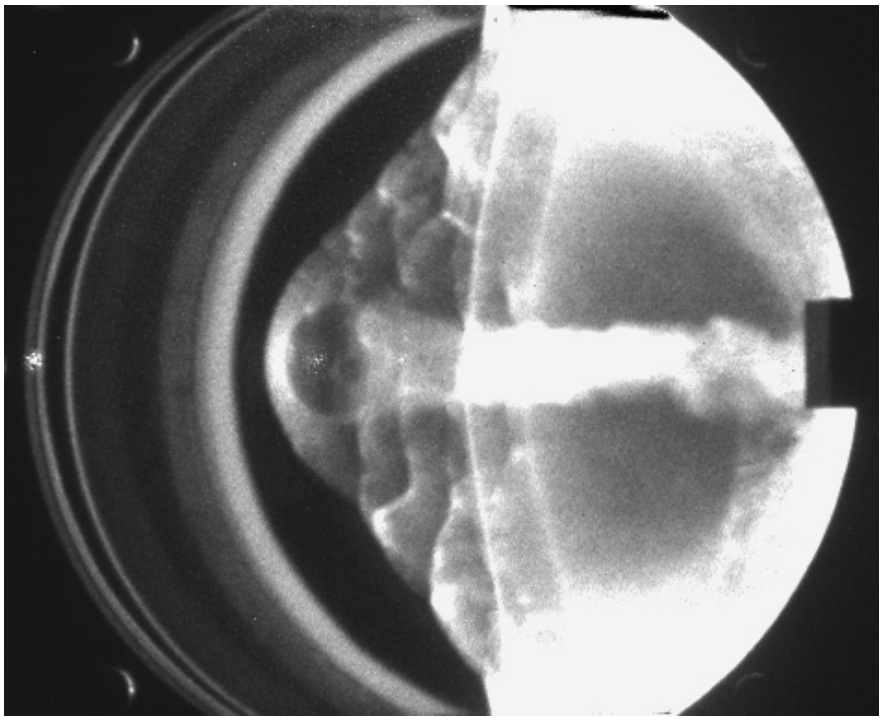

(b) ICCD

Figure B.81: Shot 1822: C_2H_4+$3O_2$+$5N_2$ at 0.500 bar, 2350 m/s.

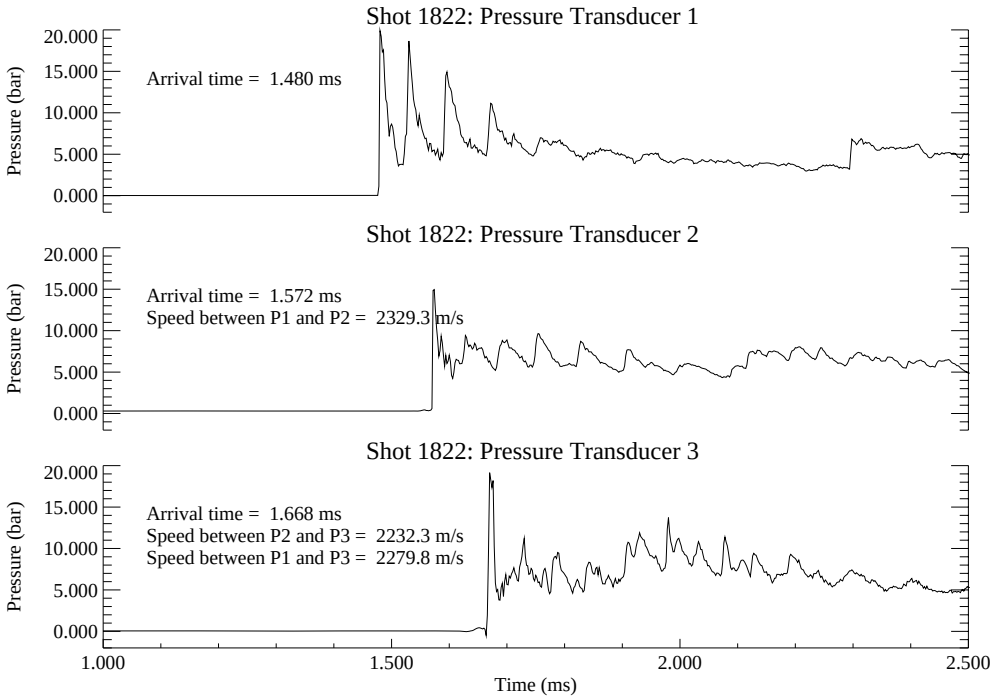

Figure B.82: Shot 1822 pressure traces.

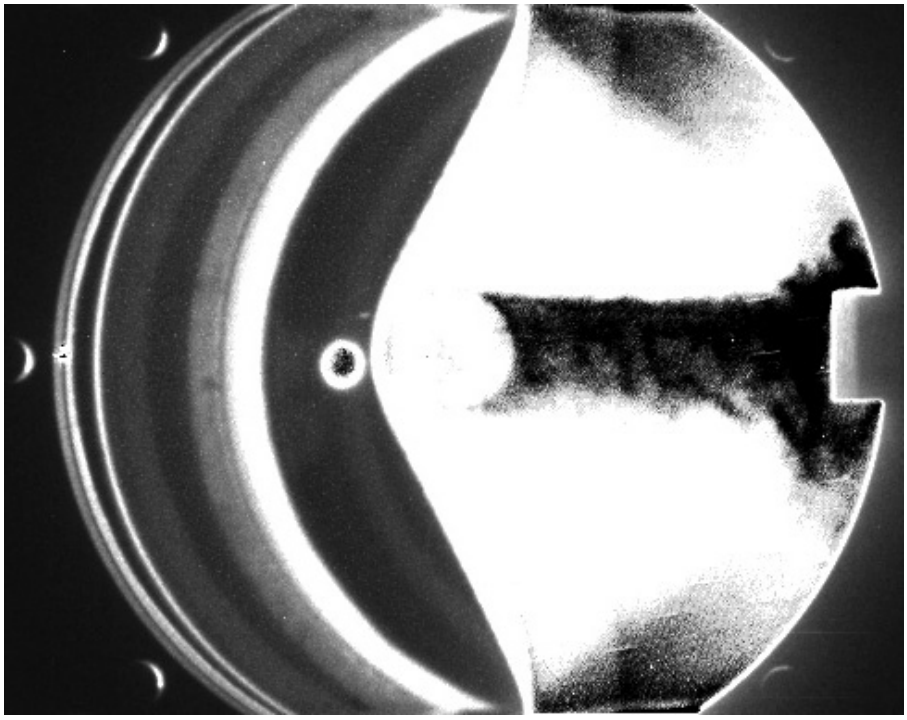

Figure B.83: Shot 1825 ICCD: C_2H_4+3O_2+5N_2 at 1.000 bar, 2330 m/s.

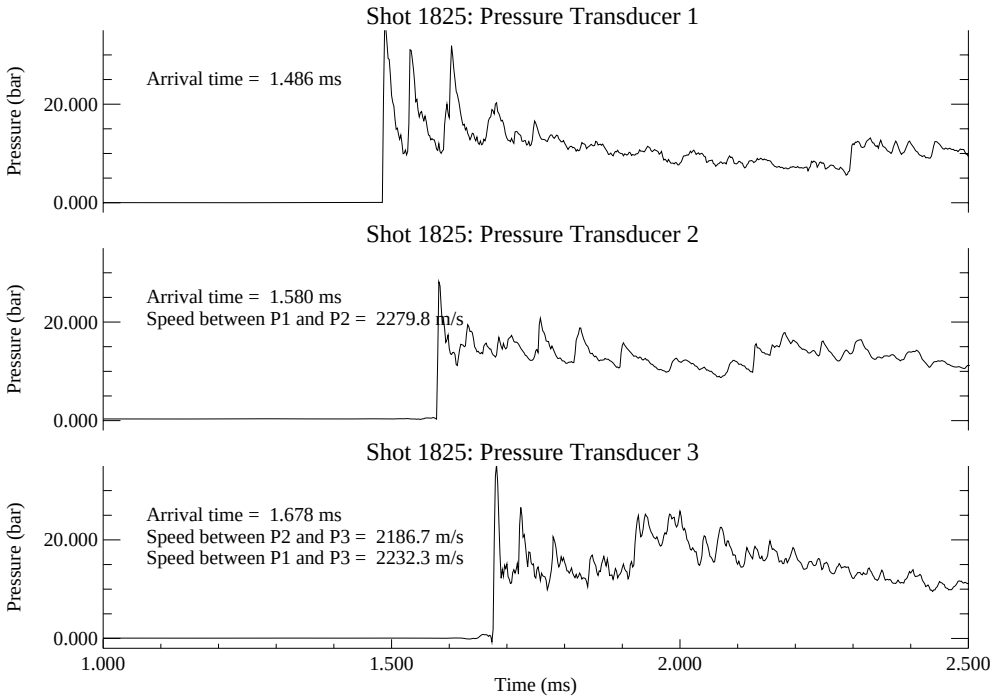

Figure B.84: Shot 1825 pressure traces.

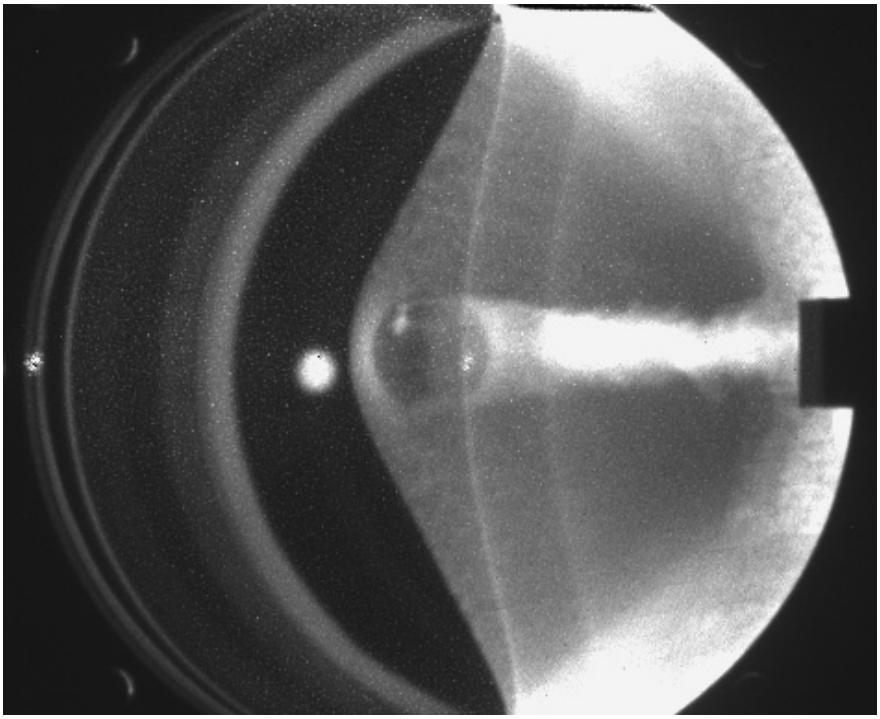

Figure B.85: Shot 1826 ICCD: $C_2H_4+3O_2+5N_2$ at 1.000 bar, 2330 m/s.

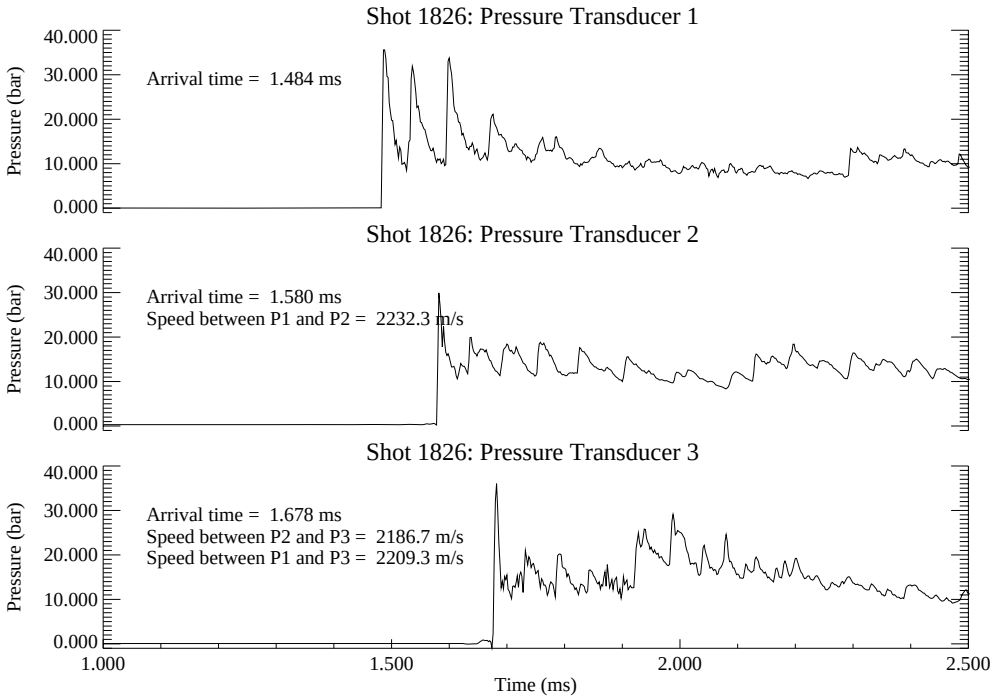

Figure B.86: Shot 1826 pressure traces.

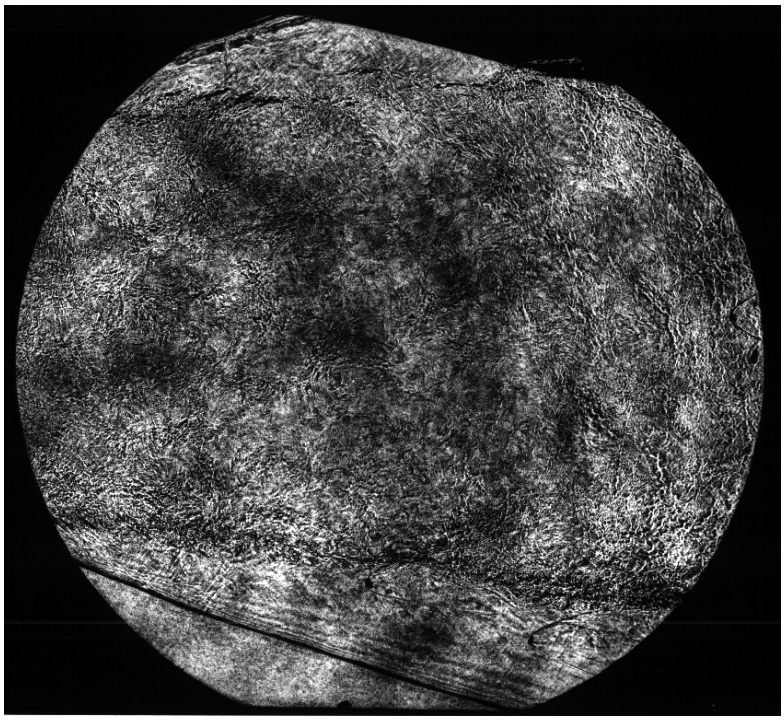

(a) Shadowgraph

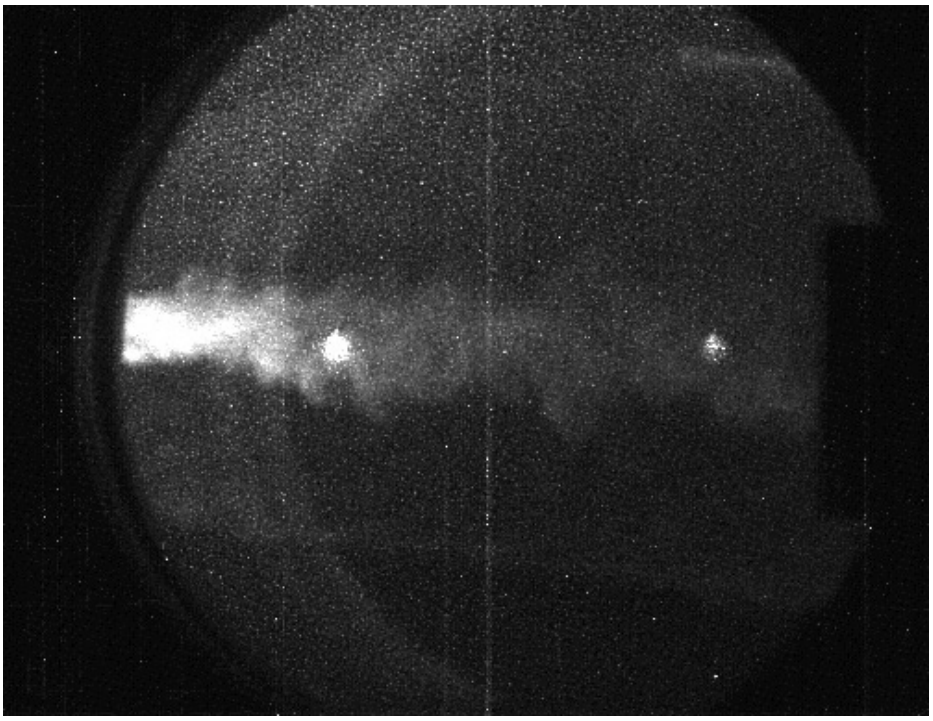

(b) ICCD

Figure B.87: Shot 1836: C_2H_2+2.5O_2+9.4N_2 at 0.500 bar, 2440 m/s.

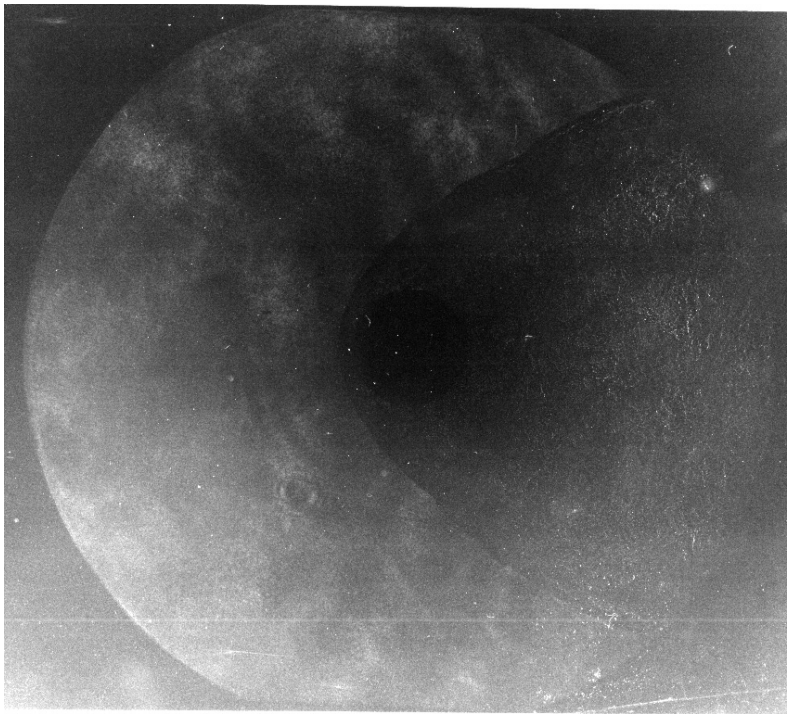

(a) Shadowgraph

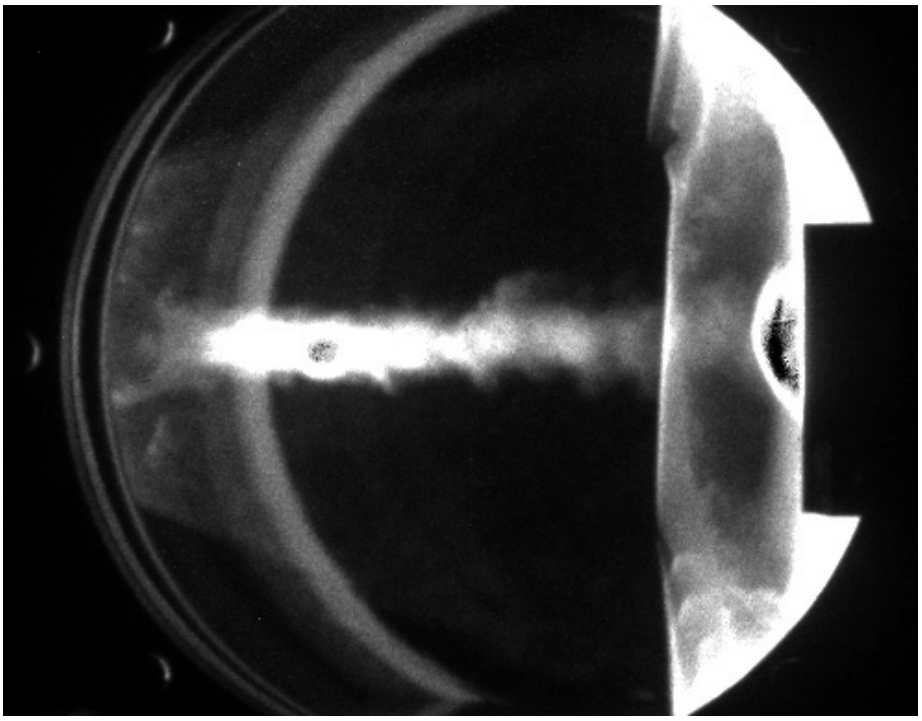

(b) ICCD

Figure B.88: Shot 1837: C_2H_2+2.5O_2+9.4N_2 at 0.800 bar, 2420 m/s.

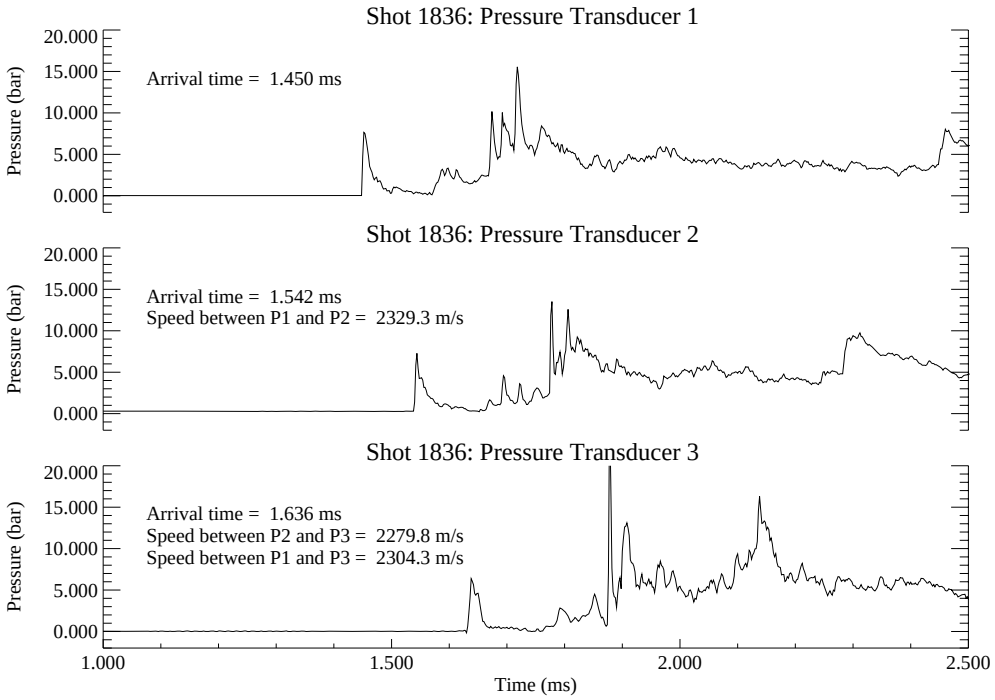

Figure B.89: Shot 1836 pressure traces.

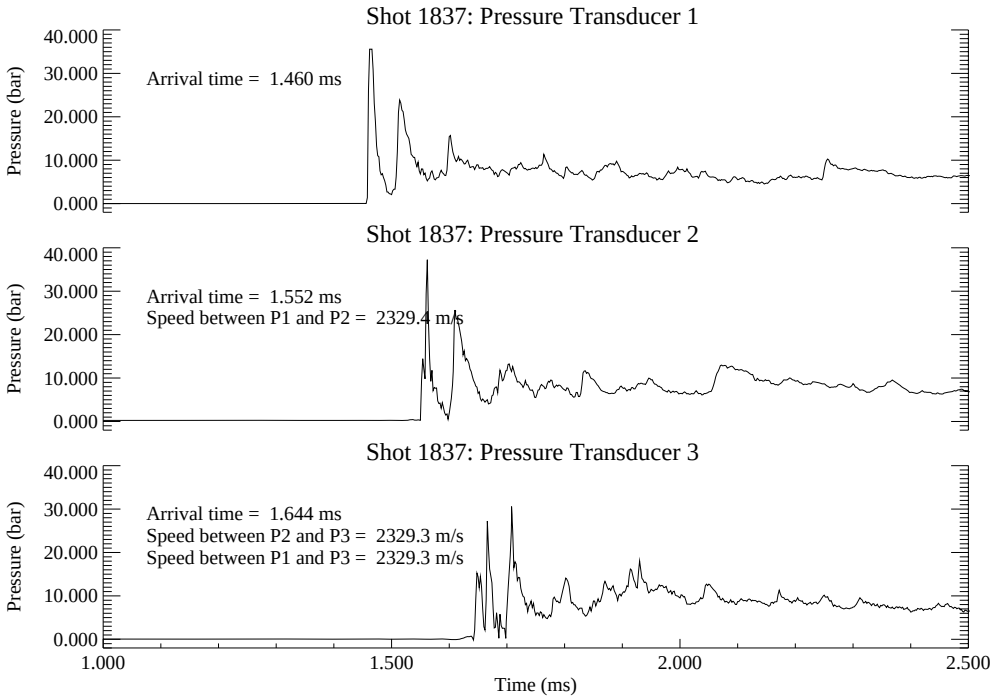

Figure B.90: Shot 1837 pressure traces.

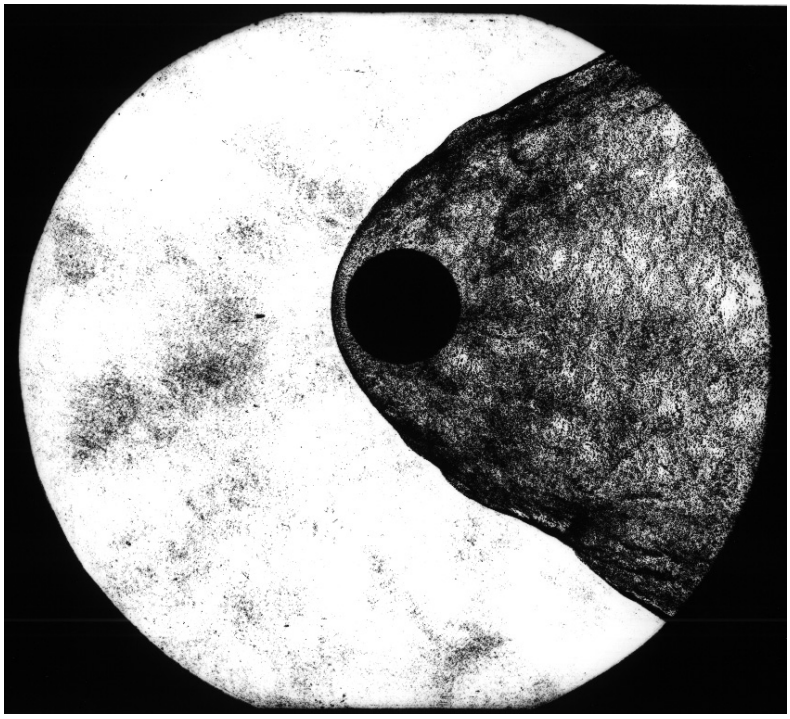

(a) Shadowgraph

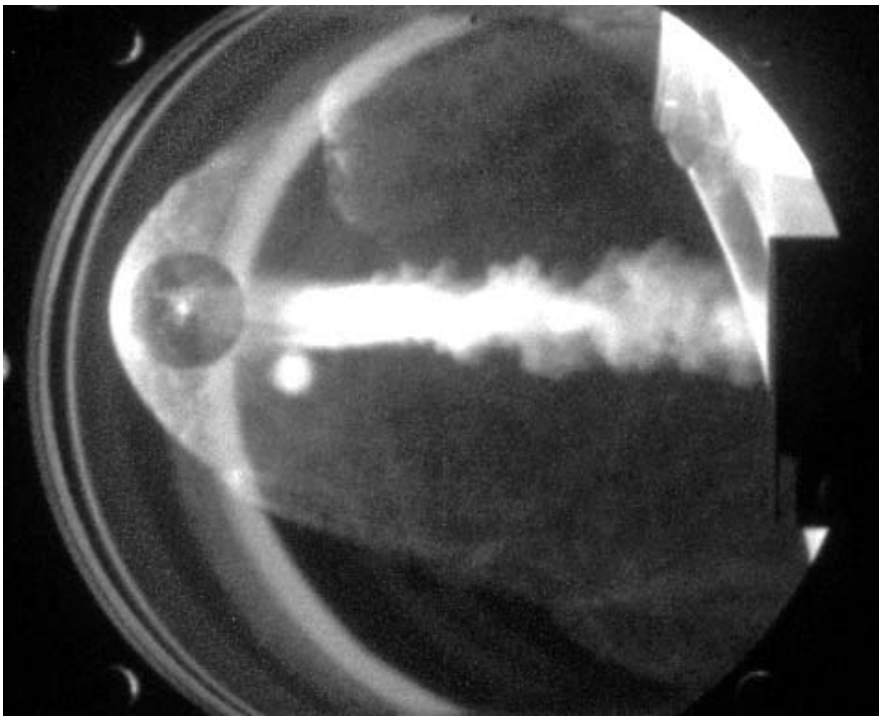

(b) ICCD

Figure B.91: Shot 1840: C_2H_2+2.5O_2+9.4N_2 at 0.820 bar, 2430 m/s.

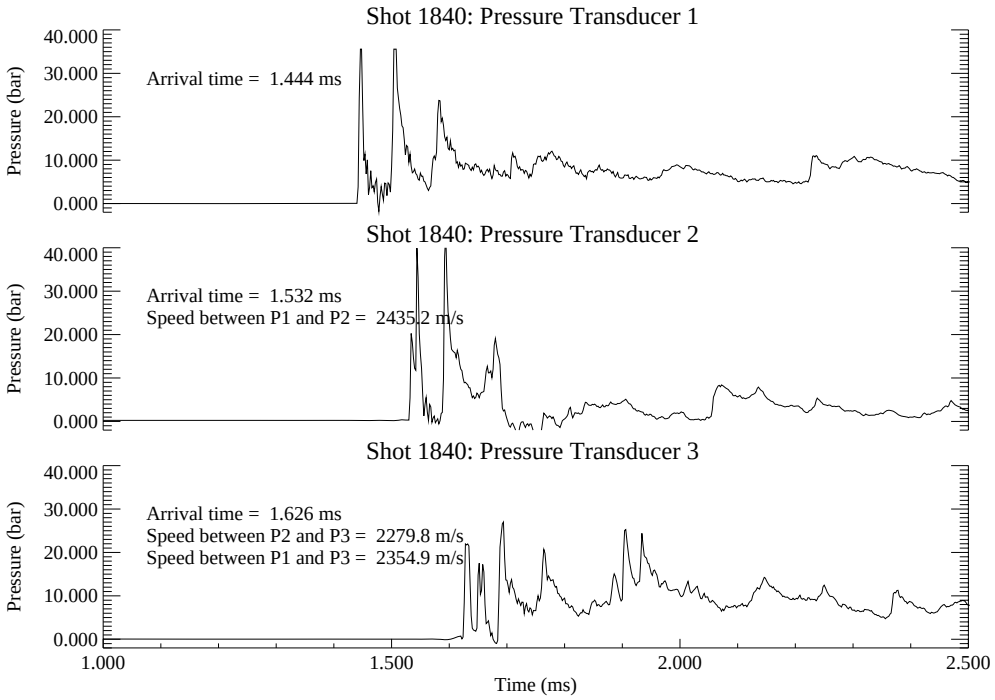

Figure B.92: Shot 1840 pressure traces.

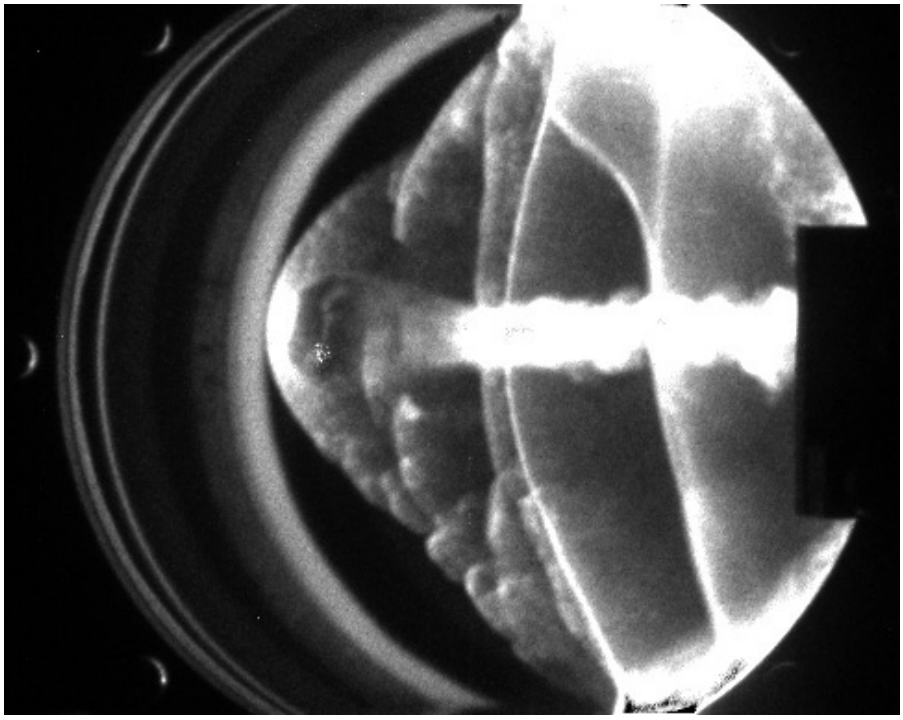

Figure B.93: Shot 1839 ICCD: C_2H_2+2.5O_2+9.4N_2 at 0.850 bar, 2380 m/s.

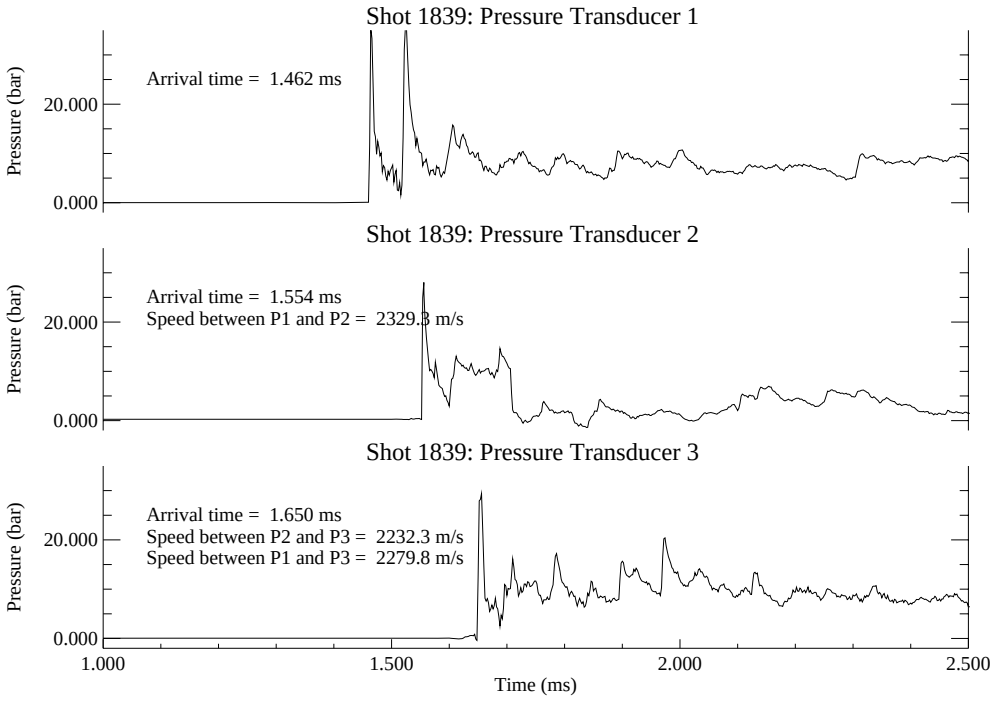

Figure B.94: Shot 1839 pressure traces.

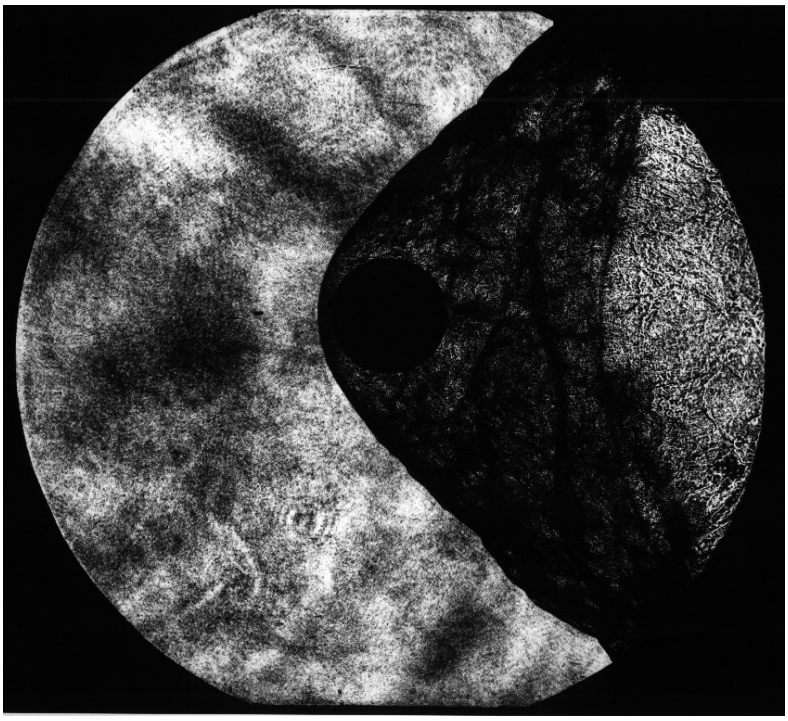

(a) Shadowgraph

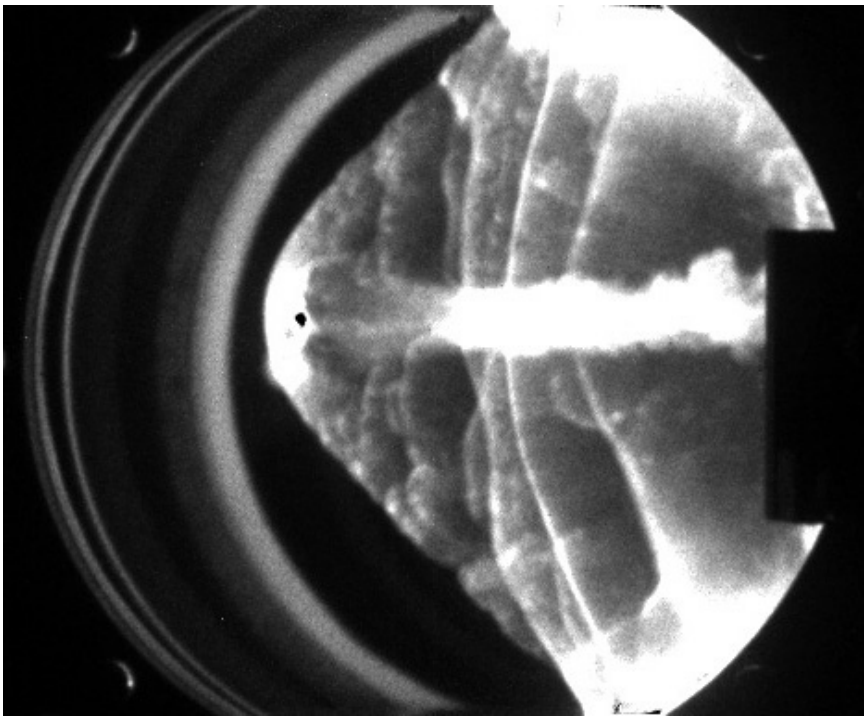

(b) ICCD

Figure B.95: Shot 1838: C_2H_2+2.5O_2+9.4N_2 at 0.900 bar, 2420 m/s.

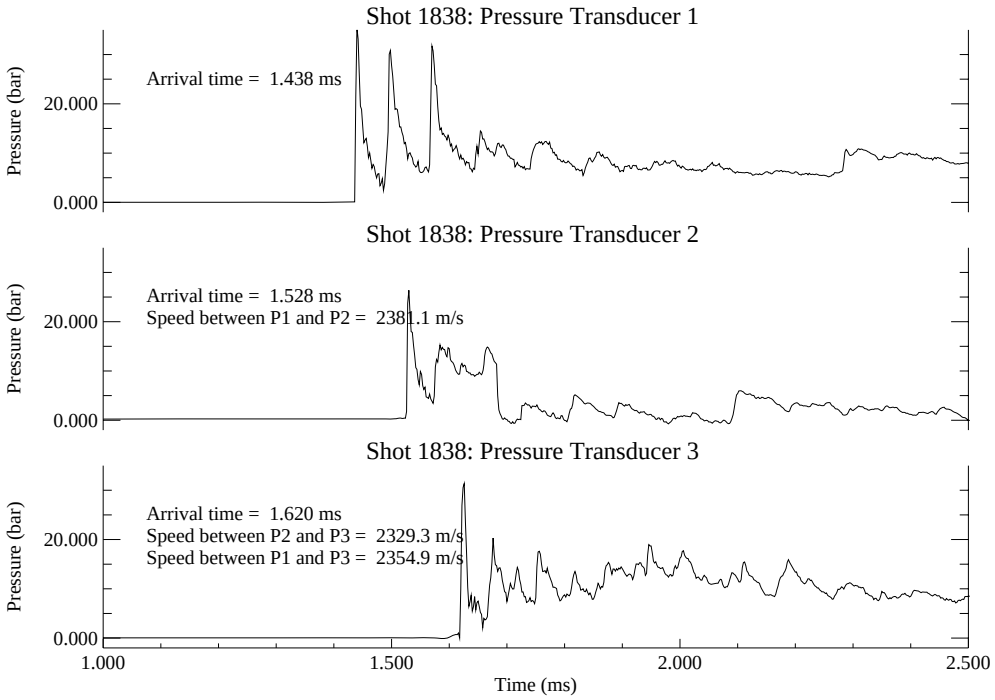

Figure B.96: Shot 1838 pressure traces.

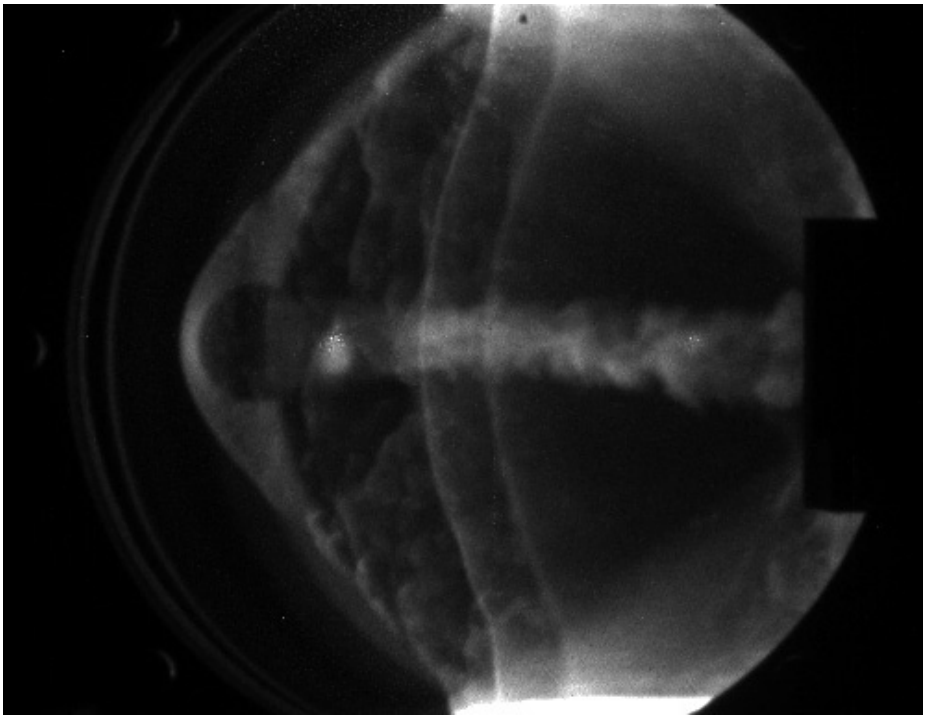

Figure B.97: Shot 1835 ICCD: C_2H_2+2.5O_2+9.4N_2 at 1.000 bar, 2420 m/s.

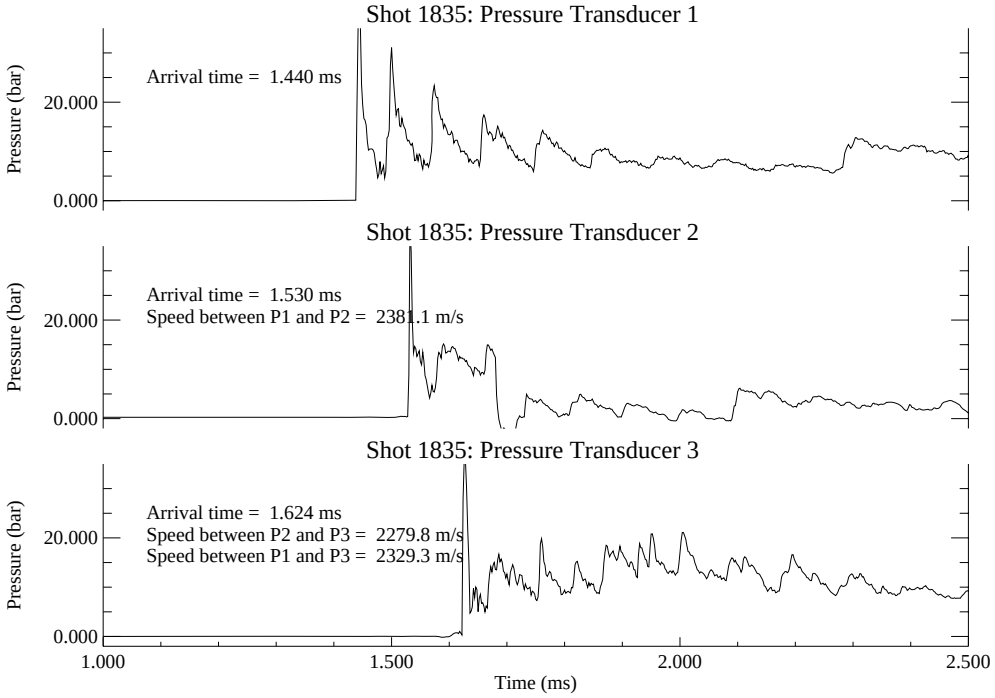

Figure B.98: Shot 1835 pressure traces.

Appendix C Hardware Drawings

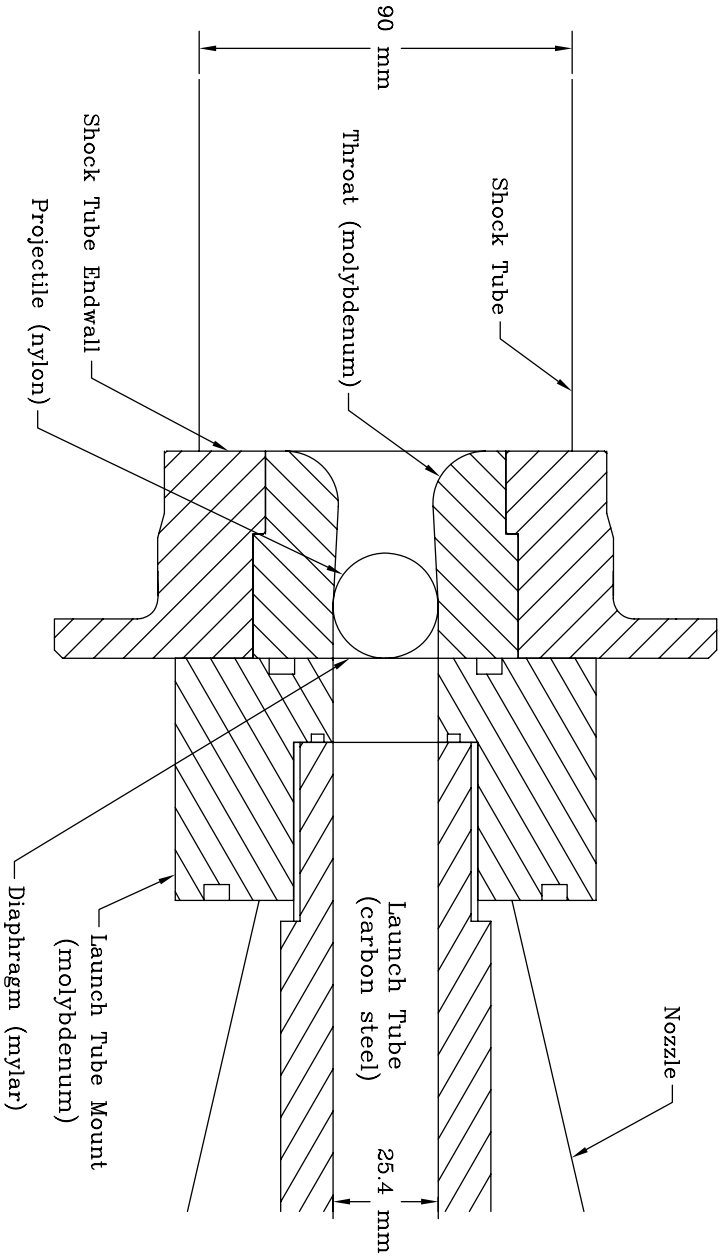

Figure C.1: Launch tube breech assembly.

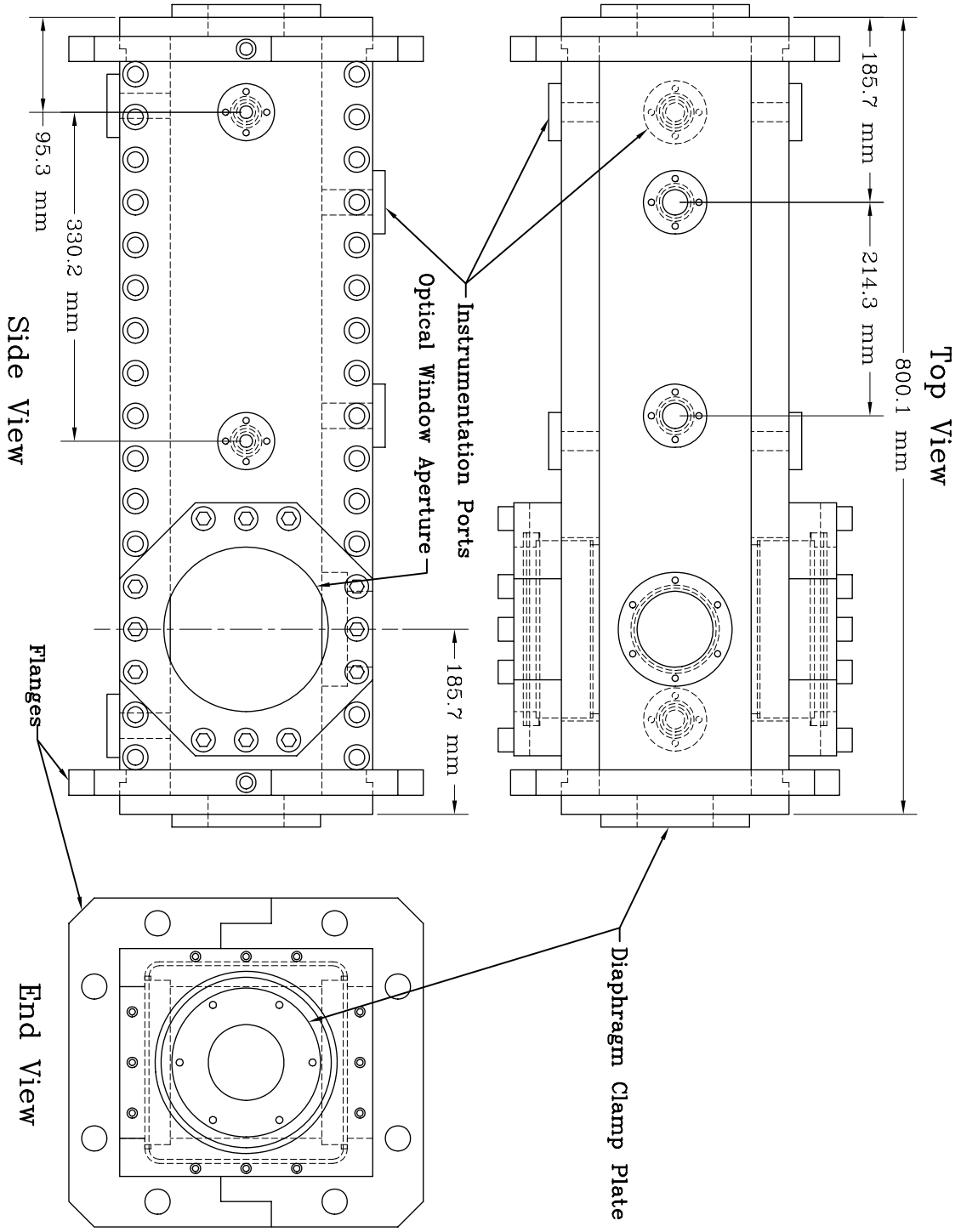

Figure C.2: Test section assembly.

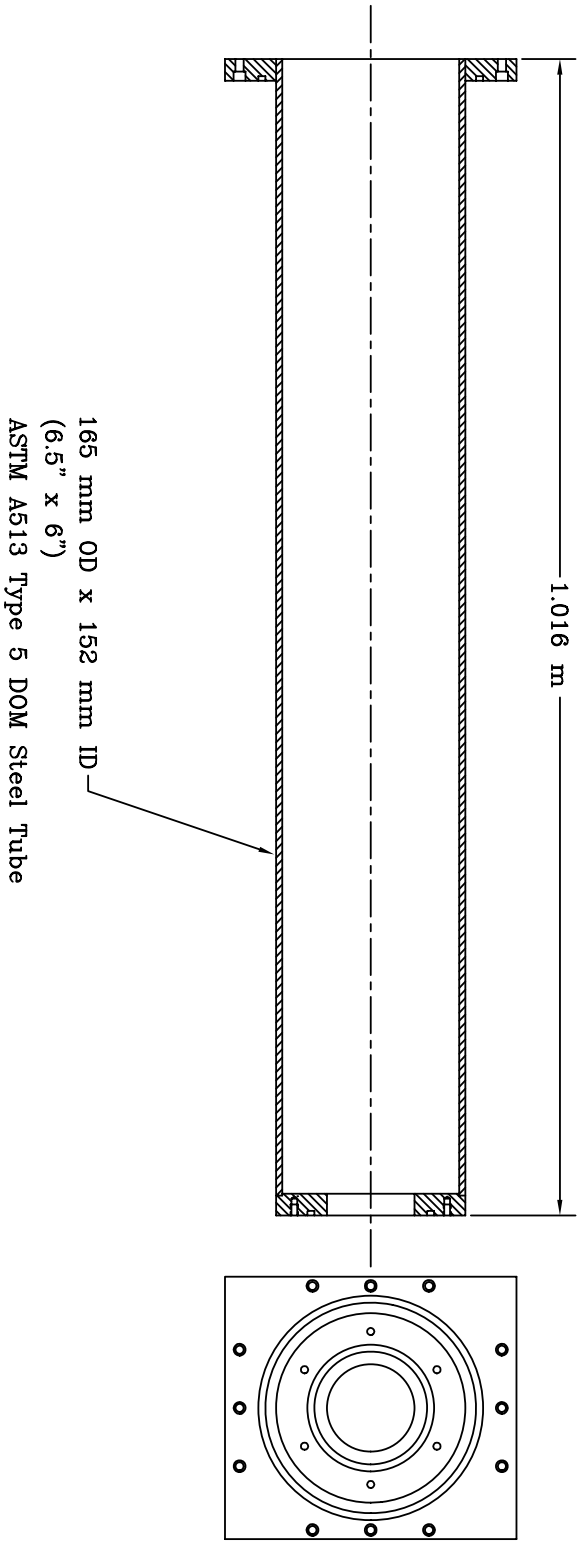

Figure C.3: Extension tube.

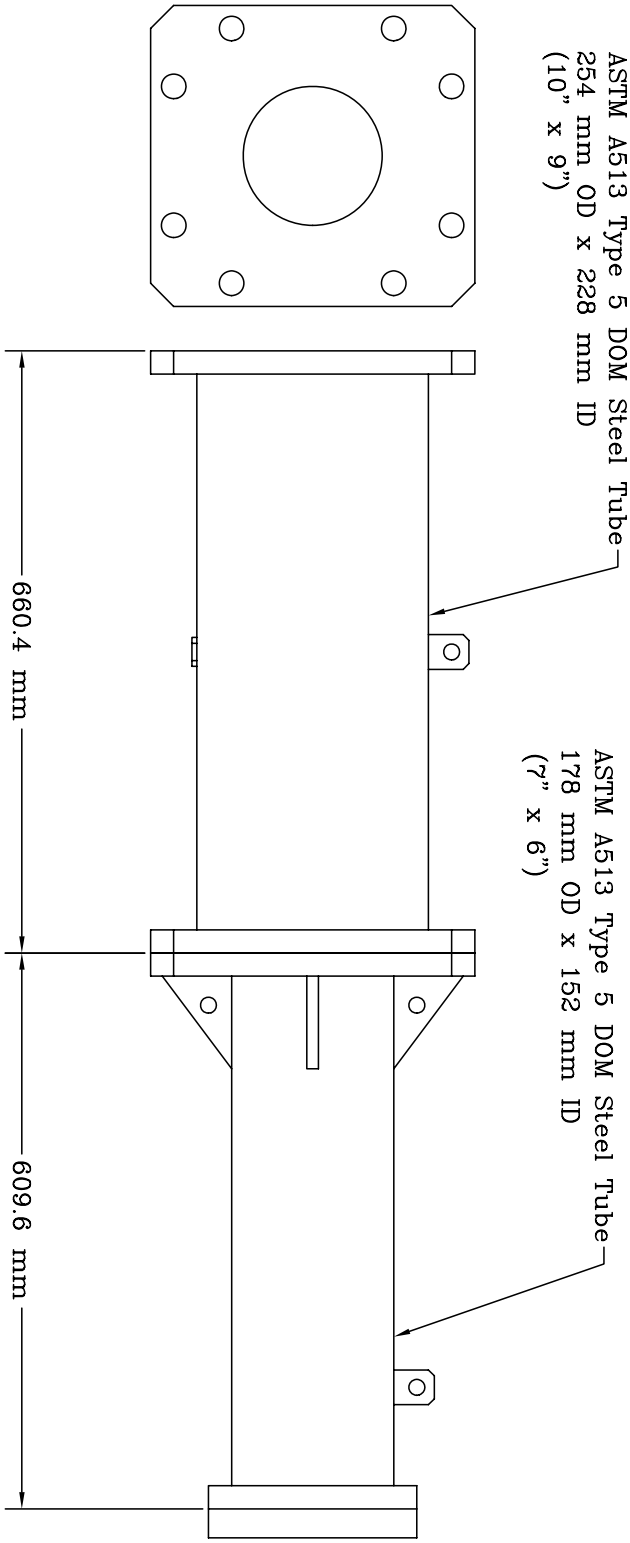

Figure C.4: Target sections.

Appendix D Gun Modeling

The projectile launching scheme utilized was similar to a conventional two-stage light gas gun, except that the second stage gas was shock heated rather than isentropically compressed, because of the bursting of the main diaphragm. In a typical two-stage gas gun, the first stage (usually powder propellant) and second stage (helium or hydrogen) are separated by a free piston. The second stage gas is compressed isentropically by the free piston, which is driven by the powder charge. When the second stage pressure reaches a particular level, a diaphragm separating the second stage from the projectile and launch tube bursts. As the projectile accelerates down the launch tube, the pressure in the second stage continues to increase, maintaining a roughly constant base pressure on the projectile.

In the present arrangement, the second stage was divided into two sections, separated by the main diaphragm. The shock wave generated by the main diaphragm burst and its reflection served to heat and compress the propellant gas (helium) in the shock tube. The conditions in the shock tube after shock reflection were roughly constant, rather than continuing to increase in pressure and temperature as in the conventional gun. This method yields lower performance than the conventional method for two reasons: 1) the propellant is compressed non-isentropically, and 2) the base pressure on the projectile is not maintained by increasing pressure in the reservoir. A more thorough discussion of these considerations is given by Berggren and Reynolds [13]. The shock heating technique was used because it required no changes from standard T5 operating procedures.

The theoretical model used to predict launcher performance consisted of a uniform reservoir representing the shock tube after shock reflection, a frictionless piston representing the projectile, and a finite-length evacuated tube representing the launch tube. Perfect, ideal gas behavior was assumed. This model diverges from reality in several significant ways. In general, the conditions in the reservoir were neither constant nor uniform. Friction and blow-by of the projectile undoubtedly reduced the launcher performance. To a lesser extent, real gas effects and gas present in the launch tube before the test represented non-idealities.

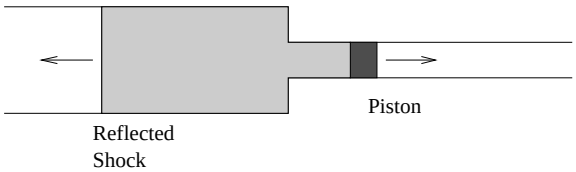

Figure D.1: Launch tube model schematic.

D.1 Method of Characteristics

This model was applied through numerical solution using the method of characteristics, of which an excellent discussion is given by Thompson [113]. The basic characteristics equations are:

$$C^{\pm} : J^{\pm} = u \pm \frac{2}{\gamma - 1} c \qquad \text{Riemann invariants} \tag{D.1}$$

$$\frac{dx}{dt}^{\pm} = u \pm c \qquad \text{Characteristics slopes} \tag{D.2}$$

Boundary conditions exist at the throat and at the projectile. The boundary condition at the throat can be modeled as an infinitely large reservoir, or by a finite area change. For an infinite reservoir, the reservoir condition does not change, and conservation of energy across the throat yields:

$$c_0^2 = c^2 + \frac{\gamma - 1}{2} u^2 \tag{D.3}$$

For a finite area change, the condition upstream of the throat varies as a simple wave propagates upstream through the reservoir. In addition to conservation of energy across the throat:

$$c_1^2 + \frac{\gamma - 1}{2} u_1^2 = c_2^2 + \frac{\gamma - 1}{2} u_2^2 \tag{D.4}$$

The value of the positive Riemann invariants in the simple wave is known:

$$J_0^+ = \frac{2}{\gamma - 1} c_0 = u_1 + \frac{2}{\gamma - 1} c_1 \tag{D.5}$$

and continuity across the reservoir-launch tube interface introduces the area ratio:

$$\frac{u_2 A_2}{u_1 A_1} = \left(\frac{c_1}{c_2} \right)^{\frac{2}{\gamma - 1}} \tag{D.6}$$

The acceleration of the projectile is given by:

$$a = \frac{P_0 A}{m} \left(\frac{c}{c_0} \right)^{\frac{2\gamma}{\gamma - 1}} \tag{D.7}$$

which can be integrated to give the velocity and position.

Significant advantage can be obtained by normalizing the dimensional variables to create non-dimensional equations. Normalizing time by $\frac{c_0 m}{P_0 A}$, length by $\frac{c_0^2 m}{P_0 A}$, velocity by c_0, and acceleration by $\frac{P_0 A}{m}$ yields the following set of equations:

$$\text{Characteristics} : \hat{J}^{\pm} = \hat{u} \pm \frac{2}{\gamma - 1} \hat{c} \tag{D.8}$$

$$\frac{d\hat{x}^{\pm}}{d\hat{t}} = \hat{u} \pm \hat{c} \tag{D.9}$$

$$\text{Infinite reservoir}: \ 1 = \hat{c}^2 + \frac{\gamma-1}{2}\hat{u}^2 \tag{D.10}$$

$$\text{Finite reservoir}: \ \hat{u}_1 = \frac{2}{\gamma-1}(1-\hat{c}_1) \tag{D.11}$$

$$\frac{\hat{u}_2}{1-\hat{c}_1}\frac{A_2}{A_1} = \frac{2}{\gamma-1}\left(\frac{\hat{c}_1}{\hat{c}_2}\right)^{\frac{2}{\gamma-1}} \tag{D.12}$$

$$\hat{c}_1^2 + \frac{\gamma-1}{2}\hat{u}_1^2 = \hat{c}_2^2 + \frac{\gamma-1}{2}\hat{u}_2^2 \tag{D.13}$$

$$\text{Projectile}: \ \hat{a} = \hat{c}^{\frac{2\gamma}{\gamma-1}} \tag{D.14}$$

$$\hat{u}_p = \int \hat{a} \tag{D.15}$$

One constraint relating the two basic flow parameters, fluid velocity $\hat{u}$ and sound speed $\hat{c}$, is provided by the reservoir, each characteristic, and the projectile. As characteristics intersect with each other, the reservoir, and the projectile, the two constraints are solved for $\hat{u}$ and $\hat{c}$, and constraints on the next set of characteristics are computed.

D.2 Discretization

The equations given above must be written in terms of quantities at previously computed characteristic nodes to give quantities at new nodes. Figure D.2 illustrates an intersection between two characteristics, with parameters at the previous nodes of the positive and negative characteristics, and the current node shown.

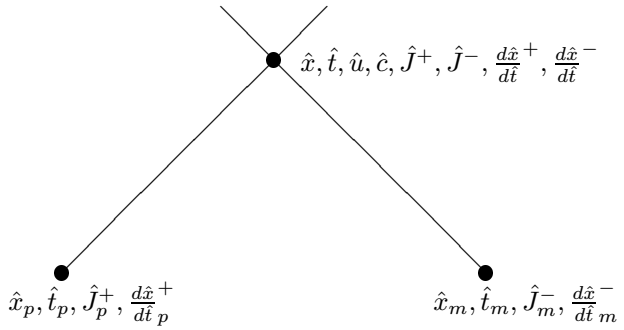

Figure D.2: Intersection between two characteristics.

Combining Eqs. (D.1) and (D.2) for the two characteristics yields the following expressions for the new node:

$$\hat{t} = \frac{\hat{x}_m - \hat{x}_p + \frac{d\hat{x}}{d\hat{t}}_p^+ \hat{t}_p - \frac{d\hat{x}}{d\hat{t}}_m^- \hat{t}_m}{\frac{d\hat{x}}{d\hat{t}}_p^+ - \frac{d\hat{x}}{d\hat{t}}_m^-} \tag{D.16}$$

$$\hat{x} = \hat{x}_p + \frac{d\hat{x}}{d\hat{t}}^{+}_{p} (\hat{t} - \hat{t}_p) \tag{D.17}$$

$$\hat{c} = \frac{\gamma - 1}{4}(\hat{J}_p^+ - \hat{J}_m^-) \tag{D.18}$$

$$\hat{u} = \hat{J}_m^- + \frac{2}{\gamma - 1}\hat{c} \tag{D.19}$$

Equations (D.1) and (D.2) then give the Riemann invariants and slopes of the next set of characteristics.

Figure D.3 illustrates a characteristic intersecting and reflecting from the reservoir. For the

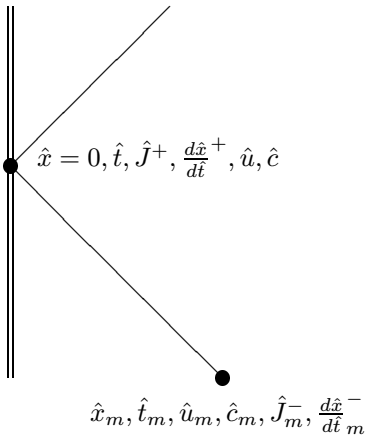

Figure D.3: Characteristic - projectile intersection.

infinite reservoir assumption, combining Eq. (D.10) and the negative forms of Eqs. (D.1) and (D.2) give the following expressions:

$$\hat{t} = \hat{t}_m - \frac{\hat{x}_m}{\frac{d\hat{x}}{d\hat{t}}^-_m} \tag{D.20}$$

$$\hat{c}^2 \left(\frac{\gamma + 1}{\gamma - 1}\right) + \hat{c}(2\hat{J}_m^-) + \frac{\gamma - 1}{2}(\hat{J}_m^-)^2 - 1 = 0 \tag{D.21}$$

$$\hat{u} = \hat{J}_m^- + \frac{2}{\gamma - 1}\hat{c} \tag{D.22}$$

For the finite reservoir assumption, Eqs. (D.21) and (D.22) are replaced by combining Eqs. (D.11 – D.13), yielding the following:

$$\hat{u}_2 \hat{c}_2^{\frac{2}{\gamma-1}} \frac{\gamma+1}{2} \frac{A_2}{A_1} = \left[1 - \sqrt{\frac{\gamma+1}{\gamma-1}\left[\hat{c}_2^2 + \frac{\gamma-1}{2}\hat{u}_2^2 - \frac{2}{\gamma+1}\right]}\right] \left[\frac{2}{\gamma+1} + \sqrt{\frac{\gamma-1}{\gamma+1}\left[\hat{c}_2^2 + \frac{\gamma-1}{2}\hat{u}_2^2 - \frac{2}{\gamma+1}\right]}\right]^{\frac{2}{\gamma-1}} \tag{D.23}$$

which, when combined with Eqs. (D.1) and (D.2), yields an equation suitable for numerical solution by Newton's method.

Figure D.4 shows a characteristic intersecting and reflecting from the projectile. Treating the projectile acceleration as constant between characteristic intersections and integrating it directly

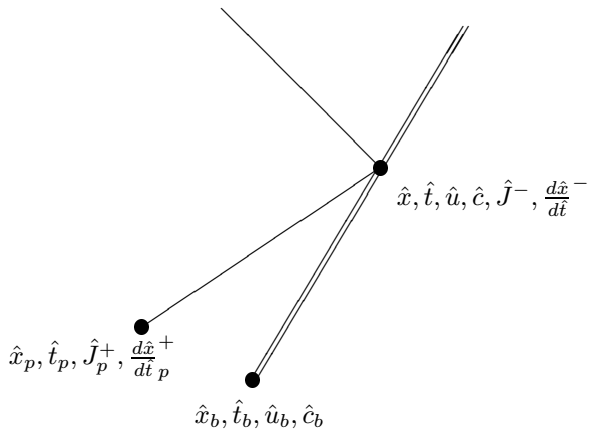

Figure D.4: Characteristic - projectile intersection.

for velocity and position, and combining the results with Eqs. (D.1) and (D.2) yields the following quadratic equation:

$$\hat{t}^2\left(\frac{1}{2}\hat{a}\right) + \hat{t}\left(\hat{u}_b - \hat{a}\hat{t}_b - \frac{d\hat{x}}{d\hat{t}}_p^+\right) + \hat{x}_b - \hat{u}_b\hat{t}_b + \frac{1}{2}\hat{a}\hat{t}_b^2 - \hat{x}_p + \frac{d\hat{x}}{d\hat{t}}_p^+\hat{t}_p = 0 \tag{D.24}$$

The other variables at the new node are then given by:

$$\hat{x} = \hat{x}_p + \frac{d\hat{x}}{d\hat{t}}_p^+(\hat{t} - \hat{t}_p) \tag{D.25}$$

$$\hat{u} = \hat{u}_b + \hat{a}(\hat{t} - \hat{t}_b) \tag{D.26}$$

$$\hat{c} = \frac{\gamma - 1}{2}(\hat{J}_p^+ - \hat{u}) \tag{D.27}$$

The advantage of non-dimensionalizing the flow variables is that the equations listed above can be solved numerically without regard for P_0, c_0, A, or m. Only γ and $\frac{A_2}{A_1}$ affect the result. Once this numerical solution is found, dimensional results can be computed directly. No further characteristics calculations are required to evaluate the effect of changes in P_0, c_0, A, or m, as long as γ and $\frac{A_2}{A_1}$ are unchanged.

Figure D.5 shows a non-dimensional x-t plot of computed characteristic interactions. The x-t path of the projectile is shown also, as the lower envelope of the characteristics reflections. The ratio of specific heats (γ) used was 1.67, and the area ratio (A_2/A_1) was 0.079, corresponding to the launch tube diameter of 25.4 mm and the shock tube diameter of 90 mm. The finite reservoir model was used.

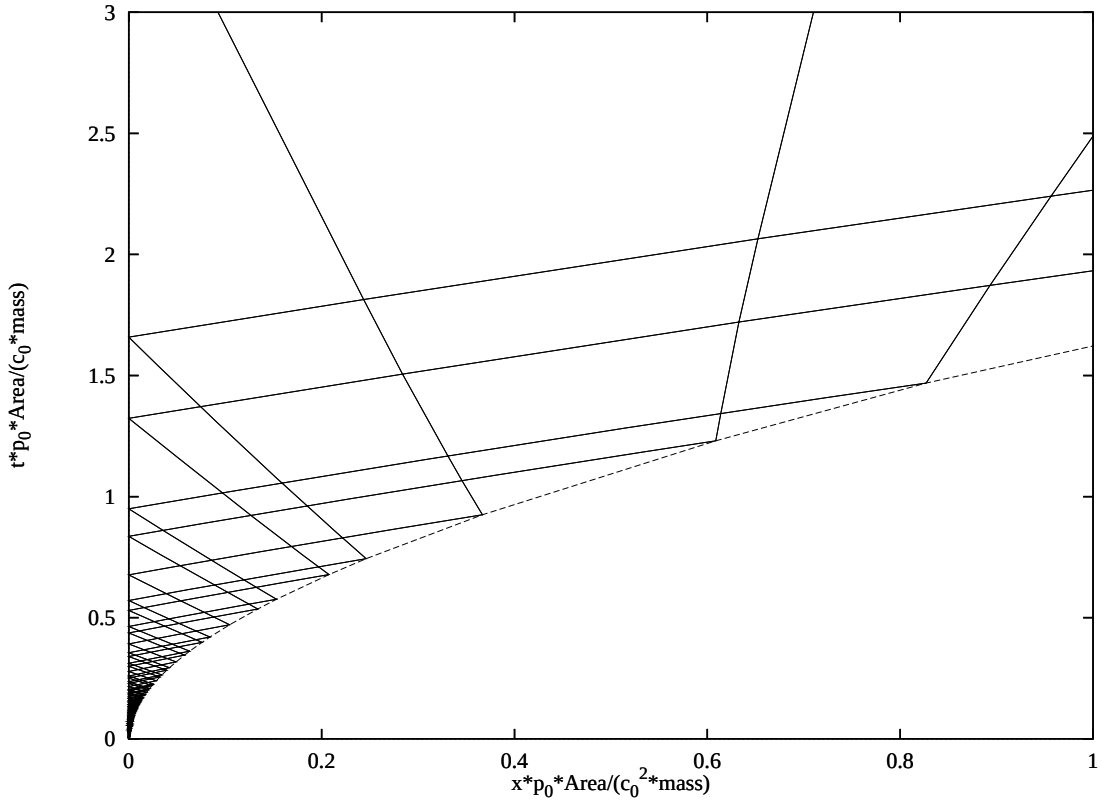

Figure D.5: Non-dimensional x-t characteristics diagram.

Appendix E Safety Assessment

January 12, 1995

GALCIT Laboratory Safety Assessment

Facility or Experiment	T5 Shock Tunnel, Detonation Wave Facility
Location	4th Floor of Guggenheim, West end of penthouse
Responsible Faculty or Staff	Joseph Shepherd
Research Associates or Students	Jacques Belanger, Michael Kaneshige

Brief Description

A series of detonation wave experiments will be carried out in the T5 shock tunnel laboratory. T5 is being modified by the addition of a launch tube, extending from the nozzle throat into the dump tank, and a test section/target section assembly, which will be mounted on the downstream door of the dump tank. The overall assembly of the gun tube and test section are shown in Fig. 5.2 and the test section itself is shown in Fig. E.1.

The high-enthalpy gas generated by T5 will accelerate a 1" diameter nylon sphere (about 10 grams) through the 10' long launch tube. Passing through the T5 dump tank with an estimated maximum velocity of 3500 m/s, the sphere will rupture a mylar diaphragm and enter the test section mated to the downstream door of the dump tank. A mixture of H_2 and O_2, with N_2 and Ar diluents, will detonate upon passage of the projectile. The kinetic energy of the projectile will be absorbed by a special catcher assembly in the target section, downstream of the test section. The T5 dump tank will be evacuated during each test, the test section will be pressurized to maximum 1 atm absolute, and the target section will contain air at 1 atm.

Below are the main steps of the procedure to be followed during each experiment:

1. Evacuate detonation wave test section and gas supply lines. Measure leak rate. If less than the acceptable level (1 mbar/15 min), proceed with test.

2. Fill detonation test section using the method of partial pressures. Monitor test section pressure to ensure integrity of seals and diaphragms. Isolate test section from gas supply system after final leak rate check.

3. Evacuate T5 components: secondary reservoir, compression tube, shock tube, and dump tank. Monitor test section pressure to ensure integrity of seals and diaphragms.

4. Pressurize T5 shock tube.

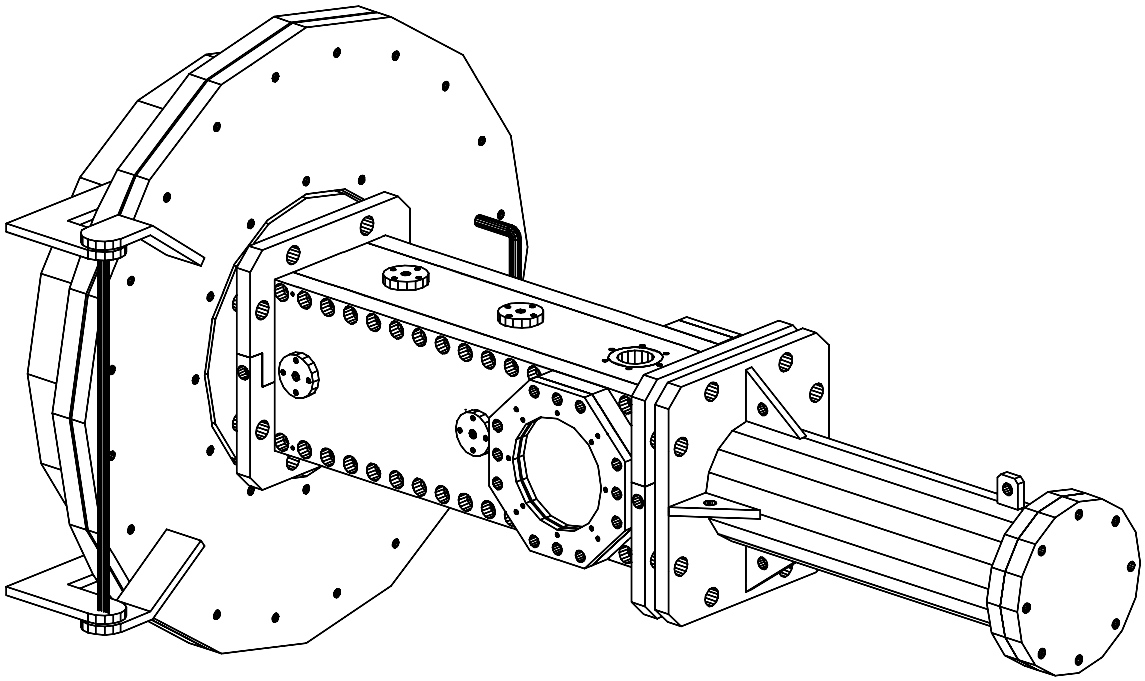

Figure E.1: Test and target sections assembled to the dump tank door.

5. Pressurize T5 compression tube.

6. Pressurize T5 secondary reservoir.

7. Launch T5 piston.

There is a check list attached to this SA that describes the portion of the experiment associated with the detonation test section. The existing check list for T5 will be used for operating T5 in the usual fashion.

See the figure below (Fig. E.2) for a schematic of the gas handling system associated with the detonation test section.

Potential for Extraordinary Hazards

Sources

Two aspects of this program present special hazards: the kinetic energy of the projectile, and the presence and use of hydrogen gas. Below, these hazards are discussed in terms of magnitude, severity, and likelihood, and the safeguards used to prevent accidents and mitigate their effects are outlined.

Magnitudes

The relative magnitudes of the different hazards can be assessed roughly by the energies involved. For instance, the maximum kinetic energy of the projectile is 61 kJ. Much of this energy will be

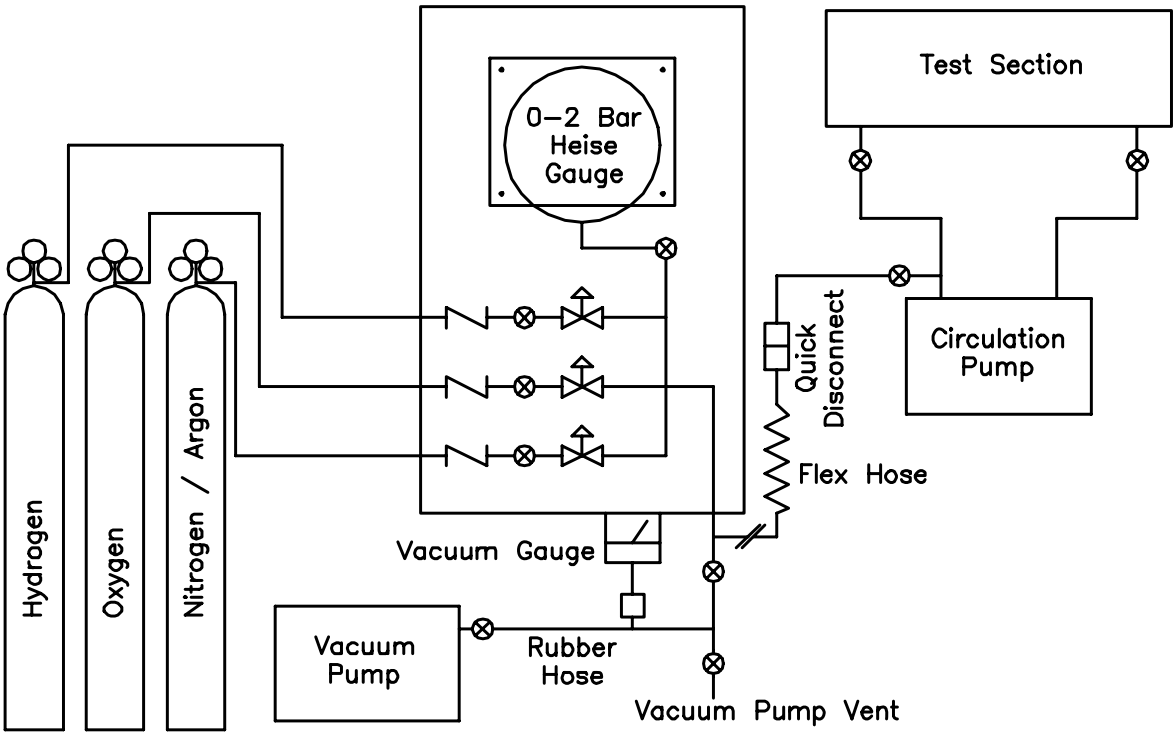

Figure E.2: Gas handling system for the detonation test section.

dissipated by the structure inside the target section, although enough will probably be absorbed by the sphere to partially melt and vaporize it (note that about 6.6 kJ are required to completely melt the projectile). The maximum energy content of the hydrogen stored in the test section is about 210 kJ. For comparison, in standard operation, the maximum energy stored in the T5 secondary reservoir is 43 MJ, and the maximum kinetic energy of the T5 piston is 5.4 MJ.

Design Philosophy

The chemical energy stored in the hydrogen will be released by an explosive combustion event. The resulting loading on the test section structure will be transient and spatially nonuniform. There are no standard design rules or codes for this situation and the usual guidelines such as Section 8 of the ASME Pressure Vessel Code do not apply. However, there is a substantial technical literature and a developing set of engineering practices for dealing with these situations. A summary of the state-of-the-art in detonation test section design and an example of a typical design is presented by Shepherd [102]. The document describes the basic philosophy of explosive containment design, which was followed in the design of the present detonation test section.

Standard mechanical engineering calculational procedures were used to compute the forces and moments on all structural members and fasteners. The calculations were as realistic as possible using hand computation. These stresses were compared to the allowable stresses in the materials, taking into account stress concentrations, reduction in strength due to flaws in the material and the

known limitations of fasteners. The test and target sections are constructed from AISI 304 stainless steel and the highest strength (ASTM A574) fasteners available are used to join the components.

The gas gun design used in the present case was carried out in a similar fashion. First detailed performance computations were carried out based on the accepted practice for gas gun design (summarized by Berggren and Reynolds [13]). Second, a detailed mechanical design was carried out for both the static and dynamic loads on the gun barrel, supporting structure and connections to the shock tube. Measured loads and accelerations from previous tests in T5 were used in conjunction with the estimated performance and structural response of the gun tube. The catcher assembly was based on prior practice [13] and experimental data obtained for hypervelocity projectiles similar to the present design [27].

The design event is a prompt detonation, which is modeled as a Chapman-Jouguet wave. However, a wide spectrum of other events can occur. The most severe events result from deflagration-to-detonation transition (DDT) and could potentially result in pressures up to four times the design loading. Historical evidence for these events (discussed by Shepherd [102]) indicates that they are very rare. For the present situation, we judge that these events are extremely unlikely since a prompt ignition source (the projectile) will always be available, the test section has a very small length-to-diameter ratio (5:1) and there are no obstructions within the test section. All of these circumstances mitigate against the likelihood of DDT occurring. However, to err on the side of safety, the test section has been designed to accommodate some significantly higher internal pressures (up to four times) than the design loading. The glass windows will fail but that is anticipated and will not pose a hazard to the personnel although some property loss may be incurred.

Design Loading

The apparatus has been designed to withstand a maximum expected loading (design loading) with a minimum factor of safety of 2, based on yield strength. The only accidents capable of approaching the ultimate strength of the structure are extraordinarily severe DDT's (see off-design case 10). Even in these cases, we do not expect to exceed the ultimate strength. The design loading is based on a projectile of maximum kinetic energy (61 kJ) and a gaseous mixture of maximum strength (undiluted stoichiometric H_2 and O_2 at 1 atm). The main loads on the structure are produced by a detonation in the test section and the impact of the projectile inside the target section. A maximum pressure of 100 atm inside the test section has been computed, based on an initial pressure of 1 atm, a detonation wave pressure ratio of 20, a normal reflection pressure ratio of 2.5 (conservative, because the actual wave will be oblique), and a dynamic loading factor of 2. This dynamic load factor accounts for the transient nature of the applied load and the elastic response of the structure. The actual value of the dynamic load factor will depend on the details of the applied load and the principal frequencies of oscillation of the structure [102]. Evaluating the modes and frequencies of a

bolted structure analytically is difficult so the largest possible value of 2 has been used.

The loading is complicated by the blast wave propagating from the launch tube, the venting of gases from the test section after rupture of the diaphragm, and by the shock wave propagating from the test section into the target section. Although detailed analyses of these dynamics have not been performed, some conservative estimates have been made of these loads, and they have been found to be negligible compared to the primary loads.

Axial loads will be imposed within the test section, target section, and the connecting members, by the projectile impulse and internal pressure. A series of honeycomb sheets, separated by aluminum plates, will collapse inside the target section upon impact of the projectile and the blast wave. Each honeycomb sheet will collapse under a certain compressive stress, so the maximum axial force transmitted through the target section is given by this stress and the sheet area. The honeycomb used is designed specifically for energy absorbing applications and is certified to crush at a specified applied pressure. Each lot is tested and certified to MIL-C-7438-G-AMD.1,Para.4.6.2.1. The honeycomb/aluminum plate catcher assembly is smaller in diameter than the target section and wooden spacers will be used to ensure clearance so that the assembly will not be canted or bind up during collapse.

Regardless of the dynamics of the projectile at impact, as long as the honeycomb is not entirely collapsed, the load transmitted through the target section and to the rest of the structure is limited to a certain maximum force. Based on a maximum honeycomb strength of 2400 psi and a 6" diameter cross section, the design axial load in the target section is 302 kN. The ends of the test section are closed except for mylar diaphragms (3" diameter). Therefore, the axial loads through the test section will be the sum of the projectile / blast wave impact loads and the pressure loads on the test section end plates. In the design case, this load is about 433 kN. Loads through the dump tank door are estimated by adding the projectile impact load, the impulse of the jet entering the dump tank, and the pressure difference force on the structure. This is about 253 kN.

The maximum momentum of the projectile is 35 N·s. Based on an estimated dump tank mass of about 2900 kg, and neglecting all friction forces on the structure, this results in a post-impact dump tank velocity of about 1.2 cm/s. This motion is relative to the T5 shock tube and nozzle, and is resisted by a vacuum force on the nozzle. Assuming no friction, this vacuum force will stop the dump tank in 3.7 ms, after 22 μm of travel. Therefore, the projectile impact will not cause significant motion of the dump tank.

Analysis of the projectile impact is based on the momentum and kinetic energy of the projectile. The amount of damage done in the impact is primarily correlated with the energy, while the forces imparted to the structure are primarily related to the momentum transfer involved. The kinetic energy of the projectile is dissipated by the deformation of the projectile, formation of a crater in the impact plate and the collapse of the honeycomb structure.

The impact plate is 2024-T351 aluminum, 1-inch thick. Material of this type and thickness was found [27] to be adequate to stop projectiles completely with initial velocities up to 6 km/s. The crater produced in the impact plate is estimated to be about 1/2-inch deep and roughly hemispherical. The shock heating resulting from the impact will be sufficient to melt the projectile. The melt will be ejected backward in a conical splash that will coat the interior of the target section.

Enough honeycomb will be used to accommodate all of the energy of the projectile. An analysis and review of experiments involving similar conditions have been performed to evaluate the momentum transfer from the projectile to the structure. The analysis indicates that the projectile will not vaporize to a significant extent, so that impulse from a vapor jet does not need to be considered. Experiments involving impacts of thermoplastic projectiles into aluminum plates found that the impacts ranged between perfectly elastic to perfectly inelastic over a range of velocities three times as great as ours. Therefore, the impulse imparted to the target structure is bounded at twice the projectile momentum. Since the force transmitted to the target section is limited by the honeycomb compressive strength as long as the honeycomb is not entirely collapsed, the purpose of the momentum analysis is only to verify that the honeycomb will not entirely collapse. After a perfectly elastic impact, the kinetic energy of the first plate in the stack will be far less than the original energy of the projectile, so there will be far more energy absorption capacity than necessary.

Ratings and Capacities

As previously mentioned, all parts of the apparatus have been designed to withstand the design loading with a minimum factor of safety of 2, based on yield strength. The actual capacities of the components, based on ultimate and yield strength, have been computed. The axial load capacities and corresponding design loads are listed below.

Table E.1: Axial loading capacities and strengths.

	Ultimate (kN)	Yield (kN)	Design Load (kN)
Test Section - Dump Tank Connection	1833	1510	302
Test Section	4804	2136	433
Test Section - Target Section Connection	1833	1510	302
Target Section	4087	1362	302
Target Section End Plate Bolts	757	606	302
Target Section End Plate	1451	1866	302

The actual loading is very transient. The axial loads will be applied over the duration of the impact, which is about 100-200 μs for a 3000 m/s projectile. The detonation pressure loading will be immediately relieved by the nonsteady expansion behind the wave and venting of the products

into the dump tank. The pressure will be reduced to a very low value within a few ms of the peak. The test section and target section have both been designed as pressure vessels. In this respect, pressure ratings and ultimate capacities have been computed. A single minimum rating of 115 bar has been determined for the entire assembly, primarily because the components will be hydro-tested as an assembly. The ultimate capacities for the subassemblies are given below.

The strength of the glass windows is difficult to estimate because of the highly uncertain properties of the glass and sensitivity of the strength to the surface condition and stress concentrations. The windows are a disk of BK7, 2.5 inch thick and 7 inch diameter contained in a steel and aluminum cell.

Table E.2: Pressure vessel capacities.

	Ultimate (bar)	Design (bar)
Test Section	462	115
Target Section	415	115

The window cells have been designed to prevent any contact of the metal surfaces with the glass, using 3 O-rings to position the windows axially and radially. In case of an exceptional DDT, the glass is expected to fail. Previous experience with these events in the PI's lab at RPI indicated that the failure mode is to produce cracks and fractures within the glass but no shattering. Previous experience indicates that a tensile strength of 3000 psi is a reasonable design criterion and plate glass can generally be expected to withstand up to 10,000 psi. Using the thin plate approximations for the stresses, this implies a maximum working pressure between 1250 and 4500 psi within the test section.

Aside from the windows, the weakest components in the structure are the fasteners. For the axial loads, the bolts on the target section end plate will fail first. This is intended to prevent the entire test section from being torn from the dump tank if the catcher fails. For the pressure loading, the test section plate bolts will fail first.

Off-Design Cases

Below is a list of off-design events possible during execution of these experiments, and an explanation and analysis of the severity of each.

1. *Test section leak into the dump tank.* Due to faulty diaphragm installation or premature diaphragm rupture, the gas inside the test section may leak into the dump tank. In the event that the dump tank is evacuated and the diaphragm ruptures, the worst case involves full 1 atm pressurization of the test section with stoichiometric H_2 and O_2. In this case, the test section

gas will expand to fill the dump tank. At the resulting low pressure, a detonation is extremely unlikely. A detonation within the dump tank would result in a maximum pressure of about 2.9 kPa, negligible compared to the rated working pressure of 50 psia. Another possibility is that the gas introduced into the test section will inadvertently fill the dump tank. This will be prevented by evacuating and filling the detonation test section prior to evacuating the dump tank. The fill pressure within the detonation test section is always less than or equal to one atmosphere so that by monitoring the pressure in the test section, leaks into the dump tank can be detected.

2. *Hydrogen leak into the working environment.* Procedures are currently in place in the T5 laboratory for the handling of hydrogen gas. Specifically, the air is monitored for hydrogen by two detectors located near the highest point in the enclosure. These detectors have a sensitivity of 500 ppm. The room is ventilated at a rate of about 17 m^3 per minute by an exhaust hood and fan over the dump tank. The lower flammability limit of hydrogen in air is 4%. If the maximum amount of hydrogen contained in the test section (1 atm fill pressure) is diluted 25 times (this requires about .44 m^3 of air), it will not be flammable.

3. *Test section leak into the target section.* Since the target section will contain air at 1 atm, a diaphragm rupture between the test section and target section will result only in the dilution of the test section. However, the target section has been designed to the same rated pressure as the test section, so that it can contain any subsequent detonation. The filling procedures will detect any leak present before the test.

4. *Deflection of projectile trajectory.* In order for useful results to be obtained, the projectile must be on target vertically within about 1/2 inch at the imaging window. However, it may deviate at least 1 inch (at diaphragm station 3) without impacting undesired parts of the apparatus. At the low end of the energy range to be explored, an inadvertent impact will have negligible destructive effects. At the high end, such an impact could result in significant equipment damage. Because of the high velocity of the projectile, very large forces are required to deflect it from its initial path. Therefore, the only possible causes of significant lateral motion are misalignment or movement of the launch tube. The launch tube alignment will be checked by visual inspection prior to each test.

5. *Misalignment or movement of the launch tube.* The launch tube will be aligned with the test section very precisely before each test (unless experience indicates that realignment is unnecessary) with a laser beam. The dynamic motion of the launch tube resulting from the stress wave propagating down the shock tube, and its effect on the motion of the projectile, is difficult to predict, however. Low energy experiments will be used to commission the system, and

experience gained in these cases will guide any action necessary to ensure adequate alignment at higher energies.

6. *Kinetic energy absorption system malfunction.* The honeycomb structure in the target section may collapse in an unexpected mode (for instance, unevenly) or could conceivably collapse fully before dissipating all of the projectile's kinetic energy. This is unlikely, because the amount of honeycomb provided for energy absorption will be significantly greater than the amount expected to be necessary. In addition, experience gained in the early, low energy experiments will guide later, higher energy experiments. The first tests will involve at least twice as much honeycomb as considered necessary.

7. *Failed detonation in the test section.* The gas mixture in the test section may fail to detonate upon passage of the projectile, perhaps due to an especially lean mixture or low projectile velocity. The projectile will certainly rupture both diaphragms, however, and the gases will be vented into the target section and the dump tank. In this case, the most significant hazard is a detonation following venting (see case 1). The loads and stresses will be no higher than those in a design event.

8. *Misfire.* In the event that an experiment is readied (T5 prepared to shoot, test section filled with detonable gas mixture) but circumstances prevent a launch, the test section gases must be vented. An accidental detonation in this situation would not generate loads greater than the design case, but it would be desirable to vent the gases to the outside environment. In this event, the pressure in the test section would be increased by the injection of diluent until rupture of the dump tank / test section diaphragm. The diluted gas mixture would vent into the dump tank, which can be vented to the environment.

9. *Premature projectile launch.* Approximately 5 atm of helium will be placed in the shock tube prior to an experiment. This helium will be separated from the dump tank vacuum by a mylar diaphragm, and the projectile will be placed on the shock tube side of the diaphragm, prior to evacuation and pressurization. The diaphragm will rupture when the shock wave reaches the end of the shock tube and launches the projectile, but it may also rupture prematurely, for instance during pressurization of the shock tube. In this case, the projectile may obtain an estimated maximum velocity of 400 m/s. Since this sequence is otherwise identical to a routine experiment, this case may be considered to be a very low energy experiment. Thus there is no special hazard presented. Note that under standard procedure, the shock tube will not be pressurized until the test section and target section are prepared.

10. *Deflagration to Detonation Transition (DDT).* The occurrence of a DDT would generate significantly greater pressures than those associated with a prompt detonation. Such an event is

considered highly unlikely in the present apparatus, based on the length scales involved and the estimated cell sizes of the intended detonations. However, the apparatus has been designed to accommodate an exceptional DDT. The windows would fail but are not expected to shatter. No personnel will be located within 80 feet of the detonation test section during firing and the windows are perpendicular to the line of sight. The flight paths of fragments are obstructed by the dump tank and surrounding equipment. The personnel will be wearing earmuffs and the vented gases will be inert (steam and nitrogen or argon).

Procedural Precautions

In addition to the design precautions mentioned above, certain procedures will be observed to minimize danger from equipment failure or the occurrence of off-design events.

1. The experiments will progress from low velocity projectile and inert fills in the detonation test section to progressively more challenging cases. A preliminary test matrix is attached. The first experiments planned will involve a minimum projectile velocity (400 m/s) and no reactants in the test section.

2. The test section and target section are considered to be pressure vessels, although of a special nature. Therefore, they will be hydro-tested to 150% of their rated pressure prior to use.

3. After any extraordinarily stressful event, such as a DDT, all structural components will be replaced or examined by non-destructive techniques (for instance radiography), and the assembly will be hydro-tested again.

4. To prevent fatigue failure, the apparatus will be periodically overhauled, and all structural bolts will be replaced.

5. Personnel access to the area around the test and target sections will be restricted to essential personnel during filling and off-limits until the shot is completed.

Conclusion

Special attention must be given to the safety of the detonation wave experiments described here, due to the unusual nature of the apparatus and the proximity to people and equipment. Application of appropriate safety factors to the design and careful evaluation of all foreseeable failure modes, along with cautious procedural safeguards, as described here, will ensure safe operation.

Check List for Detonation Tests in T5

Prepare T5, short of evacuating

Install launch tube and projectile

Prepare test section and target section

Assemble test section, target section, T5

Prepare Instrumentation

Evacuate test section

Close

_ gas valves

_ vacuum pump vent valve

Open

_ Heise gauge valve

_ Vacuum pump valve

_ Vacuum isolation valve

_ Trolley isolation valve

_ Test section gas feed valves

_ Connect quick-disconnect to trolley

_ Start circulation pump

_ Start vacuum pump

_ When Heise gauge is low, turn on vacuum gauge

_ Wait for vacuum

    _ Isolate test section and plumbing and wait 15 min

    _ Pressure should not increase more than 1 mbar

Fill test section

_ Close vacuum isolation valve

_ Turn off vacuum gauge

_ Turn off vacuum pump

_ Open vacuum vent valve

_ Total pressure desired _____ kPa

_ Gas 1 _____

_ Target fraction _____ %

_ Partial pressure _____ kPa

_ Open gas 1 ball valve

_ Fill test section to target pressure

_ Final pressure _____ kPa

_ Close gas 1 ball valve and needle valve

_ Gas 2 _____

_ Target fraction _____ %

_ Partial pressure _____ kPa

_ Target final pressure _____ kPa

_ Open gas 2 ball valve

_ Fill test section to target pressure

_ Final pressure _____ kPa

_ Close gas 2 ball valve and needle valve

_ Gas 3 _____

_ Target fraction _____ %

_ Partial pressure _____ kPa

_ Target final pressure _____ kPa

_ Open gas 3 ball valve

_ Fill test section to target pressure

_ Final pressure _____ kPa

_ Close gas 3 ball valve and needle valve

_ Close trolley isolation valve

_ Close Heise gauge valve

_ Disconnect trolley quick-disconnect

_ Circulate for _____

_ Close test section gas feed valves

_ Shut off circulation pump

Evacuate T5

Fill T5

Launch

Clean up

_ Open test section gas feed valves

_ Start circulation pump and wait 30 seconds

_ Shut off circulation pump

_ Close test section gas feed valves

Appendix F Timing Circuits

This appendix describes the implementation of an electronic circuit for control of the laser flash lamp timing for shadowgraph and differential interferometry purposes. Timing of the q-switch was performed independently, either by synchronization with a projectile detector, or by a fixed delay from the flash lamp trigger. The goal of this design was to use inputs from two upstream detectors to compute the projectile speed, compute the time of arrival of the projectile at the optical window, and deliver a trigger at a fixed interval prior to that. While a digital circuit could have been used, linear circuits were used primarily, to minimize complexity and to make use of standard, readily available components.

Fig. F.1 shows the block diagram of the intended system. As in the system described by Chernyavskii et al. [20], the three main components are two ramp generators triggered by the two upstream sensors and the comparator that generates the output signal when the second ramp overtakes the first. The ramp generator outputs increase linearly with time. The ramp rates and initial offsets

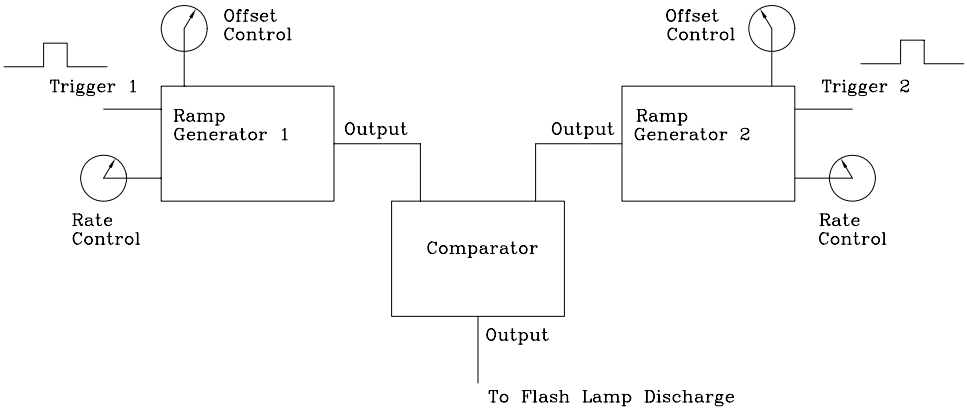

Figure F.1: Timing circuit block diagram.

can be controlled. Settings for these controls are determined as follows. As illustrated in Fig. F.2, the position of the projectile and the ramp voltages are linear with respect to time. Implicit in this analysis is the assumption that the projectile velocity is constant during its flight. Thus,

$$\text{velocity} = \frac{l_1}{t_1} = \frac{l_2}{t_2} \tag{F.1}$$

and

$$V_1 \quad = \quad V_{1,0} + k_1 t \tag{F.2}$$

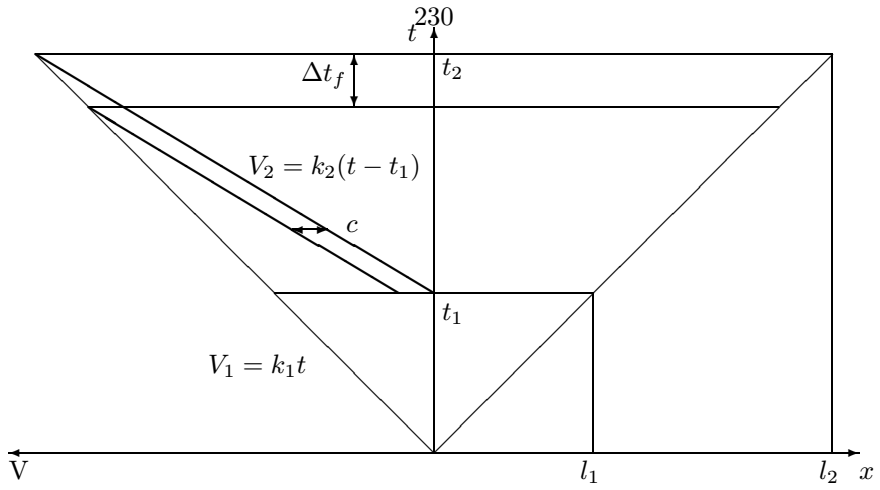

Figure F.2: V-t and X-t diagram showing active timing scheme.

$$V_2 \quad = \quad V_{2,0} + k_2(t - t_1) \tag{F.3}$$

The desired result is a signal from the comparator a fixed delay Δt_f before the projectile reaches the optical window, l_2. This time is

$$t_{fl} = t_2 - \Delta t_f = \frac{l_2}{l_1} t_1 - \Delta t_f \tag{F.4}$$

Given that the comparator will trigger when V_2 is greater than V_1, the condition at t_{fl} is:

$$V_{1,0} + k_1 \left[\frac{l_2}{l_1} t_1 - \Delta t_f \right] = V_{2,0} + k_2 \left[-t_1 + \frac{l_2}{l_1} t_1 - \Delta t_f \right] \tag{F.5}$$

Requiring that Eq. F.5 be independent of time yields:

$$\frac{k_2}{k_1} = \frac{l_2}{l_2 - l_1} \tag{F.6}$$

which is identical to the relation used by Chernyavskii et al. [20]. Eq. F.5 then reduces to:

$$c = V_{2,0} - V_{1,0} = k_1 \Delta t_f \frac{l_1}{l_2 - l_1} \tag{F.7}$$

k_1 and $V_{1,0}$ can be chosen arbitrarily, and k_2 and $V_{2,0}$ are then constrained in terms of l_1, l_2, k_1, $V_{1,0}$, and Δt_f.

Fig. F.3 shows the circuit diagram used to implement this scheme. The ramp rates k_1 and k_2 are given by:

$$k = \frac{dV}{dt} = Ci \tag{F.8}$$

where the capacitor values $C1$ and $C2$ are noted on Fig. F.3, and the current i for this circuit is given by $i = (5\text{ V})/R$, where $R1$ and $R2$ are noted on Fig. F.3. The ramp rates were controlled by the

potentiometers represented by $R1$ and $R2$. To attain different ranges of ramp rates, the capacitors $C1$ and $C2$ could be changed. The initial voltages (ramp offsets) were controlled by the variable resistors labeled "Trim Control."

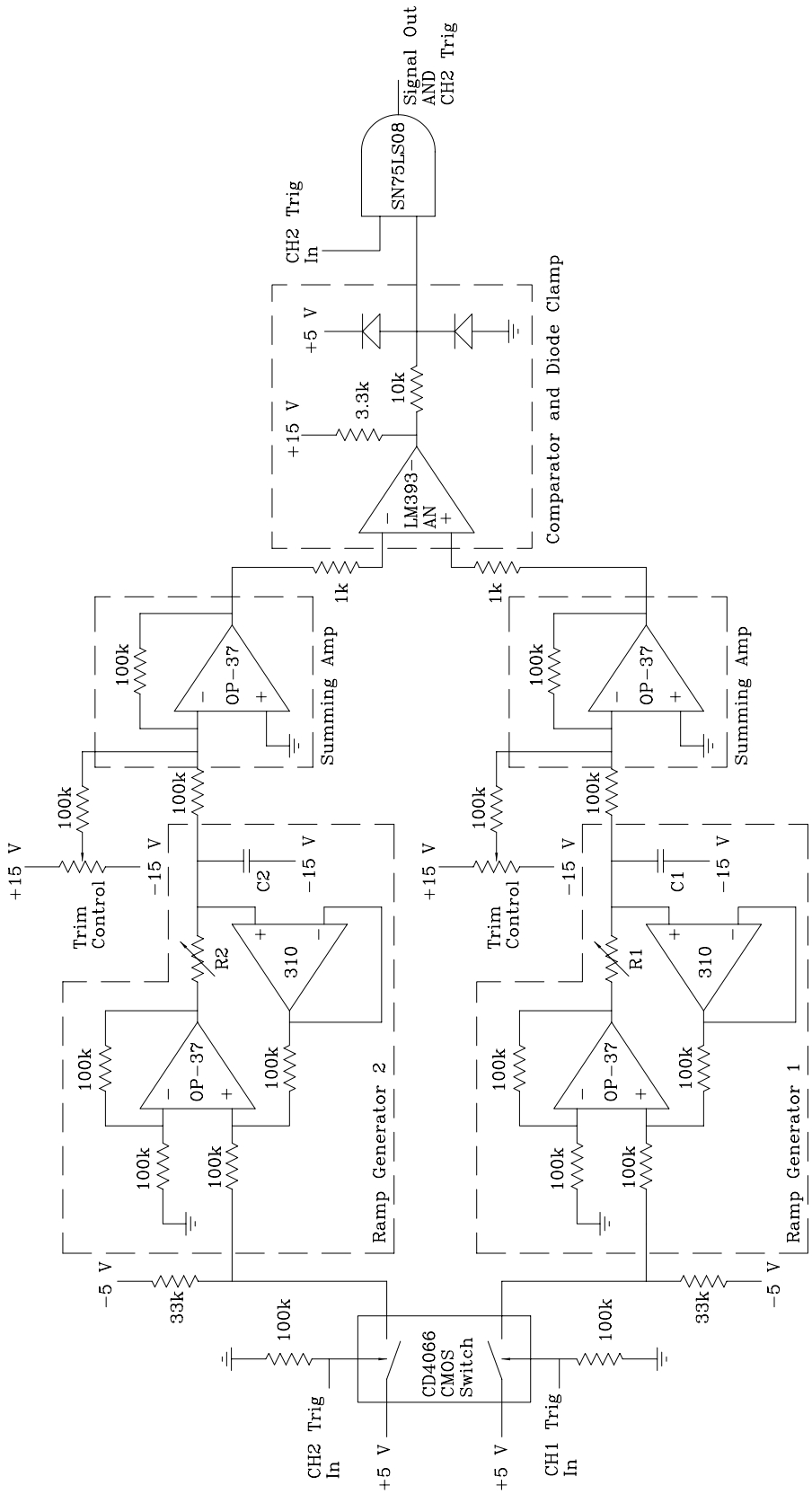

Figure F.3: Timing circuit diagram.

Appendix G Transverse Curvature of an Axisymmetric Shock

This appendix presents a proof of the expression used in Section 3.2 for the transverse curvature of an axisymmetric shock. That is, that the curvature κ_2 is given by the simple formula

$$\kappa_2 = \cos\beta / r \tag{G.1}$$

Using the shock-fitted coordinate system defined in Fig. 3.1 and illustrated again in Fig. G.1, the in-plane shock curvature, κ_1, is the curvature of the shock profile in the x-y plane. The transverse shock curvature, κ_2, is the curvature of the shock profile in the y-ζ plane. As apparent from Fig. G.1, Eq. (G.1) is equivalent to saying that the transverse radius of curvature (i.e., $1/\kappa_2$) is the distance from the shock to the axis of symmetry, in the y direction.

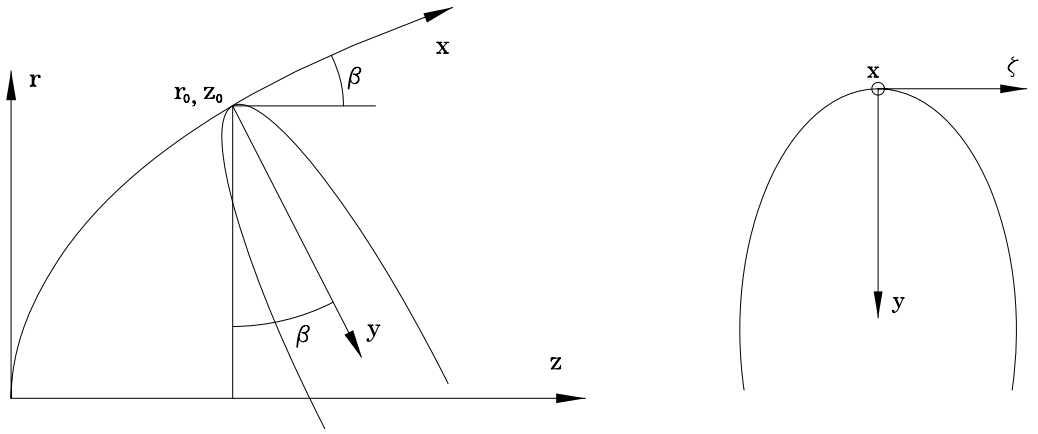

(a) Shock shape and cutting plane

(b) Shock shape in $y - \zeta$ plane

Figure G.1: Axisymmetric shock shape and cutting plane geometry and notation.

An axisymmetric shock shape can be represented by a function $z = f(r)$ that has the property that

$$\frac{df}{dr} = \frac{1}{\tan\beta} \tag{G.2}$$

where β is the shock angle.

The shock profile in the y-ζ plane is the intersection of the shock surface with the y-ζ plane. This curve may be represented by a function $y_s(\zeta)$, and since it has zero slope at $\zeta = 0$, its curvature is

given by

$$\kappa_2 = \left| \frac{d^2 y_s}{d\zeta^2} \right| \tag{G.3}$$

The equation for the intersection curve must satisfy the generating equations for both surfaces. The y-ζ plane can be represented by

$$z = z_0 + y_s \sin\beta \tag{G.4}$$

so that the curve can be represented by

$$z = f(r) = z_0 + y_s \sin\beta \tag{G.5}$$

where

$$r^2 = \zeta^2 + (r_0 - y_s \cos\beta)^2 \tag{G.6}$$

Differentiating Eq. (G.5) twice with respect to ζ,

$$\frac{df}{dr}\frac{dr}{d\zeta} = \frac{dy_s}{d\zeta}\sin\beta \tag{G.7}$$

$$\frac{d^2 f}{dr^2}\left(\frac{dr}{d\zeta}\right)^2 + \frac{df}{dr}\frac{d^2 r}{d\zeta^2} = \frac{d^2 y_s}{d\zeta^2}\sin\beta \tag{G.8}$$

Differentiating Eq. (G.6) twice with respect to ζ gives

$$r\frac{d^2 r}{d\zeta^2} = 1 + \cos^2\beta\left(\frac{dy_s}{d\zeta}\right)^2 - (r_0 - y_s\cos\beta)\cos\beta\frac{d^2 y_s}{d\zeta^2} - \left(\frac{dr}{d\zeta}\right)^2 \tag{G.9}$$

At the point $(r_0,\, z_0)$, $\zeta = 0,\ \dfrac{dy_s}{d\zeta} = 0,\ \dfrac{dr}{d\zeta} = 0,$ and $y_s = 0$. Substituting these into Eqs. (G.8) and (G.9) and combining with Eq. (G.2) yields

$$\frac{d^2 y}{d\zeta^2} = \frac{\cos\beta}{r} \tag{G.10}$$

Therefore,

$$\kappa_2 = \frac{\cos\beta}{r} \tag{G.11}$$